SIMULTANEOUS FLOW VISUALIZATION AND UNSTEADY-SURFACE-PRESSURE MEASUREMENTS IN NORMALLY AND OBLIQUELY LAMINAR IMPINGING JETS

By

Malek Omar Al-Aweni

A DISSERTATION

Submitted to
Michigan State University
in partial fulfillment of the requirements
for the degree of

Mechanical Engineering – Doctor of Philosophy

ABSTRACT

SIMULTANEOUS FLOW VISUALIZATION AND UNSTEADY-SURFACE-PRESSURE MEASUREMENTS IN NORMALLY AND OBLIQUELY IMPINGING JETS

By

Malek Omar Al-Aweni

Impinging jets are important in many engineering applications, such as heating, cooling, drying and Short Takeoff and Landing (STOL) aircrafts, as well as in understanding some of nature's phenomena, such as microbursts. There are numerous studies on the heat transfer from the surface upon which the jet impinges, but comparatively very few investigations of the space-time characteristics of the pressure fluctuations acting on the impingement wall. Moreover, the bulk of the latter investigations lack concurrent flow-field information, and therefore their conclusions regarding the pressure generation mechanisms remain largely hypothetical. The current study investigates the impinging-jet flow structures and their relation to the wall-pressure signature employing simultaneous unsteady-surface-pressure measurements, using a microphone array, and time-resolved flow visualization, using the smoke-wire technique, in an axisymmetric jet in normal and oblique impingement. The investigation is conducted at a jet Reynolds number based on diameter of 7334 for separations between the jet exit and the impingement plate ranging from two to four jet diameters, at normal and 30° oblique impingement angles.

Spectral analysis of the surface pressure fluctuations show that the flow above the wall contains higher Strouhal numbers when the plate is placed closer to the jet exit. The flow structures and mechanisms responsible for generating the pressure fluctuations at these Strouhal numbers are revealed using the simultaneous pressure and flow visualization information. It is found that within the wall-jet region, where the highest pressure fluctuations are observed, the

pressure fluctuations are predominantly influenced by the advection and evolution of the jet vortices and their interaction with each other and with the wall. These vortices are observed to exhibit one of two scenarios within the wall jet zone: to pass without mutual interaction, or to merge as they travel above the wall. In the passage scenario, as the vortex travels above the wall, it very often forms a secondary vortex, via interaction with the wall. This interaction leads to the generation of a strong negative pressure spike at the radial locations where the pressure fluctuation is large. A qualitatively similar signature is also found in the vortex merging scenario, although in this case the pressure spike is substantially stronger and secondary-vortex formation could not be seen in the smoke visualization. In order to study this phenomenon in more details, numerical computations of related model problems are carried out using Ansys Fluent. These problems involve the evolution of a single and dual axisymmetric vortex rings that interact with a flat wall. The resulting databases are analyzed by studying the volumetric distribution of the wall-pressure sources and their wall-pressure imprint using Green's function solution of Poisson's equation for pressure. The results reveal pressure signatures that are qualitatively similar to those observed experimentally in the impinging jet. The pressure-source analysis reveals the mechanisms leading to these signatures and the associated contribution of the individual flow features.

To my parents, lovely wife and my kids

ACKNOWLEDGEMENTS

I would like to start by expressing my gratefulness to my advisor Dr. Ahmed Naguib for his guidance, teaching and mentorship throughout my PhD work. He is always there with insights, patience and support. Dr. Naguib, I cannot thank you enough. I would like to thank very much my committee members (Dr. Brereton, Dr. Jaberi and Dr. Oweiss) for their discussions and comments on my work. Many thanks to all professors who taught me during my graduate study at Michigan State University.

Thank you to Michael Mclean and Roy Bailiff for their help in fabricating and setting the experimental apparatus. Thank you to my lab mates and friends Kyle Bade and Gaurang Shrikhande and to all my other friends in the ERC who made life at the laboratory enjoyable.

Special thanks to the community of East Lansing and Lansing and to the great individuals Michael Harrison, Eugenia Zacks-Carney and Peter Briggs who stood up and supported us (Libyan Students) during the Libyan revolution, a time of uncertainty.

I would to thank my friends Husam Abdurrahman and Yalla Aboushawashi for their friendship and making life enjoyable at MSU. Thank you to all my friends and class mates during the graduate study. Special thanks to Hisham Elbouzidi, a true friend in need who always believed in me.

None of this would be achievable without the love and support from my parents, the patience and the love from my wife Manar and the smile of my Kids Mayssa and Anas. My siblings Manal, Marwan, Omaima, Khawla and Boutania for their unwavering encouragement.

This study was partially supported by the National Science Foundation grant Number OISE-0611984 and the Libyan Ministry of Higher Education.

TABLE OF CONTENTS

LIST OF TABLES	VIII
LIST OF FIGURES	ix
KEY TO ABBREVIATIONS	xvii
Chapter 1: Introduction	
1.1 Background	
1.1.1 Free Jets	
1.1.2 Impinging Jets	
1.1.2.1 Governing Equation	
1.1.2.2 Literature Review	
1.2 Motivation	
1.3 Objectives	11
Chapter 2: Experimental Apparatus	13
2.1 Flow Configuration	
2.2 General Assembly of the Experimental Setup	15
2.2.1 Plate Traverse System	16
2.2.2 Jet Flow and Impingement Plate Alignment	17
2.3 Hot Wire Setup	24
2.4 Microphones Setup	28
2.5 Simultaneous Wall-Pressure Measurement and Flow Visualization Setup	34
2.5.1 Flow Visualization	34
2.5.2 Synchronized Flow Visualization and Microphones Measurements Setup	36
2.1.6 Data Acquisition Hardware	42
Chapter 3: Shear Layer Study	43
3.1 Self Similarity of the Initial Shear Layer	
3.2 Momentum Thickness	46
3.3 Power Spectral Analysis of the Initial Disturbance	50
3.4 Evolution of the Power Spectra with Downstream Distance	53
Chapter 4: Pressure Measurements	57
4.1 Root Mean Square of Pressure Fluctuations	
4.2 Power Spectral Density	62
4.1.1 Normal Impingement	
4.1.2 Oblique Impingement: Forward-Flow Side	67
4.3 Convection Velocity	73

5.1 Normal impingement	80
5.1.1 Stagnation point pressure signature	116
5.2 Oblique Impingement Forward Flow	119
5.3 Oblique impingement back flow	144
Chapter 6: Wall-Pressure Generation From Axisymmetric Vortex Rings Interact	
a Wall	
6.1 Experimental Observations	156
6.1.1 Secondary Vortex Formation	156
6.1.2 Near-Wall Vortex Merging	159
6.2 Simulation of the Model Problems	162
6.2.1 Geometry of Computational Model	162
6.2.2 Simulations Using ANSYS-Fluent	165
6.2.3 Simulation Results.	166
6.2.3.1 Model Problem I: Secondary Vortex Formation	166
6.2.3.2 Model Problem II: Near-Wall Vortex Merging	186
Chapter 7: Conclusions and Recommendations	193
APPENDICES	199
Appendix A: Jet Nozzle	200
Appendix B: Synchronization Set-up	202
Appendix C: Wave-path interpolation method	207
Appendix D: Temporal and Spatial Signature at <i>H/D</i> =3 and Normal Impingement	210
Appendix E: Comparison Between the Experimental and Computational Data Re	ported by
Shrikhande [30]	211
BIBLIOGRAPHY	217

LIST OF TABLES

Table 4.1 Summary of aver	age convection vel	locity for <i>H/D</i> =	2, 3 and 4 and	d normal and	oblique
(forward-side) i	mpingement				79

LIST OF FIGURES

Figure 1.1	Schematic drawing demonstrating vortex formation and successive vortex merging
Figure 1.2	Schematic of impinging jet flow in normal incidence
Figure 2.1	Illustration of the flow configuration and coordinate system superimposed on actual flow visualization of the impinging jet flow at normal (top) and oblique (bottom) incidence. For interpretation of the references to color in this and all other figures, the reader is referred to the electronic version of this dissertation
Figure 2.2	Impinging-jet facility at FPaCL10
Figure 2.3	Three-dimensional model of the traversing system used for holding and traversing the impingement plate
Figure 2.4	Schematic drawing of the experimental setup used to align the impingement plate relative to the jet flow
Figure 2.5	Normalized mean pressure profiles along z_p and y_p axes at H/D =4. P_s denotes the mean stagnation pressure
Figure 2.6	Normalized mean pressure profiles along z_p and y_p axes at $H/D = 8$. P_s denotes the mean stagnation pressure
Figure 2.7	Color contour maps of the normalized mean pressure. The color bar to the right provides the magnitude of the mean pressure normalized by the mean stagnation pressure at the center of the disc: profiles along the z_p (a) and y_p (b) axis at different x_j/D
Figure 2.8	Normalized mean-pressure distribution on the impingement plate24
Figure 2.9	Schematic drawing of the hot wire setup during measurement of the streamwise velocity profiles across the shear layer surrounding the jet. During calibration, the Pitot tube is moved from the location shown in the figure to be within approximately 5 <i>mm</i> from the hot wire inside the potential core
Figure 2.1	0 Sample hot-wire calibration before and after an experiment
Figure 2.1	1 Configuration of the microphone array embedded in the impingement plate: frontal view (top) and cross section A-A (bottom)
Figure 2.1	2 Image of the microphone calibration setup
Figure 2.1	3 Schematic drawing of the microphone calibration setup
Figure 2.1	4 A sample microphone calibration; sensitivity (top) and phase shift (bottom)33

Figure 2.1	5 Flow visualization images at $H/D=2$; normal ($\gamma=0^{\circ}$) (a) and oblique ($\gamma=30^{\circ}$) (b) impingement
Figure 2.1	6 Three-dimensional drawing of the flow visualization setup
Figure 2.1	7 Block diagram of simultaneous flow-visualization and pressure-measurement setup
Figure 2.1	8 A sample of the recorded FLD signal and pressure data (a) (τ is the time since the start of the data acquisition), and a zoomed-in view around the time when the first image is captured of the pressure signals and FLD signal (b): different colors correspond to signals from different microphones and the plenum pressure transduces which are much smaller in magnitude than the FLD signal
Figure 3.1	Mean velocity profiles across the shear layer, demonstrating self-similarity with respect to change in the jet velocity at $x_j/D=0.2$, also compared against shear layer solution by Lock[31]
Figure 3.2	Mean velocity profiles across the shear layer, demonstrating self-similarity with respect to downstream distance for Re_D =7,970
Figure 3.3	Growth of the shear layer momentum thickness downstream of the jet. The streamwise coordinate is normalized by jet exit diameter. Arrows indicate the resonance location $(x_{j,r})$, and the broken lines represent linear-fits of the momentum thickness data downstream of the resonance location
Figure 3.4	Growth of the shear-layer momentum thickness downstream of the jet. The streamwise coordinate is normalized by the initial momentum thickness. Arrows indicates the resonance location $(x_{j,r})$
Figure 3.5	Momentum thickness variation with Reynolds numbers at $x_j/D = 0.2$
Figure 3.6	Normalized velocity <i>rms</i> profile across the shear layer for different Reynolds number at resonance locations
Figure 3.7	Velocity power spectra (normalized by the square of the jet exit velocity) versus frequency at $x_j/D = 0.2$ and $y_j/D = y_{j0.5}$
Figure 3.8	Velocity power spectra (normalized by the square of the jet exit velocity) versus Strouhal number based on momentum thickness at $x_j/D = 0.2$ and $y_j/D = y_{j0.5}$ 5
Figure 3.9	Streamwise-velocity power spectral density versus Strouhal number at different x_j/D locations downstream of the jet for $Re_D = 7.334$.

Figure 3.1	0 Streamwise-velocity power spectral density versus Strouhal number with impingement plate present at <i>H/D</i> =4
Figure 4.1	Effect of impingement angle on pressure rms distribution in the radial direction for $H/D=2$
Figure 4.2	Effect of the impingement plate location on pressure <i>rms</i> distribution in the radial direction for normal impingement
Figure 4.3	Effect of the impingement plate location on pressure <i>rms</i> distribution in the radial direction for oblique impingement at <i>H/D</i> =2, 3 and 462
Figure 4.4	Wall-pressure power spectral density at different radial locations for normal impingement and (a) $H/D=2$, (b) $H/D=3$ and (c) $H/D=4$. Plots a1, b1 and c1 correspond to the stagnation zone ($r/D=0-1$) and plots a2, b2 and c2 correspond to the wall-jet zone ($r/D=1.33-2.33$)
Figure 4.5	Wall-pressure power spectral density at different radial locations in the wall-jet zone for normal impingement and $H/D=3$
Figure 4.6	Wall-pressure power spectral density at different radial locations for oblique impingement (forward-flow side) and (a) $H/D=2$, (b) $H/D=3$ and (c) $H/D=4$. Plots a1, b1 and c1 correspond to $r/D=0-1$, and plots a2, b2 and c2 correspond to $r/D=1.33-2.33$
Figure 4.7	Wall-pressure power spectral density at different radial locations for oblique impingement (back-flow side) and (a) <i>H/D</i> =2, (b) <i>H/D</i> =3 and (c) <i>H/D</i> =472
Figure 4.8	Auto-correlation of the time series measured at r/D =0.67 (blue line), and cross-correlation between the time series measured at r/D =0.67 and r/D =1.00 (red line)76
Figure 4.9	Flooded-color contour maps of the cross-correlation and implied convection velocities at $H/D=2$; (a) normal impingement, (b) oblique- impingement (forward flow)78
Figure 5.1	Spatial pressure signature and associated flow visualization for vortex passage in normal impingement at <i>H/D</i> =2
Figure 5.2	Spatial pressure signature at different time instants demonstrating the convective nature of the wall-pressure: $H/D=2$ and normal impingement. Closed symbols represent actual measurements, and open symbols show the interpolated values84
Figure 5.3	Spatial pressure signature and associated flow visualization of vortex merging in normal impingement at <i>H/D</i> =2
Figure 5.4	Temporal pressure signature in the range r/D =0.67-1.67 for normal impingement and H/D =2

Figure 5.5	Vortex passage temporal pressure signature at r/D of 0.67 in normal impingement at H/D =2. Broken line near the left edge of each image marks the jet centerline while the other broken line marks the radial location at which the shown pressure signature is measured.
Figure 5.6	Vortex passage temporal pressure signature at r/D of 1 in normal impingement at H/D =2. Broken line near the left edge of each image marks the jet centerline while the other broken line marks the radial location at which the shown pressure signature is measured.
Figure 5.7	Vortex passage temporal pressure signature at r/D of 1.33 in normal impingement at H/D =2. Broken line near the left edge of each image marks the jet centerline while the other broken line marks the radial location at which the shown pressure signature is measured.
Figure 5.8	Vortex passage temporal pressure signature at r/D of 1.67 in normal impingement at H/D =2. Broken line near the left edge of each image marks the jet centerline while the other broken line marks the radial location at which the shown pressure signature is measured.
Figure 5.9	Vortex merging temporal pressure signature at r/D of 0.67 in normal impingement at H/D =2. Broken line near the left edge of each image marks the jet centerline while the other broken line marks the radial location at which the shown pressure signature is measured.
Figure 5.1	O Vortex merging temporal pressure signature at r/D of 1 in normal impingement at $H/D=2$. Broken line near the left edge of each image marks the jet centerline while the other broken line marks the radial location at which the shown pressure signature is measured.
Figure 5.1	1 Vortex merging temporal pressure signature at r/D of 1.33 in normal impingement at $H/D=2$. Broken line near the left edge of each image marks the jet centerline while the other broken line marks the radial location at which the shown pressure signature is measured.
Figure 5.1	2 Vortex merging temporal pressure signature at r/D of 1.67 in normal impingement at $H/D=2$. Broken line near the left edge of each image marks the jet centerline while the other broken line marks the radial location at which the shown pressure signature is measured.
Figure 5.1	3 Short-time power spectral density for pressure signatures extracted at <i>r/D</i> of 0.67-1.67 during vortex passage
Figure 5.1	4 Short-time power spectral density for pressure signatures extracted at <i>r/D</i> of 0.67-1.67 during vortex merging
Figure 5.1	5 Temporal pressure signature associated with secondary vortex at $r/D=1.33$, for $H/D=3$ and normal impingement. Broken line near the left edge of each image marks

	the jet centerline while the other broken line marks the radial location at which the shown pressure signature is measured	7
Figure 5.16	Flow visualization images showing the process of first and second vortex pairing downstream of the jet for <i>H/D</i> =4	0
Figure 5.17	Flow visualization images showing the merging process of three vortices for <i>H/D</i> =4	
	Temporal pressure signature in the range r/D =0-1.33 for normal impingement and H/D =4	4
(Power spectral density of pressure signals obtained over the range r/D of 0-1.33 during the passage of vortices resulting from merging of three and four structures in normal impingement and $H/D=4$	5
Figure 5.20	Temporal pressure signature at $r/D=0$, for $H/D=3$ and normal impingement11	8
Figure 5.21	Temporal pressure signature at $r/D=0$, for $H/D=4$ and normal impingement11	9
	Spatial pressure signature and associated flow visualization for vortex merging in oblique impingement (forward flow) at $H/D = 2$	1
	Temporal pressure signals at r/D of 0.33 to 1.67 beneath the forward flow in oblique impingement at $H/D = 2$; (red arrows point to two negative peaks per cycle)12	
_	Vortex merging temporal pressure signature at r/D of 0.33 beneath the forward flow n oblique impingement at $H/D = 2$	
	Vortex merging temporal pressure signature at r/D of 0.67 beneath the forward flow n oblique impingement at $H/D = 2$	
_	Vortex merging temporal pressure signature at r/D of 1 beneath the forward flow in oblique impingement at $H/D = 2$	
	Vortex merging temporal pressure signature at r/D of 1.33 beneath the forward flow n oblique impingement at $H/D = 2$	
	Vortex merging temporal pressure signature at r/D of 1 beneath the forward flow in oblique impingement at $H/D = 2$	
	Power spectral density for vortex merging at r/D of 0.33-1.67, measured beneath the forward flow in oblique impingement and $H/D = 2$	
	Spatial pressure signature and associated flow visualization for vortex passage in oblique impingement, forward flow, at $H/D = 2$	3
	Temporal pressure signals at r/D of 0.33 to 1.67 beneath the forward flow in oblique mpingement at $H/D = 2$	

Figure 5.32 Vortex passage temporal pressure signature at r/D of 0.33 beneath the forward flow in oblique impingement at $H/D = 2$
Figure 5.33 Vortex passage temporal pressure signature at r/D of 0.67 beneath the forward flow in oblique impingement at $H/D = 2$
Figure 5.34 Vortex passage temporal pressure signature at r/D of 1 beneath the forward flow in oblique impingement at $H/D = 2$
Figure 5.35 Vortex passage temporal pressure signature at r/D of 1.33 beneath the forward flow in oblique impingement at $H/D = 2$
Figure 5.36 Vortex passage temporal pressure signature at r/D of 1.67 beneath the forward flow in oblique impingement at $H/D = 2$
Figure 5.37 Power spectrum density for vortex passage at r/D of 0.33-1.67
Figure 5.38 Spatial pressure signature and associated flow visualization for vortex passage in oblique impingement, back flow, at $H/D = 2$
Figure 5.39 Temporal pressure signals at r/D of 1 to 2 beneath the back flow in oblique impingement at $H/D = 2$
Figure 5.40 Vortex passage temporal pressure signature at $r/D=1$ in oblique impingement, back flow side and $H/D=2$
Figure 5.41 Power spectrum density for vortex passage at r/D of 1 in oblique impingement, back-flow side and $H/D = 2$
Figure 5.42 Flow visualization images showing secondary vortex formation on the back-flow side of oblique impingement at <i>H/D</i> =2
Figure 5.43 Flow visualization images showing (a) vortex passage and (b) vortex merging in oblique impingement back flow side at <i>H/D</i> =3
Figure 6.1 Example of the surface pressure signature during the flow evolution leading to the formation of a secondary vortex in normal impingement at <i>H/D</i> =3
Figure 6.2 Spatial pressure signature associated with merging of two vortices above the wall in normal impingement for <i>H/D</i> =2
Figure 6.3 Sketch illustrating the numerical domain and boundary and initial conditions for two different cases: (a) one vortex ring and (b) two vortex rings
Figure 6.4 Vorticity field evolution obtained from the simulation of an axisymmetric vortex ring interacting with a flat wall by Shrikhande[32]
Figure 6.5 Azimuthal vorticity field and associated wall-pressure signature of the axisymmetric vortex ring-wall interaction problem at three consecutive times over a time period

	vortices in the impinging jet flow; the blue line is the pressure signature computed from the solution of Poisson's equation and the red line is the pressure signature	=-
Figure 6.6	obtained from the Fluent solution	
Figure 6.7	Decomposition of the surface pressure signature and associated vorticity field at τ =(second; the total signature(a), primary vortex signature (b), secondary vortex signature (c) and boundary layer signature (d)	
Figure 6.8	Wall-pressure signature computed for the flow field with negative vorticity and positive pressure source criteria	81
Figure 6.9	Surface pressure signature of the simulated vortex ring flow at consecutive times covering the same duration as the results shown in Figure 6.5	82
Figure 6.1	O Surface pressure signature computed for the primary vortex in the simulated vorte ring flow at consecutive times covering the same duration as the results shown in Figure 6.5	
Figure 6.1	1 Surface pressure signature computed for the secondary vortex in the simulated vortex ring at consecutive times covering the same duration as the results shown in Figure 6.5	84
Figure 6.1	2 Surface pressure signature computed for the boundary layer in the simulated vortex ring at consecutive times covering the same duration as the results shown in Figure 6.5	
Figure 6.1	3 Simulation of two Guassian vortex rings with initial locations of $(r = 0.018 m, x_p = 0.022 m)$ and $(r = 0.018 m, x_p = 0.035 m)$	89
Figure 6.1	4 Flow visualization images at <i>H/D</i> =3 and normal impingement showing two vortice merging downstream of the jet (pointed by arrows)	
Figure 6.1	5 Vorticity field and associated wall-pressure signal obtained from the simulation of the flow produced by two vortex rings above a wall with initial core center location of (r =0.018 m , x_p =0.01 m) and (r =0.029 m , x_p =0.01 m)	S
Figure A.	1 Detailed CAD drawing of the jet (dimensions in mm): end (top left) and side (top right), and isometric (bottom) views	.01
Figure B.	1 Three dimensional drawing of the flow visualization setup	03
Figure B. 2	2 Block diagram of flow-visualization and pressure-measurement setup	:04

Figure B. 3	A sample of trigger and FLD signals used to synchronize image and data acquisition
Figure C. 1	Synthetically generated sine wave signals with $\pi/6$ phase delay in between to simulate the spatio-temporal pressure variation created by a traveling pressure wave
Figure C. 2	Comparison between the spatial profile of the generated and the interpolated sine waves
Figure D. 1	Temporal pressure signature at <i>H/D</i> =3 at normal impingement
Figure E. 1	Vorticity (ω_{θ}) contour of the experimental flow-field at t=0.3 s (measured relative to the time of occurrence of the velocity field used to set the initial Gausian vortex parameters for the computation: t=1.4s relative to the solenoid opening) [30]21
Figure E. 2	Vorticity (ω_{θ}) contour of the simulated flow-field at t=0.3s [30]
C	Vorticity (ω_{θ}) contour of the experimental flow-field at t=0.5 s (measured relative to the time of occurrence of the velocity field used to set the initial Gausian vortex parameters for the computation: t=1.4s relative to the solenoid opening) [30]212
Figure E. 4	Vorticity (ω_{θ}) contour of the simulated flow-field at t=0.5s [30]
C	Vorticity (ω_{θ}) contour of the experimental flow-field at t=0.8 s (measured relative to the time of occurrence of the velocity field used to set the initial Gausian vortex parameters for the computation: t=1.4s relative to the solenoid opening) [30]213
Figure E. 6	Vorticity (ω_{θ}) contour of the simulated flow-field at t=0.8s [30]
	Vorticity (ω_{θ}) contour of the experimental flow-field at t=1 s (measured relative to the time of occurrence of the velocity field used to set the initial Gausian vortex parameters for the computation: t=1.4s relative to the solenoid opening) [30]214
Figure E. 8	Vorticity (ω_{θ}) contour of the simulated flow-field at t=1s [30]21:
_	Comparison of the temporal evaluation of the vorticity at the center of the primary vortex. Results from simulations based on three-parameter r, z and avg (r,z) Gaussian profiles are compared with those from MTV experiments [30]21:
Figure E. 1	0 Axial- (z), and radial- trajectories of the center of the primary vortex210

KEY TO ABBREVIATIONS

A,B	King's law coefficients for the hot-wire calibration
c	Speed of sound
D	Jet exit diameter
D_m	Mass diffusion coefficient
E	Voltage
$E_{\mathcal{C}}$	Temperature-corrected hot-wire voltage
E_m	Measured hot-wire voltage
e_{ij}	Strain rate tensor
f	Frequency in Hz
Н	Separation distance between the jet exit and the center of the impingement plate
l	Side length of plane wave tube
m	Number of data points corresponding to the time offset in the two-point correlation
	calculation
L	Number of independent samples in a time series
M	Mode number
N	Number of samples in a time series
n	An integer representing the sample number in the recorded time series
P	Mean wall pressure
P_d	Dynamic pressure based on the jet exit velocity $P_d = 0.5 \rho U_j^2$
P.,	Mean pressure at the stagnation point on the impingement plate

PSDPower spectral density Power spectral density of wall-pressure fluctuation PSD_{pp} PSD_{uu} Power spectral density of velocity fluctuation p Wall-pressure fluctuation Root mean square of the wall-pressure fluctuation p_{rms} Pressure source qInitial radius of the vortex core used to initialize the numerical simulations R_c Jet Reynolds number based on the jet exit velocity and the jet exit diameter Re_D Polar coordinates in the plane of the impingement plate r, θ Radial and normal coordinates, respectively, of the initial vortex core center used to r_o, x_{po} initialize the numerical simulation St_D Strouhal number based on the jet exit velocity and the jet exit diameter Strouhal number based on the jet exit velocity and momentum thickness of the shear St_{Θ} layer near the jet exit ScSchmidt number T_{w} Hot-wire temperature T_{cal} Fluid temperature during hot-wire calibration T_{m} Fluid temperature during hot-wire measurements UMean streamwise velocity

U_j	Jet exit velocity
u_r, u_{xj}	Radial and wall-normal velocity components respectively
u_{c}	Convection velocity of the wall-pressure disturbances
x_p, y_p, z_p	Cartesian coordinates with origin at the center of the impingement plate
x_j, y_j, z_j	Cartesian coordinates with origin at the center of the jet exit
$x_{j,r}$	Resonance location downstream of the jet exit
γ	Inclination angle of the impingement plate relative to the jet axis
γij	Rotation rate tensor
τ	Time
Γ	Vortex circulation
λ	Wavelength
Θ	Momentum thickness of the jet shear layer
$arTheta_i$	Initial momentum thickness of the jet shear layer
ν	Fluid kinematic viscosity
ρ	Fluid density
ω	Vorticity
ω_0	Maximum initial vorticity used to initialize the numerical simulations
$\omega_{ heta}$	Out of plain (azimuthal) vorticity
Φ	Power spectrum

 Φ_{uu} Power spectrum of velocity fluctuation

Chapter 1: Introduction

1.1 Background

1.1.1 Free Jets

Before presenting essential background information about impinging jets, it is important to introduce free-jet fundamentals to summarize basic understanding of the flow dynamics near the jet exit. This is essential as the flow structures generated in the free jet are similar to those in the impinging jet prior to impingement.

There are different types of jet flow depending on the jet exit geometry, which for instance can be round, rectangular, triangular or any other shape. In addition, the jet may emerge from a simple sharp-edged orifice, at the end of a long-pipe flow, or from a plenum after passing through a contoured-contraction. In the latter case, a favorable pressure gradient is produced in the flow direction, minimizing the initial shear-layer thickness at the jet exit.

A round jet with contoured-contraction nozzle, which is selected for the current investigation, produces a "top-hat" mean velocity profile (representing a potential core surrounded by a free shear layer near the nozzle lip) at the nozzle exit which is inviscibly unstable to small perturbations that grow exponentially over a short distance from the jet exit. The early stage of shear-layer-disturbance amplification is predicted well using linear instability theory; Drubka et al [1].

The basic hydrodynamic instability problem was known and was formulated in the nineteenth century for different types of flow by Helmholtz, Kelvin, Reynolds and Rayleigh; Drazen [2].

The study of instability of the free shear layer was initiated by Lord Rayleigh in 1879, but there had been no further investigations until 1950s [3]. There used to be a confusion regarding whether temporal or spatial instability theory was relevant; the shape of the eigenmodes seemed to persistently be predicted by spatial theory, whereas the experimental measurements of the streamwise growth rate better agreed with temporal theory [1].

Initially, a shear layer with relatively thin thickness at the jet exit grows downstream of the orifice. Shortly after, the shear layer starts to form sinusoidal instability waves which ultimately lead to three-dimensional turbulent flow farther downsteram. For the same jet exit diameter, the wavelength of the initial shear layer instability depends on the Reynolds number based on the jet diameter (i.e. on the jet velocity). Increasing the Reynolds number (jet velocity) raises the favorable streamwise pressure gradient along the nozzle length and consequently lessens the initial shear layer thickness at the jet lip. Thinner shear layers result in smaller wavelengths of the initial instability, which accelerates transition to turbulence (i.e. shortens the distance to where turbulence develops). The most amplified linearly-unstable mode in free shear layers can be computed from the solution of the Rayleigh equation and is found to be (St_{θ} = 0.016); Michalke [3].

In round jets, the initial shear layer instability leads to the "roll-up" of the shear layer to form axisymmetric vortex rings at a rate depending on Reynolds number and environmental forcing. As they advect downstream, these vortices increase in size by merging. Figure 1.1 depicts a sketch of successive vortex rings formation and merging. After the vortex rings initially form due to the shear layer instability, they start to mutually interact, which leads them to merge. This action generates a pressure disturbance at half the initial instability frequency (a sub-harmonic) that is fed back acoustically to the separation point of the shear layer at the jet exit, sustaining the

initial pairing mechanism; this is also known as self-forcing. When the flow structures are coherent; especially at low Reynolds number, another pairing takes place downstream of the jet, as shown in Figure 1.1, imposing a quarter-harmonic feedback. Popiel et al [4] utilized the smoke-wire flow visualization technique in free and impinging round jets to get physical insight into the jet vortex dynamics. They observed vortex initiation, vortex pairing and the fluid entrainment process. In the latter process, fluid from the surroundings is entrained into the main jet flow as the vortex size is increased due to the roll-up action. This growth has a limit at which the internal vortex ring diameter tends to zero; i.e. when the vortex core size becomes of the order of half the jet diameter.

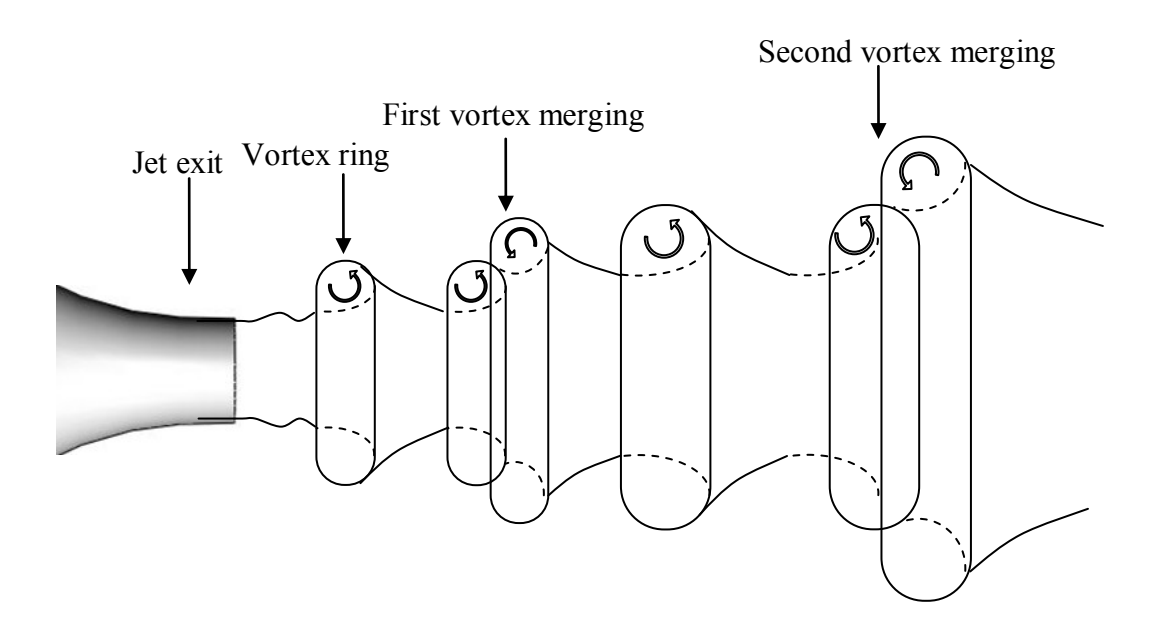


Figure 1.1 Schematic drawing demonstrating vortex formation and successive vortex merging

The number of vortices involved in a merging can be controlled when synthetic forcing of the jet flow is applied. Ho and Huang [5] studied the spread of a two-stream mixing shear layer, when perturbed near the sub-harmonic of the most amplified frequency. The mode number M

which also refers to the number of vortices merging depends on the forcing frequency to be the M^{th} sub-harmonic of the initial frequency of the linearly growing disturbance.

1.1.2 Impinging Jets

When a jet flow is incident on a solid wall, at distance H away from the jet exit, in such a way that the primary jet flow direction is perpendicular or has some non-normal angle of incidence relative to the plane of the wall, a normal or oblique, respectively, impinging jet is established. Figure 1.2 demonstrates a schematic of an impinging jet in normal incidence with commonly used terminology for different flow-field zones. There are three main zones: free-jet, wall-jet, and stagnation zone. The latter is characterized by higher mean static pressure, which reaches its maximum value at the stagnation point. The stagnation zone is typically taken to be the region where r/D < 1, and the wall jet zone corresponds to the domain r/D > 1.

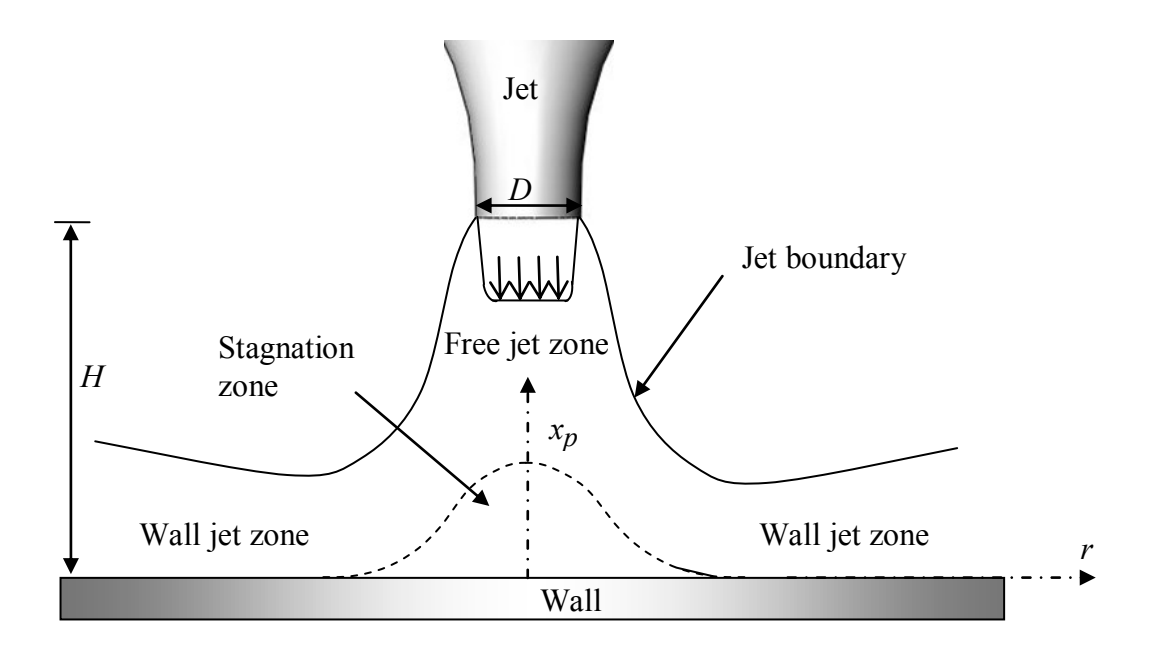


Figure 1.2 Schematic of impinging jet flow in normal incidence

Impinging jets are important in many engineering applications such as heating, cooling and drying. An important application of impinging jets is impinging-jet array used for cooling turbine blades. The types of flow structures developing above the impingement wall play a key role in the forced convection heat transfer. Impinging jets are also essential in understanding the behavior of some of nature's phenomena such as microburst, and they play a crucial role in blown flap configuration in Short Takeoff and Landing (STOL) aircrafts.

The impinging jet flow structures produce significant fluctuating wall-pressure, which can cause flow-induced noise and vibration. In order to predict or, at minimum, avoid or attenuate these undesirable effects, it is essential to understand the mechanisms leading to the unsteady pressure generation in impinging jets. Previous literature on the topic (summarized below) has predominantly only employed wall-pressure measurements, relying on the spatial-temporal characteristics of the wall pressure to hypothesize the nature of the pressure generating mechanisms/flow structures. However, in order to make unambiguous statements about the nature of the pressure generating mechanisms, it is essential that flow field information is available simultaneously with the pressure measurements. The current work aims to remedy this limitation by conducting time-resolved flow visualization simultaneously with wall-pressure measurements.

1.1.2.1 Governing Equation

Before going through some of the previous studies of wall-pressure fluctuations in impinging jets, it is important to introduce basic aspects regarding the generation of pressure fluctuations by vortical structures (which is also imperative when discussing the results of the current study). Bradshaw and Koh [7] manipulated the right hand side of Poisson's equation (1.1), which is derived by taking the divergence of the momentum equation for incompressible flow, to be in

terms of the rate of strain tensor and vorticity. To do so, they expanded the velocity gradient tensor on the right hand side of equation (1.1) into a summation of symmetric (strain rate) and antisymmetric (rotation) parts, e_{ij} and γ_{ij} respectively (see equations (1.3) and (1.4)), to arrive at equation (1.2) in terms of strain e_{ij} e_{ji} and vorticity 0.5 $\omega_i \omega_i$: or the pressure 'source' strength $q = e_{ij}e_{ji} - 0.5 \omega_i \omega_i$, for brevity.

$$-\rho \frac{\partial^2 p}{\partial x_i \partial x_i} = \frac{\partial u_i}{\partial x_j} \frac{\partial u_j}{\partial x_i}$$
(1.1)

$$-\rho \frac{\partial^2 p}{\partial x_i \partial x_i} = e_{ij} e_{ji} - 0.5 \,\omega_i \omega_i \tag{1.2}$$

$$e_{ij} = \frac{1}{2} \left(\frac{\partial u_i}{\partial x_j} + \frac{\partial u_j}{\partial x_i} \right)$$
 (1.3)

$$\gamma_{ij} = \frac{1}{2} \left(\frac{\partial u_i}{\partial x_j} - \frac{\partial u_j}{\partial x_i} \right) \tag{1.4}$$

Blake [8] gives the solution of Poisson's equation as a summation of a volume integral and a surface integral which bounds the volume encompassing the flow domain. For the present flow, the surface would consist of the impingement plate surface plus an infinite hemispherical shell. The resulting solution, which is given by equation (1.5), can be used to compute the pressure on the impingement plate surface where $x_p = 0$ (x_p is the wall-normal coordinate) and the "prime" denotes the pressure source location. Focusing on the volume integral, which represents the effect of structures within the body of the flow, the denominator of the integrand is the distance

between the point on the impingement plate where the pressure is calculated and the pressure source. Therefore the larger this distance is, the weaker the pressure imposed on the plate due to a disturbance located (x'_p, y'_p, z'_p) . The numerator of the volume integral consists of a positive definite strain rate term and negative definite vorticity term. Hence, regions of high strain rate/vorticity impose positive/negative pressure on the wall.

$$p\left(x_{p} = 0, y_{p}, z_{p}\right) = \frac{1}{2\pi} \int \left(\frac{\left(e_{ij}e_{ji}(x_{p}^{'}, y_{p}^{'}, z_{p}^{'}) - \frac{1}{2}\omega_{i}\omega_{i}(x_{p}^{'}, y_{p}^{'}, z_{p}^{'})\right)}{\sqrt{x_{p}^{'} + \left(y_{p} - y_{p}^{'}\right)^{2} + \left(z_{p} - z_{p}^{'}\right)^{2}}}\right) dV'$$

$$-\frac{1}{2\pi} \int \frac{\mu \left(\frac{\partial^2 v}{\partial z^2}\right)_{(y'_p, z'_p)}}{\sqrt{\left(y_p - y'_p\right)^2 + \left(z_p - z'_p\right)^2}} dS'$$
(1.5)

1.1.2.2 Literature Review

Hall and Ewing [10] investigated the development of large-scale structures in normally impinging jets using the two-point correlation of fluctuating wall pressure measurements for jet exiting from a long pipe with H/D=2 and Reynolds numbers based on diameter and jet mean (9.54 m/s and 20.5 m/s) velocity of 23300 and 50000. The root-mean-square pressure fluctuation distribution along the radial axis depicted a peak near r/D=1.5 and their spectral analysis indicated a peak (normalized frequency, or Strouhal number based on jet diameter of 0.5-0.7) associated with quasi-period passage of turbulent structures. The peak was found to shift to lower frequency as the flow evolved in the radial direction.

The Hall and Ewing [10] investigation was expanded upon by Hall and Ewing [11], who utilized two-point statistics and instantaneous measurements of the fluctuating pressure field and included measurements for H/D=2 and 4. Azimuthal Fourier decomposition revealed that the pressure fluctuations were three-dimensional in the stagnation zone and more two-dimensional in the wall jet zone for both cases. The strength of the pressure fluctuations in the stagnation zone, which the authors linked to the flow structures forming in the free jet prior to its impingement on the plate, decreased with increasing distance between the jet exit and impingement plate location. Wavelet analysis indicated that the asymmetric mode has high- and low-frequency components while the axisymmetric mode has only high-frequency oscillations. The high-frequency component occurred in both stagnation and wall jet zones while the low-frequency, which is primarily associated with the asymmetric mode, was found only in the stagnation zone.

Recently El-Anwar et al [12] examined the spatio-temporal characteristics of the fluctuating wall pressure generated by axisymmetric jet, placed four diameters away from the wall, in normal and oblique incidence. They employed 30 microphones arranged in radial and azimuthal configurations. The general characteristics of the wall-pressure *rms* (root mean square) and spectra were consistent with those found by Hall and Ewing [11] in the case of normal impingement. In the oblique impingement case, they found substantial asymmetry in the wall pressure field involving intensification as well as attenuation of the pressure fluctuations. The former was observed in the forward flow side with the latter in the back flow side.

Jiang *et al.* [13] extended the study of El-Anwar *et al.* [12] to include a round jet emerging from a sharp-edged opening; also in normal and oblique incidence. The results showed significant fundamental difference in the pressure fluctuations and spectral characteristics between the jet with sharp-edged exit and that emerging from a contoured nozzle. Additionally,

Jiang *et al.* hypothesized that the asymmetry in the wall-pressure-field characteristics in the oblique impingement can be explained by how a vortex ring with an axis tilted relative to an impingement wall interacts with the wall. Moreover, they indicated the necessity of simultaneous flow and wall-pressure field measurements for validation of this hypothesis.

In impinging jets, vortical structures form downstream of the jet due to the shear layer instability and, depending on the distance to the impingement plate, they may perform one or more vortex merging before they encounter the wall. When the vortices interact with the wall and turn to travel parallel to it, they induce boundary layer separation which evolves into a secondary vortex with vorticity of opposite sign to the primary one. There are a good number of studies that examined the boundary layer separation in impinging jets. Harvey and Perry [14] were first to observe the process of the boundary layer separation and the formation of a secondary vortex downstream of the associated primary vortex in impinging jets. Diddin and Ho [15] investigated the laminar boundary layer for a forced air jet in normal impingement. Phaselocked flow visualizations and phase-averaged hot wire measurements using, multiple parallel wires, revealed boundary layer separation, leading to formation of a secondary vortex with counter sense of rotation with respect to the primary vortex, in vicinity of $1 \le r/D \le 1.2$. Diddin and Ho also reported a convection velocity values of $0.61U_o$ (primary vortex) and $0.73U_o$ (secondary vortex). Their wall pressure measurements showed high pressure fluctuations at the beginning of the separation. They concluded that the unsteady pressure gradient in the inviscid region retards the flow in the viscous region and a consequent shear layer at the viscous-inviscid interface region separates and rolls up into the secondary vortex.

Landreth and Adrain [16] conducted flow field measurements using PIV (Particle Image Velocimetry) in an impinging water jet. The instantaneous velocity, vorticity and rate-of-strain

fields disclosed that vortices interact with the wall in the wall jet zone, inducing boundary layer separation and vortex breakaway within the wall jet. They conjectured that the flow structures found in these experiments may be similar to the ones occurring in microburst phenomena.

1.2 Motivation

There are many investigations of the impinging jet flow that focused on the heat transfer from the impingement plate (e.g. [20]-[24]) and on the flow field (e.g. [4], [15] and [16]). In contrast, there a lot less studies concerned with the space-time characteristics of the fluctuating wall pressure. Examples from these few studies are [10] and [11], employing two-point wall-pressure and wall-pressure-sensor array measurements, respectively. More recently, [12] and [13] utilized an extensive wall-pressure microphone array to measure the unsteady surface pressure caused by a jet impinging on a flat wall at normal and oblique incidence.

Understanding the relation between the unsteady surface-pressure field and the flow structures is crucial for constructing physical models for the prediction of the surface pressure as well as for feedback flow control based on the latter. The aforementioned literature offers substantial information regarding space-time characteristics of the surface pressure; nonetheless the interpretations of these results regarding their association with specific flow field structures remain hypothetical, given the lack of concurrent flow information. To address this limitation Al-Aweni and Naguib [25] carried out wall-pressure measurements concurrently with capturing of flow-field information by using simultaneous unsteady-surface pressure measurements from a microphones array and flow field visualization using the smoke-wire technique. However, the low sampling rate of 30 frames per second of the flow visualization only provided static images of the flow field. The current investigation is designed to address this limitation by conducting

simultaneous time-resolved flow field visualization, with sampling rate of 2000 frames per second, and unsteady-surface pressure measurements.

1.3 Objectives

The objectives of the current study may be summarized as follows:

- 1- To conduct space-time wall-pressure measurements using a microphones array. The statistics of the resulting database, such as spatial distribution of *rms* and spectral analysis, will be compared to existing literature.
- 2- To carry out simultaneous time-resolved flow visualization and unsteady surface pressure measurements. The recorded time-resolved wall-pressure signature will be analyzed to identify instants in time and locations in space where significant pressure generation takes place. The spatio-temporal evolution of the flow structures in the vicinity of these significant "events" will be examined using the flow visualization images. The outcome will be used to understand the flow structures/mechanisms responsible for surface pressure generation, and to explain trends in the statistical quantities obtained in addressing objective number 1.
- 3- To apply Direct Numerical Simulation (DNS) using ANSYS Fluent to study simple model problems that, as will be shown, are relevant to understanding the influence of vortex-vortex and vortex-wall interactions within the wall jet zone of impinging jets on surface-pressure generation. The model problems of interest are those of single and two co-rotating axisymmetric vortex rings interacting with a wall.

The rest of the current study is organized to present the experimental apparatus in Chapter 2, Chapter 3 is a shear layer study to document the flow characteristics at the jet exit (i.e. the initial condition), Chapter 4 gives analyses of statistical results of the wall pressure, Chapter 5

represents an exploration of pressure-generating flow structures/mechanisms by utilizing the simultaneous time-resolved flow visualization and unsteady surface pressure measurements, and Chapter 6 gives details of the DNS results using ANSYS Fluent

Chapter 2: Experimental Apparatus

This chapter demonstrates the different experimental setups employed in this study for velocity and pressure measurements as well as for flow visualization. After depicting the flow configuration with the proper nomenclature and coordinate system, this section introduces the general assembly of the experimental apparatus as well as the different measurement tools such as the pressure transducer, the hot wire anemometer and the microphones which are used for mean-pressure, flow-velocity and unsteady-pressure measurements, respectively. This study is predominately experimental but is also involves some computations for more physical insights. The details of the computations are given in Chapter 6.

2.1 Flow Configuration

The flow configuration at the focal point of the present investigation is illustrated in Figure 2.1, along with relevant nomenclature and coordinate system. Note that in addition to using two Cartesian systems, one at the center of the plate and the other at the center of the jet exit (as shown in

Figure 2.1), a polar coordinate system (r, θ, x_p) is employed with r measured from the center of the impingement plate and $\theta = 0^{\circ}$ coincident with the forward-flow direction.

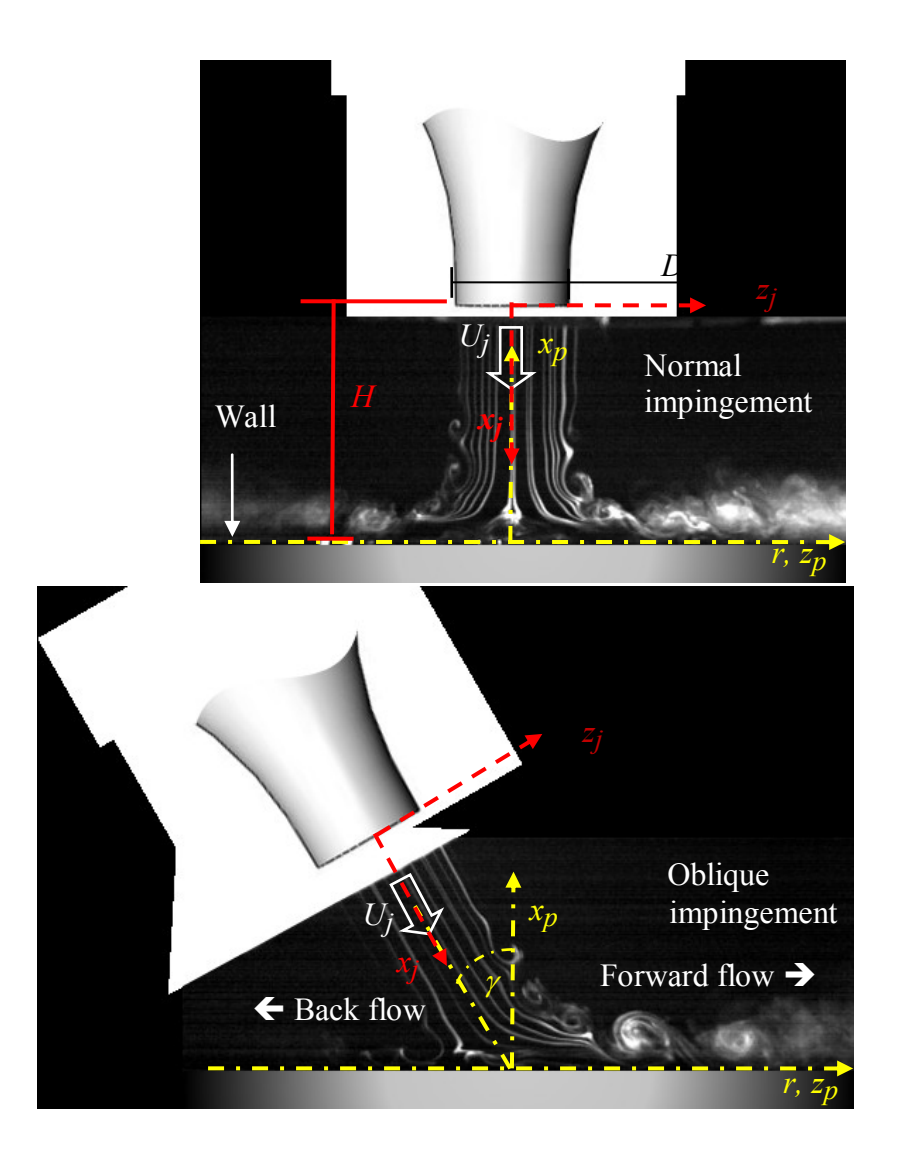


Figure 2.1 Illustration of the flow configuration and coordinate system superimposed on actual flow visualization of the impinging jet flow at normal (top) and oblique (bottom) incidence. For interpretation of the references to color in this and all other figures, the reader is referred to the electronic version of this dissertation.

The experimental setup consists of an axisymmetric air jet, with a top-hat exit velocity profile, emerging at the end of a fifth-order-polynomial contoured nozzle with exit diameter D = 25 mm, and impinging on a flat, circular disc. The diameter of the disc is 12D, which is more than an order of magnitude larger than the jet diameter to minimize disc-edge effects on the

measurements. The impingement disc is located a distance H away from the jet exit and could be inclined to cause deviation from normal impingement by an angle γ (see Figure 2.1)

2.2 General Assembly of the Experimental Setup

Figure 2.2, shows the jet flow facility located in the Flow Physics and Control Laboratory (FPaCL) at Michigan State University. A Dayton (model 4C108) blower is used to blow air through a 3 inch diameter PVC pipe. In order to minimize the effect of the vibration generated by the blower on the flow, the blower is situated on a separate table from that of the jet, and the blower's exit pipe diameter is smaller than the inner diameter of the PVC pipe to avoid hard coupling between the blower and facility which can transmit vibrations to the flow and the measurement instrumentation. The air then flows into a 12×12×30 inch flow conditioning box/settling chamber, which decreases the turbulence intensity of the flow to be less than 1 % when measured using a hot wire anemometer at the exit plane of the nozzle and a jet velocity of 4.5 m/s. The flow conditioning box sits on three thumb screws that are attached to a steel frame structure designed to hold the conditioning box. The three screws are employed to adjust the elevation as well as the orientation of the jet flow exiting through the nozzle at the downstream end of the settling chamber.

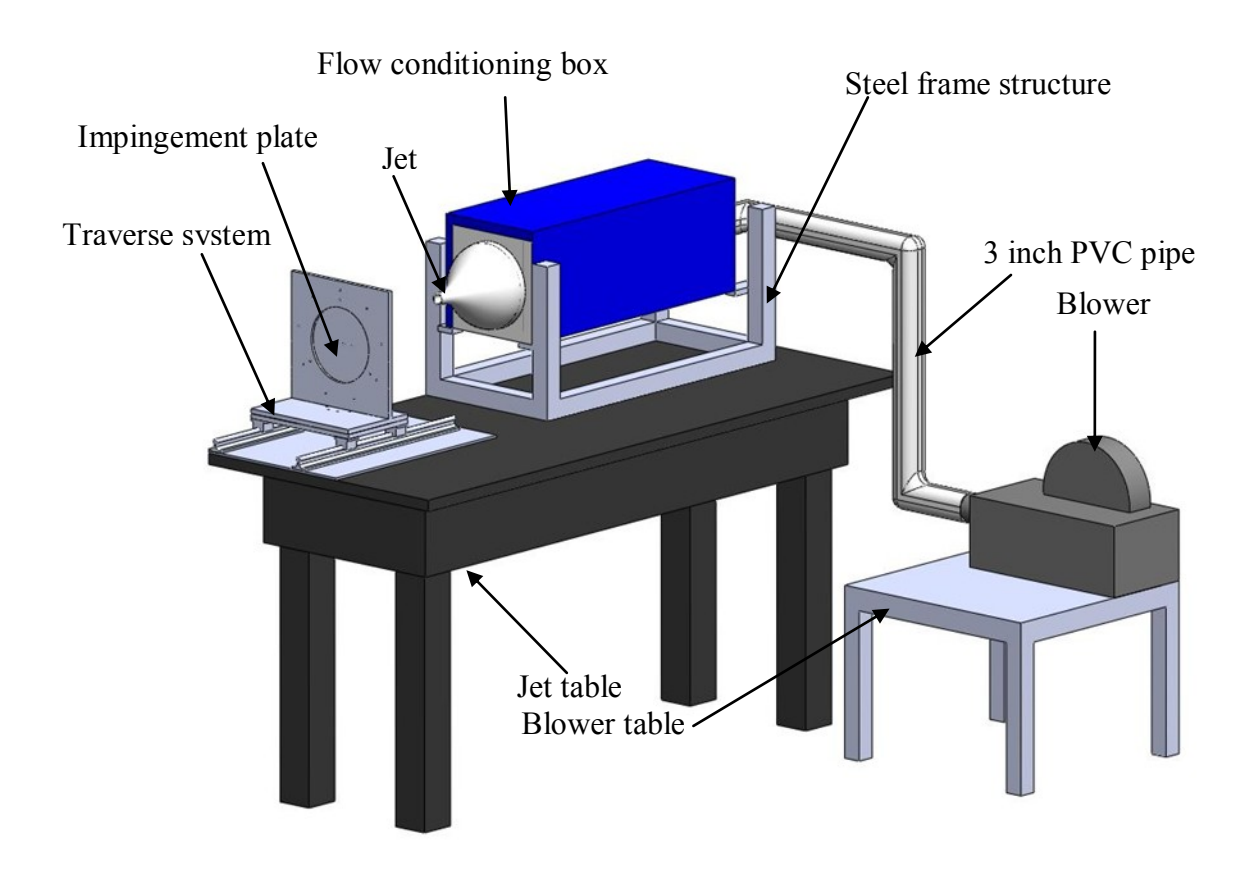


Figure 2.2 Impinging-jet facility at FPaCL

2.2.1 Plate Traverse System

A traversing system, shown in Figure 2.3, placed in front of the jet is employed to hold the circular impingement disc normal to the jet exit as well as to change the jet-to-impingement-plate separation distance H. The traverse, which is made from aluminum, is also designed to enable setting of different impingement angles γ to $\pm 90^{\circ}$ with increments of 10° . The vertical square plate seen in Figure 2.3 with $18\times18\times0.5$ inch in dimensions has a circular recess to accommodate the 12 inch diameter impingement disc. The recess has 32 through holes spaced 11.25° apart along the azimuthal direction to enable the impingement disc to rotate about the x_p axis and it

also has a 9 inch diameter hole in the middle to pass through all wires from the microphones embedded in the impingement disc for surface pressure measurements. A manual Velmex traverse (model A1506P40-S1.5-TL), with total travel length of 4.5 inch and accuracy of 0.001 inch, can be mounted to the aluminum platform at different locations along the streamwise direction in 1.5 inch increments. By coupling the traverse to the lower horizontal plate, the spacing between the jet exit and the impingement plate can be adjusted to within 0.001 inch. In order to identify the manual traverse position corresponding to H=0, the impingement plate is brought very close to the jet orifice, practically touching.

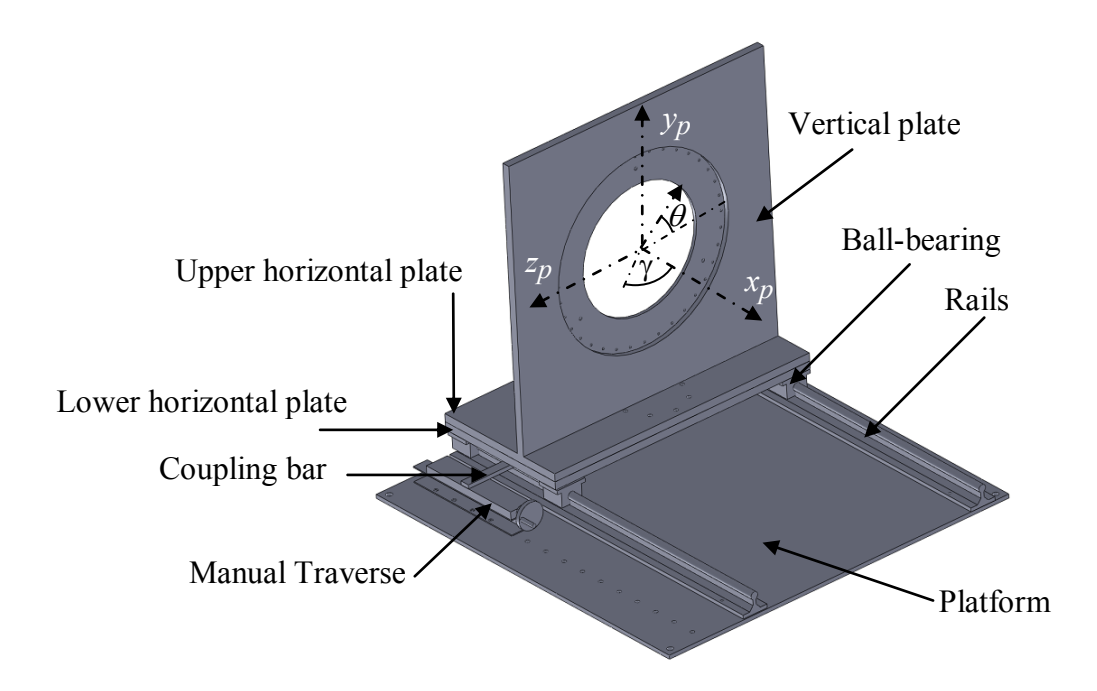


Figure 2.3 Three-dimensional model of the traversing system used for holding and traversing the impingement plate

2.2.2 Jet Flow and Impingement Plate Alignment

The jet flow needs to be centered and perpendicularly oriented with respect to the impingement plate when γ is set to zero. To accomplish this, the setup shown in Figure 2.4 is used to measure the azimuthal profiles of the mean pressure acting on the impingement plate at

different x_i locations downstream of the jet exit using pressure taps embedded in the impingement plate (see Figure 2.4). The relative positioning of the jet and traversing system and the jet orientation are adjusted until these profiles demonstrate good axisymmetry about the center of the impingement plate. Once this is attained, the jet flow is considered to be properly aligned relative to the impingement plate. For the purpose of these measurements, a PVC circular impingement disc with 12 inch diameter is fabricated with 33 through holes to accommodate pressure taps of 1 mm diameter. The disc contains one tap at the center with the remaining taps arranged in + configuration centered around the central tap at an inter-tap spacing of 2 mm. The PVC disc also has four threaded holes used for mounting on the vertical aluminum plate of the traversing system. The pressure taps are inserted into the PVC disc to be flush with the surface facing the jet exit and connected to a Scanivalve pressure scanner (model: 4809-1346) via tight fitting viny tubes. The PVC disc is mounted on the traverse system such that the four tap radial "arrays" forming the sides of the + configuration coincide with $\theta = 0^{\circ}$, 90° , 180° and 270° . The output terminal of the pressure scanner is connected to a 10 torr Baratron transducer (model: 223BD-00010ACU). The transducer is employed to measure the pressure at all 33 pressure taps using the pressure scanner to connect to one pressure tap at a time when triggered by a homemade switch circuit. Another pressure transducer, from All Sensors Corporation (0.5 INCH-G-4V), is employed to read data from the center tap simultaneously with every reading from the Baratron transducer. This measurement is used to normalize all pressure readings, so that the effect of small variation in the jet velocity during a pressure scan is not falsely interpreted as relating to the symmetry characteristics of the pressure distribution. A LabVIEW program is used to acquire the data from the pressure transducers via a PC-based Analog-to-Digital converter (A/D), and to trigger the switch circuit driving the pressure scanner. The data from the pressure transducers are averaged over 10 seconds acquisition period with 1 kHz sampling frequency.

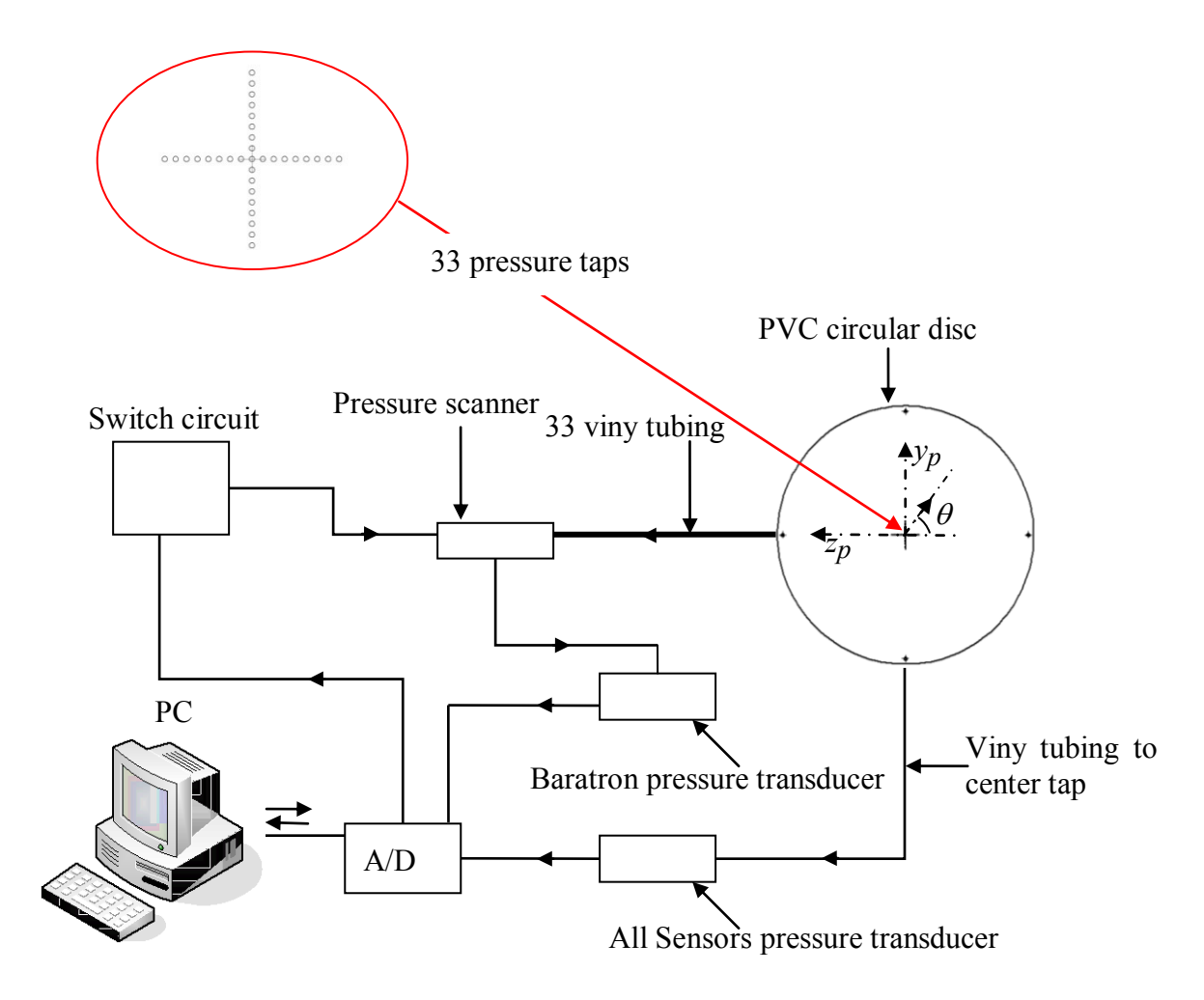


Figure 2.4 Schematic drawing of the experimental setup used to align the impingement plate relative to the jet flow

The two tap radial arrays coincident with $\theta = 90^{\circ}$ and 270° are aligned with the y_p axis forming a vertical column of 17 pressure taps and the ones coincident with $\theta = 0^{\circ}$ and 180° line up with the z_p axis forming a horizontal row of the same number of taps. In order to center the jet with the impingement plate, both pressure profiles along the z_p and y_p axes should peak at, and have symmetry about the center tap. Moreover, these two profiles should collapse on top of each

other for an axisymmetric flow. The aforementioned symmetry and agreement of the pressure profiles should occur at least two different locations of the plate downstream of the jet flow to assure the jet centering and perpendicularity to the impingement plate. Figure 2.5 and Figure 2.6 depict pressure profiles, normalized by the concurrent mean pressure from the center tap at r/D = 0, along the z_p (blue circles) and y_p (red circles) axes at H/D = 4 and H/D = 8 respectively. Both figures depict a mean pressure distribution which has a peak at the center point (r/D = 0) and demonstrates good symmetry about the peak in the vertical and horizontal directions (i.e. along the y_p and z_p axes).

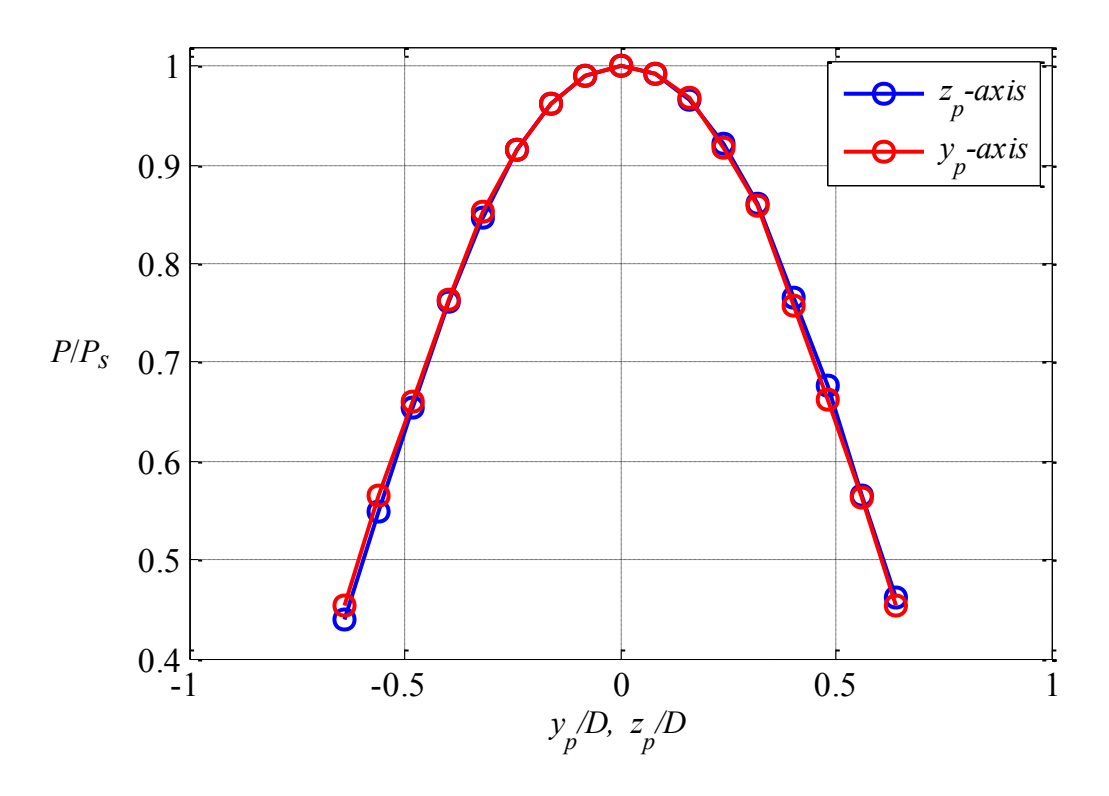


Figure 2.5 Normalized mean pressure profiles along z_p and y_p axes at H/D =4. P_s denotes the mean stagnation pressure

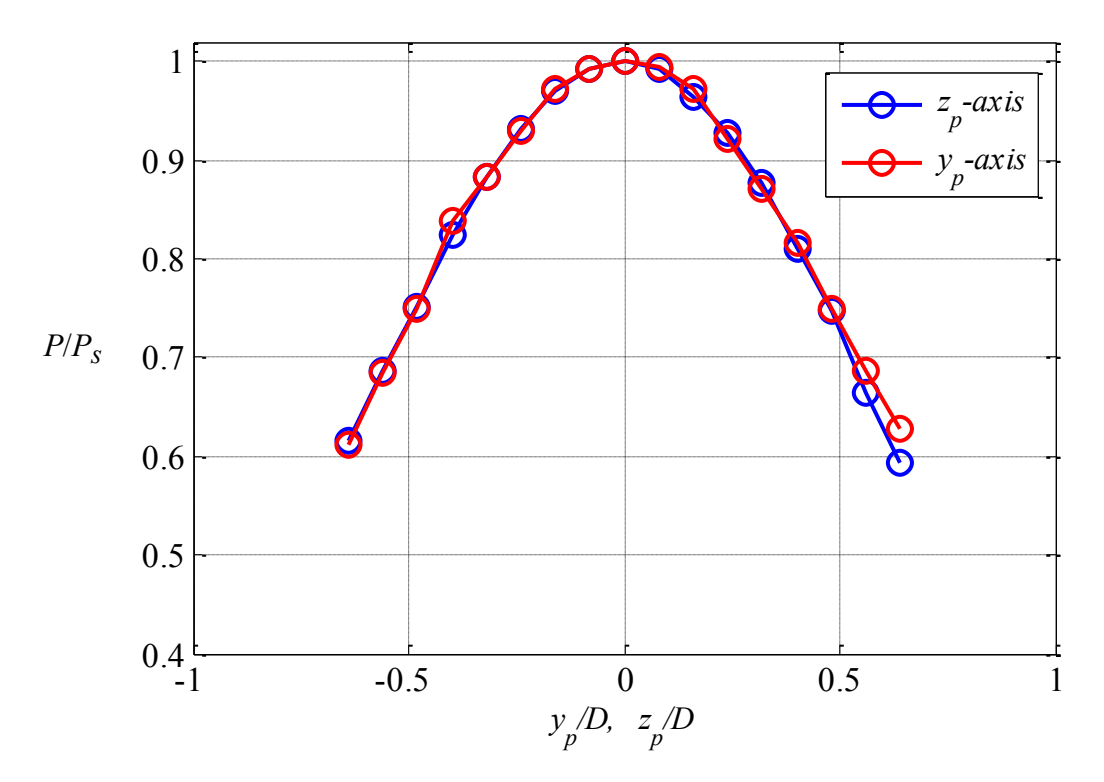


Figure 2.6 Normalized mean pressure profiles along z_p and y_p axes at H/D = 8. P_s denotes the mean stagnation pressure

Additional pressure profiles across the jet in y_p and z_p directions were measured at different locations downstream of the jet (along x_j axis). Figure 2.7 shows the normalized pressure profiles measured along the z_p (Figure 2.7a) and the y_p axis (Figure 2.7b). The data are displayed in the form of a two-dimensional flooded color contour plot with the color indicating the value of the normalized pressure as given by the color bar on the right hand side of the figure. One can see the symmetry around the center r/D=0 (z_p/D and $y_p/D=0$) for the pressure distribution along both axes, which is a good indication that the jet is perpendicular to the impingement plate.

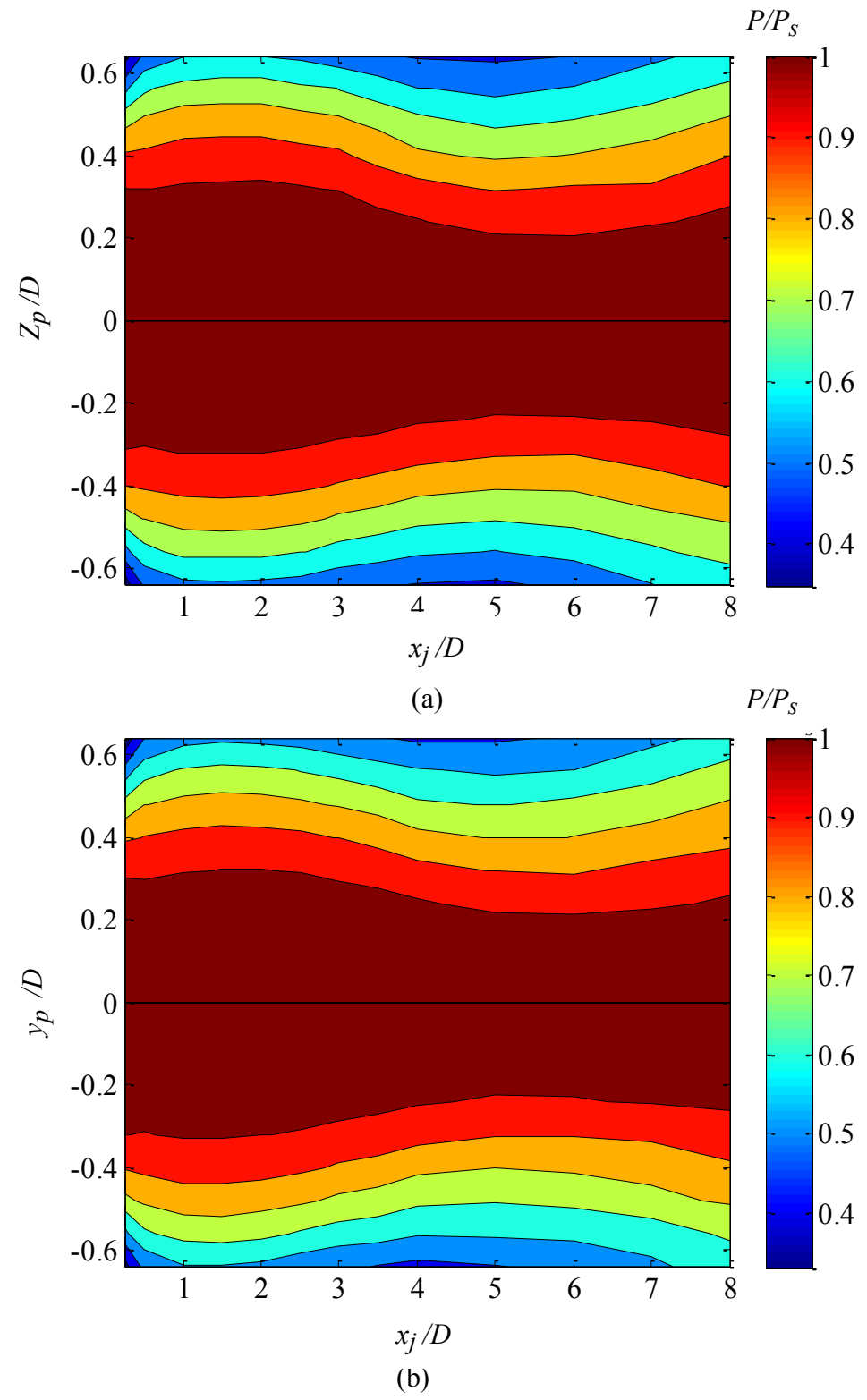


Figure 2.7 Color contour maps of the normalized mean pressure. The color bar to the right provides the magnitude of the mean pressure normalized by the mean stagnation pressure at the center of the disc: profiles along the z_p (a) and y_p (b) axis at different x_j/D

In order to verify the axisymmetry of the jet in the y_p - z_p plane, mean pressure measurements were carried out at different angles θ . For these measurements, the PVC disc was located at x_p/D = 4 and the jet velocity was set to 13.8 m/s. Pressure measurements from all taps were acquired for 10 seconds at 8 different azimuthal positions from $\theta = 0^\circ$ to 90° in 11.25° increment. This provides the equivalent of nine azimuthal arrays of pressure data at different radial locations from r/D = 0 to 0.64 with an increment of r/D = 0.08. Each azimuthal array contains 33 pressure data points spaced 11.25° apart. Figure 2.8 depicts the resulting pressure distribution over a circular area with radius of r/D = 0.64. As would be expected, the pressure peaks near the center point and decays gradually in the outward radial direction. The standard deviation of the azimuthal variation of the pressure measurements at each radial location was computed and the highest value found was 2.86% of the azimuthally averaged pressure at the same radius. This confirms that the impingement plate is properly centered relative to the jet flow, and it indicates good axisymmetry quality of the mean jet flow.

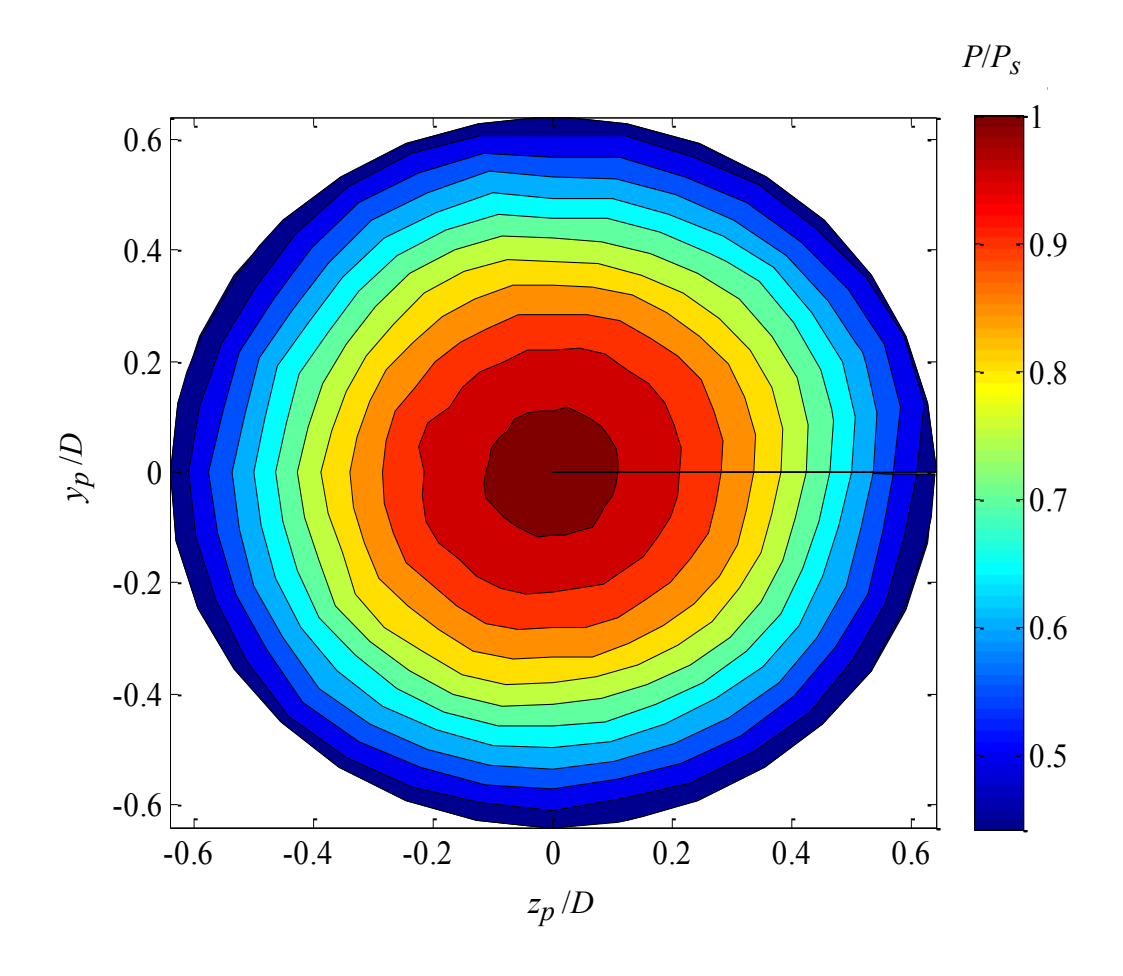


Figure 2.8 Normalized mean-pressure distribution on the impingement plate

2.3 Hot Wire Setup

Figure 2.9 demonstrates a block diagram of the hot wire setup employed to study the initial shear layer characteristics. A hot wire made from tungsten with 5 μm diameter and active sensing length of 1 mm (giving a length-to-diameter ratio of 200) is used to measure the mean and fluctuating component of the streamwise velocity profiles across the shear layer. The hot wire is operated in constant temperature mode using a mini CTA 54T30 from Dantec operated at an overheat ratio of 0.68 (i.e. operating to cold resistance ratio of 1.68). The CTA output is linked to an oscilloscope (Tektronix TS1002B) to monitor the measurement signal before it is fed to an Analog-to-Digital converter (ADC) for recording. To enhance the measurement resolution of the fluctuating component of the signal, an offset circuit is used to center the hot

wire output around zero over the range of flow velocities employed, and the offset signal is amplified by the instrumentation amplifier onboard the A/D. In parallel, the raw (un-shifted) hotwire output was also recorded. In post processing, the offset signal is reduced by the amplifier gain (done transparently to the user within the LabVIEW VI) and the two signals are added together before converting the resulting voltage into a velocity time series using the hot wire calibration.

The hot wire is mounted on a stepper-motor-driven traverse system to vertically move the wire across the jet along the y_i axis with a resolution of 0.0002 inch/step. A dial gage (with accuracy of 0.0005 inch) is used to monitor the hot wire movement and to define a reference location for the hot wire motion. A Pitot tube with an outside diameter of 3 mm, connected to a 10 torr Baratron pressure transducer (model: 223BD-00010ACU) with sensitivity of 0.75 mV/Pa is placed in the jet flow potential core for hot wire calibration. To correct the hot wire response for any variation in the ambient temperature, the flow temperature is measured by a an Omega DP-25-TH thermistor with a sensitivity of 100 mV/deg C, placed downstream of the hot wire and Pitot tube. The platform carrying the hot wire traverse system is clamped to the impingement plate traverse system, shown in Figure 2.3, to allow adjustment of the hot-wire location in the x_i direction. A LabVIEW program is employed to acquire the temperature, the hot wire voltage and the Pitot tube pressure through a National Instruments 12-bit PCI-6024E ADC. The program also controls the stepper motor via 4 bits of the parallel output provision on the PCI-6024E coupled with a stepper motor controller card (The Motion Group, Model: 5618M-0605) and records the locations of the hot wire relative to a reference point near the jet flow field, arbitrarily selected to be at $x_i=0.5$ mm and $z_i=0$, with the wire outside the shear layer on the potential core side.

Measurements were taken at 100 points in the y_j direction over a range which encompasses the shear layer. The spacing between successive measurement locations is 0.015mm for measurements at $x_j/D=0.02$ and 0.32mm for $x_j/D=4$.

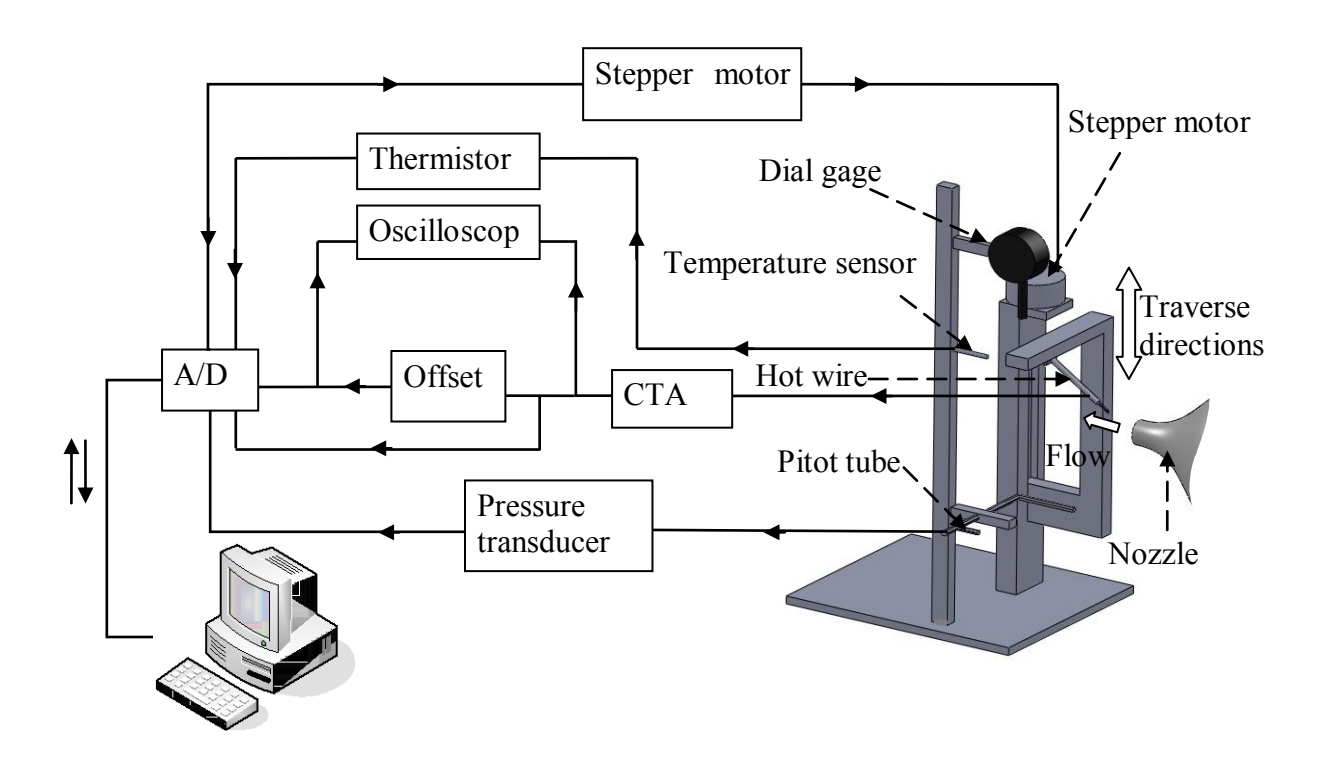


Figure 2.9 Schematic drawing of the hot wire setup during measurement of the streamwise velocity profiles across the shear layer surrounding the jet. During calibration, the Pitot tube is moved from the location shown in the figure to be within approximately 5 *mm* from the hot wire inside the potential core

The stepper motor is calibrated in order to determine the hot-wire vertical movement corresponding to one stepper motor's revolution. A SD970IS Canon digital camera is employed to capture several images of the hotwire at different vertical positions (y_j) versus stepper motor's known number of revolutions. The camera is placed to view the field of interest with resolution of 0.038 mm/pixel. The hot wire is imaged at a certain vertical location and then the stepper motor is employed with known number of revolutions to move the hot wire to a different vertical

location where a second image is captured. Comparing the two images, where the hot wire is at the same horizontal pixel number but at a different vertical pixel number. The difference in the number of pixels in the vertical direction corresponds to the hot wire movement. The distance the hot wire traveled is computed by multiplying the number of pixels and the imaging resolution, which is determined by using a reference object with known dimensions in the image. It was found that one stepper motor revolution corresponds to one millimeter hot wire travel (or 0.005 mm/step, 0.0002 inch/step, for 200 steps per revolution). Finally, when reversing the direction of traversing, provisions were taken to eliminate the backlash.

The hot wire was calibrated against the Pitot tube before and after each experiment. Both the hot wire and the Pitot tube were brought into the potential core of the jet flow and positioned as close as possible but with enough separation to eliminate any flow disturbance produced by one of the probes on the other. A LabVIEW program is designed to measure the hot wire voltages and Pitot tube pressures at different jet velocities. After correcting the raw hot wire voltages for any variation in the temperature during calibration using equation (2.1), the velocities (computed from the dynamic pressure measured by the Pitot tube) and the corrected hot wire voltages are fit to King's Law form ($E^2 = A + B U^n$, where n = 0.4 - 0.45) using least-squares methods. For each fit, typically 8 calibration data points are used over the velocity range 4 -12 m/s. Once calibration is done, the Pitot tube is removed from the potential core of the jet flow.

Figure 2.10 depicts sample hot-wire calibrations before and after conducting measurements. The two curves agree to within a maximum deviation of 1.1%, validating that no significant change in the wire's calibration has taken place during the measurements.

$$E_{c} = E_{m} \left[\frac{T_{w} - T_{cal}}{T_{w} - T_{m}} \right]^{1/2}$$
 (2.1)

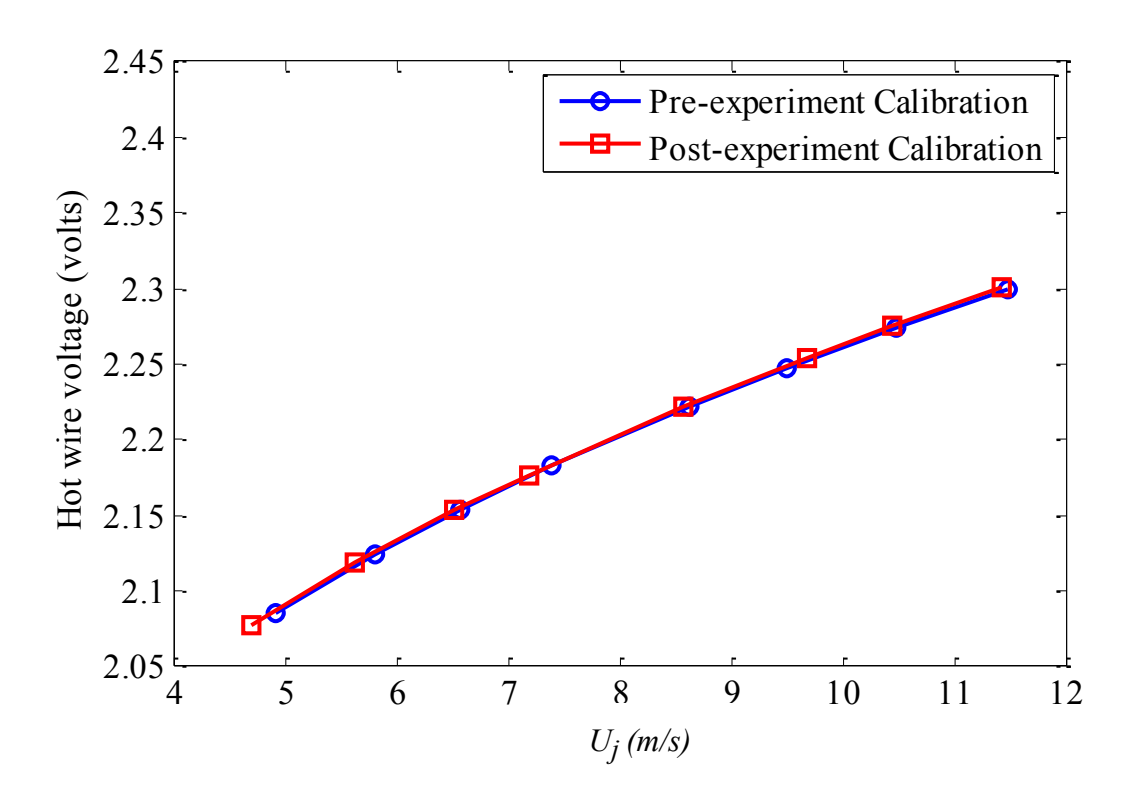


Figure 2.10 Sample hot-wire calibration before and after an experiment

2.4 Microphones Setup

In Chapters 4 and 5, unsteady-surface-pressure (p) data are acquired using eight microphones embedded in the impingement plate with a sensing hole flush with the impingement plate surface as shown in Figure 2.11. Each microphone is a Panasonic WM-61A electret microphone with a package diameter of 6 mm and a sensing-hole diameter of 2 mm (0.08D). The microphones have nominal sensitivity of -35 ± 4 dB (relative to 1V/Pa; which correspond to $17.8^{+10.4}_{-6.6}$ mV/Pa) and frequency response range of 20-20,000 Hz. They are connected to an electrical signal conditioning circuit that is powered by 9 DC volts. The sensors are configured into a radial array,

with an inter-sensor spacing of 0.33D starting from r/D = 0, that can be placed at different azimuthal locations.

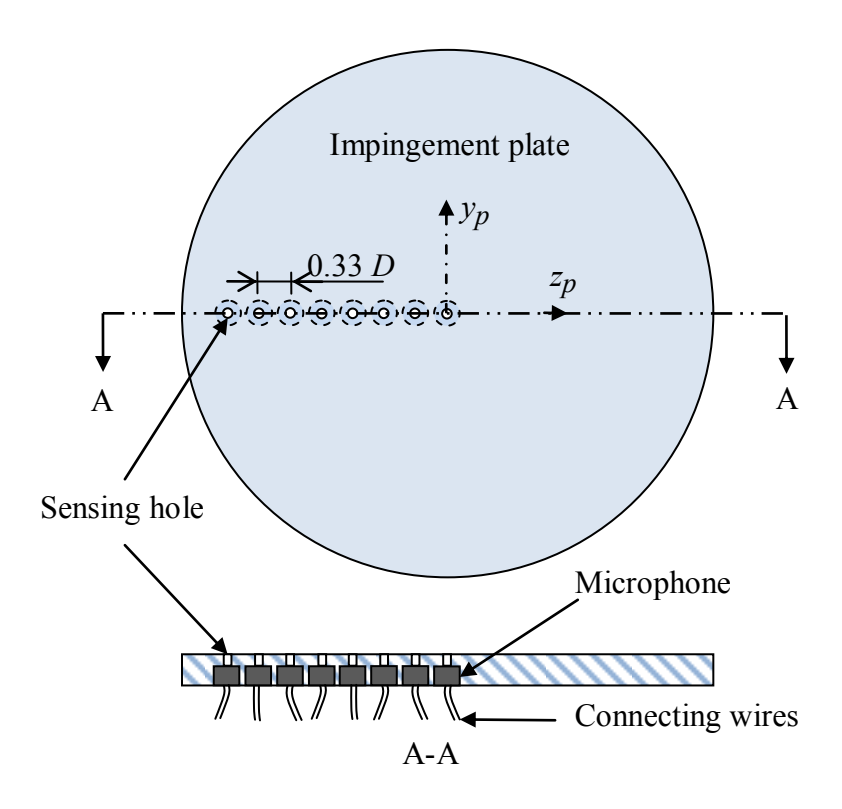


Figure 2.11 Configuration of the microphone array embedded in the impingement plate: frontal view (top) and cross section A-A (bottom)

Even though the employed electret microphones have a known nominal frequency response and sensitivity, they need to be calibrated individually. The frequency response of all microphones is obtained from calibration against a Brüel and Kjær microphone (model 4938-A-011) in a plane wave tube (PWT). The calibration procedure is similar to that employed by Daoud and Naguib [26]. Figure 2.12 depicts an image of the calibration setup, while Figure 2.13 gives a schematic drawing of the calibration arrangement. A plane wave tube made of PVC material with square cross-section of 0.5×0.5 inch is clamped against the impingement plate. The tube's wall is removed on the side where it is in contact with the impingement plate such that the

microphones are exposed to the propagating acoustic waves along the tube; i.e. the impingement surface replaces one of the tube's side walls. The tube also has eight holes opposite to the impingement wall to mount the reference microphone to calibrate against at the same cross sections of the tube where the array microphones are located.

As shown in Figure 2.13 a speaker is placed at one end of the plane wave tube to generate acoustic waves (of white noise in the present work) that travel parallel to the axis of the tube. Waves with wavelength λ remain planar (i.e. having the same pressure magnitude and phase over a given cross section) as they propagate in a square duct with solid walls when $\lambda > 2l$ or f < c/2l (where l is the side length of the tube, f is the sound frequency and c is the speed of sound); e.g. Kinsler *et al* [27]. For the PWT used in the current work, planar waves are generated for f < 13780 Hz. Thus, within this frequency range, the microphone to be calibrated and the reference microphone (B&K) are subjected to the same sound wave pressure magnitude and phase since they are mounted at the same cross section.

During calibration, sound is generated by Dayton Audio speaker (Model: RS150S-8) driven by the output from Agilent 33120A function generator coupled with Hafler-P1000 audio amplifier. With the speaker turned on, two signals are acquired simultaneously using a LabVIEW¹ program; one from the B&K microphone and the other from the microphone to be calibrated. The calibration provides both the microphone sensitivity and phase response over the range of frequencies of interest. The sensitivity response is employed to convert the microphone output voltage to pressure, and the phase response is used to compute the time delay between the measured and actual pressure.

¹ Mic-plate Calibration_V2_SimpleDAQ.vi

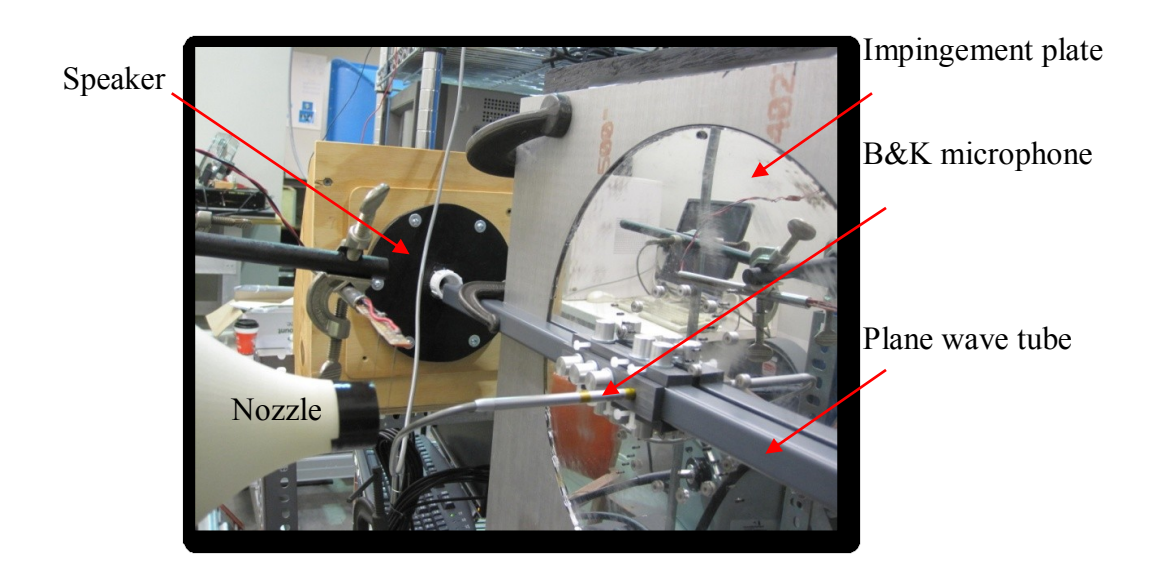


Figure 2.12 Image of the microphone calibration setup

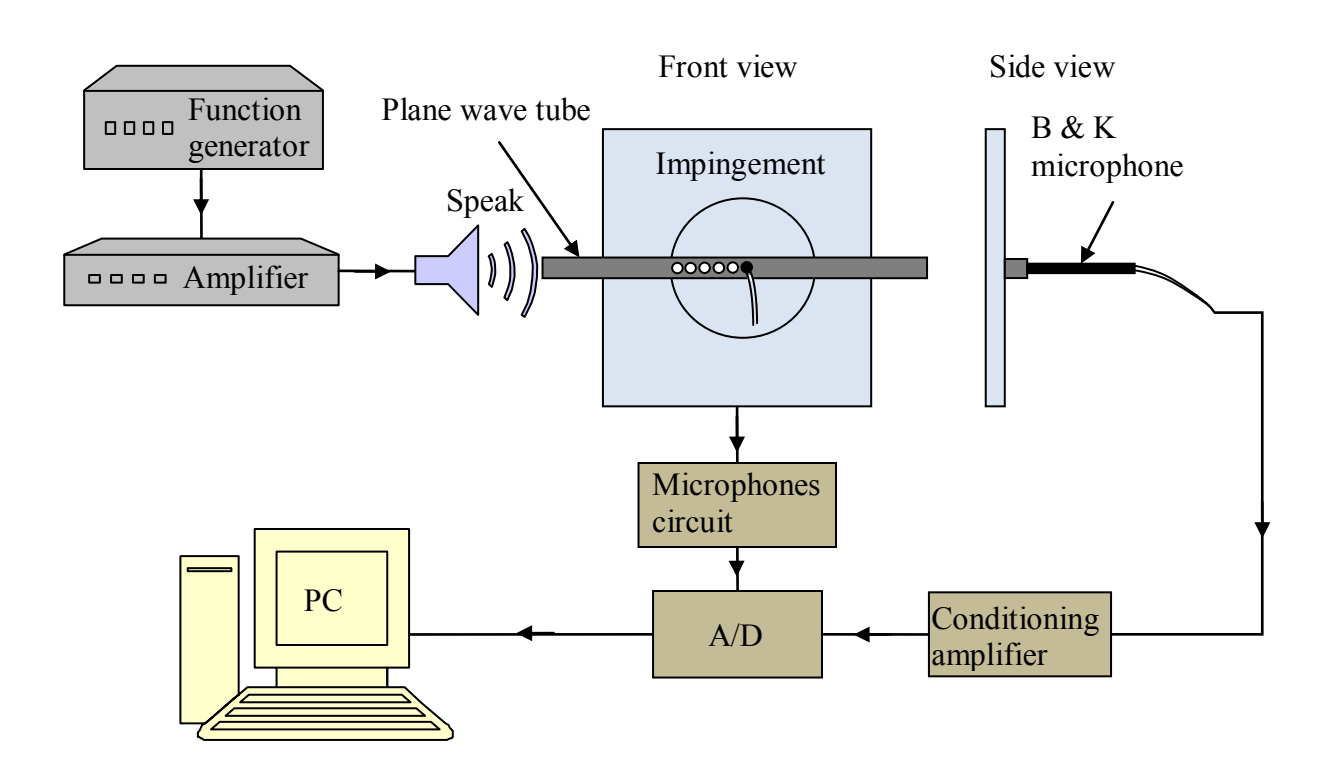


Figure 2.13 Schematic drawing of the microphone calibration setup

The procedure described above is used to determine the frequency response for all microphones. Figure 2.14 shows sample microphone calibration results, where the top plot represents the sensitivity and the bottom one depicts the phase response data. The microphones have mean sensitivities falling in the range 14-22 mV/Pa over the frequency band of interest of 50-5000 Hz. The phase variation is very small within the calibration frequency range and it follows a straight line with very shallow slope. The slope of this line (when plotted in radians versus radians/s) gives the time delay between the actual and measured pressures. This slope is extracted by fitting a straight line to the phase calibration data. The computed time delays for all microphones are in the range $0.3 - 3.3 \mu s$. Thus, the maximum mismatch in the actual time of the measured pressure signal from all microphones is 3 μs , which is more than three orders of magnitude smaller than the period of the highest frequency of significant pressure unsteadiness found in this study (5 m s, corresponding to 200 Hz). Thus, for all practical purposes, the measured pressure signal accurately represents the actual pressures values occurring simultaneously at the locations of the microphones in the array.

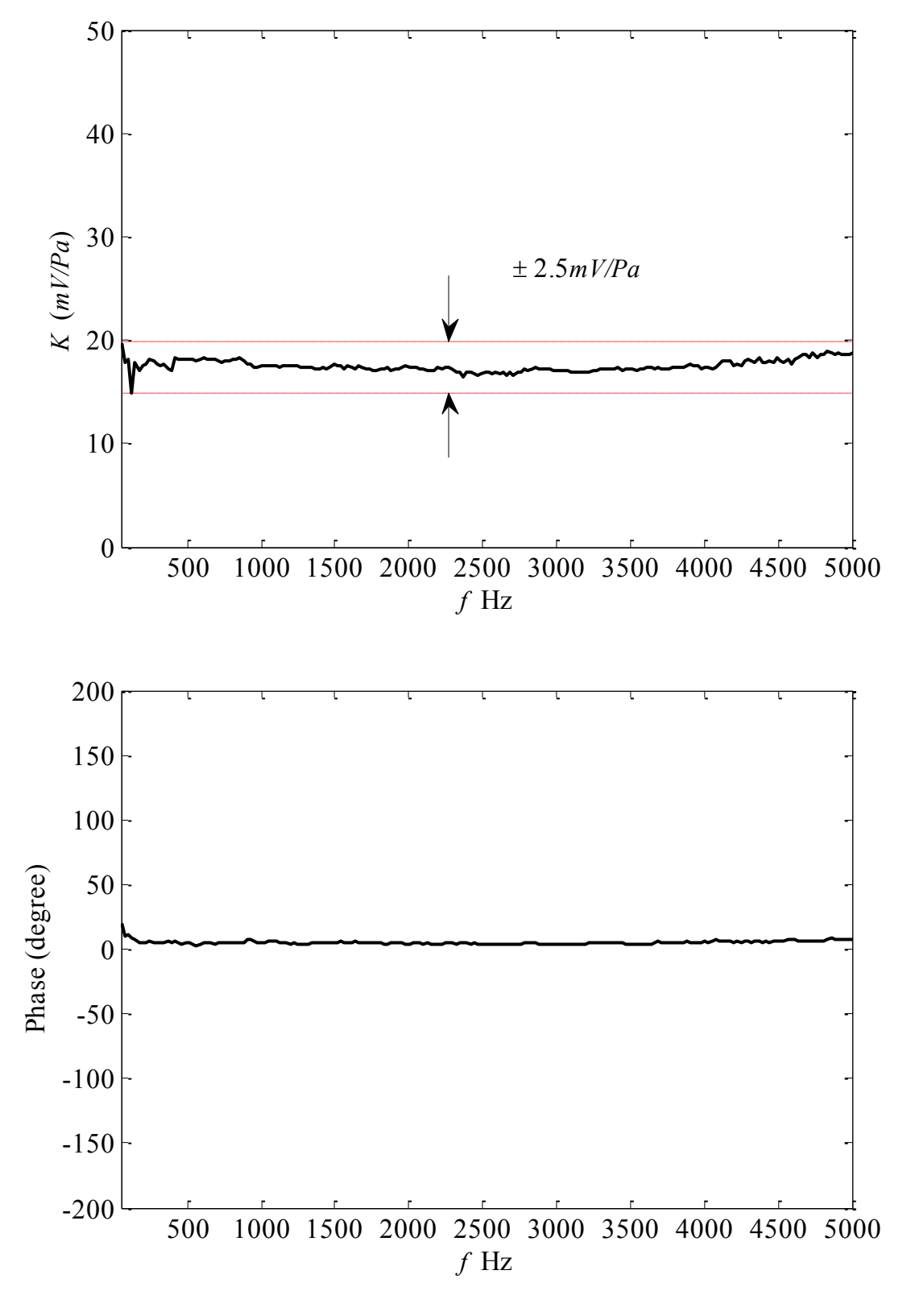


Figure 2.14 A sample microphone calibration; sensitivity (top) and phase shift (bottom)

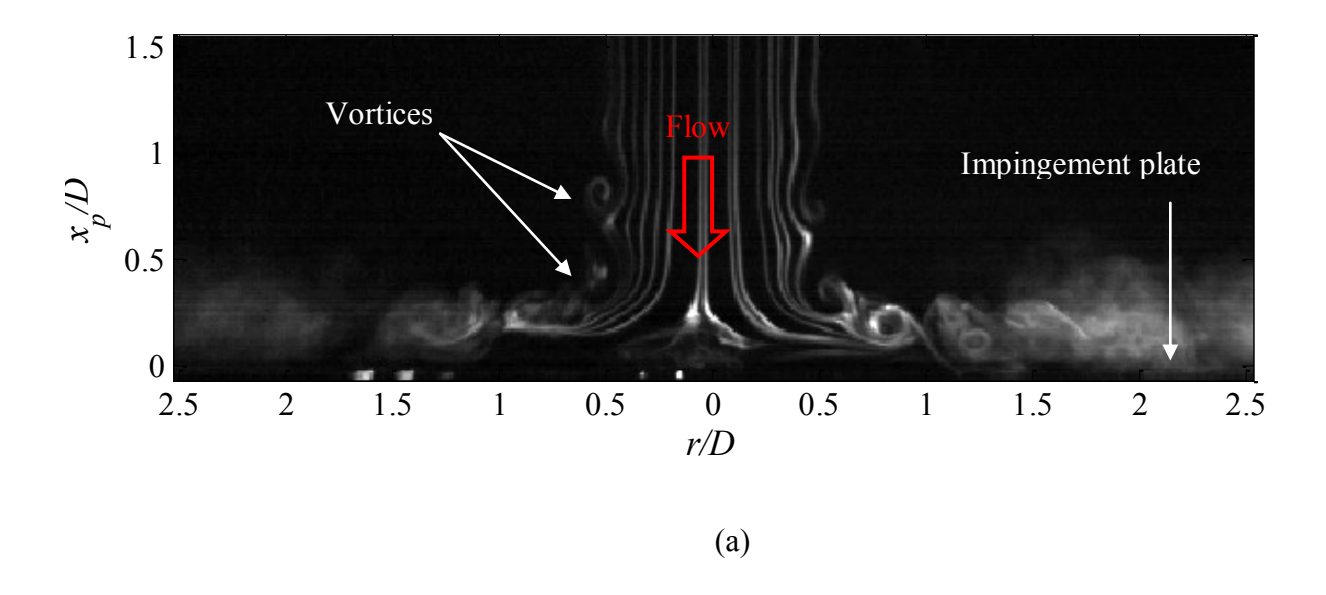
2.5 Simultaneous Wall-Pressure Measurement and Flow Visualization Setup

2.5.1 Flow Visualization

A passive scalar, such as dye or smoke, is a diffusive pollutant in a flowing fluid that is present in such low concentration that it has no dynamical effect on the motion of the fluid itself; Warhaft [28]. Flow-visualization using a passive scalar may be used to experimentally observe vortex rings; such as found in axisymmetric jets. While this technique has led to many great insights, the results should be interpreted with care. If a scalar is to mark the vorticity, there are two important factors to be considered. One is to inject the scalar near where vorticity is produced, for example at the nozzle lip to visualize a vortex ring. Another is that it is important to realize that the rate of diffusion of vorticity and that of a passive scalar are generally different and hence the scalar field may not represent the vorticity field after a time interval from the initial introduction of the smoke into the flow [29]. An imperative parameter is Schmidt number (Sc), which is defined as the ratio of the kinematic viscosity and diffusion coefficient of the scalar. Ideally, it is desirable to have Schmidt number close to one. Another important effect to be considered is that in the regions where stretching of vorticity occurs the marker scalar diminishes in the core of vortices, which makes it difficult to visualize the flow in these regions, [29]. Cimbala et al. [30] used smoke wire to visualize the near and far wake of the flow over a two-dimensional circular cylinder by placing the smoke wire at different locations downstream of the cylinder. They used smoke generated from oil with diffusion coefficient of about $D_m = 2 \times 10^{-5}$ $10^{-6} \text{ cm}^2/\text{s}$ in air, kinematic viscosity of $v \approx 0.16 \text{ cm}^2/\text{s}$, so the effective Schmidt number v/D_m is of order 10^5 . This means that the smoke diffuses much slower than the actual vortical structure.

When Cimbala *et al.* [30] placed the smoke-wire just downstream of the cylinder; the vortex street is clearly marked and remains visible to the downstream end of the photograph. However, when the smoke wire is moved to different locations farther downstream, the vortices are seen to be less well defined, disappearing all together for wire placement sufficiently far from the cylinder. Cimbala *et al.* concluded that the visualization is useful only for a finite distance downstream of the smoke wire and to obtain an accurate description of the entire developing flow field, it is necessary to place the smoke wire at various positions.

Figure 2.15 depicts an example from the current study of two images of flow visualization of the impinging jet in normal (Figure 2.15a) and oblique (Figure 2.15b) impingement. Similar images will be discussed in more details later in the document. It is noteworthy that in the present study, the smoke travels a distance of a few jet diameters (from the jet exit to the side edge of the image). This is in comparison to the study of Cimbala *et al*, where the imaged range extended over a much larger domain in terms of a characteristic flow scale (100-125 cylinder diameters). Therefore, given the relative compactness of the visualized domain in the present work, it is expected that the visualization gives a good description of the underlying flow structure. Moreover, the growth in size of the flow structures as a result of viscous diffusion, which is proportional to $\sqrt{v\tau}$ (where v is the kinematic viscosity and τ is the time for the flow structures to travel the flow domain), can be estimated by approximating the time for the flow structure to convect throughout the flow domain of 6 diameters. This estimation is found to be of 0.85 *mm* which is very small when compared to the size of the flow structures (about tenth of the smallest observed vortex size in the vicinity of the impingement wall).



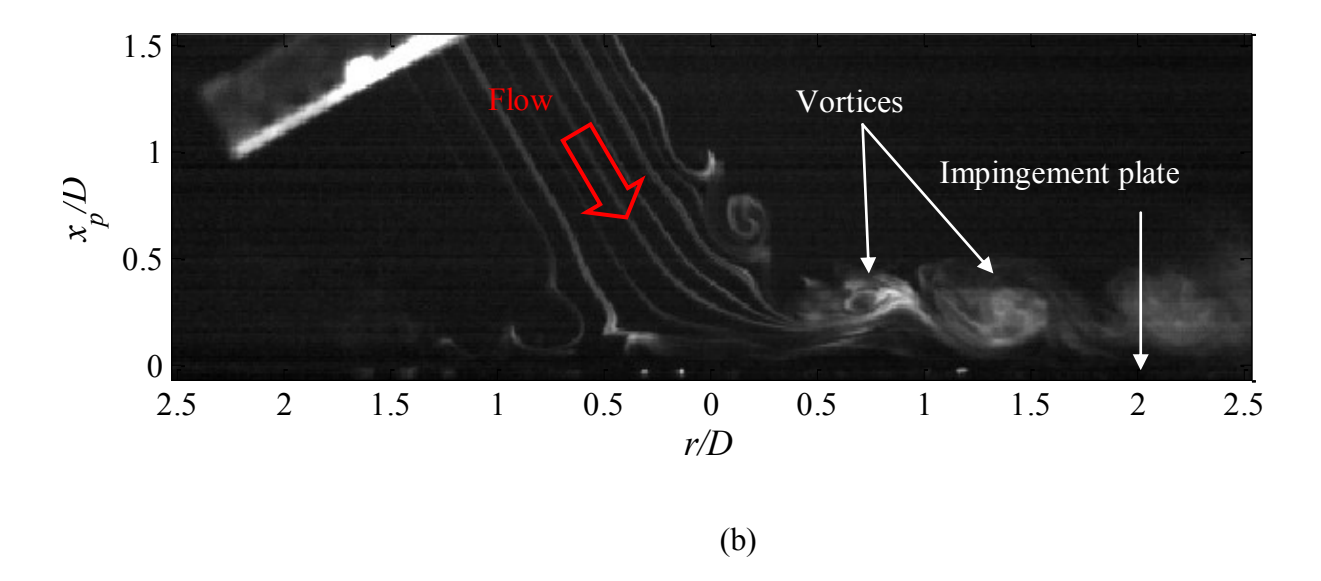


Figure 2.15 Flow visualization images at H/D=2; normal ($\gamma=0^{\circ}$) (a) and oblique ($\gamma=30^{\circ}$) (b) impingement

2.5.2 Synchronized Flow Visualization and Microphones Measurements Setup

Figure 2.16 depicts three-dimensional drawing of the flow visualization setup; the figure depicts the physical arrangement of the hardware while Figure 2.17 displays a block diagram of

the method used for synchronization of the flow visualization and pressure measurement. A stainless steel 'smoke wire', with 0.1*mm* diameter, is placed horizontally in the symmetry plane of the axisymmetric jet at a location immediately downstream of the nozzle exit. The wire is coated with small drops of model-train oil, which form streaklines when heating the wire using a DC voltage that is applied across the wire for 2 seconds. Simultaneously, high-speed camera (REDLAKE, MotionPro x4) is employed to capture the top view of the streaklines. The camera is capable of acquiring 8-bit black and white images at a rate of 5000 frames per second with full resolution of 512×512 pixels and over 200,000 frames per second with reduced resolution. The light source is SAITM Universal Basic Light employing General Electric ELH 300W tungstenhalogen lamp; this system provides a continuous collimated beam of uniform intensity to illuminate the smoke.

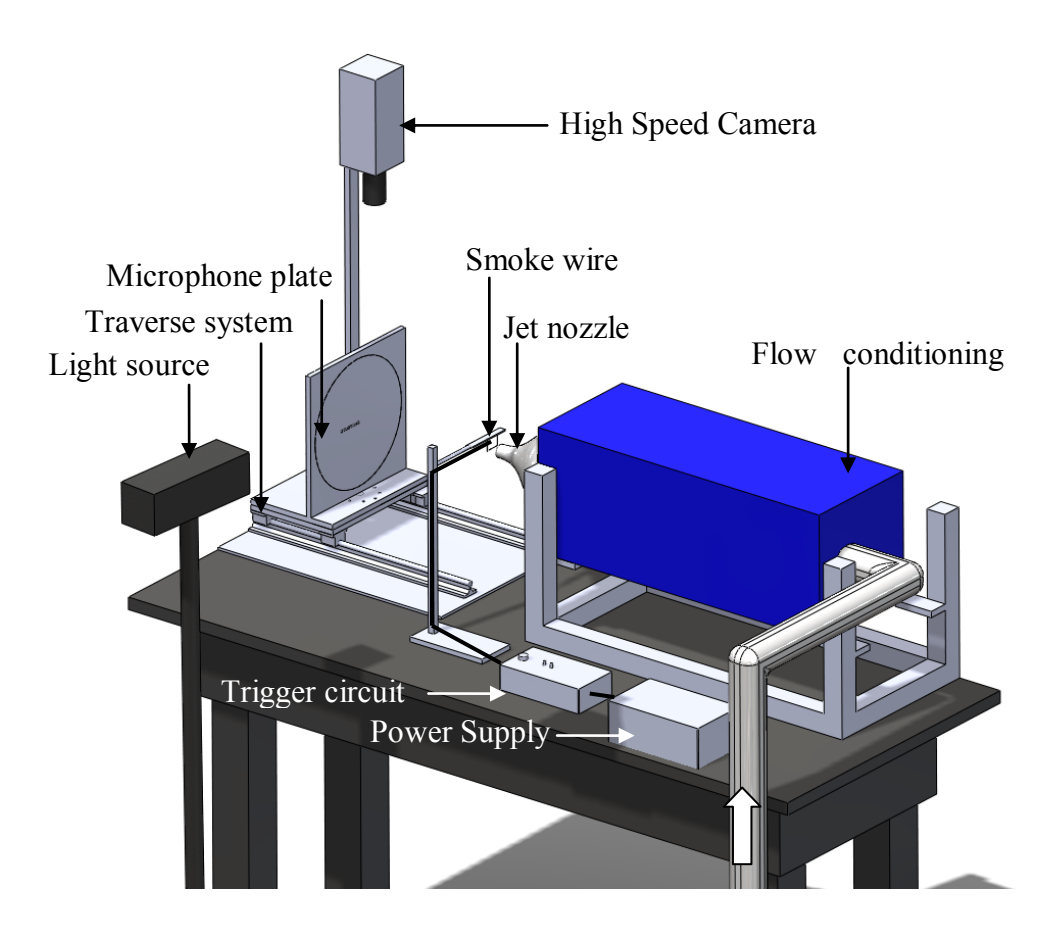


Figure 2.16 Three-dimensional drawing of the flow visualization setup

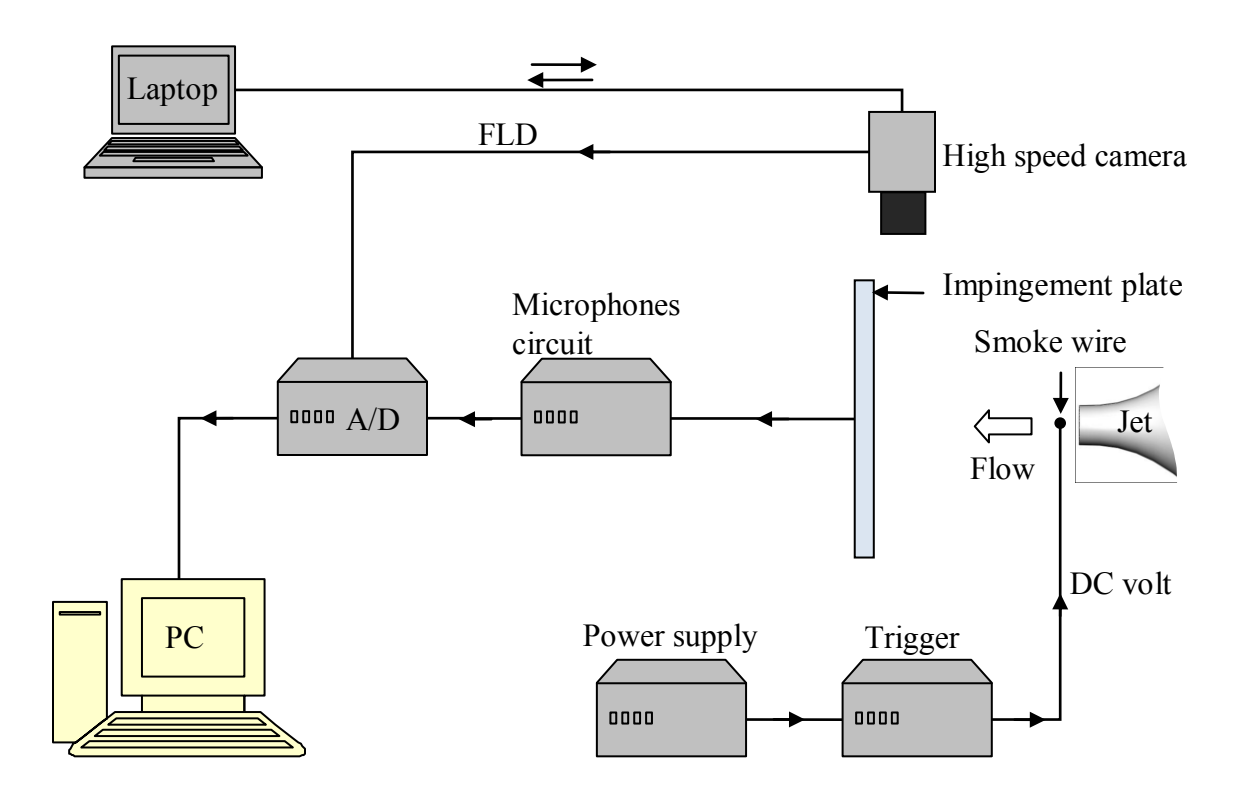


Figure 2.17 Block diagram of simultaneous flow-visualization and pressure-measurement setup

Synchronization of image and data acquisition is based on employing the field (FLD) signal of the high speed camera as a 'master clock'. The FLD signal rate changes when varying the image sampling rate such that one pulse is produced per image. By acquiring this signal simultaneously with the microphone data, it is possible to identify the times at which images are captured by the camera. The precise time of the image capture, for 2000 frames/second sampling rate, is during the 250 μ s period when the camera shutter is open. Since this time difference is negligible relative to the flow time scales (less than 5 ms in the flow investigated), the image capture instant is taken as that of the rising edge of the FLD signal.

A LabVIEW program and Motion Studio software are employed at the same time in order to capture the synchronized flow-visualization images and pressure data; the Motion Studio software is designed to grab images while the LabVIEW program is used to acquire the pressure data and the FLD signal. In operation, the unsteady-surface pressure, FLD signal and

plenum pressure acquisition program is started first, and shortly after the Motion Studio is run to acquire images. The trigger to heat the smoke wire (which imposes 7 DC volts across the wire) is provided from a manual switch that is toggled after the start of the image acquisition program. An example is shown in Figure 2.18 of the acquired pressure data and FLD (blue line with circles) signal. When the camera is not capturing images, the FLD signal is zero, as illustrated early in time in the plot in Figure 2.18. Once image acquisition commences, a square wave pulse is initiated and is sustained during the images acquisition. Each image is taken during the pulse peak of the FLD signal, where the first image corresponds to the first peak. Determining the exact time instant of the image during the pulse period can be neglected since the pulse duration, which is the lens exposure time, is small enough as mentioned before.

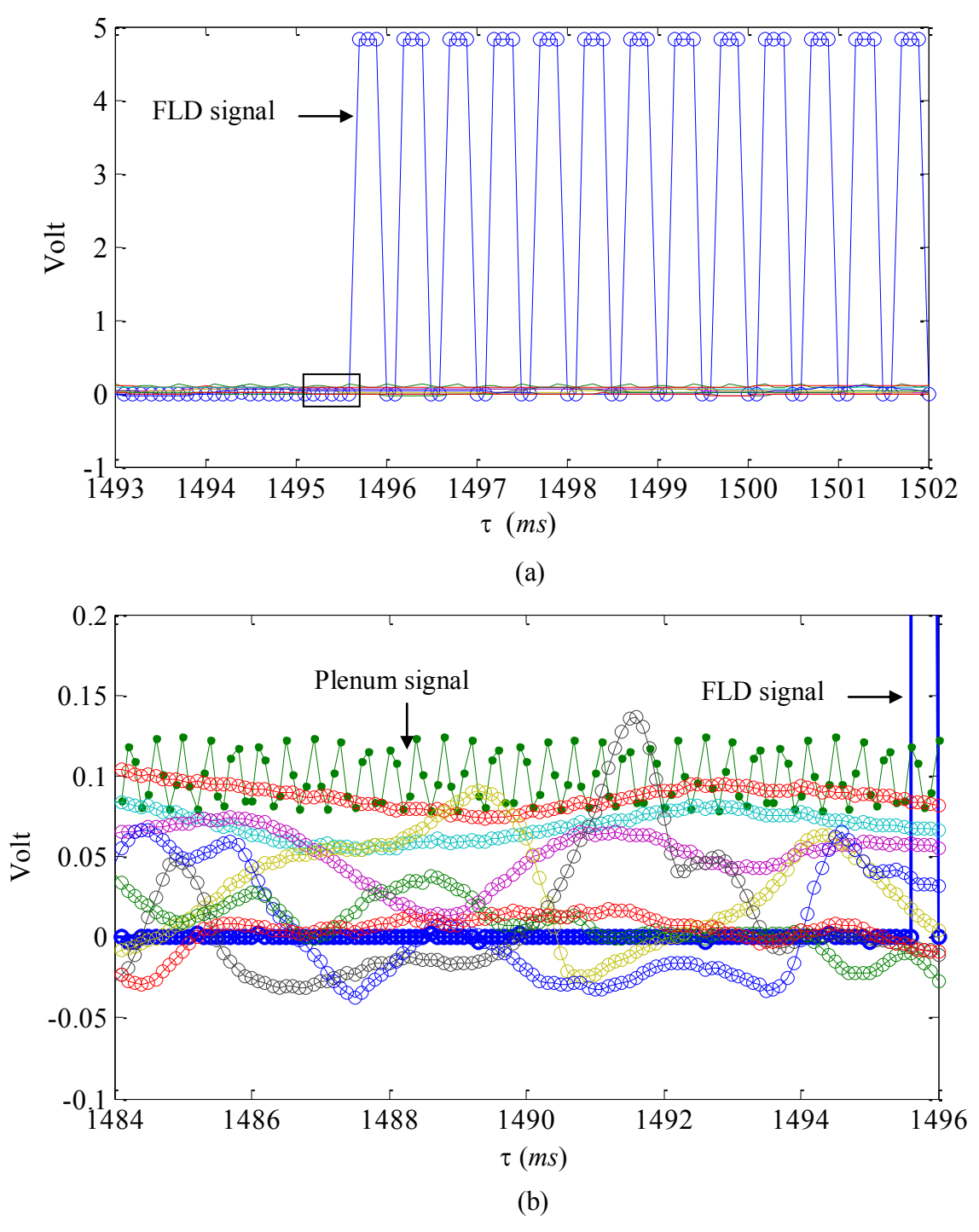


Figure 2.18 A sample of the recorded FLD signal and pressure data (a) (τ is the time since the start of the data acquisition), and a zoomed-in view around the time when the first image is captured of the pressure signals and FLD signal (b): different colors correspond to signals from different microphones and the plenum pressure transducer, which are much smaller in magnitude than the FLD signal.

2.1.6 Data Acquisition Hardware

All signals are acquired using a multiplexed 12-bit National Instrument analog to digital (A/D) desktop computer card (NI PCI-6024E); the data acquisition broad has 16 single-ended analog inputs, or 8 differential channels, with capability of 200 kHz maximum sampling frequency. The board is employed to obtain the data from the radial array of eight microphones as well as the plenum pressure using a 10 torr Baratron pressure transducer. The latter is used to identify the jet exist velocity after it has been calibrated against a Pitot tube placed in the potential core of the jet. For the shear-layer study, the same NI PCI-6024-E board is used to drive the stepper motor (using parallel input/output provisions) to traverse the hot wire probe as well as to acquire data from the hot wire. The board has maximum time delay of 0.08 ms, which is negligible relative to flow time scale.

Chapter 3: Shear Layer Study

After assembling the jet facility and making the necessary alignments, it is important to verify the quality of the flow that exits from the jet opening. This chapter provides results from a study of the initial jet shear layer characteristics and a comparison of these with knowledge in the existing literature on jet flows. A hot-wire anemometry setup (discussed in Chapter 2) is employed to measure the streamwise velocity component (in the x_j) direction while traversing the hot wire across the shear layer in the y_j direction. Self-similarity of the mean velocity profiles, shear-layer momentum thickness and fluctuating-velocity spectral analysis are examined and found to agree well with literature.

3.1 Self Similarity of the Initial Shear Layer

Having checked the axisymmetry of the mean jet flow (in chapter 2), it is also important to document the shear layer characteristics as well as its initial evolution in the streamwise direction; i.e. the "initial condition" of the investigated flow. This was accomplished by measuring the mean and fluctuating streamwise velocity profiles across the jet shear layer. Preliminary data were first recorded, using the hot wire, with large traversing steps to obtain a coarse jet velocity profile and identify the shear layer location. Once the edges of the shear layer were located, fine traversing steps were employed to properly resolve the thin high-shear region. Typically, the traversing step was chosen to produce 100 measurement locations within the shear layer. These measurements were repeated at different locations downstream of the jet $(x_j/D = 0.02, 0.2, 0.4, 0.6, 0.8, 1, 2, 3 \text{ and 4})$ and jet velocities of 5, 10 and 20 m/s. Binary data files were

recorded at every measurement location containing 20 seconds of hot wire, temperature and jet velocity time-series data sampled at 10 kHz.

Figure 3.1 depicts the expected self-similarity, with changing jet velocity, of the mean velocity profile across the shear layer where the cross-flow coordinate, measured from the centerline of the shear layer (where $U = U_j/2$), is normalized by the momentum thickness Θ , which is calculated using equation (3.1). Note that the integral (3.1) is truncated on the lowspeed side of the shear layer such that the low limit of the integration corresponds to the location at which jet velocity is 10% of the jet exit velocity. This procedure is used to reduce the hot-wire rectification error produced from the reverse flow that may occur at the outer edge of the shear layer. All the profiles were measured at $x_i/D=0.2$ for three different Reynolds numbers; the profiles collapse very well which indicates self-similarity. In addition, the profiles from the hotwire measurements are compared to the shear-layer similarity solution (solid line in Figure 3.1) obtained by Lock [31] from numerically solving the boundary-layer equations subject to boundary conditions corresponding to two parallel streams with one stream having zero velocity (table VI in Lock [31]). The results from the experimental measurements depict generally good agreement with the numerical solution, which suggests that the jet flow is laminar at the exit. There is some small discrepancy between the theoretical and experimental profiles towards the edges of the shear layer. However, this discrepancy is likely due to the fact that in the experiments, the shear layer is axisymmetric, whereas the theoretical solution is for a twodimensional shear layer. Nevertheless, for the lowest Reynolds number (thickest shear layer) the ratio of the shear-layer thickness (measured between $U/U_i = 0.05$ to 0.95) to jet radius is 0.0696 which is much smaller than one, suggesting that the two-dimensional solution should at least give a reasonable representation of the axi-symmetric shear layer velocity profile. A theoretical solution for the axisymmetric shear layer could not be found.

$$\Theta = \int_{\mathcal{Y}U=0.1Uj}^{\mathcal{Y}U=Uj} \frac{U(y)}{U_j} \left(1 - \frac{U(y)}{U_j} \right) dy \tag{3.1}$$

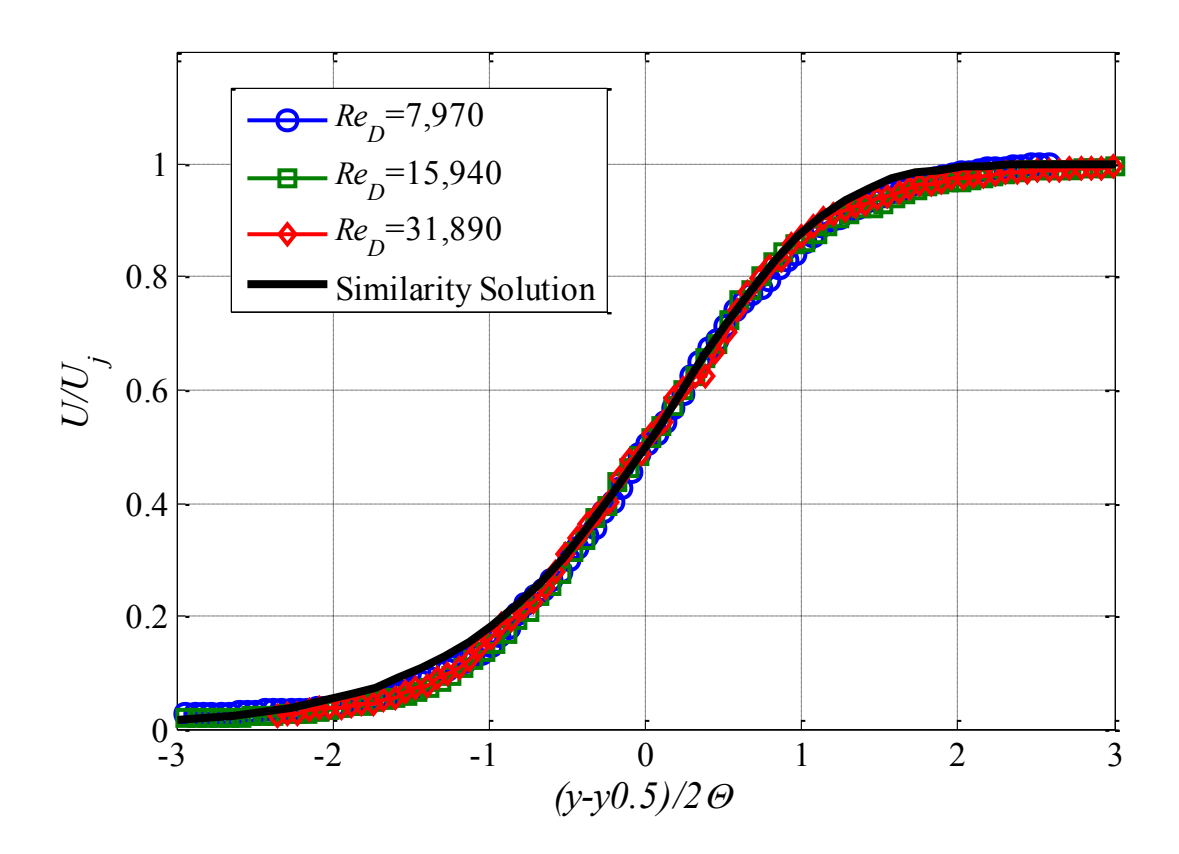


Figure 3.1 Mean velocity profiles across the shear layer, demonstrating self-similarity with respect to change in the jet velocity at $x_j/D=0.2$, also compared against shear layer solution by Lock[31]

Self-similarity of the mean-velocity profiles obtained at different locations downstream of the jet (x_j) and Reynolds number of 7,970 is demonstrated in Figure 3.2. The profiles collapse over the range of $x_j/D=0.2-1$. It is noteworthy that the self-similarity of the profiles shown in Figure

3.2 is obtained at streamwise locations upstream of the resonance location (a description of resonance is given in the next paragraph). It is found that self-similarity with respect to downstream distance for a certain jet velocity is achieved when all profiles are measured at locations either upstream or downstream of the resonance location. In other words, a profile at location upstream of the resonance is not self-similar with another profile measured downstream of the resonance location.

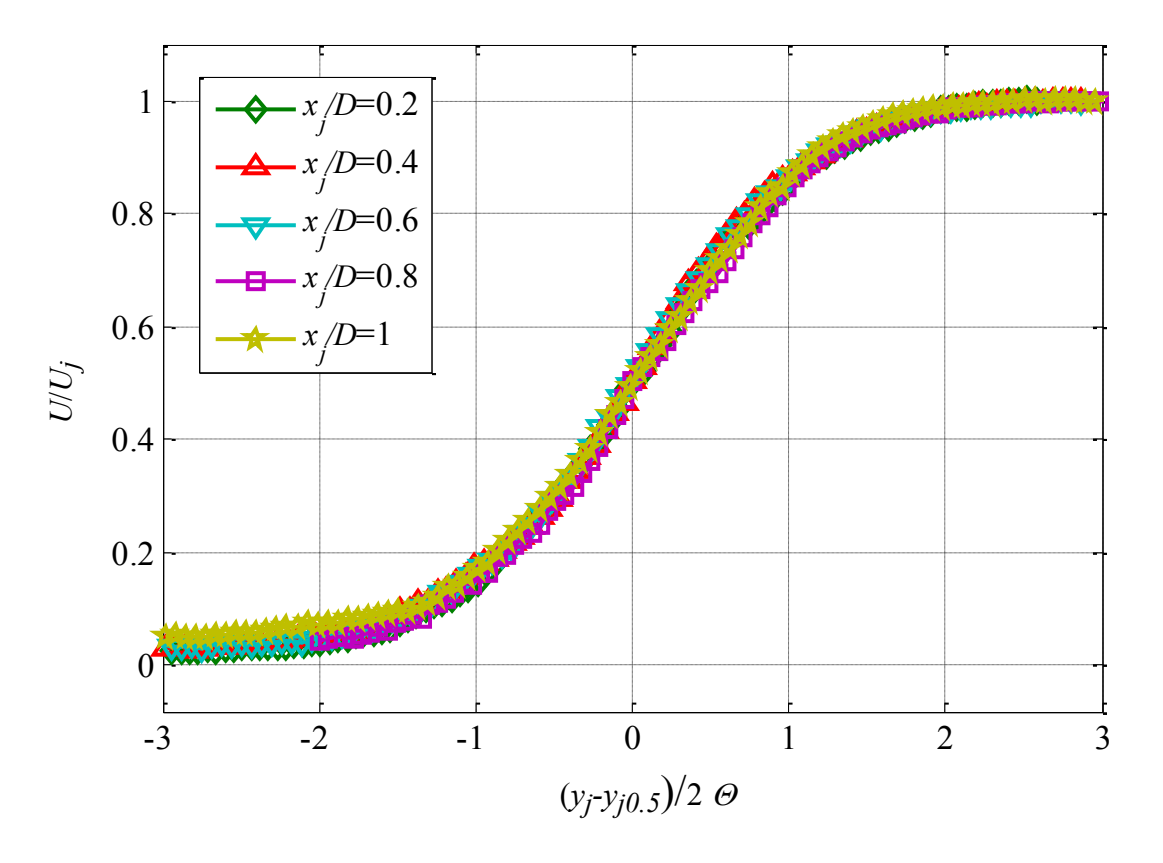


Figure 3.2 Mean velocity profiles across the shear layer, demonstrating self-similarity with respect to downstream distance for Re_D =7,970

3.2 Momentum Thickness

Figure 3.3 and Figure 3.4 show normalized shear-layer momentum-thickness growth with downstream distance from the jet exit (in Figure 3.3 downstream locations are normalized by the

jet diameter D while in Figure 3.4 they are normalized by the initial momentum thickness Θ_i) for three different Reynolds numbers (Re_D =7,970–15,940 and 31,890), where Θ_i is the initial momentum thickness (measured at x_i/D =0.02). The momentum thickness of the three different Reynolds numbers grows linearly, albeit very slowly, near the jet exit. This initial slow growth results in the momentum thickness having practically the same value at x_i/D =0.02, 0.2 and 0.4 after which there is a fairly abrupt increase in the spread rate of the shear layer at Re_D =31,890. This trend also occurs for the lower Reynolds numbers but at farther downstream locations, as identified by the three arrows in

Figure 3.3. Drubka *et al.* [1] showed that the location at which the spread rate of the shear layer increases abruptly is where the fundamental and sub-harmonic modes of the initial shear layer instability have the same phase speed leading to the establishment of resonance between the two modes. They also found this location to occur two initial (fundamental) wavelengths downstream of the jet exit. When the momentum thickness growth is plotted versus x_j normalized by the initial momentum thickness Θ_i (Figure 3.4), the resonance locations and the momentum thickness evolutions for the three different Reynolds number collapse very well.

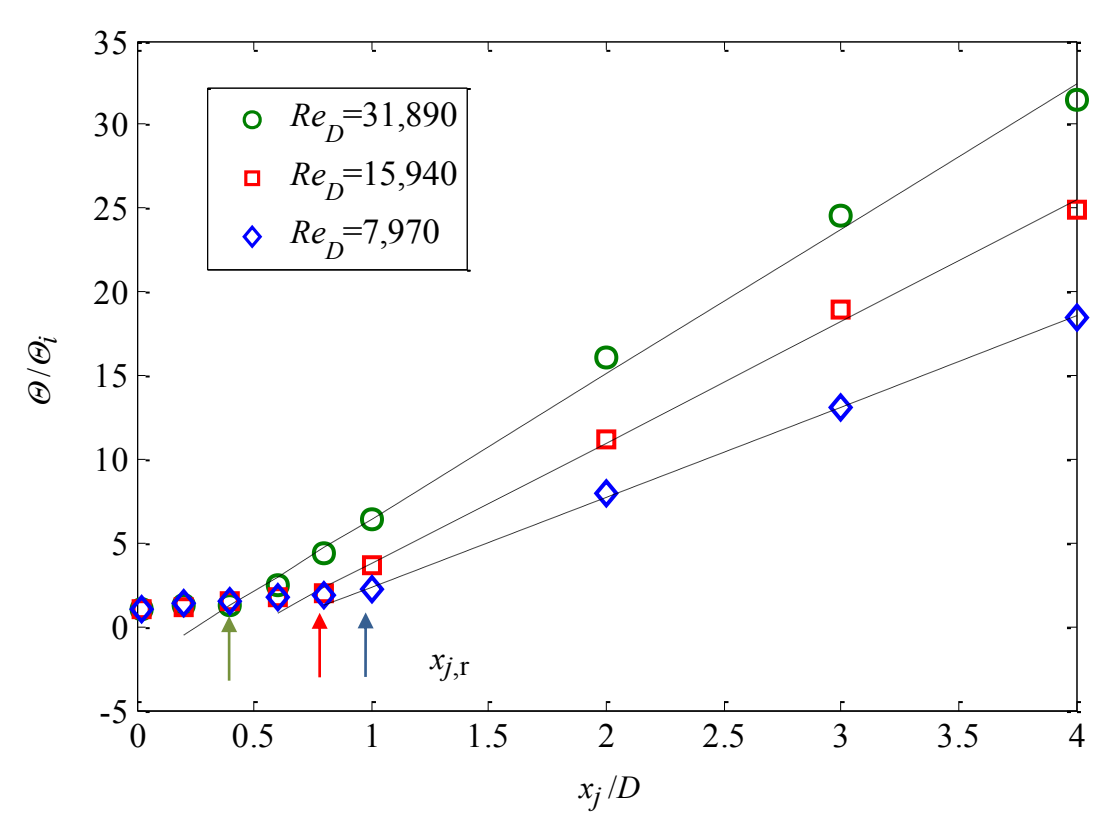


Figure 3.3 Growth of the shear layer momentum thickness downstream of the jet. The streamwise coordinate is normalized by jet exit diameter. Arrows indicate the resonance location $(x_{j,r})$, and the broken lines represent linear-fits of the momentum thickness data downstream of the resonance location

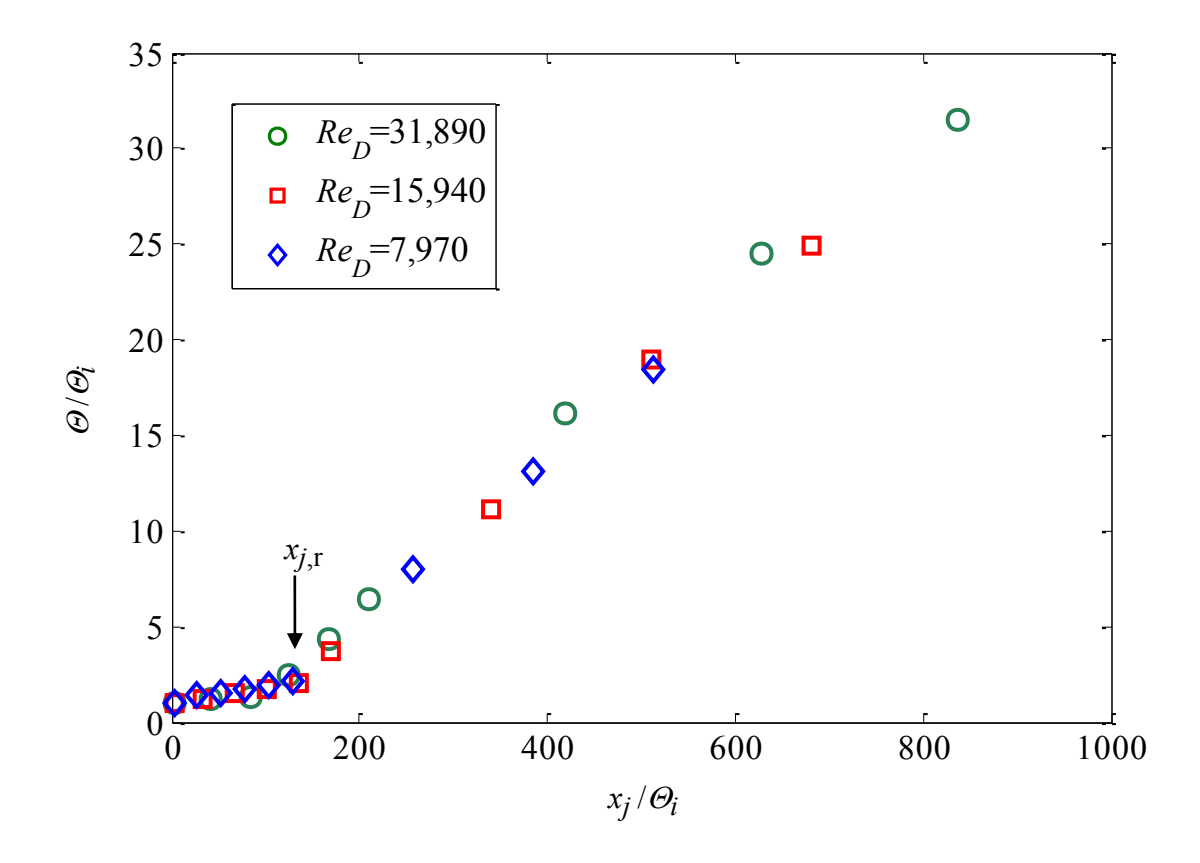


Figure 3.4 Growth of the shear-layer momentum thickness downstream of the jet. The streamwise coordinate is normalized by the initial momentum thickness. Arrows indicates the resonance location $(x_{i,r})$

Figure 3.5 depicts the dependence of the natural logarithm of the momentum thickness on the natural logarithm of the Reynolds number of Re_D = 7,970, 15,940 and 31,890 at x_j/D =0.2. The behavior is practically linear (on this logarithmic plot) with a slope of -0.44, based on a least-squares fit. This is consistent with the results of Drubka et al [1] who found the slope to be -0.5 for a different range of Reynolds numbers: $39,000 \le Re_D \le 85,000$ at $x_j/D = 0.07$. Though the present results are obtained at $x_j/D = 0.2$, as seen from Figure 3.3, there is very little change in the momentum thickness between the jet exit and $x_j/D = 0.02$. The -0.44 slope found in Figure

3.5 suggests that the boundary layer at the exit of the jet is laminar, exhibiting approximately inverse square root dependence on jet velocity.

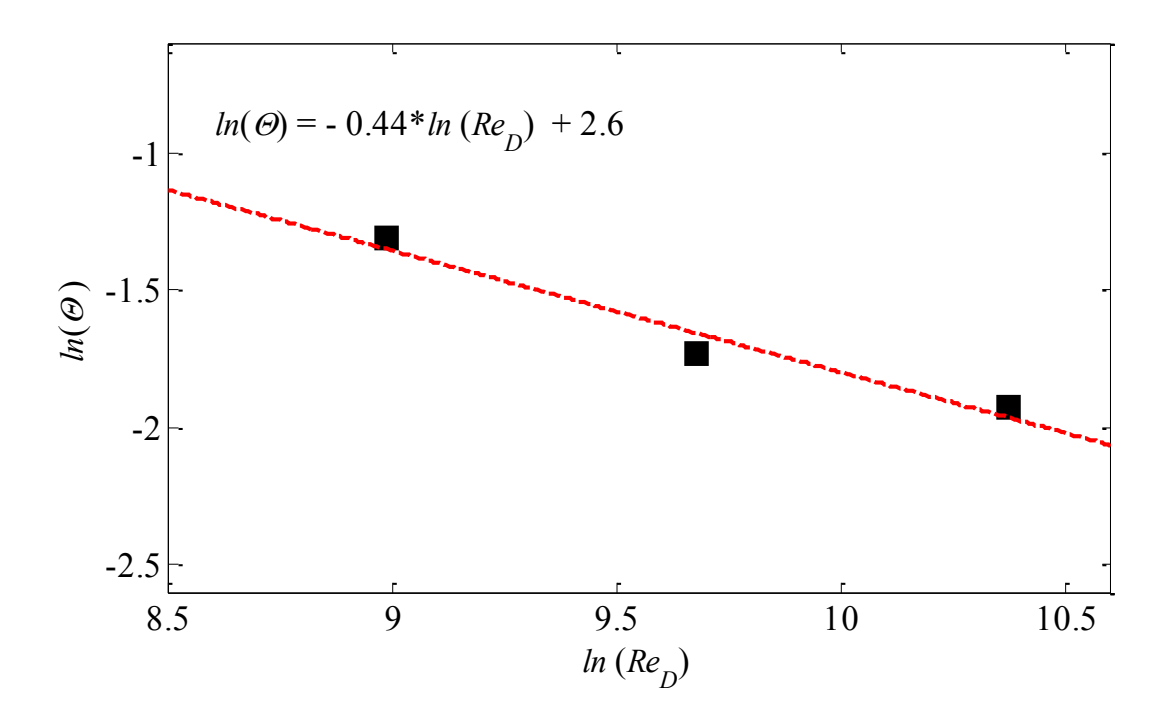


Figure 3.5 Momentum thickness variation with Reynolds numbers at $x_i/D = 0.2$

3.3 Power Spectral Analysis of the Initial Disturbance

Before characterizing the initial shear layer in terms of spectral analysis, it is important to depict the root mean square (rms) profile across the shear layer. Figure 3.6 shows normalized velocity rms profiles across the shear layer at resonance locations for three different Reynolds numbers. The rms magnitude generally increases with increasing Reynolds numbers. At Re_D of 7,970 the magnitude is very low in comparison to the other two. The rms profile at Re_D of 15,940 peaks near y_j - $y_{j0.5}$ =0.7 whereas the profile associated with the Re_D of 31,890 peaks near the center.

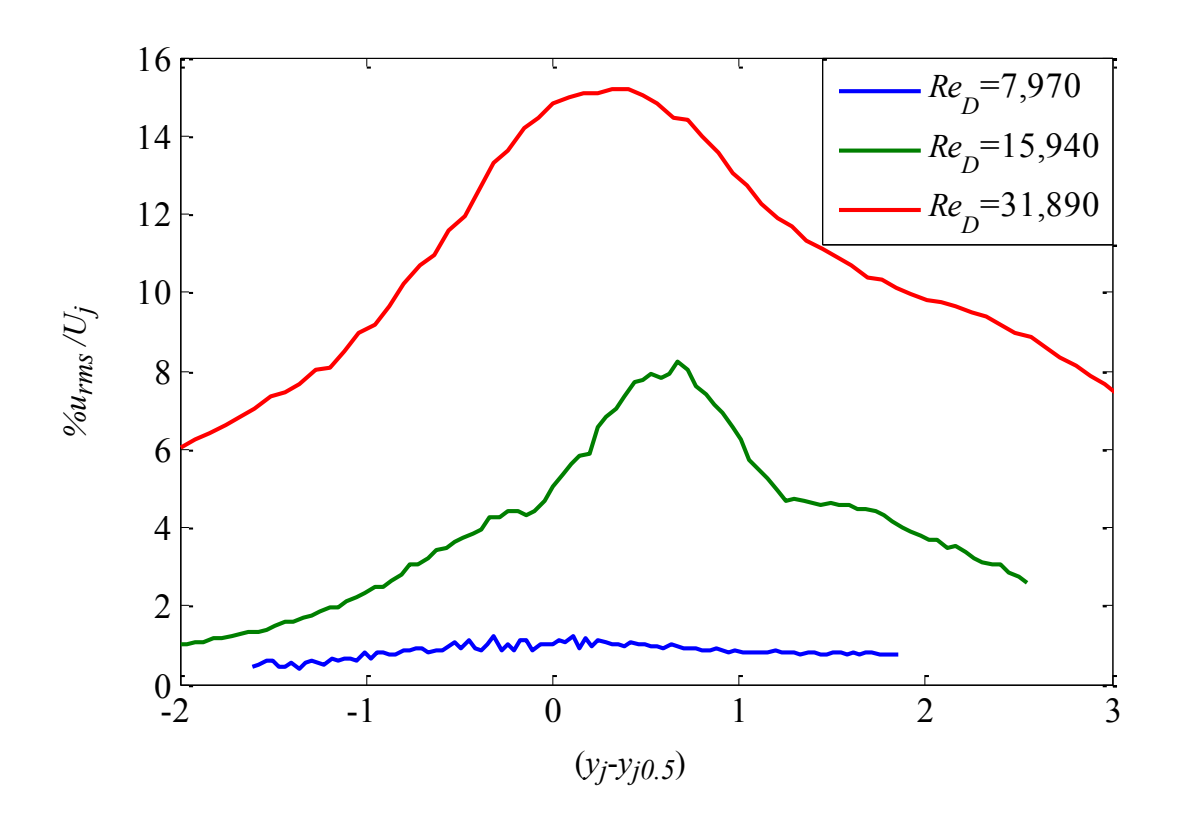


Figure 3.6 Normalized velocity *rms* profile across the shear layer for different Reynolds numbers at resonance locations

Figure 3.7 shows velocity power spectra at $x_j/D = 0.2$, plotted versus frequency in Hz, and Figure 3.8 depicts the same spectra versus Strouhal number based on momentum thickness for three different Reynolds numbers. The power spectra are computed for a location in the middle of the shear layer, where $U(y_j)/U_j = 0.5$. Each spectrum is the result of an average of spectra obtained from 400 records, each containing 500 data points. The corresponding resolution is 20 Hz and the random uncertainty is 5%. At the low Reynolds number, four spectral peaks that rise above the otherwise broad spectrum are seen in the frequency range 200-400Hz. These peaks shift toward higher frequencies with increasing Reynolds number, which is an expected behavior due to the jet velocity increase. In other words, the shear layer instability should have higher

frequency at higher jet velocities. This trend is also accentuated by the decrease in the shear layer thickness with increasing jet velocity. In Figure 3.8, where the power spectra versus the Strouhal number are displayed, the spectral peaks for all three Reynolds numbers lie in the range of St_{Θ} =0.01-0.02 which encompasses the well known St_{Θ} = 0.016, corresponding to the most unstable mode based on linear stability analysis (e.g. see Michalke [3]).

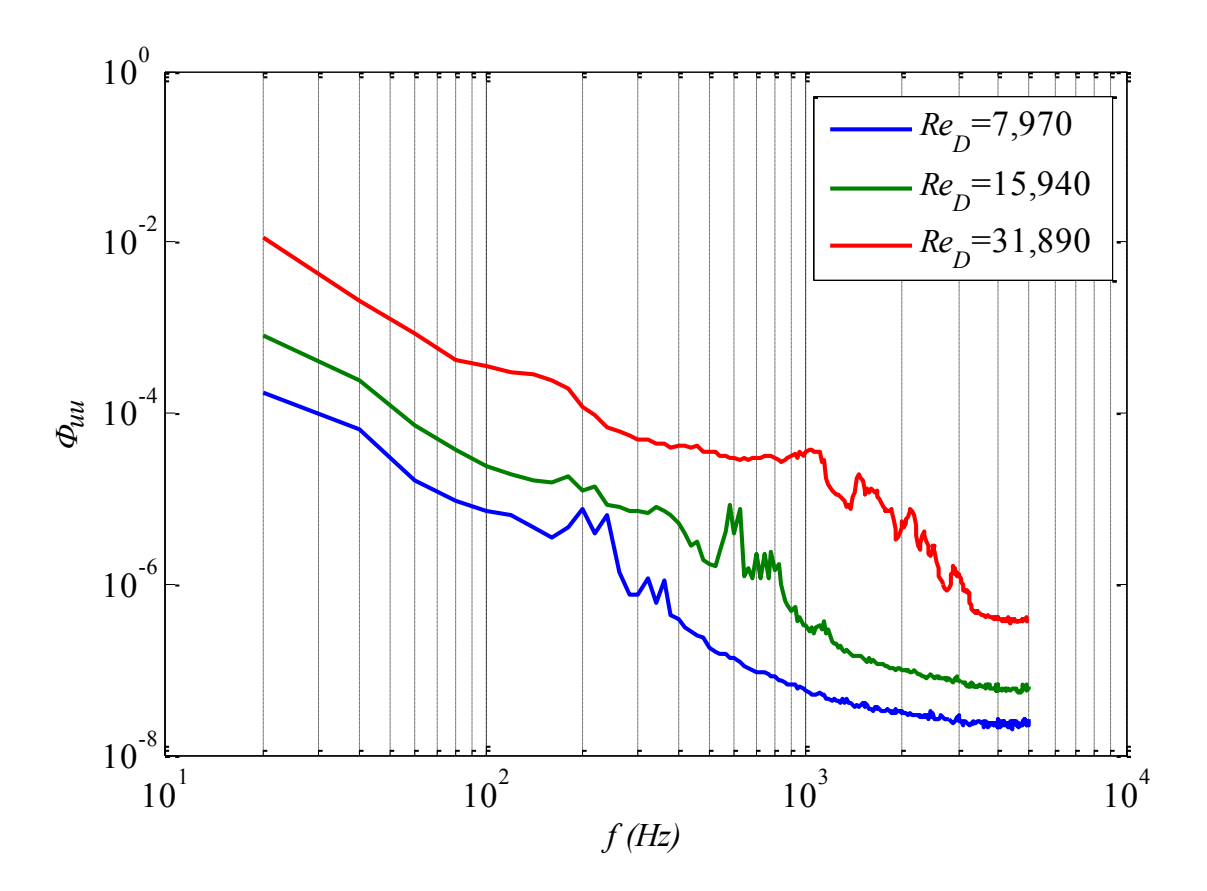


Figure 3.7 Velocity power spectra (normalized by the square of the jet exit velocity) versus frequency at $x_i/D = 0.2$ and $y_i/D = y_{i0.5}$

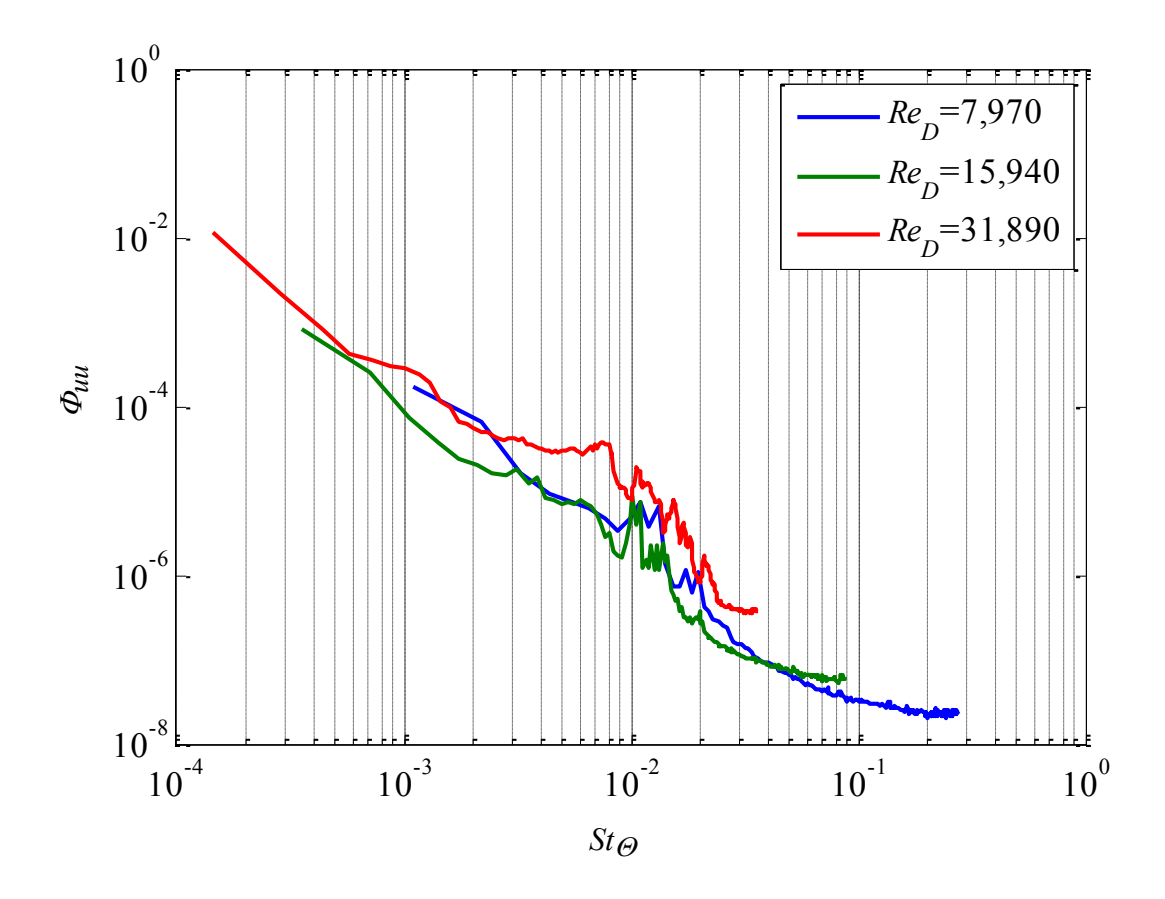


Figure 3.8 Velocity power spectra (normalized by the square of the jet exit velocity) versus Strouhal number based on momentum thickness at $x_i/D = 0.2$ and $y_i/D = y_{i0.5}$

3.4 Evolution of the Power Spectra with Downstream Distance

This section is intended for examination of the frequency content of the jet velocity fluctuation before impingement at the same flow conditions at which unsteady pressure measurements are done (see Chapter 4 for pressure data details). This examination will be helpful in drawing some preliminary conclusions regarding the relationship between the flow and the pressure fluctuations. Hot wire measurements are taken at different x_j/D locations without the presence of the impingement plate. The hot wire is placed approximately in the middle of the shear layer of the jet flow, where the fluctuations are strongest.

Figure 3.9 depicts power spectral density of the velocity fluctuation at different locations downstream of the jet: $x_i/D=1$, 2, 3 and 4. The spectra are obtained with a resolution of 2.44 Hz and 5% of random uncertainty. The figure shows a peak near $St_D \approx 1.3$ with very low energy at $x_i/D=1$ and 2. At $x_i/D=2$ the figure depicts two other spectral peaks at lower Strouhal numbers that are approximately sub-harmonics of the higher one found at $x_i/D=1$ and 2. Of these two peaks, the peak at Strouhal number of $St_D \approx 0.62$ has more energy than the one at the Strouhal number of $St_D \approx 0.32$. Farther downstream at $x_i/D=3$, the magnitude of the peak at the lower frequency increases whereas that at $St_D \approx 0.62$ decreases. At $x_i/D = 4$ the peak at $St_D \approx 0.32$ becomes dominant and the one at $St_D \approx 0.62$ is not discernible. This behavior of the dominant frequency switching to lower "half-frequency" with increasing downstream distance is expected because of the well known phenomenon of vortex pairing of the jet vortices; i.e. when two vortices merge, they result in a drop in the vortex passage frequency to half of its value before pairing, Narayanan and Hussain [33]. From Figure 3.9, one may conclude that the initial instability of the shear layer forms at $St_D \approx 1.3$ (corresponding to $St_{\Theta} \approx 0.02$; see Figure 3.8), then the first vortex merging takes place between $x_i/D = 1$ and 2, dropping the dominant Strouhal number by half to $St_D \approx 0.62$. The second merging starts before the flow structures reach the location $x_i/D = 2$ and is completed by $x_i/D = 4$, causing another decrease in the Strouhal number to $St_D \approx 0.32$.

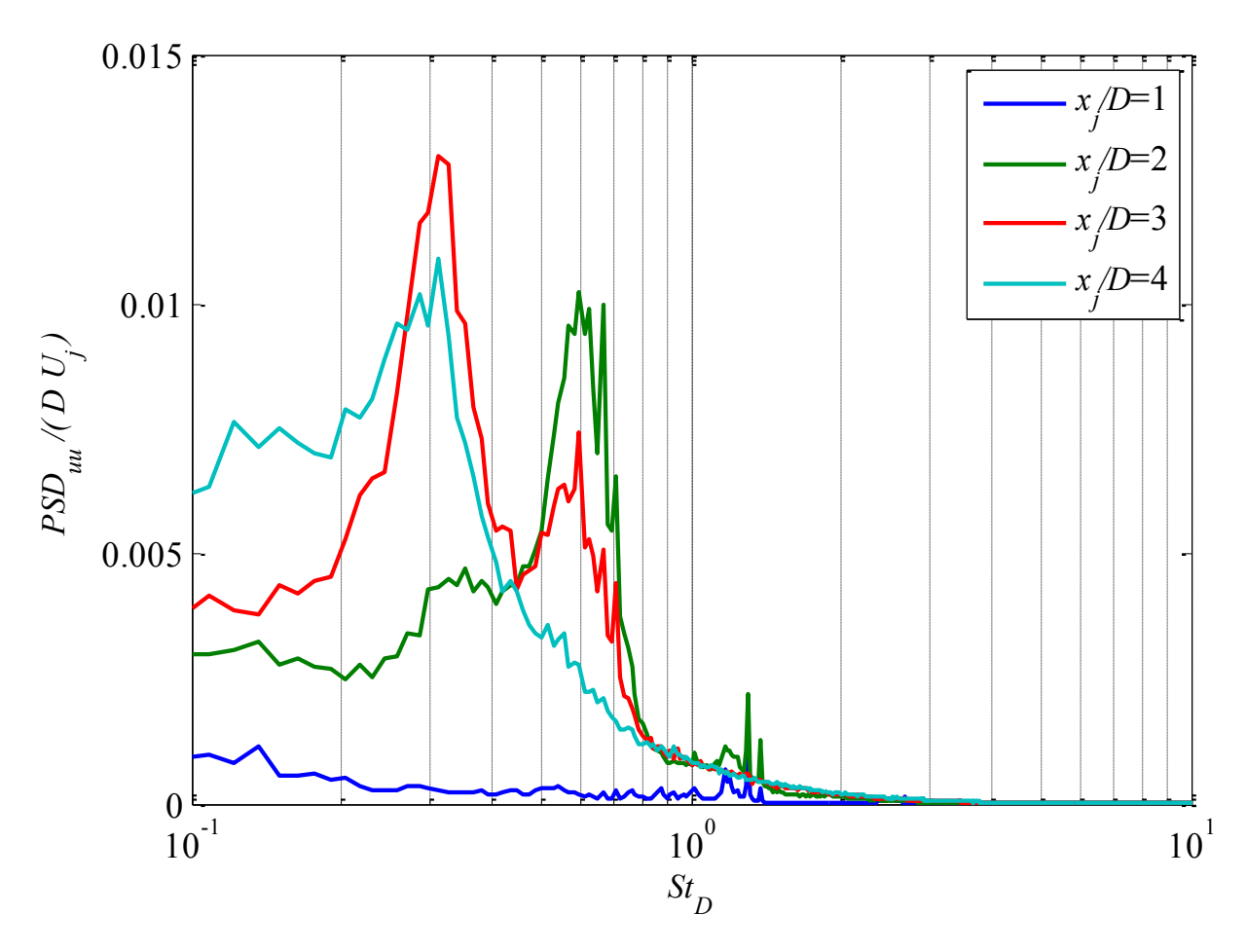


Figure 3.9 Streamwise-velocity power spectral density versus Strouhal number at different x_j/D locations downstream of the jet for $Re_D = 7,334$.

Hot-wire measurements similar to those discussed above are repeated with the presence of the impingement plate at H/D=4, but this time excluding the measurements at $x_j/D=4$ (because of the plate's presence at that location). The resulting spectra are shown in Figure 3.10 with 2.44 Hz resolution and 5% random uncertainty. Spectra at $x_j/D=1$, 2 and 3 look qualitatively similar to those observed in Figure 3.9 without the presence of the impingement plate. From Figure 3.9 and Figure 3.10 one may conclude that the velocity fluctuation in the flow approaching the impingement plate is predominantly focused at $St_D\approx0.32$ for H/D=4 because of two vortex

pairings taking place before reaching the plate. For smaller H/D values where only one or no vortex pairings take place before impingement, it is expected that the dominant velocity fluctuation frequency will shift to the higher harmonics of $St_D\approx0.64$ and 1.3, respectively.

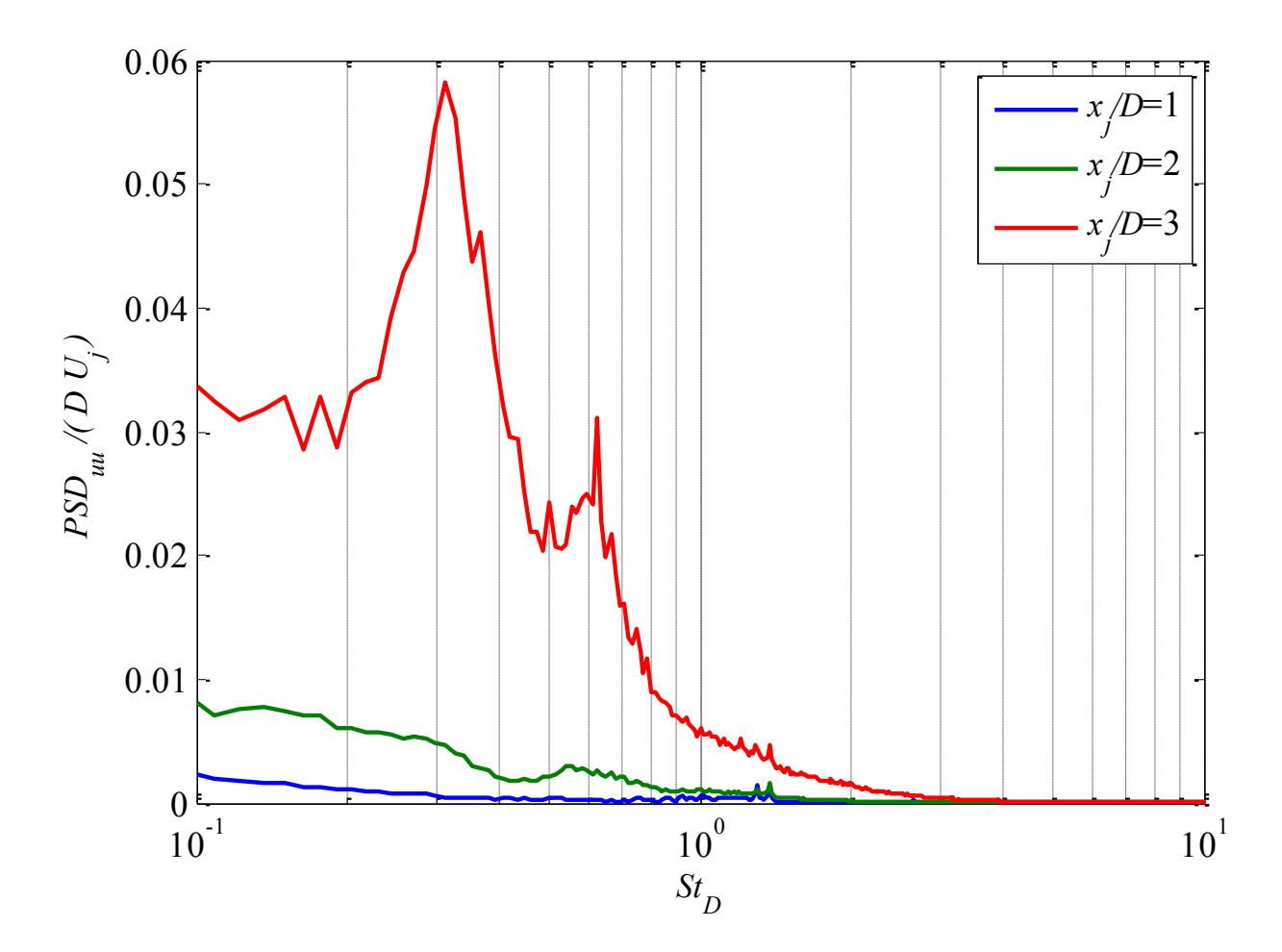


Figure 3.10 Streamwise-velocity power spectral density versus Strouhal number with impingement plate present at H/D=4

Chapter 4: Pressure Measurements

Part of the motivation of this study is to verify some of the conclusions made by prior studies based on inference of the flow structures from the statistical characteristics of the unsteady surface pressure alone. Therefore, it is instructive to examine the statistical characteristics of the wall-pressure data obtained in the present study before considering the added insight of simultaneously examining the flow field (from flow visualization) and wall-pressure. This chapter provides a report on the statistical analysis of the space-time surface-pressure data obtained in the current work. Root mean square, spectral analysis and space-time cross-correlations of the surface-pressure measurements are computed and compared against counterpart results in the existing literature. The physical interpretations of these results will be addressed in chapter 5 where the simultaneous flow-field information is also examined.

4.1 Root Mean Square of Pressure Fluctuations

For H/D=2, Figure 4.1 depicts the radial distribution of the root mean square of the pressure fluctuation (p_{rms}) normalized by the dynamic pressure $(P_d=0.5\rho U_j^2)$ with 2.5% maximum random uncertainty demonstrated by the error bars. The error bars were computed using $(1/\sqrt{2L})$ [34], where L is number of independent samples). The results for normal impingement are shown in circles connected by solid line segments. The p_{rms} distribution exhibits a peak in the wall-jet zone at r/D of 1.33. Similar peaks were found in [10] and [12] at r/D=1.5 and 1.67 respectively. In addition, in these two studies a second peak is found in the stagnation zone at r/D=0.5 and r/D=0.67, respectively. The reason for the absence of a similar peak in the present study is

unknown; however Re_D for the present study is less than that for both [10] and [12] (Re_D = 7,334 in comparison to 23,300 and 16,500 respectively). Furthermore, in [10], the jet emerges at the end of a fully-developed turbulent pipe flow, and in [12], which was conducted at MSU, the quality of the flow axisymmetry was unsatisfactory (in fact this was the motivation for the design and fabrication of a new nozzle in the present work).

Figure 4.1 also depicts the results along the radial direction for oblique impingement with $\gamma = 30^{\circ}$, $\theta = 0^{\circ}$ and 180° where the radial range from r/D = 0.67 to r/D = 2.33 on the left side of the plot corresponds to the back flow and the range from r/D = 0.67 on the left side to r/D = 2.33 on the right side of the plot corresponds to the forward flow. The distinction between the back and forward flow is taken at r/D = 0.67 rather than r/D = 0 because the stagnation point shifts towards the back-flow side (e.g. see [35]) to approximately r/D = 0.5 for $\gamma = 30^{\circ}$, which is determined from the flow visualization in the present work as will be shown in chapter 5. Unlike the normal impingement case, the rms profile in the oblique impingement is asymmetric around the center of the plate with the forward side demonstrating higher fluctuations level. The figure shows two peaks; one at r/D = 1 in the back flow side and the other at r/D = 1.33 in the forward flow side. The latter is sharper and stronger than the one in the back flow side. In addition, it appears that the local minimum found at r/D = 0 in normal impingement now shifts to the back flow side at r/D = 0.33; this can be associated with the shift of the stagnation point, where fluctuations are minimum.

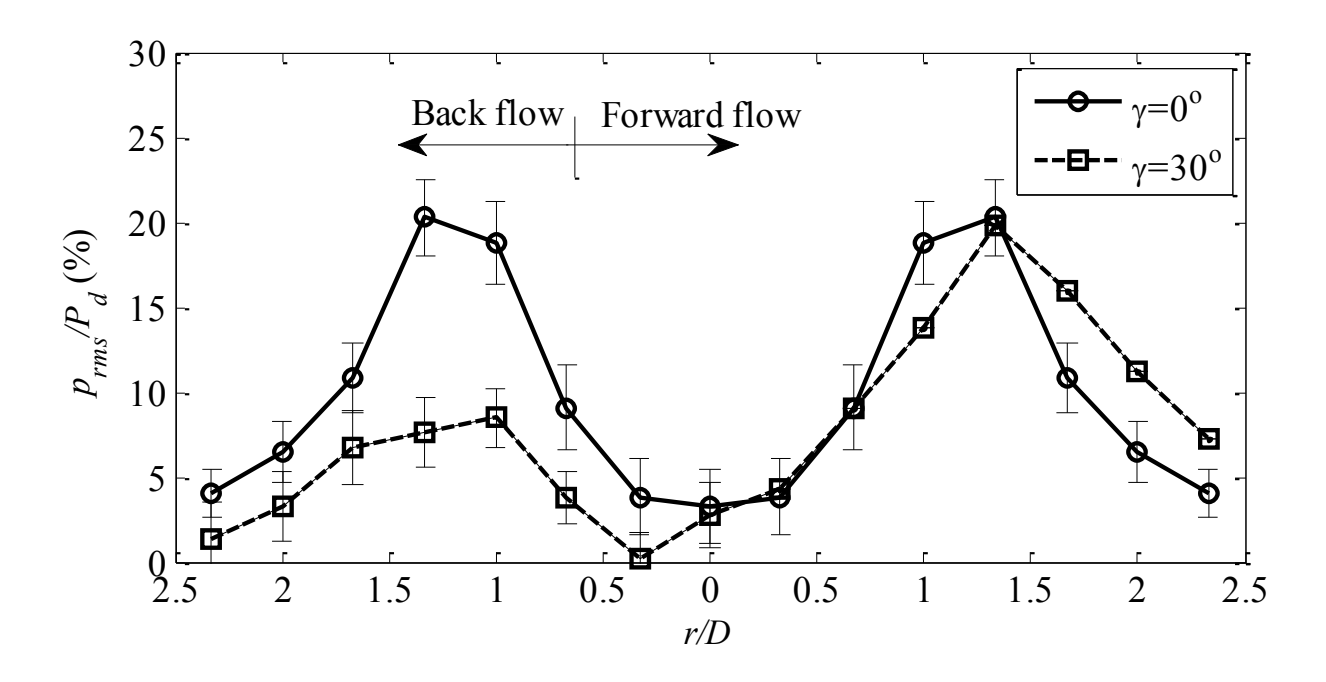


Figure 4.1 Effect of impingement angle on pressure rms distribution in the radial direction for H/D=2

Figure 4.2 shows the dependence of the radial distribution of the root mean square of the pressure fluctuation on H/D for the normal impingement case. In the figure, p_{rms} is normalized by the dynamic pressure and is known to within 2.5% maximum random uncertainty. The peak observed earlier in Figure 4.1 at r/D=1.33, for H/D=2, gets broader and weaker with movement of the impingement plate away from the jet. At H/D=4 this peak also includes r/D=1 and 0.67 radial locations. In addition, the local minimum at the stagnation point (r/D=0) increases in magnitude at larger H/D values with no significant broadening. This increase causes p_{rms} at stagnation to reach a value where it is approximately 75% of the peak value found at r/D=1.33 at H/D=4, in comparison to 15% at H/D=2. Curiously, for all H/D values, the rms decays rapidly in the radial range r/D>1.33 to a magnitude of about 5%.

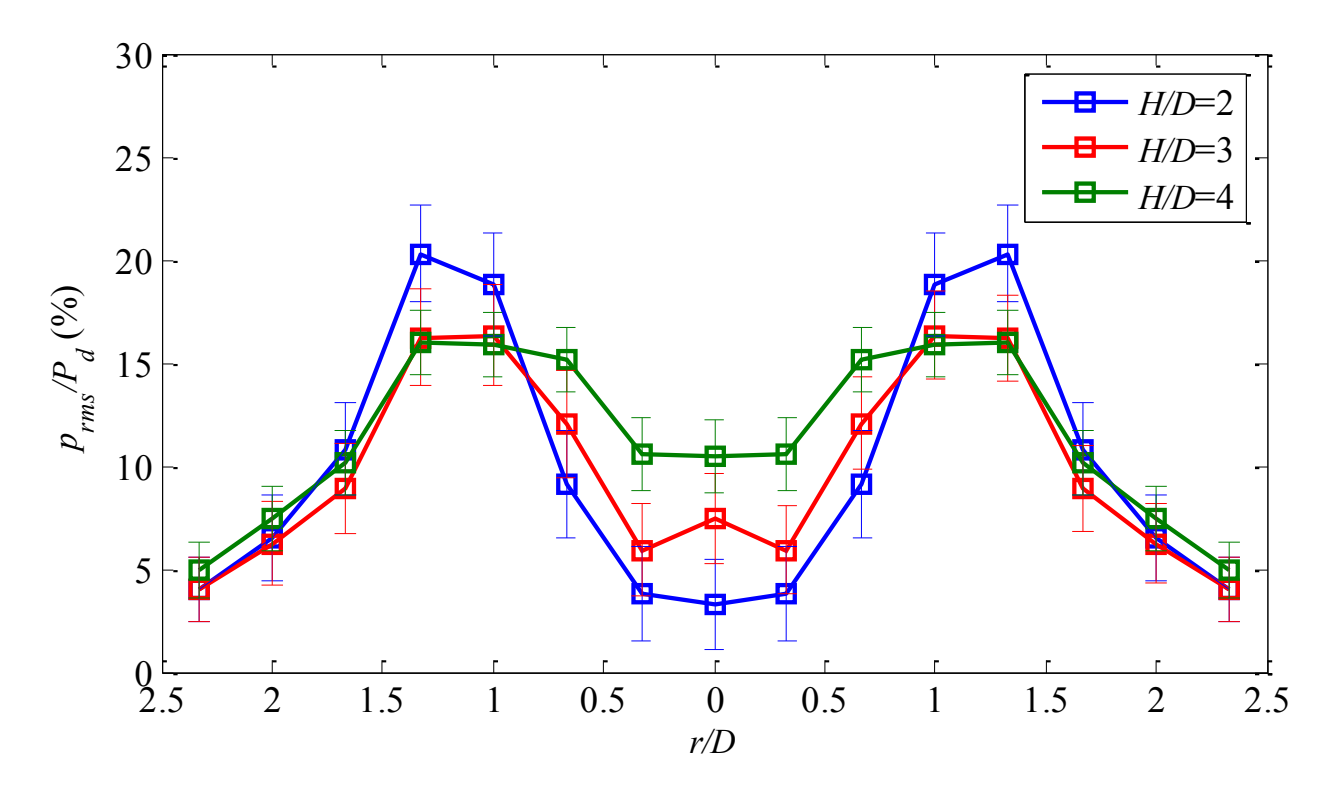


Figure 4.2 Effect of the impingement plate location on pressure *rms* distribution in the radial direction for normal impingement

The influence of H/D on the radial distribution of p_{rms} for the oblique-impingement case is depicted in Figure 4.3. The rms distribution for H/D=3 agrees very well with its counterpart for H/D=2 in the range of r/D=0.33 on the back flow side to r/D=2.33 on the forward flow side, and both are very close to the rms distribution for H/D=4 in the range of r/D>0.33 in the forward flow side. The rms distribution for the latter H/D portrays a weaker peak compared to those found at H/D=2 and 3 at the radial location of r/D=1.33. The peak location is in the forward flow side and it is similar to that found at r/D=1.67 by El-Anwar et al [12]; the discrepancy in the peak location might be related to the higher Reynolds number of 16,500 by the latter study, but it is more likely due to the lack of satisfactory flow axisymmetry in [12], as explained in the discussion of Figure 4.1

On the other hand, for the back-flow side, the *rms* distributions for the different H/D locations in the radial range of 0.33 < r/D < 1.33 (in the left side of the plot) show substantial differences when compared to those on the forward flow side. The back-flow *rms* distribution at H/D=2 exhibits a weak broad peak at r/D=1 in the back flow side. This peak significantly grows in strength as the plate is placed farther away from the jet to the point that the peak becomes stronger than its counterpart on the forward-flow side; thus, creating an opposite scenario to that for H/D=2 where the forward-flow peak is stronger than the back-flow peak. It is noteworthy that the local minimum in the *rms* distribution at H/D=4 is at r/D=0.33, which is on the forward-flow side; whereas for the other two H/D values, the minimum is located at r/D=0.33 (left side of the plot). In all cases, the *rms* decay at large r/D values is stronger on the back-flow compared to the forward-flow side. Specifically, by the end of the measurement domain (r/D=2.33), p_{rms} decays to approximately 2% on the back-flow side, in contrast to around 8% for the forward flow side.

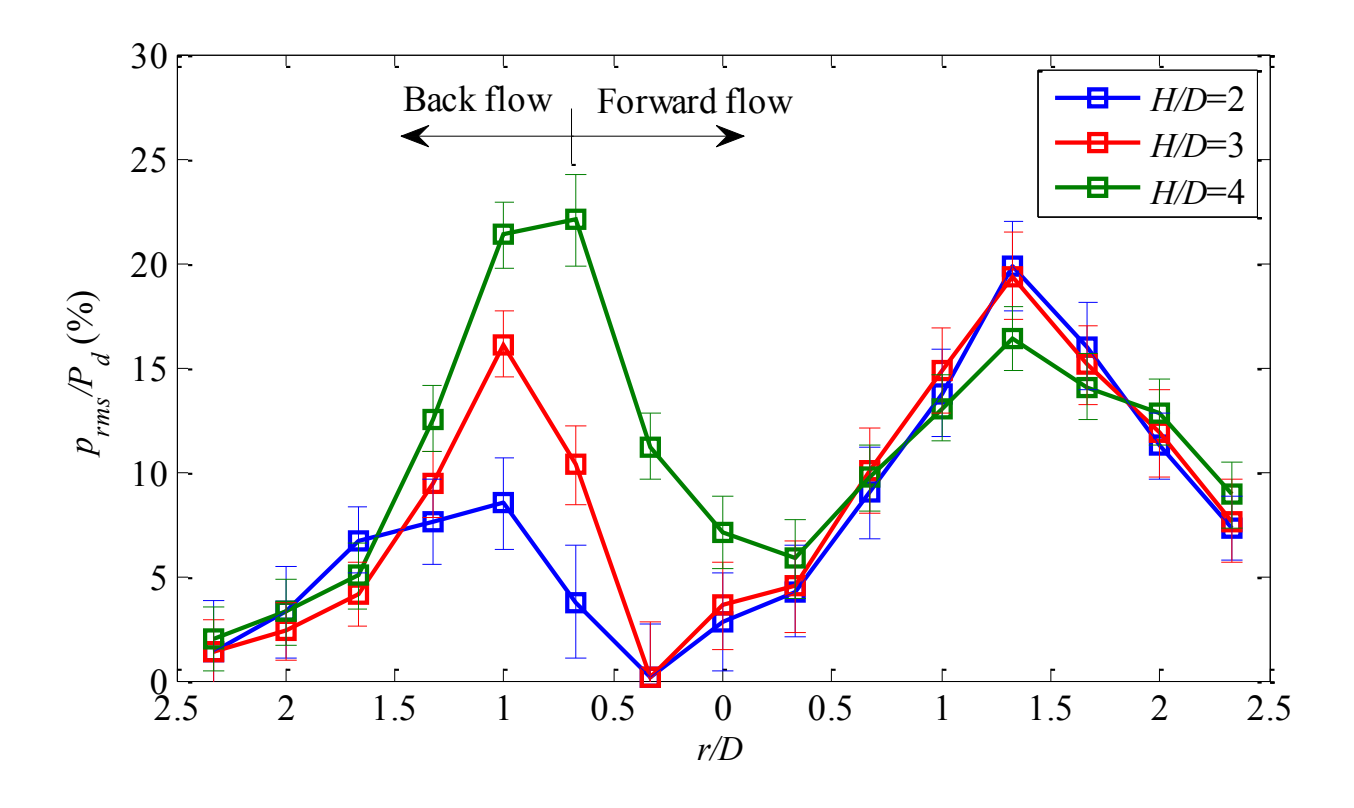


Figure 4.3 Effect of the impingement plate location on pressure rms distribution in the radial direction for oblique impingement at H/D=2, 3 and 4

4.2 Power Spectral Density

4.1.1 Normal Impingement

To obtain information regarding the frequency content of the pressure fluctuations, information from power spectral density (PSD) are utilized. Each spectrum is obtained from taking the fast Fourier transform (FFT) of 800 512-point pressure data records. To produce the PSD for each of the records, the FFT is multiplied by its conjugate and divided by the number of points in the record and the frequency resolution. The average PSD, which is arrived at by averaging the PSD results from all records, has 9.76 Hz frequency resolution and 2.5% random uncertainty. Figure 4.4(a), 4.4(b), and 4.4(c) depict the power spectral density for H/D=2, 3 and

4, respectively; where plots a1, b1 and c1 show results obtained from microphones located in the range r/D=0-1 (stagnation zone), and plots a2, b2 and c2 yield data for r/D=1.33-2.33 (wall-jet zone). The spectra in Figure 4.4(a) exhibit multiple peaks at $St_D \approx 0.64$, $St_D \approx 1.3$, $St_D \approx 1.9$ and $St_D \approx 2.5$ with their strength decaying with increasing Strouhal number. Notably, the higher Strouhal numbers are harmonics of the lower one at 0.64. Overall, the level of the spectrum is relatively low at r/D=0 but it increases gradually in the radial direction, reaching peak level in the range r/D=1 - 1.33 before decaying with further increase in the radial coordinate. The peak at Strouhal number of 0.64, which is the strongest, is initially very broad with low magnitude at r/D=0 and 0.33 then it becomes sharp and distinct in the radial range of 0.67 to 1.67 before it weakens. The physical interpretation of these peaks and their evolution in the radial direction will be discussed in chapter 5 with the aid of the time-resolved flow visualization.

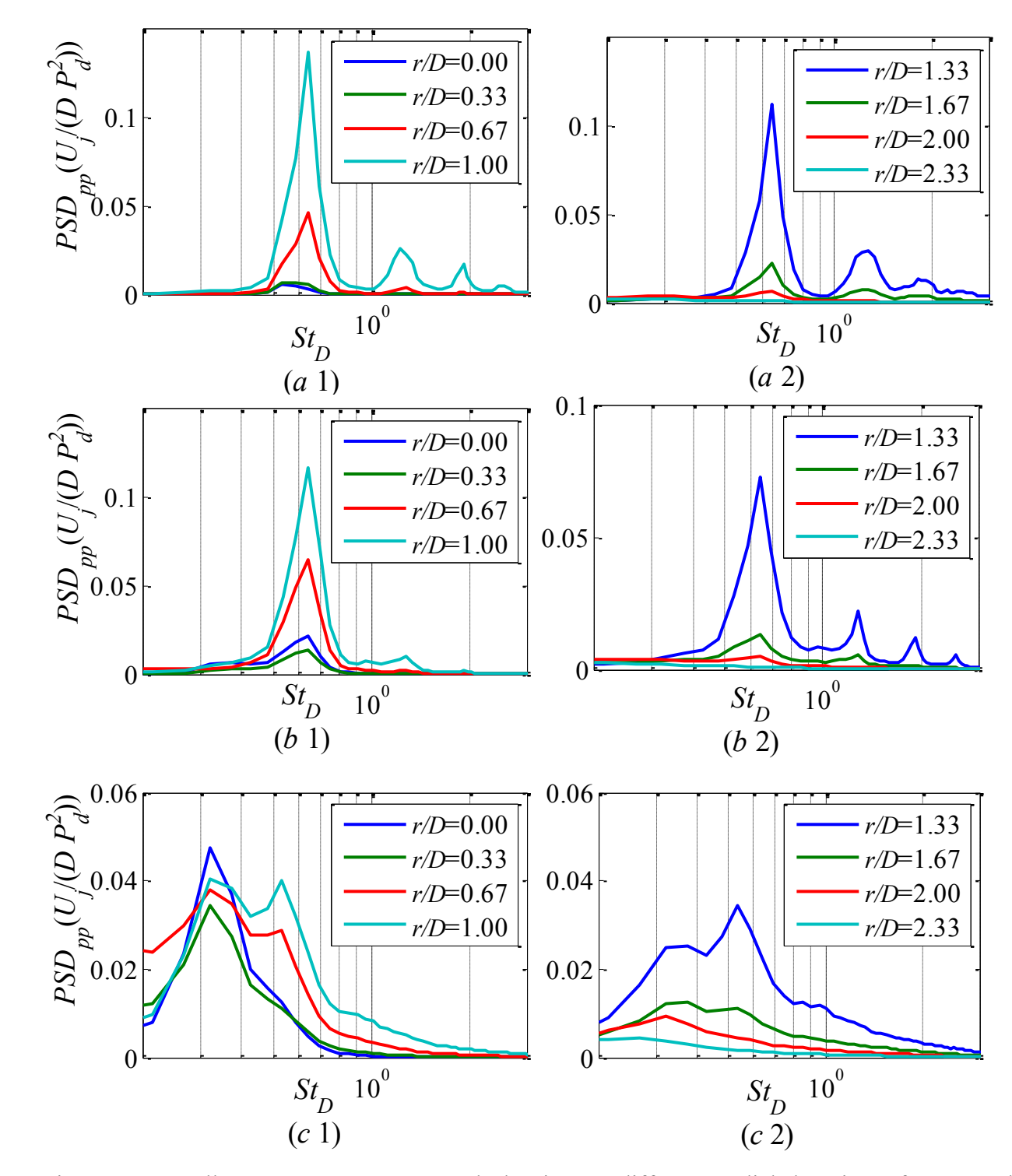


Figure 4.4 Wall-pressure power spectral density at different radial locations for normal impingement and (a) H/D=2, (b) H/D=3 and (c) H/D=4. Plots a1, b1 and c1 correspond to the stagnation zone (r/D=0-1) and plots a2, b2 and c2 correspond to the wall-jet zone (r/D=1.33-2.33)

The power spectral density plots for H/D=3 and normal impingement, shown in Figure 4.4(b), exhibit a strong peak at Strouhal number of 0.64 similar to the one found at H/D=2 in normal impingement. The magnitude of this peak is comparably low in the center of the stagnation zone (at r/D=0 and r/D=0.33), but it increases to reach its maximum value at the start of the wall jet zone (r/D=1). At this radial location another peak appears with relatively low magnitude at Strouhal number of approximately 1.3; the first higher harmonic of 0.64. This peak becomes more distinct and sharper at r/D=1.33 where other higher-order harmonics also become apparent at $St_D\approx1.9$ and 2.5. Beyond this radial location the spectral peaks generally decrease with no strong evidence of the two higher Strouhal numbers of 1.9 and 2.5. In general, the magnitude of these peaks is less than their counterpart at H/D=2. Figure 4.4(b2), which depicts the power spectral density for H/D=3 in the wall-jet region, is re-plotted using logarithmic scale for both axes in Figure 4.5. Significantly, at r/D=2.33 the spectral peaks disappear all together, and the spectrum becomes broadband and featureless. This suggests that the wall-pressure generating sources become turbulent and disorganized by the end of the radial measurement domain.

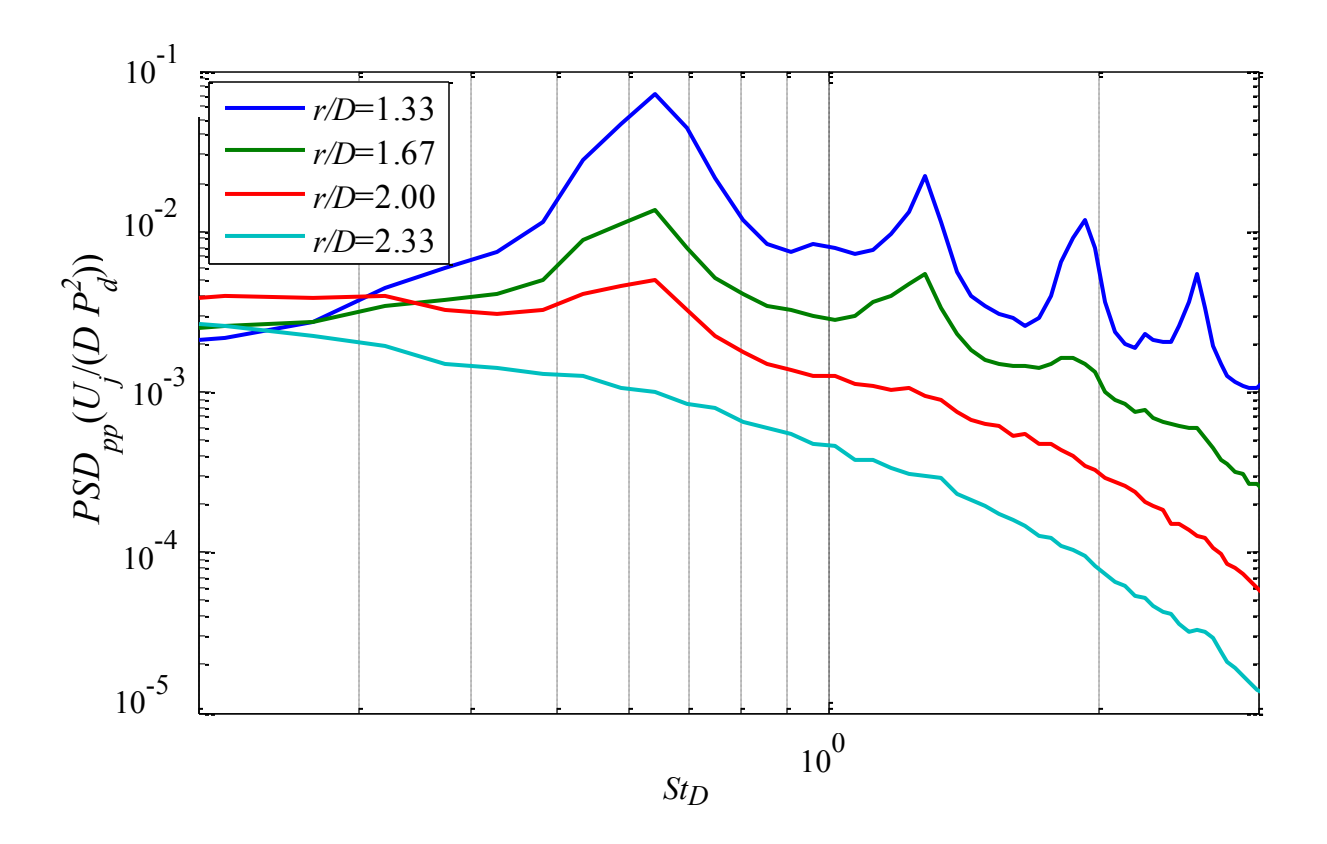


Figure 4.5 Wall-pressure power spectral density at different radial locations in the wall-jet zone for normal impingement and H/D=3

The power spectral density results at H/D=4 depict some different characteristic features in terms of Strouhal numbers than those at H/D=2 and 3 locations. Figure 4.4(c) shows these results for H/D=4, where Figure 4.4(c1) represents data obtained in the stagnation zone and Figure 4.4(c2) yields data captured in the wall-jet zone. The spectra in Figure 4.4(c1) exhibit a dominant peak at $St_D \approx 0.32$ with a magnitude that is highest at r/D=0 and is of comparable value at the other radial locations. This shows that most of the pressure fluctuations near stagnation are concentrated at $St_D \approx 0.32$. A second peak at $St_D \approx 0.53$ is also distinctly seen at r/D=0.67 and 1.0, but not at r/D=0 and 0.33 (though it may be swamped in this case by the dominant peak at $St_D \approx 0.32$). The magnitude of the second peak increases gradually until it reaches approximately

the same magnitude as the peak at $St_D \approx 0.32$ at r/D=1. In Figure 4.4(c2), displaying the spectra for the well-jet region, both peaks ($St_D \approx 0.32$ and 0.53) continue to appear. Farther downstream at r/D=1.33 the peak at the higher Strouhal number becomes stronger than the $St_D \approx 0.32$ peak before both peaks start to weaken with further increase in r/D with the $St_D \approx 0.53$ peak decaying faster. It is interesting to note that the peak at $St_D \approx 0.32$ corresponds to the first sub-harmonic of the dominant peak at $St_D \approx 0.64$ found for H/D=2 and 3, whereas the peak at $St_D=0.53$ has no obvious relation to the spectral peaks seen for the smaller jet-to-impingement-plate separations. Interpretation of this peak and other spectral peaks discussed in the above analysis is left to Chapter 5.

4.1.2 Oblique Impingement: Forward-Flow Side

Power spectral density results are also computed for the oblique-impingement forward-flow case for H/D=2, 3 and 4 locations. Figure 4.6, which depicts these results, is constructed in a similar way to Figure 4.4 of the normal impingement case. In general, the spectra show an increase in magnitude in the radial direction, reaching a peak at r/D=1.33 before decaying. This behavior is consistent with the rms pressure distribution shown in Figure 4.1. The spectra in the radial range $0 \le r/D \le 1$ exhibit a strong peak at Strouhal number in the vicinity of 0.64. The peak has low magnitude at r/D=0 but it increases in strength with increasing radial coordinate. The peak reaches its maximum magnitude at r/D=1.33 and then starts to decrease monotonically with increasing r/D. At r/D=0.67 another peak at a lower Strouhal number of 0.32 is observed which does not exist in the normal impingement spectra for H/D=2 (Figure 4.4(a)). However, a similar peak is observed for H/D=4 (Figure 4.4(c)) in the normal impingement case. Thus, the

appearance of a peak at St_D of 0.32 may be related to the extra distance of shear-layer development before reaching the impingement plate in both H/D=4 (normal impingement) and H/D=2 (oblique impingement on the forward-flow side). Aside from the two peaks at Strouhal numbers of 0.32 and 0.64, the spectra in the radial range of 1.33 $r/D \le 2.00$ depict several higher harmonic peaks with insignificant magnitudes.

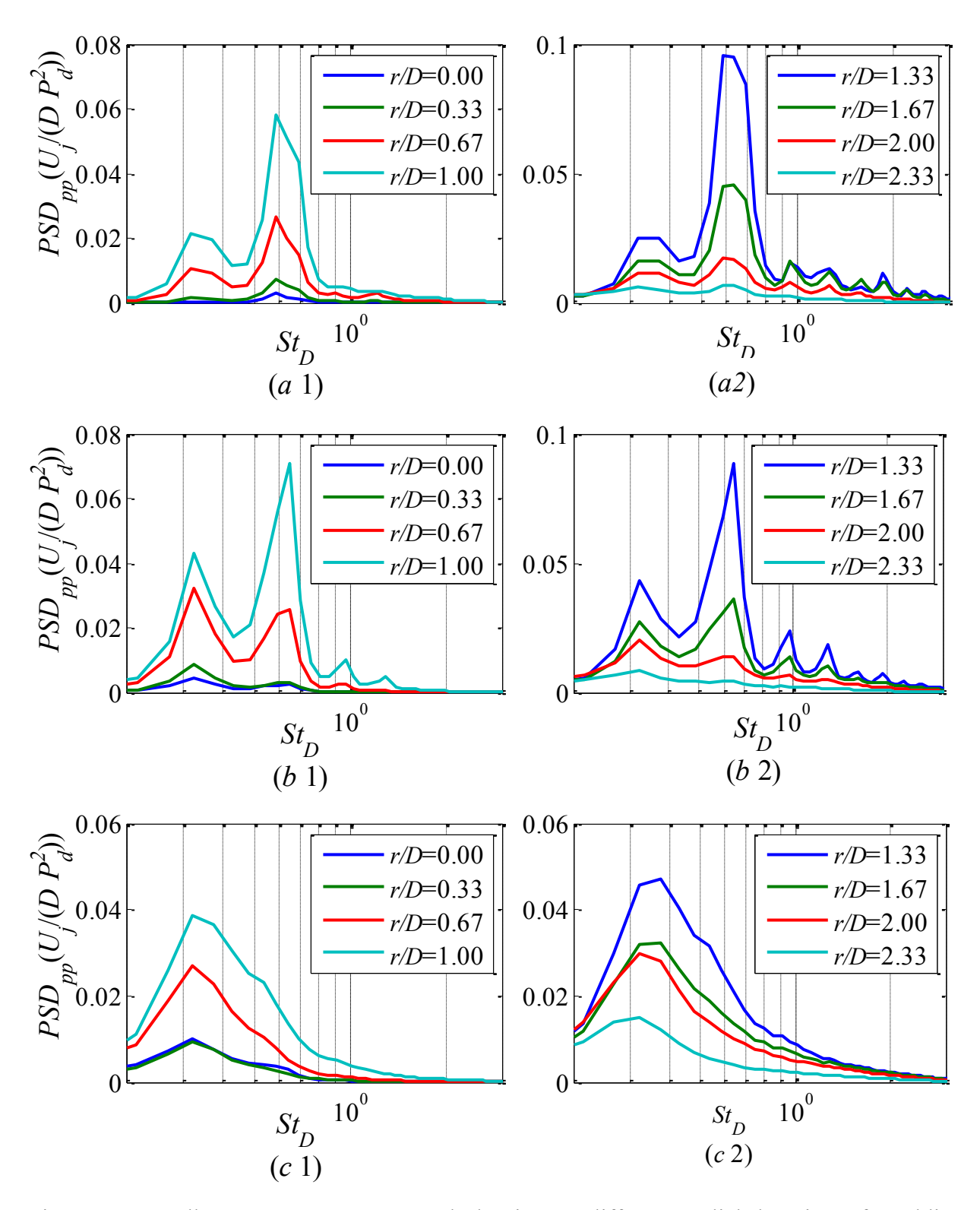


Figure 4.6 Wall-pressure power spectral density at different radial locations for oblique impingement (forward-flow side) and (a) H/D=2, (b) H/D=3 and (c) H/D=4. Plots a1, b1 and c1 correspond to r/D=0-1, and plots a2, b2 and c2 correspond to r/D=1.33-2.33

Figure 4.6(b) demonstrates the power spectral density plots for the oblique impingement, forward-flow side, and H/D=3 location. In general, the results are very similar to those observed for oblique impingement at H/D=2, with dominant spectral peaks at Strouhal numbers of 0.32 and 0.64. Nevertheless, there are few differences in terms of the magnitude of the spectral peaks. For instance, the peak at $St_D \approx 0.32$ at this H/D location is stronger at the smaller radial locations of r/D=0 and 0.33 than in the case of H/D=2. Moreover, the peak is more pronounced, with larger magnitude than the one at H/D=2. Additionally, two harmonic peaks at $St_D \approx 0.97$ and $St_D \approx 1.3$ with low magnitudes are seen at r/D=1 which continue to exist and become more pronounced at r/D=1.33 among several other harmonic peaks at higher Strouhal numbers and large radial locations. Figure 4.6(c) depicts power spectral density results for oblique impingement (forward-flow side) and H/D=4. The spectra are dominated by the peak at $St_D \approx 0.32$ for all radial locations investigated, with no higher-order harmonics observed.

Oblique Impingement: Back-Flow Side Figure 4.7 (a) depicts the Power spectral density results for H/D=2, illustrating the spectra at radial locations of $r/D \ge 1$ since the ones at r/D < 1 represent the forward-flow side due to the stagnation point shift towards the back-flow side (as mentioned in section 4.1). Similar results for H/D=3 and 4 may be found in Figure 4.7(b) and Figure 4.7(c), respectively. The spectra in Figure 4.7(a) exhibit a distinct sharp peak at Strouhal number of 1.3 at r/D=1 and 1.33 radial locations with the largest peak magnitude found at r/D=1. Two additional spectral peaks, one at higher Strouhal number of approximately 2.5 and the other at lower Strouhal number of 0.64, with comparatively low magnitudes are also present at the aforementioned radial locations. The spectra at r/D=1.33 and 1.67 show weak evidence of

low-frequency spectral peak at Strouhal number of 0.32. The rest of the spectra at locations of r/D > 1.33 show no significant spectral features.

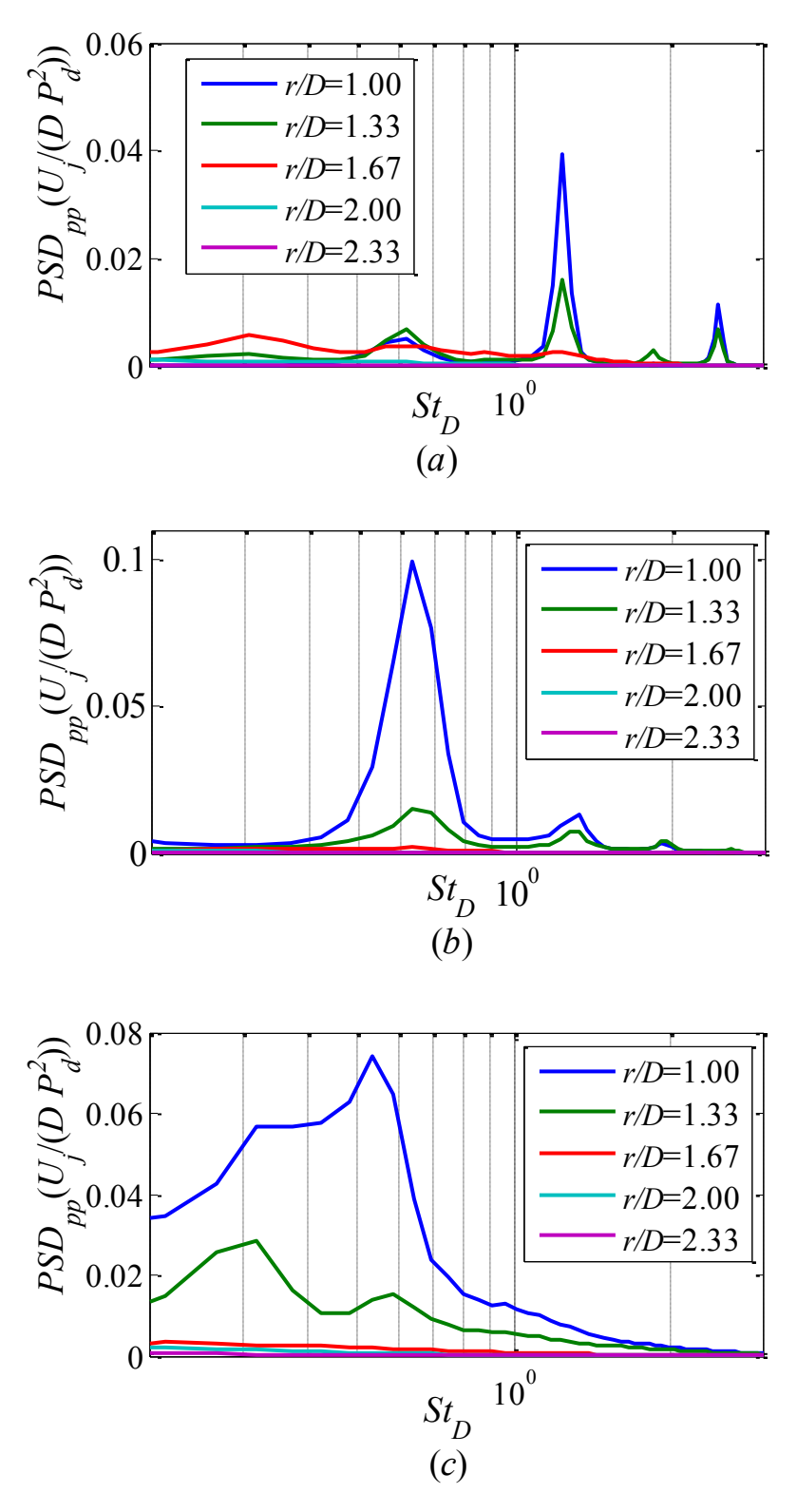


Figure 4.7 Wall-pressure power spectral density at different radial locations for oblique impingement (back-flow side) and (a) H/D=2, (b) H/D=3 and (c) H/D=4

For H/D=3, the spectra seem to portray spectral features only at radial locations of r/D=1 and 1.33 and no other significant spectral features elsewhere. The spectra depict a peak at Strouhal number of $St_D\approx0.64$ with higher magnitude at r/D=1. The magnitude of this peak decreases drastically at r/D=1.33. Additionally, two peaks with relatively low magnitude at Strouhal numbers of 1.3 and 1.9 are observed. These peaks represent higher harmonics of 0.64.

Similar to H/D=3, for H/D=4, prominent peaks are only seen for the spectra measure at r/D=1 and 1.33. Peaks are observed at Strouhal numbers of $St_D\approx 0.32$ and 0.53 similar to those found in normal impingement. At r/D=1 the magnitude of the peak at $St_D\approx 0.53$ is higher than the peak $St_D\approx 0.32$. Both peaks generally decay by r/D=1.33, however the peak at higher Strouhal number does so at a faster rate. Notably, the frequency of the peak at $St_D\approx 0.53$ shifts to a slightly higher Strouhal number at r/D=1.33. Both peaks continue to weaken farther out in the radial direction. Overall, both the spectra and rms results suggest that the pressure fluctuations and the structures responsible for their generation decay at a fairly fast rate with increasing r in the back-flow direction.

4.3 Convection Velocity

The cross-correlation between two discrete-time pressure signals can be defined by:

$$R_{p1p2}(m) = \frac{\sum_{n=0}^{N-1} p_1(n) p_2(n-m)}{p_{1rms} p_{2rms}}$$
(4.1)

Where n is an integer representing the sample number in the recorded time series, N is the total number of samples and m is an integer denoting the delay of p_2 with respect to p_1 . "xcorr" (a matlab function) in employed to compute cross-correlation in this study. Cross-correlation is a useful tool to identify the presence of convective flow features. For instance, consider two microphones separated by a distance Δr in the flow direction. The pressure signature generated by a particular flow structure will be captured by the upstream microphone first at some time τ_0 . At some later time $\tau_0 + \Delta r/U_c$ (where U_c is the convection velocity of the flow feature), the structure reaches the second microphone, producing a similar pressure signature. If the pressure generation is dominated by this flow structure, then applying the cross-correlation analysis to the time series acquired from the aforementioned microphones will produce the largest correlation magnitude at time offset between the two signals equal to $\Delta r/U_c$, which together with knowing Δr , yields the convection velocity of the structure. Because the correlation is computed from a statistical average over the entire time series, the computed convection velocity represents an average for all structures traveling between the two microphones. In the current investigation, the cross-correlation is computed between discrete pressure time series measured from a reference microphone (the reference microphone is taken at r/D=0.67 for H/D=2 and 3 and at r/D=0 for H/D=4) and those from the rest of the microphones in the radial array. The analysis provides the average convection velocity in the radial direction. The reason for choosing the reference microphone at r/D=0.67 for H/D=2 and 3 and at r/D=0 for H/D=4 is that the jet vortical structures first interact with the impingement plate in the vicinity of r/D=0.67 for the former cases and near r/D=0 for the latter (this will be illustrated in section 5.1 with the aid of the flow visualization).

Figure 4.8 depicts an example of cross-correlation between a time series obtained from the microphone at r/D=0.67 with itself (which is the auto-correlation, shown using a blue line) and with measurements from the microphone at r/D=1.00 (red line). As expected, the auto-correlation at r/D=0.67 shows a maximum peak at τ =0. Additional peaks with smaller magnitude exist at other time offsets and they decay in strength with increasing offset; this is due to the quasi-periodic behavior of the signal. On the other hand, the cross-correlation (red line) between the time series obtained at r/D=0.67 and r/D=1.00 has its largest peak at non-zero time offset ($\tau_{\rm delay}$). This time delay represents the average time taken by the pressure-generating flow structures to travel the distance between the two microphones. Dividing the radial spacing between the microphones by the cross-correlation time delay, one can find the average convection velocity of the structures.

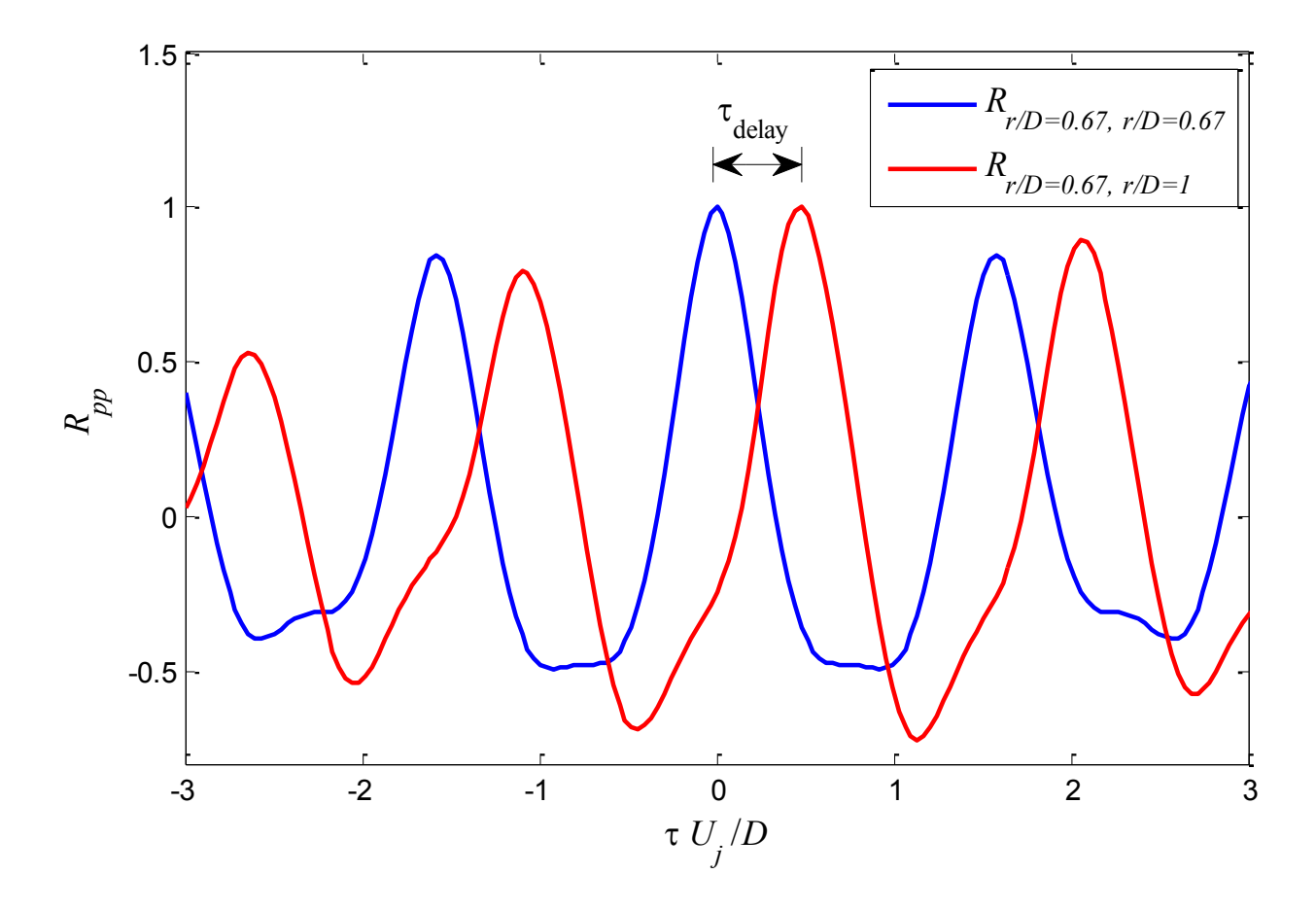


Figure 4.8 Auto-correlation of the time series measured at r/D=0.67 (blue line), and cross-correlation between the time series measured at r/D=0.67 and r/D=1.00 (red line)

The cross-correlation is displayed using flooded-color contour plots in Figure 4.9 for H/D=2. For H/D=3 and 4, the plots are qualitatively similar and hence they are omitted for brevity. In Figure 4.9, the abscissa is the radial coordinate normalized by the jet diameter D, the ordinate represents the time offset normalized using the jet exit velocity U_j and diameter D, and the color bar yields the cross-correlation magnitude. Each plot in the figure also contains a broken line which is a linear curve-fit to the correlation ridge defined by the loci of the maximum correlation peaks at the different radial locations. The inverse slope of this line yields the average convection velocity, as indicated on the plot.

Figure 4.9a shows the cross-correlation for normal impingement, while Figure 4.9b represents the oblique impingement forward-flow side. No results are shown for the back-flow side because of the short distance, relative to the current pressure measurement spatial resolution, that the vortical structures travel before they dissipate on this side, which will be discussed in more details in section 5.3. For normal impingement, Figure 4.9a depicts high and low correlation magnitudes that correspond to the local minima and maxima of the cross-correlation similar to those shown in Figure 4.8. In general, the correlation exhibits a maximum-correlation ridge that has a constant slope (indicated by the broken line), which corresponds to convection velocity of $0.49U_j$ in the range of $0.67 \le r/D \le 2.00$. At radial locations where r/D < 0.67, the slope is smaller which implies higher convection velocity. However, this radial range is within the potential core of the jet flow and therefore there are no flow structures present within this range. As will be seen from the simultaneous flow visualization and pressure data (section 5.1), the smaller slope within r/D < 0.67 is representative of potential flow modulation that creates pressure fluctuations that are *almost* in phase in this zone.

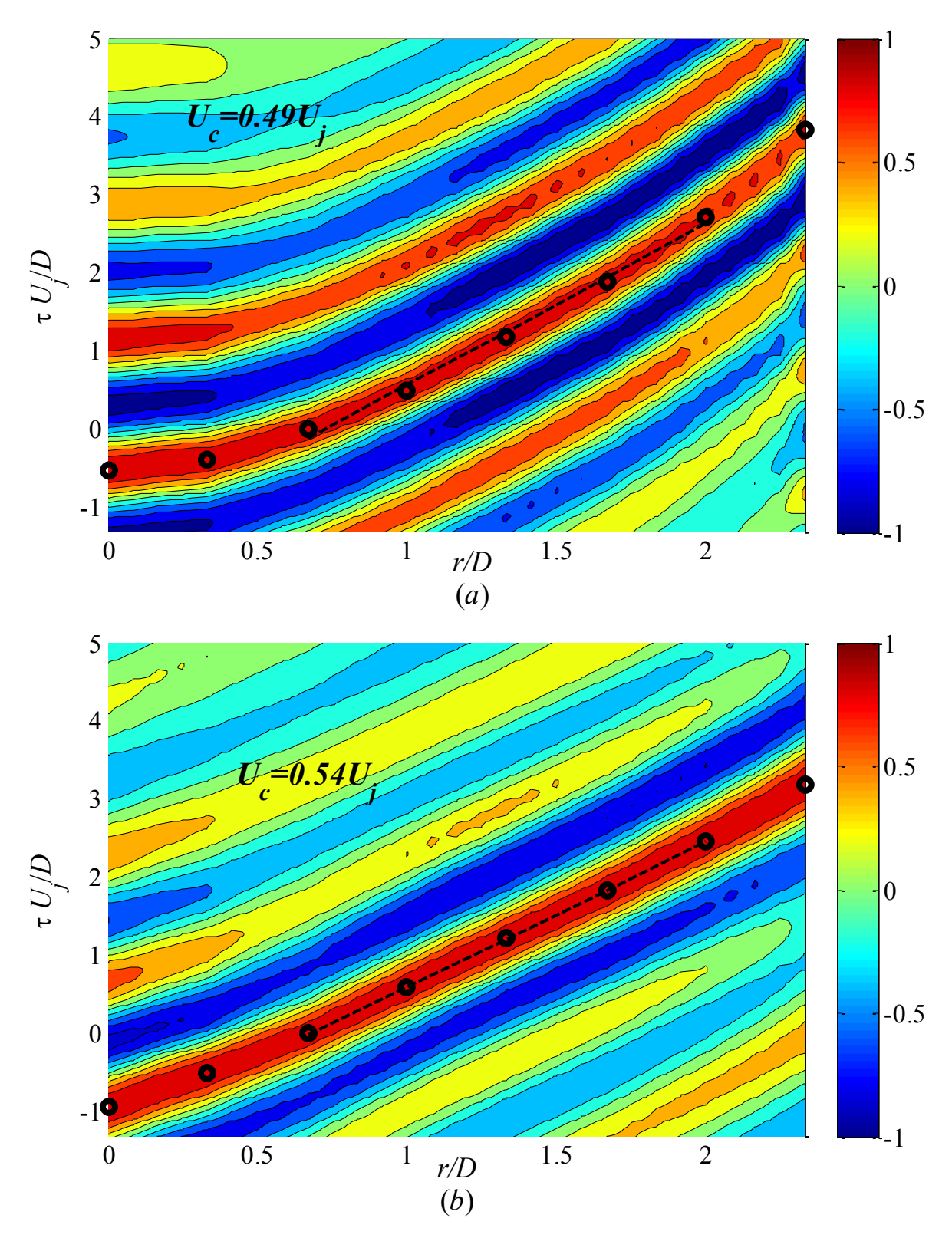


Figure 4.9 Flooded-color contour maps of the cross-correlation and implied convection velocities at H/D=2; (a) normal impingement, (b) oblique- impingement (forward flow)

The cross-correlation for the oblique-impingement case, Figure 4.9b also exhibits a maximum correlation ridge that has a practically constant slope, with implied average convection velocity of $0.54U_j$. Unlike normal impingement, this constant slope is observed over the entire measurement domain, including the radial range where r/D < 0.67. This is likely because in oblique impingement the stagnation point shifts towards the back flow side.

Similar cross-correlation figures (not included in this document) for *H/D*=3 and 4 and normal and oblique (forward-side) impingement are also carried out. Table 4.1 presents a summary of the convection velocity values resulting from the correlation analysis for *H/D*=2, 3 and 4 and both normal and oblique (forward-side) impingement. The table also depicts the radial range for which the maximum-correlation ridge is linearly curve-fitted. Overall, the oblique-impingement (forward-side) convection velocity is higher than its normal-impingement counterpart. The convection velocity values generally fall in the range of 50%-60% of the jet exit velocity.

Table 4.1 Summary of average convection velocity for *H/D*=2, 3 and 4 and normal and oblique (forward-side) impingement

H/D	Normal impingement		Oblique impingement: Forward flow	
	Convection velocity,	fitting range	Convection velocity,	fitting range
2	$0.49U_{j}$	r/D=.67-1.67	$0.54U_{j}$	r/D=.67-1.67
3	$0.54U_j$	r/D=0.33-1.33	$0.58U_j$	r/D=0.33-1.33
4	$0.49U_{j}$	r/D=.67-1.67	$0.57U_{j}$	r/D=.67-1.67

Chapter 5: Simultaneous Time-Resolved Flow

Visualization and Unsteady Surface-Pressure

Measurements

This chapter is focused on interpretation of surface-pressure data in relation to flow-field information by utilizing the simultaneous time-resolved flow visualization and unsteady-surface pressure measurements described in Chapter 4. The analysis is conducted by first identifying persistent flow structures and their mutual interaction with each other and with the wall in the flow visualization, then closely examining the corresponding spatial and temporal wall-pressure signatures and their evolution from the microphone data. The results presented are for H/D=2, 3 and 4, in both normal and oblique impingement with ReD=7,334.

This chapter is divided into three main sections; normal impingement, oblique impingement forward-flow side and oblique impingement back-flow side. Each section starts off with an analysis of the flow structures observed for H/D=2, followed by an analysis of the flow structures as they evolve farther downstream of the jet for larger jet-to-impingement plate spacing: H/D=3 and 4.

5.1 Normal impingement

In normal impingement, where the jet axis makes an orthogonal angle with the impingement plate, only results from placement of the microphone array on one side where $\theta = 0^{\circ}$ is considered because of flow symmetry.

Figure 5.1 depicts spatial pressure signatures on the wall at consecutive times for the jet in normal impingement for H/D=2 and a period of 13 ms. The plots in this figure consist of images from the time-resolved flow visualization accompanied with the concurrent surface pressure signatures; each signature contains pressure data at 29 radial locations. Only 8 out of the 29 pressure data are experimentally measured using microphones located at r/D of 0, 0.33, 0.67, 1, 1.33, 1.67, 2 and 2.33 while the rest are interpolated using a method that capitalizes on the convective nature of the pressure signature (as found from the cross-correlation analysis in section 4.3). The interpolation is used to compute the pressure at three additional spatial locations equally spaced between the locations of two successive microphones, taking into account the average time delay (computed from the cross-correlation) between the time series measured at the two microphones. Specifically, the interpolated pressure time series at location r_i , $p(t;r_i)$, falling between microphone locations r_m and r_{m+1} corresponds to linear interpolation of the two time series $p(t;r_m)$ and $p(t+\tau_{delay};r_{m+1})$ according to:

$$p(t,r_i) = \frac{(r_{m+1} - r_i)p(t,r_m) + (r_i - r_m)p(t + \tau_{delay}, r_{m+1})}{(r_{m+1} - r_m)}$$
(5.1)

This "wave-path" interpolation method would work perfectly, for example, in interpolating coarse measurements of the unsteady pressure produced by a constant amplitude propagating acoustic wave. In this case, the spatial structure of the wave can be recovered with arbitrarily fine resolution from measurements at only two spatial locations (this is demonstrated in Appendix C). The technique will more generally work well for interpolating any propagating-disturbance signal that only changes linearly in the direction of propagation. Higher order, non-linear, variation of the signal cannot be recovered, and therefore to maximize the fidelity of the

interpolated data, the spacing between the measurement locations should be as small as possible. In the present work, the microphone spacing, one-third of the jet diameter, is approximately equal to or less than the size of the vortical structures seen in flow visualization (which dominate the pressure generation process, as will be discussed). So, the underlying assumption of our interpolation scheme is that these structures evolve very little (i.e. linearly at best) over a distance comparable to, or smaller than their size. Therefore, we believe the method gives reasonable results for the measurements carried out in this work.

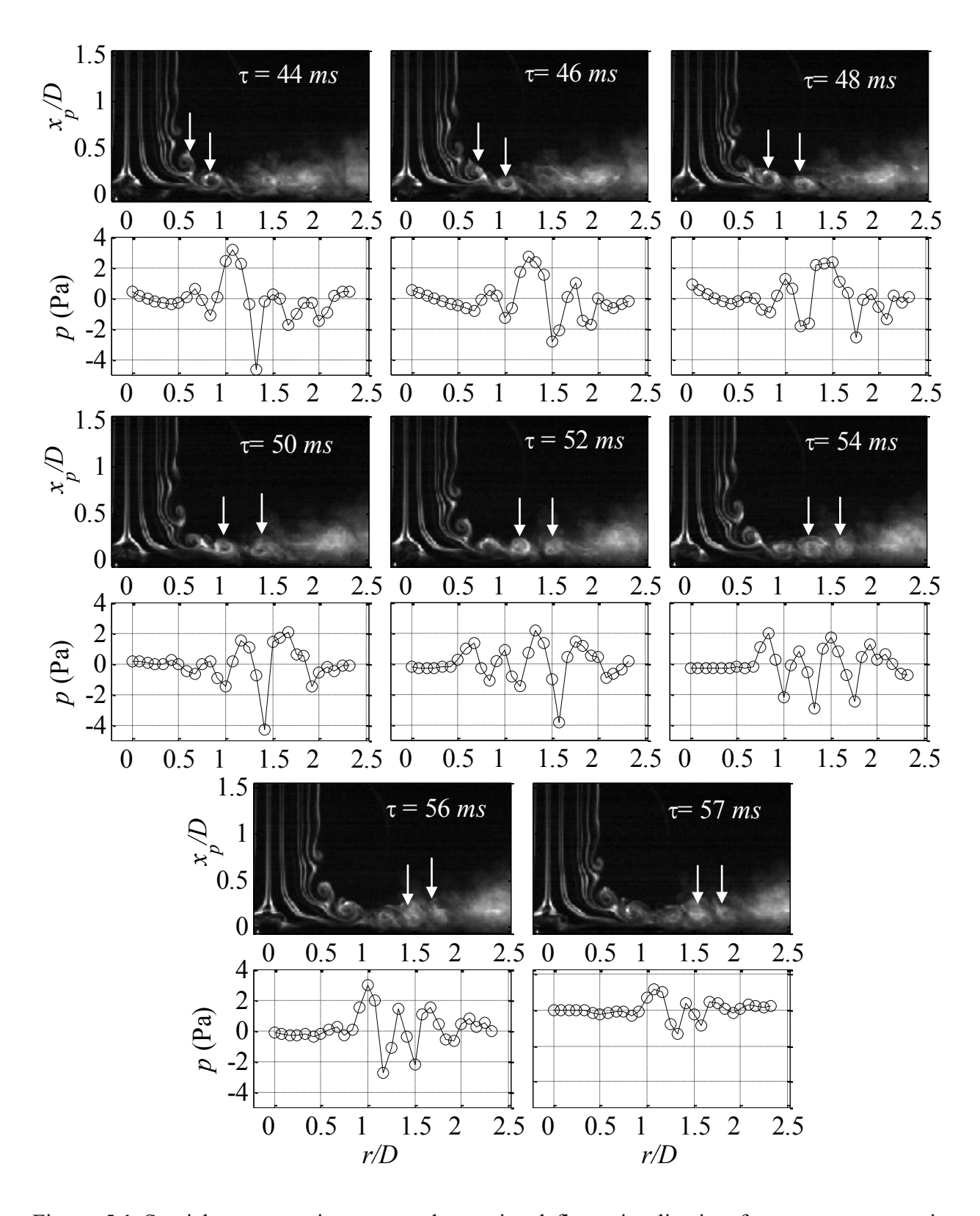


Figure 5.1 Spatial pressure signature and associated flow visualization for vortex passage in normal impingement at H/D=2

Figure 5.2 depicts a sample spatial pressure signature at three different time instants, where the filled circles correspond to pressure data measured at the microphones locations and the empty circles are the interpolated pressure data. The figure shows that the pressure signature is highly convective (i.e. wavelike) in nature with the signature at the later time delays looking predominantly as a translated version of the initial signal at τ =0.

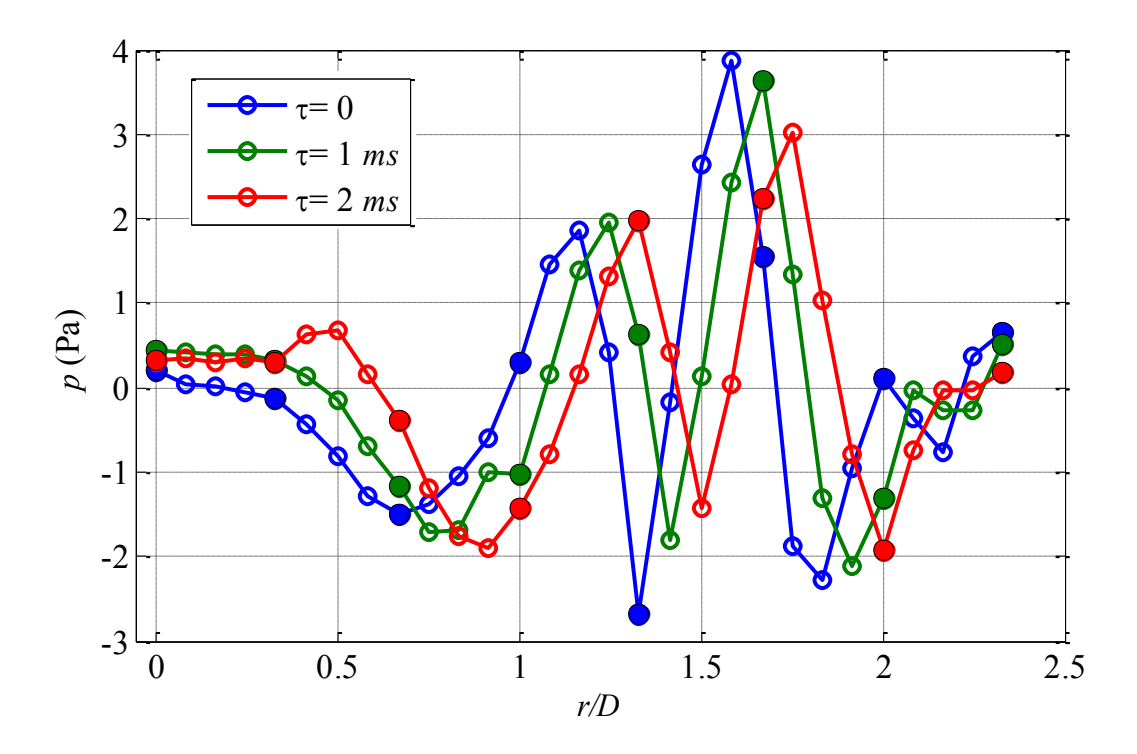


Figure 5.2 Spatial pressure signature at different time instants demonstrating the convective nature of the wall-pressure: H/D = 2 and normal impingement. Closed symbols represent actual measurements, and open symbols show the interpolated values

The image at τ =44 ms, in Figure 5.1 shows two vortices (pointed to by arrows) approach the wall. When these vortices "first encounter" the wall, a negative pressure peak is seen to form beneath each vortex (at τ =46 and 48 ms). Subsequently, the vortices change their convection direction to travel parallel to the wall while remaining separated from each other. In the vicinity of r/D=1-1.5, the vortex core size seems to become smaller as the vortex ring diameter increases;

this mechanism is known as vortex stretching which is generally known to increase the vorticity component in the stretching (azimuthal) direction. This is plausibly the reason for the increase in the strength of the associated negative pressure peak beneath the vortex, which is apparent in the surface pressure readings. After passing r/D=1.5, the vortices appear to diffuse and the surface-pressure signature directly underneath weakens. Notably, the vortices in this case maintain sufficient radial spacing that prevents the vortices from interacting with one another while traveling past the wall. This scenario of vortices passing above the wall without interacting with one another will be referred to as "vortex passage" throughout this document. The change in the magnitude of the negative pressure peaks found beneath the vortex structures in the radial direction during observation of these vortices is consistent with the rms distribution shown in Figure 4.1. Specifically, the pressure rms profile peaks at r/D=1.33 where the pressure spatial signature also demonstrates a maximum negative magnitude in the same vicinity.

Figure 5.3 demonstrates a different behavior of the vortex structures as they convect past the wall over a period of 8 ms. The image at $\tau = 3ms$ shows two adjacent vortical structures on the wall, pointed to by the white arrows, notably with inter-spacing less than those seen for the vortex passage in Figure 5.1 (at 46 ms). These vortices impose a broad negative pressure peak on the wall that is located directly beneath them. The signature gets wider in the radial direction as a positive pressure peak develops upstream of the trailing vortex at $\tau = 4 ms$, apparently due to the entrained flow towards the wall by the vortices. The positive peak gains more strength at $\tau = 5 ms$ while the negative peak remains as strong as before while lying beneath the two vortices in the radial range 0.8 < r/D < 1.4. In the flow visualization image at $\tau = 6 ms$, the downstream vortex starts to displace away from the wall (apparently because of the flow induced by the trailing vortex) while the trailing one moves closer to the wall (seemingly due the downward velocity

induced by the downstream vortex. This interaction between the two vortices continues until they merge completely. The broad negative-pressure signature beneath the vortices develops into a much narrower and stronger negative spike at $\tau = 8$ ms beneath the trailing vortex. This strengthening of the negative pressure peak could be due to the movement of the trailing vortex closer to the wall; this can also be explained by referring to the solution of Poisson' equation (1.5), where the wall-pressure strength is inversely proportional to the distance between the wall and the pressure source. However, though cannot be seen in the visualization, we believe this fast and dramatic development of the negative-pressure spike is caused by the formation of a secondary vortex from the interaction of the trailing vortex with the wall. The physics of this process are examined in section 6.2. By the time that the vortex structures reach r/D=1.5, merging is complete. Farther downstream, the merged vortical structure appears to become incoherent and diffuse, and the associated pressure signature weakens. The vortex evolution scenario depicted in Figure 5.3 in which the jet vortices interact and merge as they advect past the wall will be referred to as "vortex merging". Like the vortex-passage scenario, the radial evolution of the pressure signature in the vortex merging scenario is consistent with the radial profile of p_{rms} . Specifically, with increasing r/D, the initially very weak pressure for r/D < 0.5increases in strength in the domain where the signature of the jet vortices and their induced flow can be felt. The strength of this signature peaks around r/D = 1.3 due to the mutual interaction of the vortices, before decaying due to the vortices breaking up.

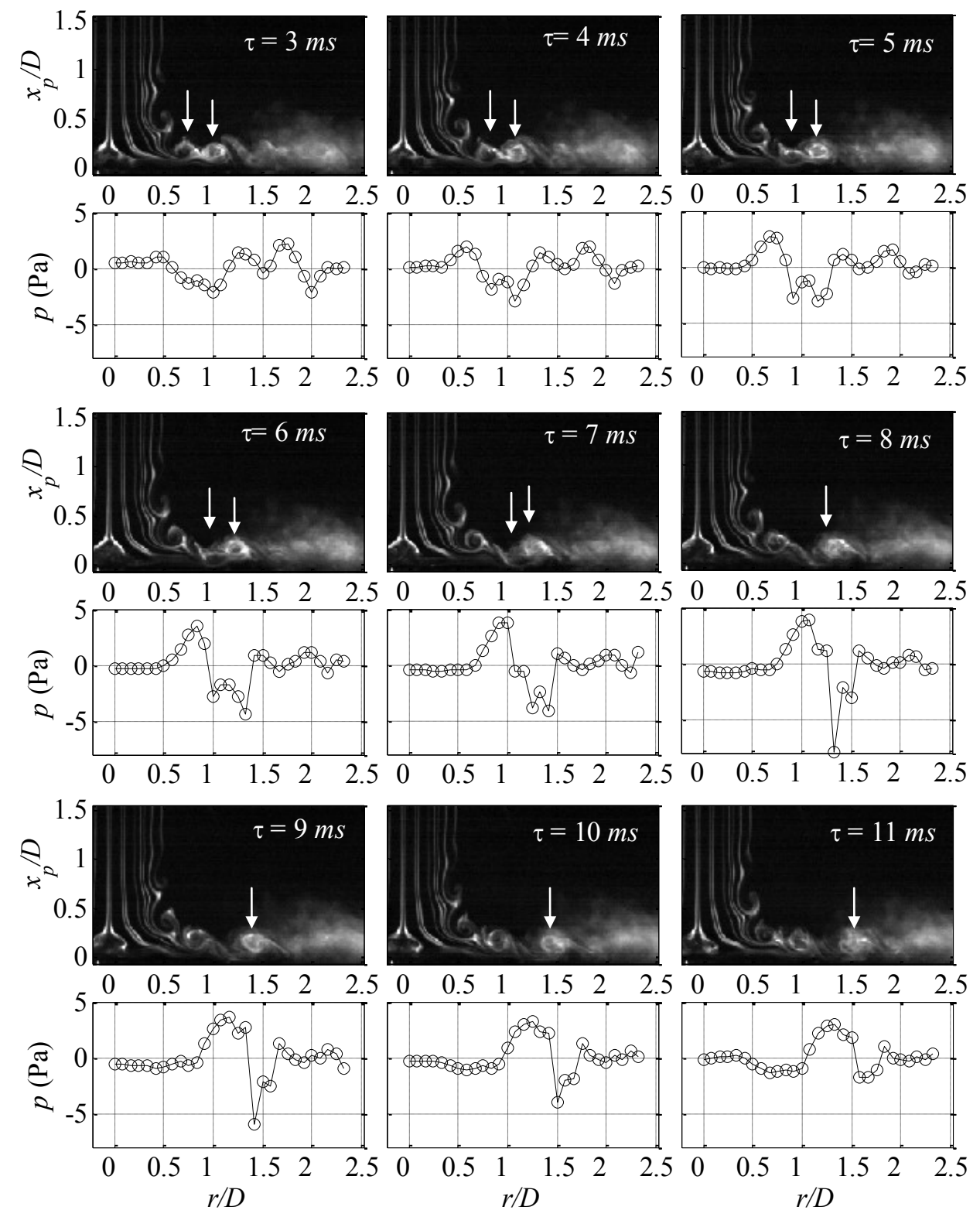


Figure 5.3 Spatial pressure signature and associated flow visualization of vortex merging in normal impingement at H/D=2

It is also instructive to examine the temporal characteristics of the pressure signature associated with the vortex merging and vortex passage scenarios. Figure 5.4 represents temporal pressure signals from the microphones located in the range of r/D=0.67-1.67 for a period of time of 70 ms, which includes the durations of vortex passage and vortex merging shown in Figure 5.1 and Figure 5.3 respectively. The signal at r/D=0.67 demonstrates two different charactristic signatures: one which has a shape like the letter w (i.e. w-like), which is associated with vortex merging, and the other which is a sinusoidal-like signature, which is associated with vortex passage. Each of the temporal signatures associated with vortex merging (w-shaped), which are present during the time of 0-30 ms at r/D=0.67, is also seen in the signals measured at r/D=1.0and 1.33 at a later time. Based on this and the discussion of Figure 5.3 it is evident that the double negative peaks in the "w" pressure signature are the result of the successive passing of two adjacent vortices that eventually merge (see also Figure 5.9, Figure 5.12 and associated discussion). Thus, the distance between the two negative peaks in the "w" signature decreases with increasing r/D with the peak beneath the trailing vortex (i.e. occurring later in time within the "w signature"; also pointed to with a red arrow in Figure 5.4) becoming stronger most of the time. By the time these peaks are seen at r/D=1.67, they merge into one peak, reflecting merging of the vortices.

The temporal signal in the period of time of 30-50 ms at r/D=0.67, which is sinusoidal-like, corresponds to the vortex passage period. The time delay between the negative peaks is larger compared to the ones associated with vortex merging (i.e. that between two negative peaks within a single w-shaped signature) which implies that the inter-vortex distance in this case is greater, and as a result merging is not observed. The signature appears at later times at larger radial locations as it remains beneath the vortices as they convect in the outward radial direction

(one of these peaks is marked with red arrow in Figure 5.4). However, the initially sinusoidal-like signature at r/D=0.67 becomes skewed forming periodic negatitve pulses when the vortices get stronger in the range of r/D = 1.33-1.67. Such distortion would produce muliple harmonics in the pressure spectrum, which is likely the reason for the multiple peaks seen in the power spectral density in Figure 4.4.

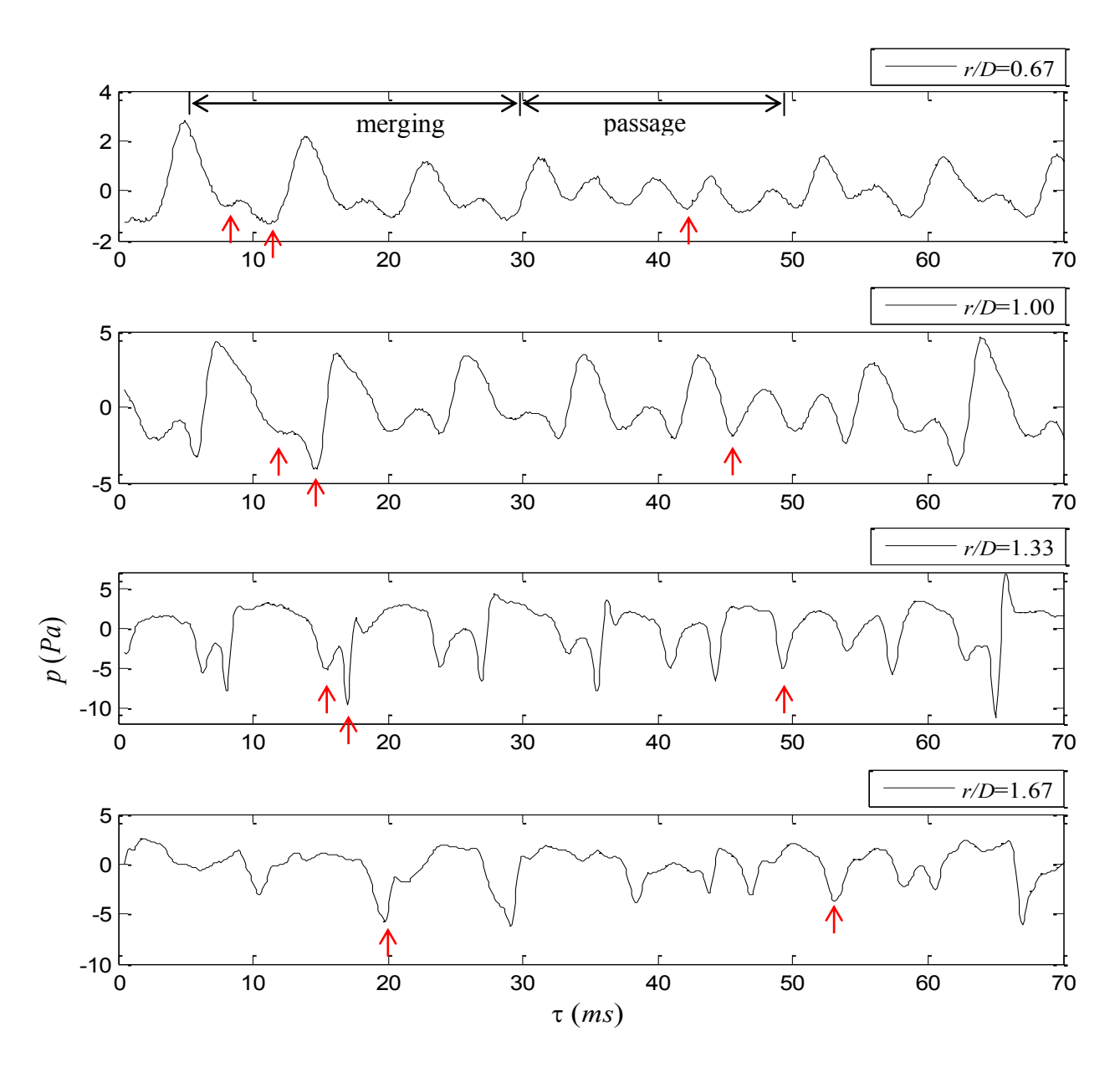


Figure 5.4 Temporal pressure signature in the range r/D =0.67-1.67 for normal impingement and H/D=2

To provide additional support for the discussion of Figure 5.4, a sample temporal pressure signature at r/D=0.67 associated with vortex passage during $\tau=40-52$ ms is tracked as it propagates farther out in the radial direction as shown in Figure 5.5, Figure 5.6, Figure 5.7 and Figure 5.8. In each figure, the pressure-signature plot is accompanied by flow-visualtion images at different time instants during the same period to caputure the concurrent flow features. In Figure 5.5, the temporal signature at r/D = 0.67 portrays two local minima and a maxima which are marked by vertical broken black lines. The flow visulization images acquired at the time instants indicated by the broken black lines are shown next to the temporal signature. The images include a broken line depicting the radial location at which the temporal signature is acuired. Figure 5.5 and Figure 5.6 show that the pressure temporal signatures at r/D=0.67 and 1 are fairly sinusoidal. The corresponding flow visualization images show that negative peaks exist immediately beneath vortices while positive peaks coincide with the period in between two successive vortices. The vortices have a sufficiently large distance in between such that merging does not occur. By the time the vortices reach r/D=1.33 and 1.67, the negative pressure peaks become tronger, and the pressure signature becomes pulse-like. The corresponding flow visualization images show that the vortical structures remain apart with no sign of merging during this period.

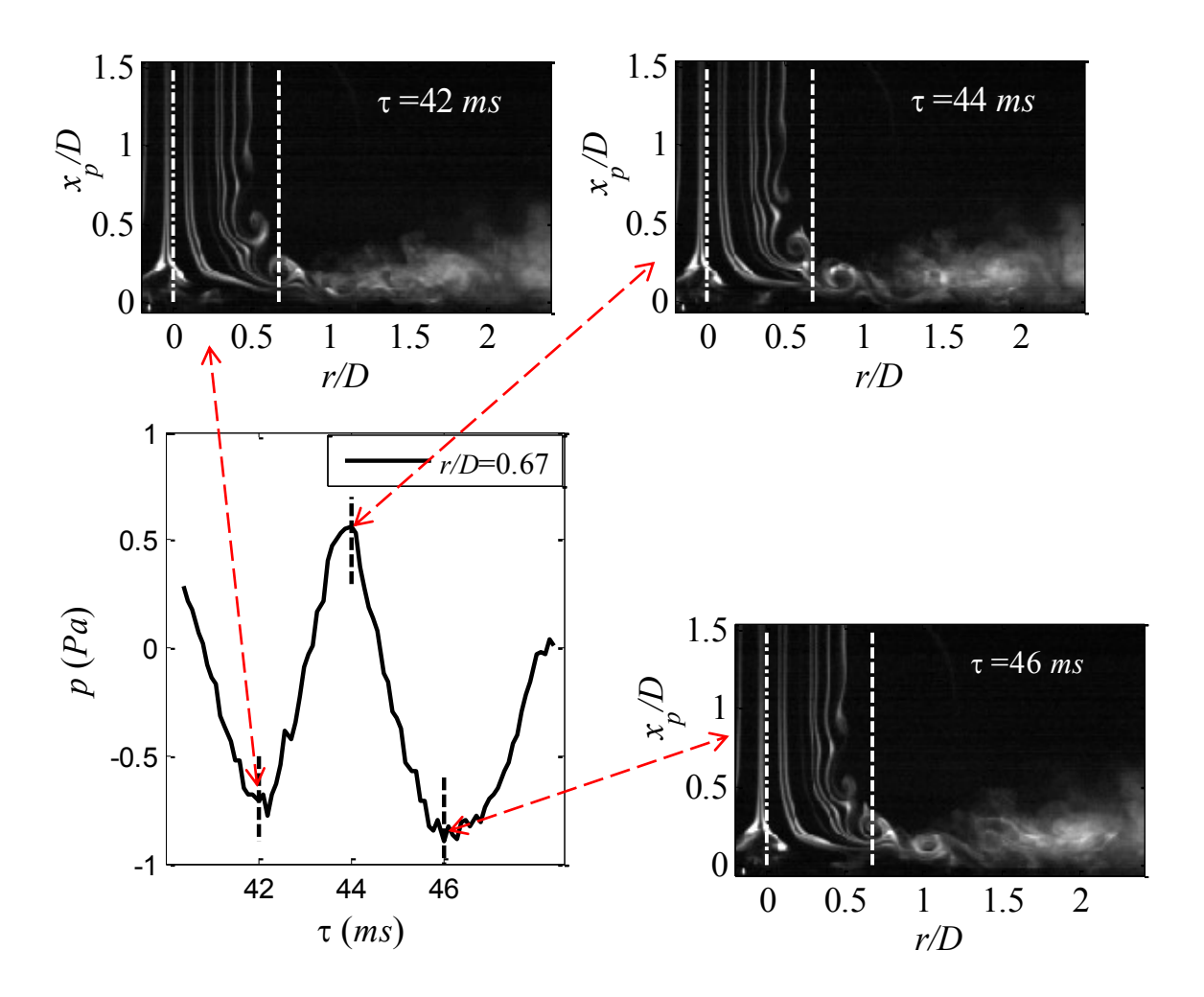


Figure 5.5 Vortex passage temporal pressure signature at r/D of 0.67 in normal impingement at H/D=2. Broken line near the left edge of each image marks the jet centerline while the other broken line marks the radial location at which the shown pressure signature is measured.

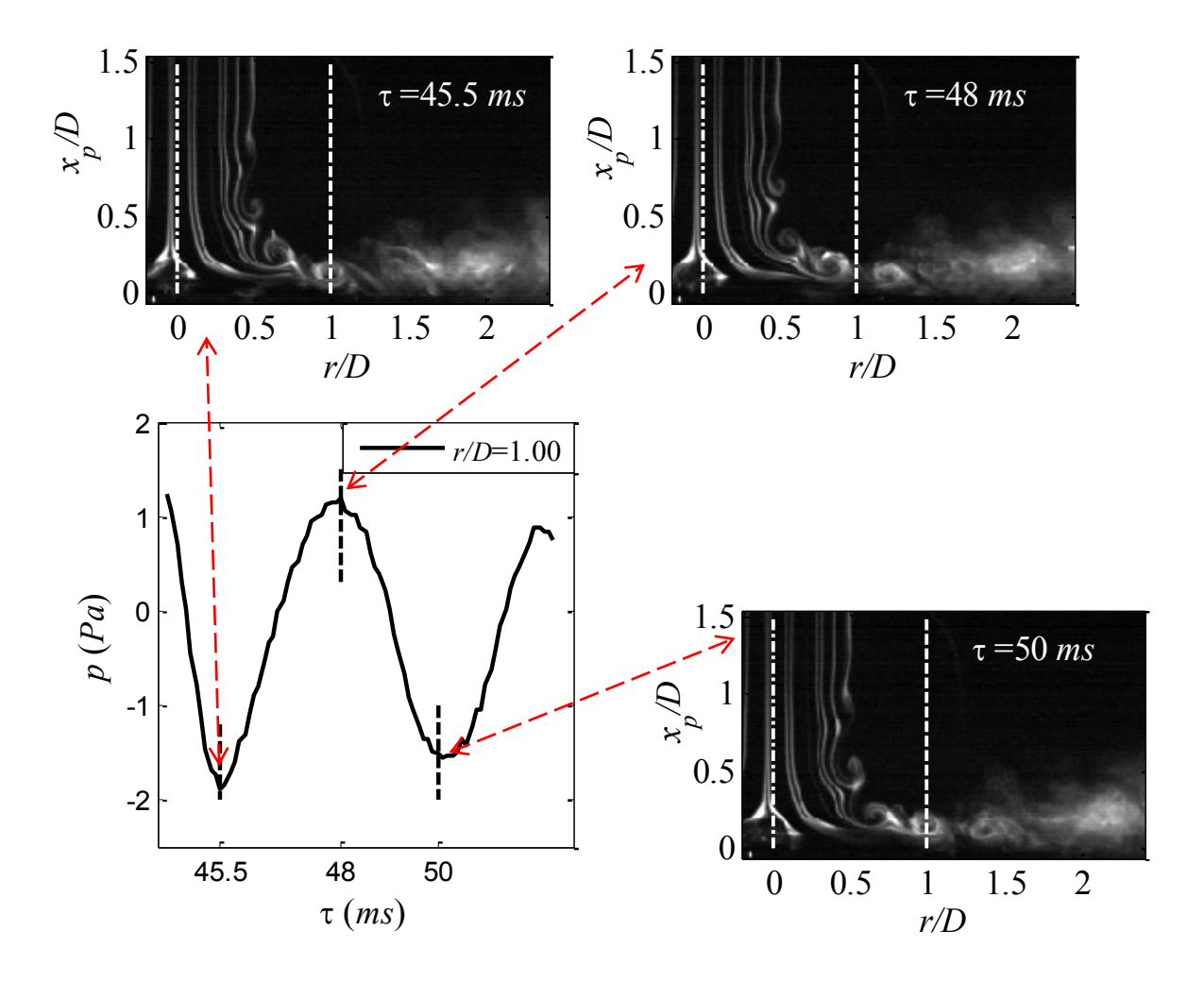


Figure 5.6 Vortex passage temporal pressure signature at r/D of 1 in normal impingement at H/D=2. Broken line near the left edge of each image marks the jet centerline while the other broken line marks the radial location at which the shown pressure signature is measured.

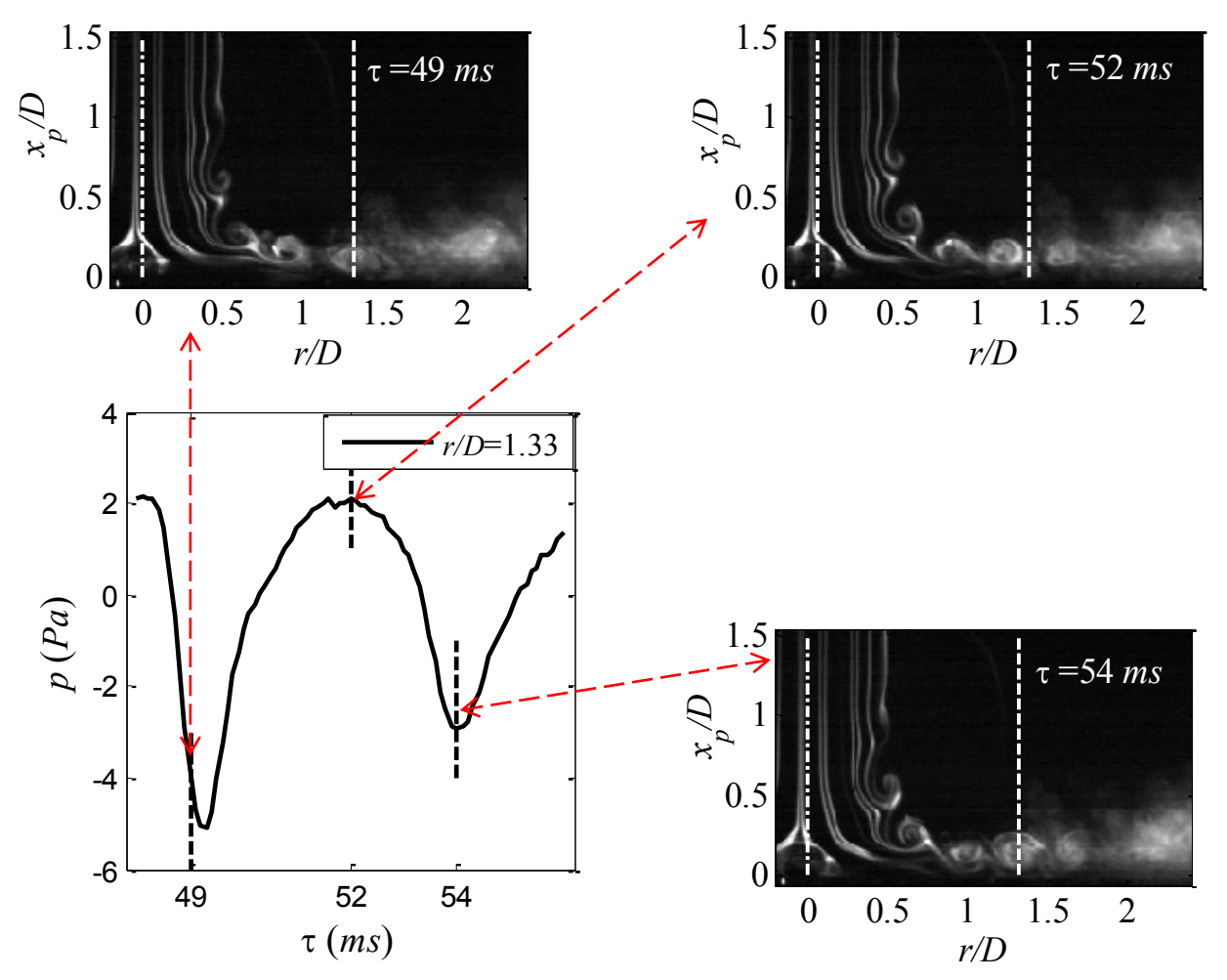


Figure 5.7 Vortex passage temporal pressure signature at r/D of 1.33 in normal impingement at H/D=2. Broken line near the left edge of each image marks the jet centerline while the other broken line marks the radial location at which the shown pressure signature is measured.

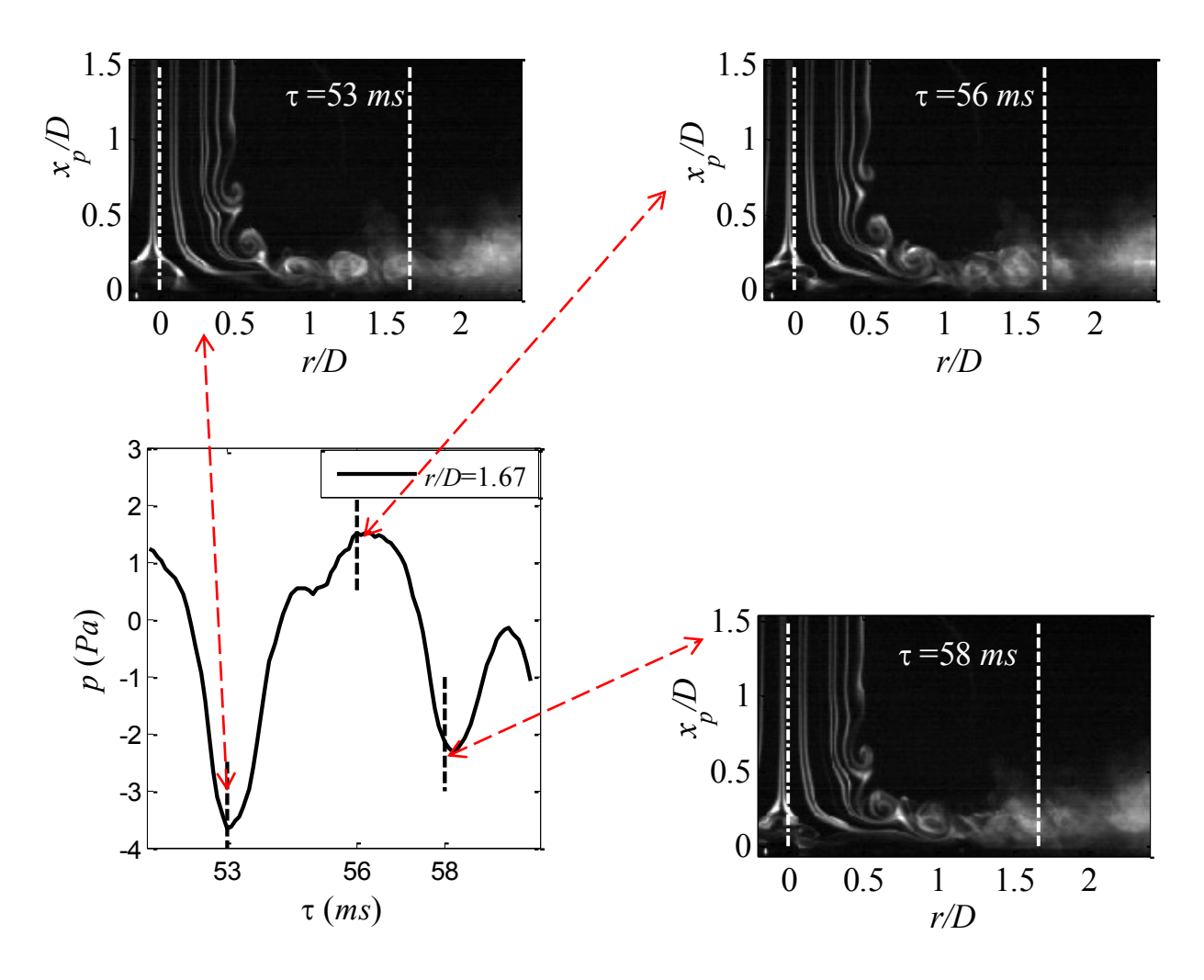


Figure 5.8 Vortex passage temporal pressure signature at r/D of 1.67 in normal impingement at H/D=2. Broken line near the left edge of each image marks the jet centerline while the other broken line marks the radial location at which the shown pressure signature is measured.

A temporal pressure signature sample associated with the vortex merging scenario at r/D=0.67 during τ = 4-15 ms is also tracked as the evolving vortices convect farther out in the radial direction, as shown in Figure 5.9, Figure 5.10, Figure 5.11 and Figure 5.12. The signatures provided in the figures are accompanied with their corresponding flow visualization images in the same way as in Figure 5.5 through Figure 5.8. By examing the signature at r/D = 0.67, a comparatively strong positive peak is present at τ = 5 ms; the corresponding flow visualization image shows no vortical structure at this radial location, which is marked by a vertical white

broken line. Moreover, two adjacent vortices which crossed this location at earlier time, shown in the same image, are likely to induce flow towards the wall at this location and as a result impose a positve pressure peak. The image taken at $\tau = 7.5$ ms reveals a vortical structure at r/D=0.67 location which is imposing the local negative peak found in the signature, while a similar structure does not exist at r/D = 1 location at this time instant. Additionally, the corresponding signature at the latter location is depecting a positive peak as result of the induced flow by a vortex located immediately downstream of r/D = 1, which form from merging of two vortices at earlier time. The vortex shown in the image at $\tau = 7.5$ ms at r/D = 0.67 travels farther out in the radial location to be at r/D = 1 in the image taken at $\tau = 11$ ms while a following vortical structure reaches r/D = 0.67. Inspecting both signatures at this time at the two radial locations (r/D = 0.67and 1), one can see that both signatures have negative peaks. The negative peak shown in the siganture at r/D = 0.67 at $\tau = 11$ ms which is associated with the trailing vortex is stronger than the one at $\tau = 7.5$ ms; this is believed to be due to the leading vortex imposing a downward induced velocity on the trailing one, causing the latter to be closer to the wall. Similar mechanism seems to occur in producing the temporal signature at r/D = 1 with the negative peak associated with the trailing vortex found to be stronger than that associated with the leading vortex.

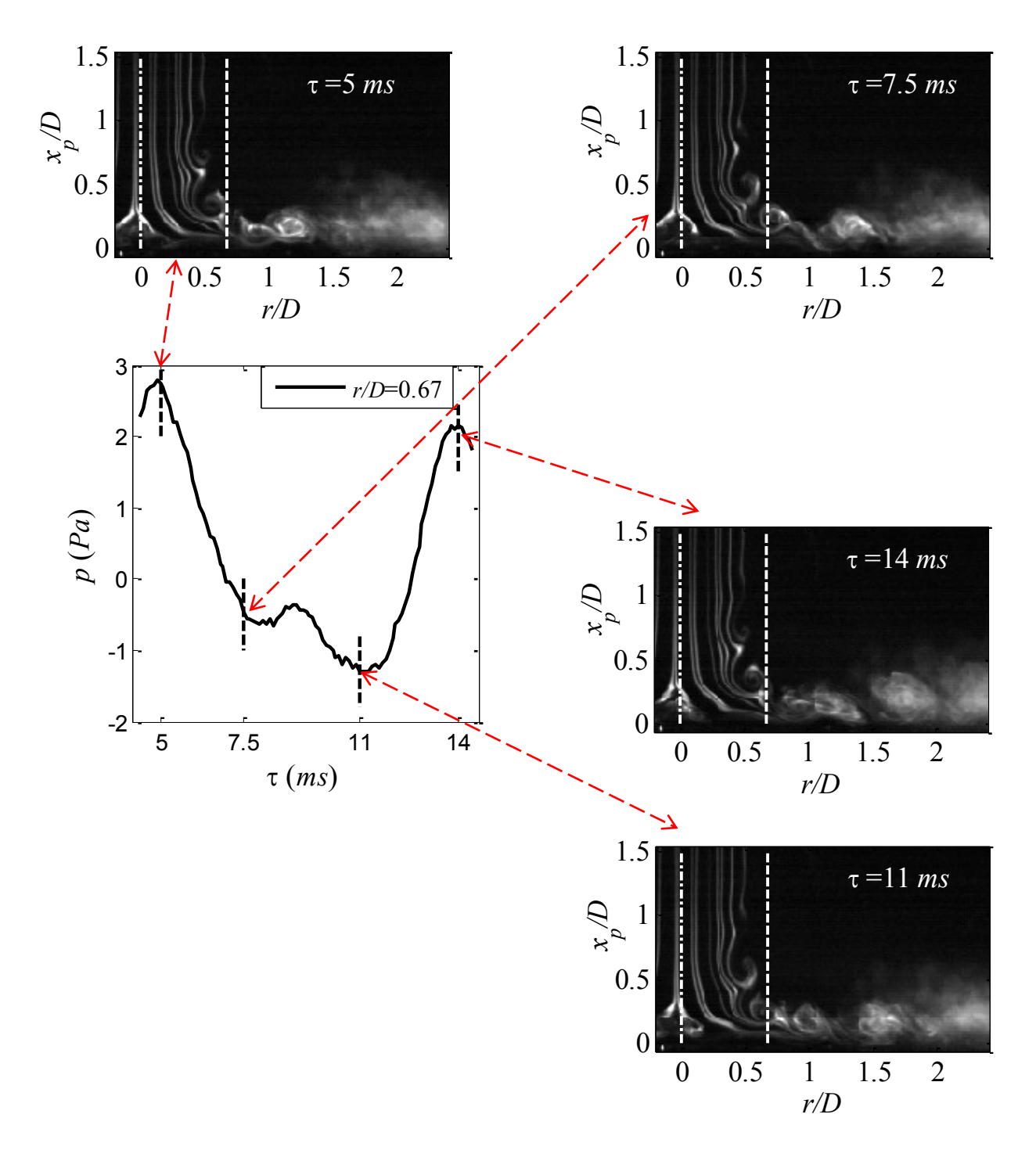


Figure 5.9 Vortex merging temporal pressure signature at r/D of 0.67 in normal impingement at H/D=2. Broken line near the left edge of each image marks the jet centerline while the other broken line marks the radial location at which the shown pressure signature is measured.

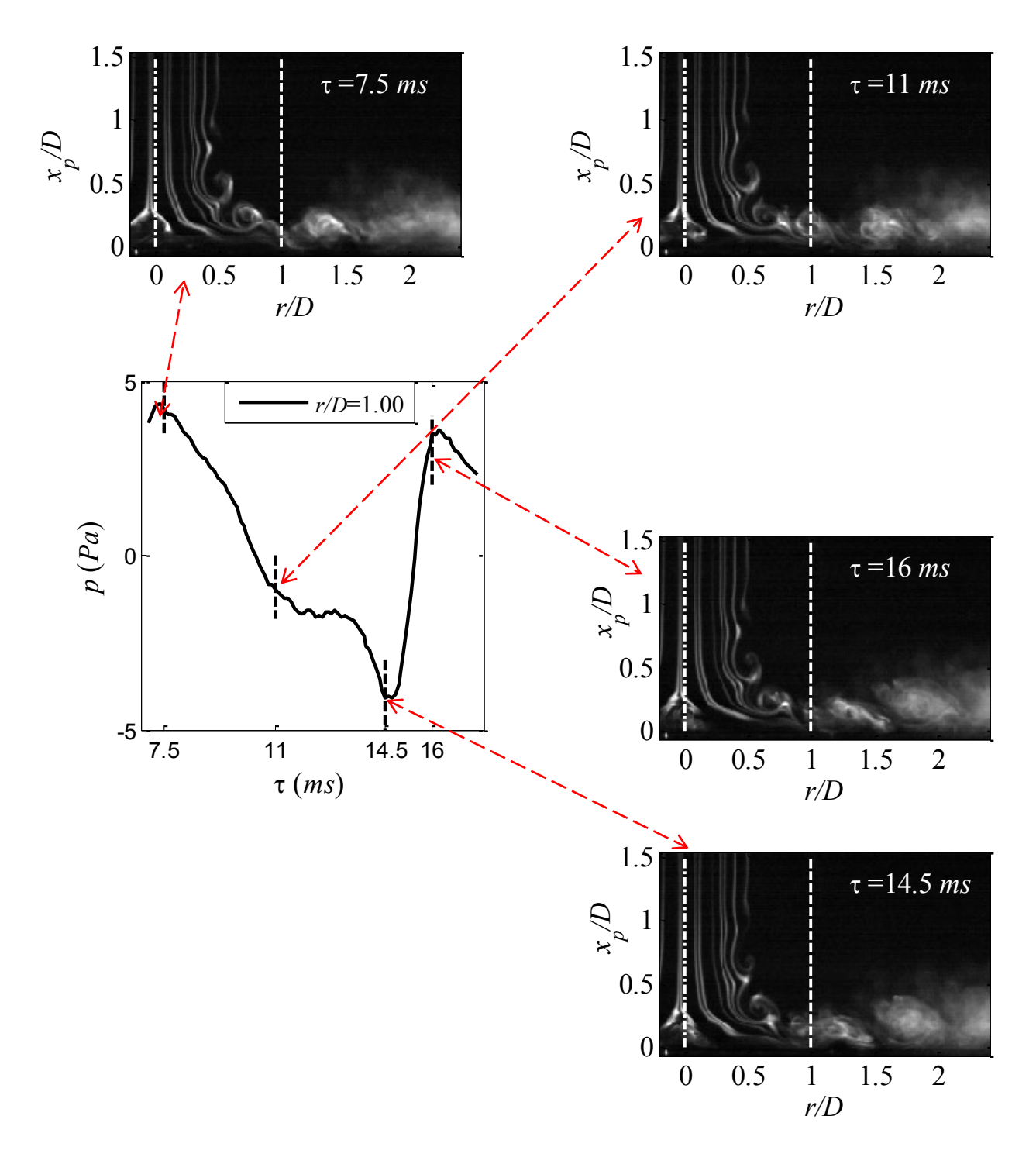


Figure 5.10 Vortex merging temporal pressure signature at r/D of 1 in normal impingement at H/D=2. Broken line near the left edge of each image marks the jet centerline while the other broken line marks the radial location at which the shown pressure signature is measured.

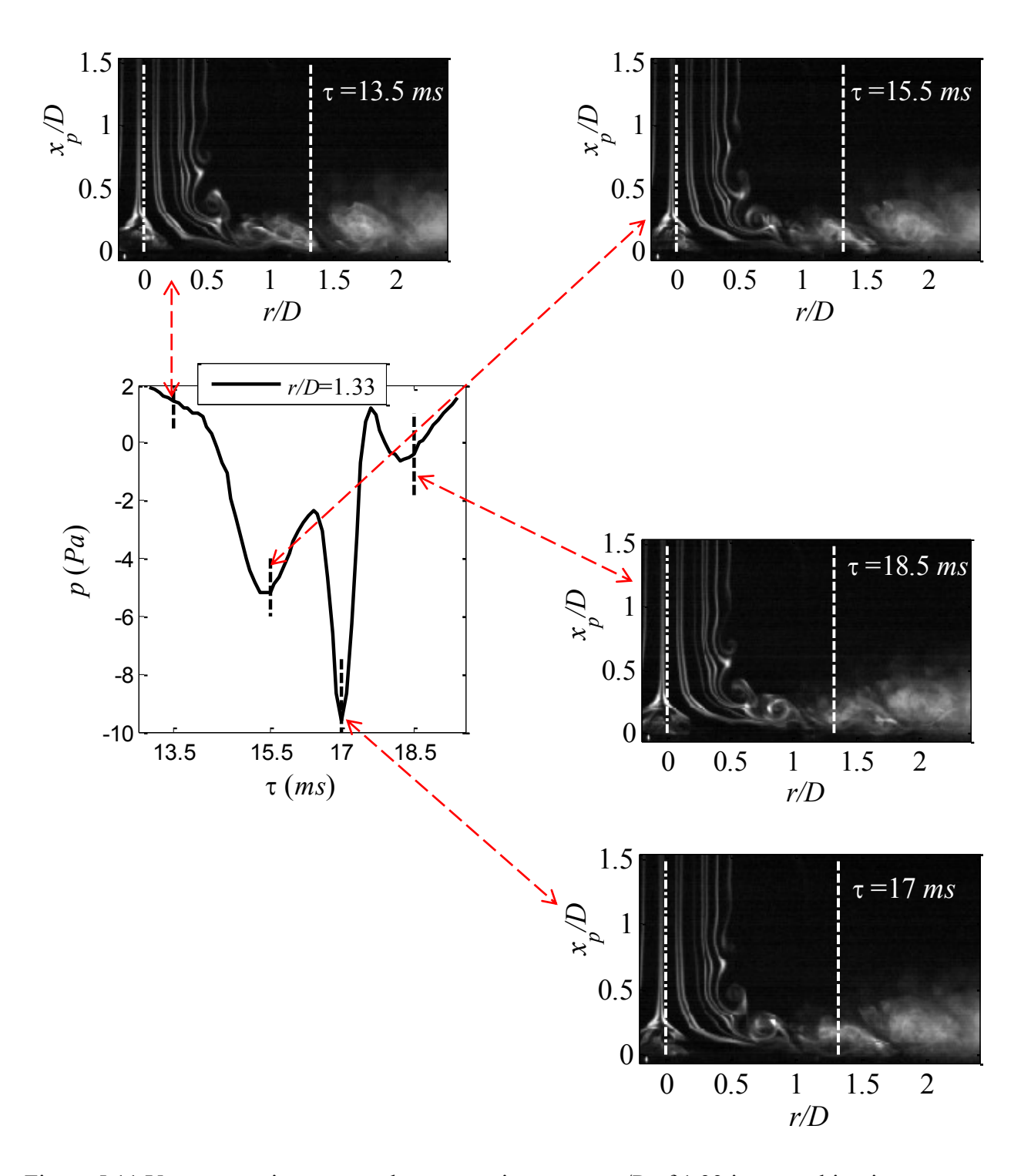


Figure 5.11 Vortex merging temporal pressure signature at r/D of 1.33 in normal impingement at H/D=2. Broken line near the left edge of each image marks the jet centerline while the other broken line marks the radial location at which the shown pressure signature is measured.

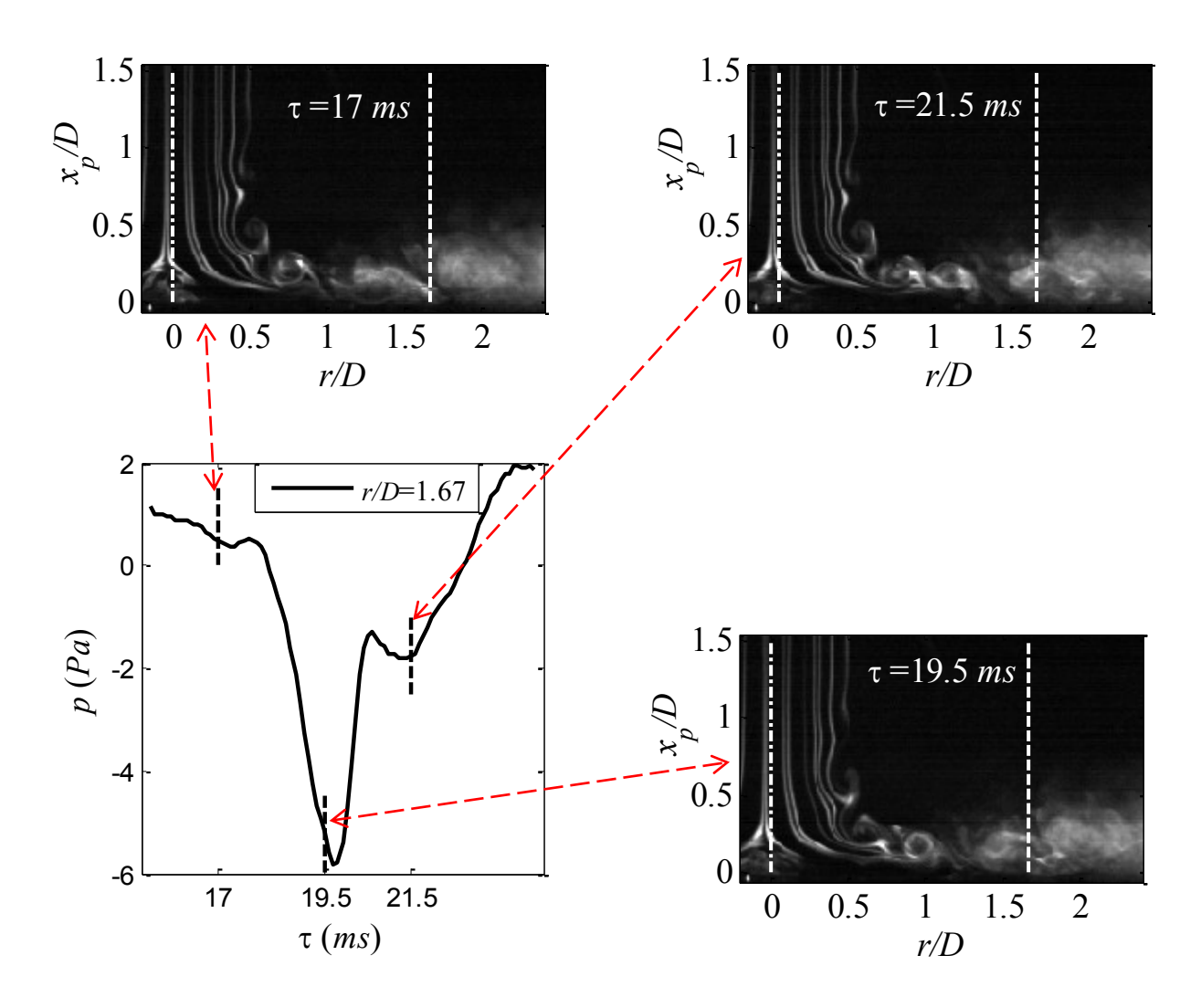


Figure 5.12 Vortex merging temporal pressure signature at r/D of 1.67 in normal impingement at H/D=2. Broken line near the left edge of each image marks the jet centerline while the other broken line marks the radial location at which the shown pressure signature is measured.

Figure 5.11 and Figure 5.12 depicts the temporal pressure signature corresponding to the flow stuctures disscussed in connection with Figure 5.9 Figure 5.10 when these structures reach r/D =1.33 and 1.67 locations at later times. Qualitatively, a similar pattern to that found at r/D = 1 is observed at r/D = 1.33 location with the pressure signature being perdominantly composed of two negative peaks and the peak associated with the trailing vortex. At r/D = 1.33, however, the trailing vortex peak becomes much stronger, spiking to a value of about -10 Pa which is reached in a very short time scale. It is believed that the spike at r/D=1.67 at instant 19.5 ms is due to the

formation of the secondary vortex; eventhough the flow visualization quality at this instant does not prove such statement, the phenomena becomes clear with the aid of the computational results in chapter 6.

The vortex merging observed in Figure 5.9 through Figure 5.12 seems to be complete near r/D=1.3-1.6. Observations of flow visualization of many instances involving the vortex merging scenario show that this location could vary between different instances. In other words, the whole mechanism involving the vortex-vortex interaction/merging can start earlier or later than seen in Figure 5.9 through Figure 5.12, and as a result, the temporal signatures shown may shift to radial locations different from those at which they are captured in Figure 5.9 through Figure 5.12.

At this point, it is important to learn if the two observed mechanisms of vortex merging and vortex passage can clarify the characteristics of the long-time statistics computed in Chapter 4; specifically the long-time averaged power spectral density. For this reason, the frequency content is examined for the short temporal pressure signals depicted in Figure 5.4 for the periods associated with vortex merging and vortex passage individually. The power spectral density shown in Figure 5.13 is computed with 9.76 Hz resolution for the signals associated with vortex passage at r/D=0.67-1.67. The spectra in the range of r/D=0.67-1.33 demonstrate a dominant peak near $St_D\approx1.3$, which would correspond to the vortex passage along the radial direction. Since the flow visualization show no vortex pairing to take place before impingement, this frequency should be the same as that at which the initial shear layer instability forms at the jet exit (which leads to the formation of the vortices via shear-layer roll-up). Similar peak, at $St_D\approx1.3$, is found in the long-time-averaged power spectral density results in Figure 4.4. The spectrum at r/D=1.33 in Figure 5.13 shows two additional peaks Strouhal numbers higher than

 $St_D\approx 1.3$. These peaks are harmonics of $St_D\approx 1.3$, and their appearance reflects the distortion in the originally sinusoidal signal, which becomes more pulse-like and negatively skewed at r/D=1.33. At r/D=1.67 the peak shifts to a lower Strouhal number of 0.94. There is no concrete explanation for this shift as the smoke in the flow visualization images get quite diffuse at this large r/D value, and thus it is difficult to explain this shift in terms of the observed flow structure.

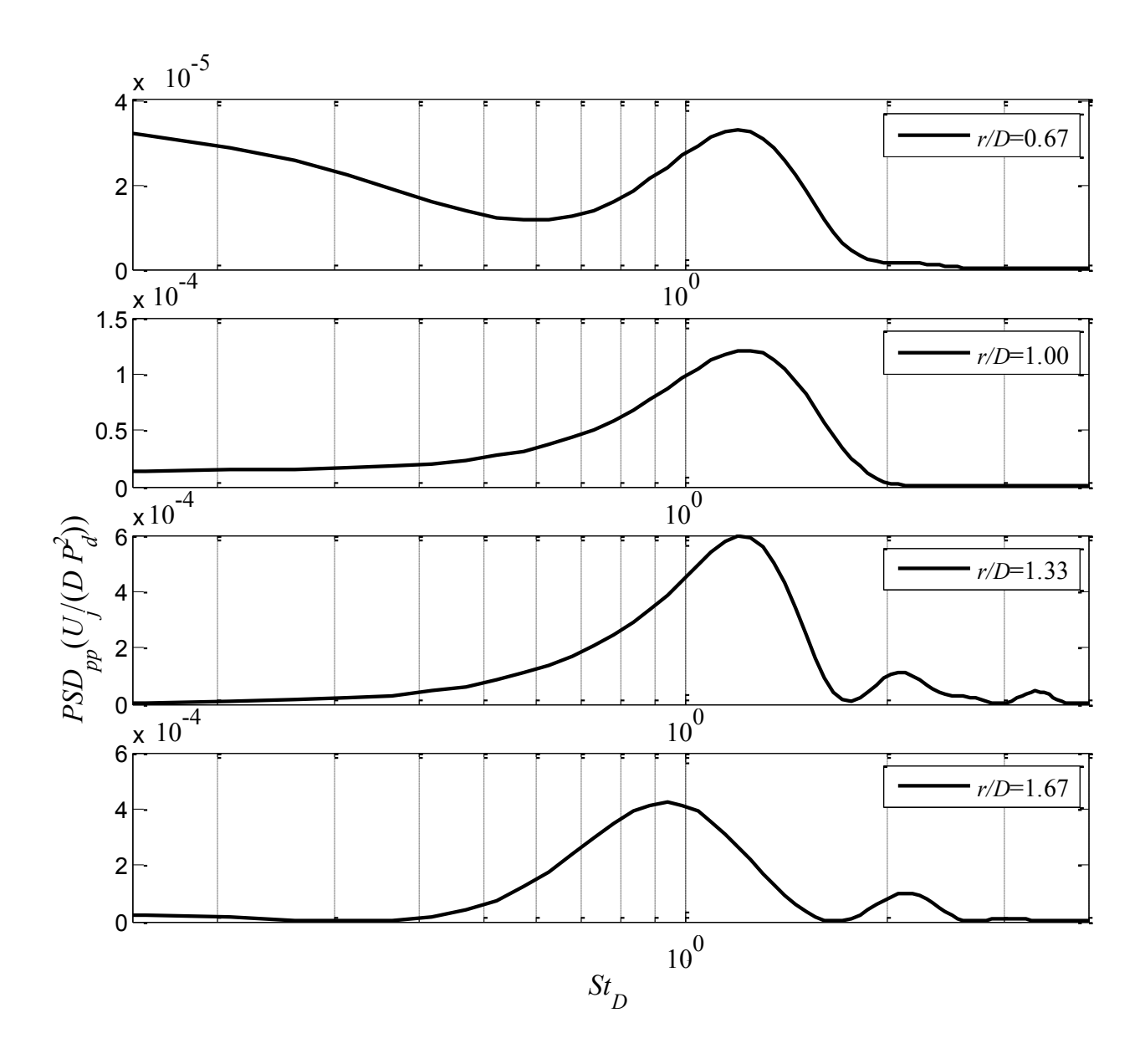


Figure 5.13 Short-time power spectral density for pressure signatures extracted at r/D of 0.67-1.67 during vortex passage

The power spectral density results shown in Figure 5.14 are obtained from signals measured at r/D of 0.67 to 1.67 during vortex merging. A prominent peak near Strouhal number of 0.64 is apparent at all radial locations with the maximum magnitude occurring at r/D of 1.33. A second peak at approximately 1.3, which is harmonic of $St_D\approx0.64$, is present at r/D of 0.67, 1 and 1.67 with much less magnitude than the peak at lower Strouhal number. Peaks at the same Strouhal

numbers are observed in the averaged power spectral density for normal impingement in Chapter 4, which are shown in Figure 4.4. Based on analysis of the simultaneous flow visualization and pressure results it is now evident that the physical interpretation of these two peaks is that vortices approach the wall at $St_D\approx1.3$ and the merging of each pair leads the Strouhal number to drop to half to its value (i.e. $St_D\approx1.3$). Nonetheless, as discussed previously, during the vortexmerging scenario, the pressure signature are no purely sinusoidal at any of the radial locations, and therefore the spectrum contains higher harmonics of the dominant frequency during and after merging ($St_D\approx0.64$), including $St_D\approx1.3$, which would explain the reason behind the co-existence of the two Strouhal numbers $St_D\approx0.64$ and 1.3.

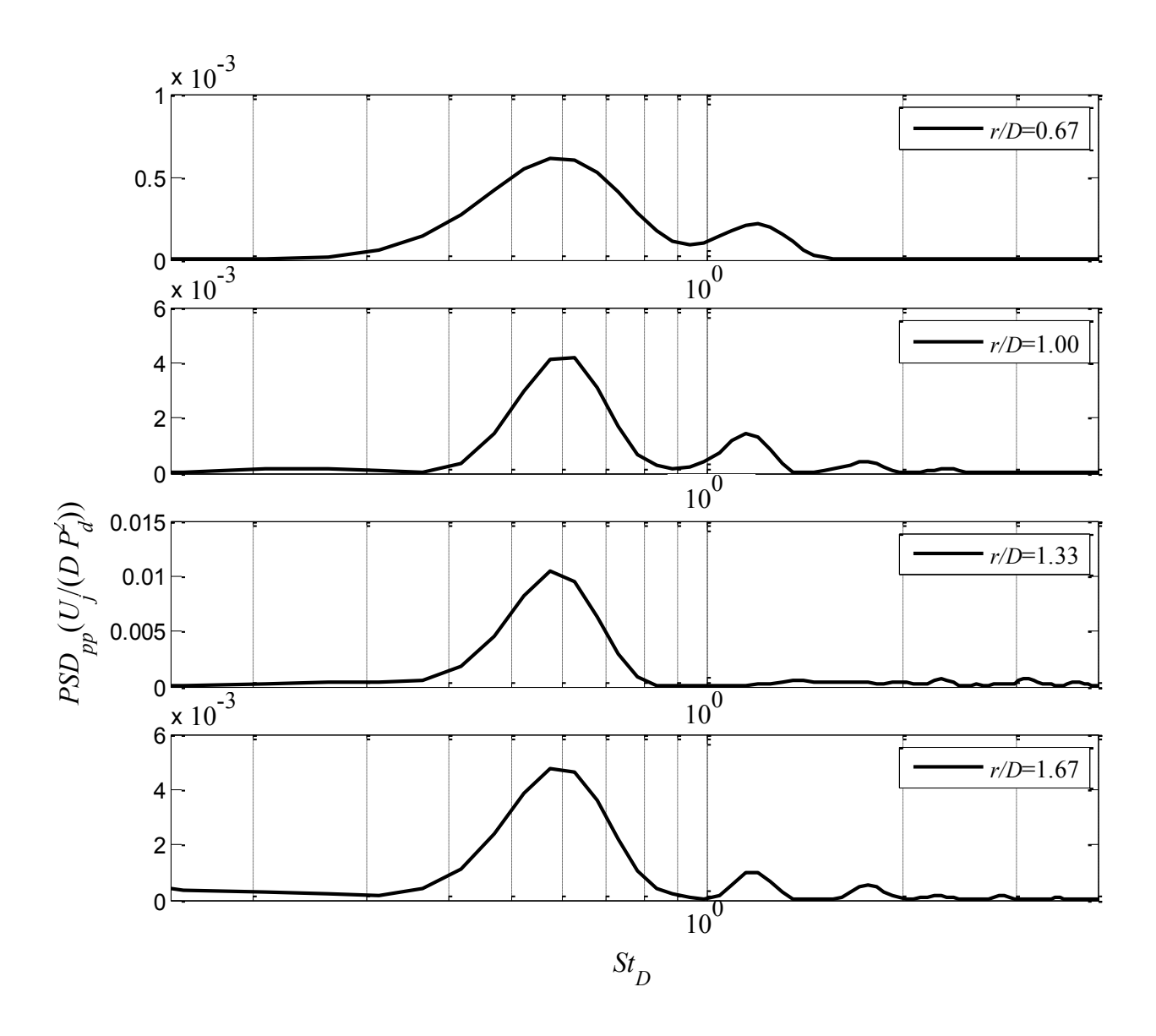


Figure 5.14 Short-time power spectral density for pressure signatures extracted at r/D of 0.67-1.67 during vortex merging

From the analysis in this section till this point for normal impingement at H/D=2, one can conclude that the jet forms vortex ring structures at a rate of St_D of 1.3. These vortices then interact with the wall and change their convection direction to be parallel to the wall. Two different mechanisms are detected during convection; vortex merging (when the vortices pair above the wall, causing the associated frequency of pressure fluctuations to be half of the initial

shear layer instability frequency) and vortex passage (when the vortices maintain their initial formation rate in the shear layer). A significant question that naturally arises is which of these two mechanisms is more persistent. To answer this question, a random sample from flow visualizations is selected which contains 100 vortices convecting above the wall. It is found that 78 out of 100 vortices pair above the wall causing 39 vortex merging incidences and only 22 vortices pass with no sign of merging.

Simultaneous time-resolved flow visualization and unsteady surface pressure measurements are also carried out at H/D locations of 3 and 4 in normal impingement to study the influence of the separation between the impingement plate and the jet on the pressure-generating flow structures. Analysis similar to that conducted on the measurements for H/D=2 location is also applied for the measurements obtained at H/D=3 and 4. This includes examination of the spatial and temporal pressure signatures concurrently with the flow visualization images as well as short-time power spectral density analysis. To avoid redundant figures while explaining the flow development with increasing H/D, analogous physics, such as vortex passage and vortex merging mechanisms, will be illustrated with the aid of the previous figures for H/D=2, and additional figures will only be introduced to discuss new concepts.

Examining the high-speed flow visualization videos for H/D=3 in normal impingement, it is found that vortices which form from the shear layer roll up (at a rate equal to the frequency of the initial shear-layer instability) almost always pair before they encounter the wall. Clearly, this is related to the extra distance available for the shear layer development before being influenced by the impingement plate when compared to the H/D=2 case. Spatial and temporal pressure signatures figures (constructed similar to Figure 5.3 and Figure 5.4 for H/D=2 but are not included in this document) show that the merged vortices impinge on the wall and change

direction to convect parallel to the wall. As they do so, the vortices impose negative pressure peaks that also travel underneath the vortex structures in the radial direction. Unlike when the jet is placed at H/D=2, the microphones located at r/D=0 and 0.33, in H/D=3 case, also sense the pressure fluctuation resulting from this vortex passing effect. The reason behind this is likely that at H/D=3 the vortices are larger and stronger, because of the merging mechanism, and hence the unsteady velocity they induce within the potential core become significant, and result in associated *potential* velocity fluctuations.

Since the vortices pair before they reach the wall at H/D=3 and then move in the radial direction above the wall with no sign of additional merging, one would expect that the vortices passing rate will be half of the frequency of the initial shear layer instability. This is verified when the Strouhal number mode is obtained from short temporal signals by computing the power spectral density, similar to what was done for H/D=2.

When vortices interact with the wall at H/D=2, there is no sign of secondary vortex formation; this might be because the size of secondary vortex is too small at this H location to be resolved in the visualization. However, this is not the case at H/D=3, where secondary vortex formation is visible. After completing the first pairing downstream of the jet and before impinging on the wall, the vortex structures become larger and stronger which could be the reason for the secondary vortex separation to be apparent at this H location.

Figure 5.15 depicts a 12 ms-long temporal pressure signature associated with the secondary vortex at r/D=1.33. The signature portrays two local minima in a raw: a strong minimum occurs at $\tau=87.5$ ms with magnitude of -3 Pascal, and a weaker one takes place at $\tau=90$ ms with magnitude near zero Pascal. By inspecting the related flow visualization images, it is found that the strong local minimum at $\tau=87.5$ ms corresponds to the secondary vortex, which is moving

ahead of the primary one. On the other hand, the weaker local minimum at τ =90 ms corresponds to the primary vortex. From this figure it appears that the secondary vortex produces a stronger pressure signature than the primary one; Further investigation using numerical simulation, which is reported in Chapter 6, clarify the physical reasons leading to the observed difference in the pressure signature of the primary and secondary vortices.

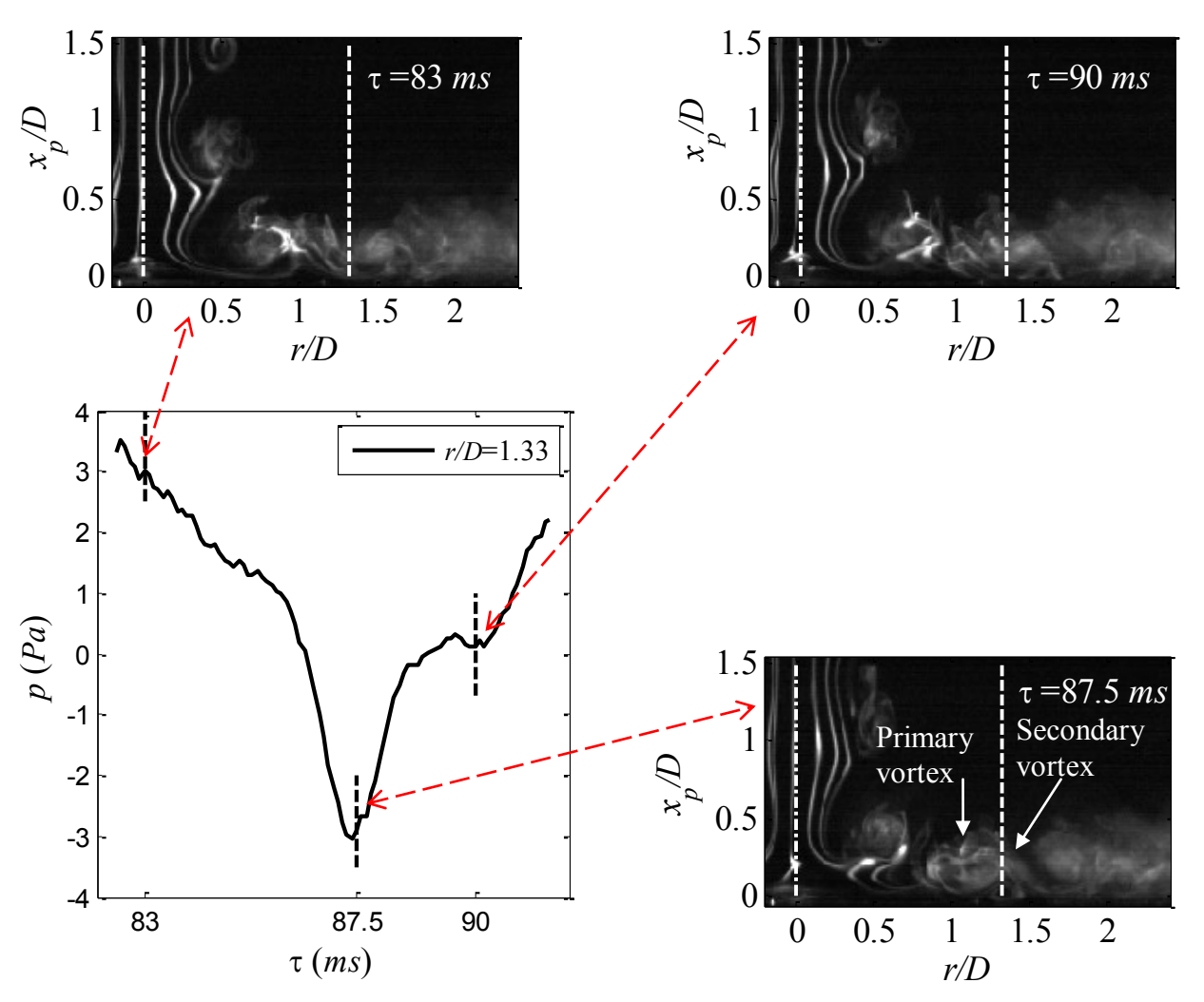


Figure 5.15 Temporal pressure signature associated with secondary vortex at r/D=1.33, for H/D=3 and normal impingement. Broken line near the left edge of each image marks the jet centerline while the other broken line marks the radial location at which the shown pressure signature is measured.

In order to keep the big picture together, the results from the long-time power spectral density analysis for normal impingement (Figure 4.4) are revisited. The spectra for H/D=2 and normal impingement show two main Strouhal numbers of 1.3 and 0.64. Using the simultaneous timeresolved flow visualization with pressure measurements in this chapter, it is verified that the higher Strouhal number of $St_D \approx 1.3$ corresponds to the vortex passage mechanism, where vortices form at the frequency of the initial shear layer instability and then convect above the wall in the radial direction without interacting. The lower Strouhal number of $St_D \approx 0.64$ (and its higher harmonics including $St_D \approx 1.3$) relates to the vortex merging mechanism occurring above the wall within the domain 1.3 < r/D < 1.6. When the impingement plate is placed at H/D=3 (Figure 4.5(b)), the spectra depict a prominent peak at $St_D \approx 0.64$ which is consistent with the observation that merging almost always occurs before reaching the plate. Notably, in this case higher harmonics of 0.64 Strouhal number are absent in the wall-pressure spectrum in the stagnation zone, presumably because the first merging is completed before the vortices reach the impingement plate, leading to simple periodic passage of the vortices through the stagnation zone. Placing the impingement plate farther downstream at H/D=4, the spectra show two distinct peaks at Strouhal numbers of 0.32 and 0.53. Following the fact that after merging, the vortex passage Strouhal number is halved, it is evident that the Strouhal number of 0.32 is the result of a second merging that takes place prior to reaching the impingement plate at H/D=4. Similar to H/D = 3, no higher harmonics of 0.32 Strouhal number are observed in the wall-pressure spectrum (Figure 4.4(c)), which is likely due to the completion of the second vortex merging upstream of impingement. On the other hand, the origin of the Strouhal number of 0.53 is difficult to conjecture since this Strouhal number it is not a sub-harmonic of that of the initial

shear layer instability. In the following, further investigations are discussed which aim to identify the flow physics leading to the observation of the Strouhal number of 0.53, as well as to verify that the Strouhal number of 0.32 is indeed related to the second vortex pairing.

Inspecting the flow visualization images for H/D=4, it is found that there are two kinds of merging that occur before the impingement plate in terms of the number of vortex rings involved in each merging. Figure 5.16 depicts flow visualization images at consecutive times tracking vortical structures as they evolve downstream of the jet. The figure presents the case where a total number of four vortex rings merge before they encounter the wall. This starts with two successive pairings that take place near $x_1/D=2$ location. The image at $\tau=0.5$ ms shows two vortices (pointed to by broken red arrows), which pair at $\tau=11$ ms (solid red arrow). Two other vortices also come into view at the same time (pointed to by broken yellow arrows), which also eventually pair. The flow visualization image at $\tau=16.5$ ms portrays the two vortical structures that are products of the two earlier pairings (pointed to by red and yellow solid arrows). These two vortical structures then merge at $\tau=27$ ms to form one larger structure that is the product of four vortices (pointed to by blue solid arrow); this structure is the result of a second merging/pairing.

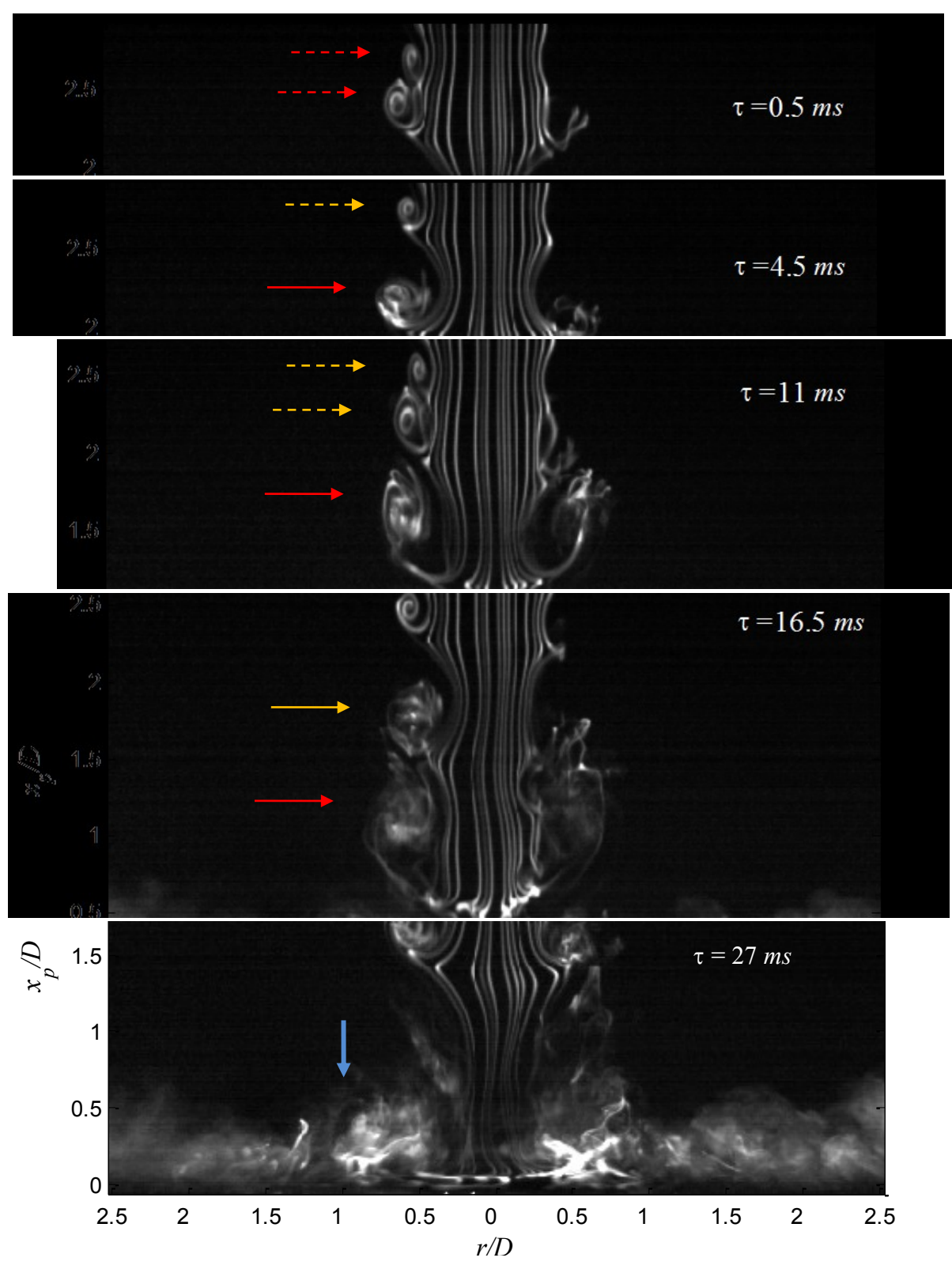


Figure 5.16 Flow visualization images showing the process of first and second vortex pairing downstream of the jet for H/D=4

The alternative scenario of vortex merging for H/D=4 is when three, rather than four, vortices merge before they impinge on the wall. Figure 5.17 depicts flow visualization images at consecutive times tracking three vortices as they evolve before they reach the plate. The three vortices, shown in the image at $\tau=20$ ms, and pointed to by green broken arrows, form immediately after the four vortices shown in Figure 5.16. In the three-vortex merging process, two vortices pair first, as shown in the image at $\tau=24$ ms, then they "drag" the third one behind to merge with them; as shown in the image at $\tau=32$ ms, pointed to by the green solid arrow.

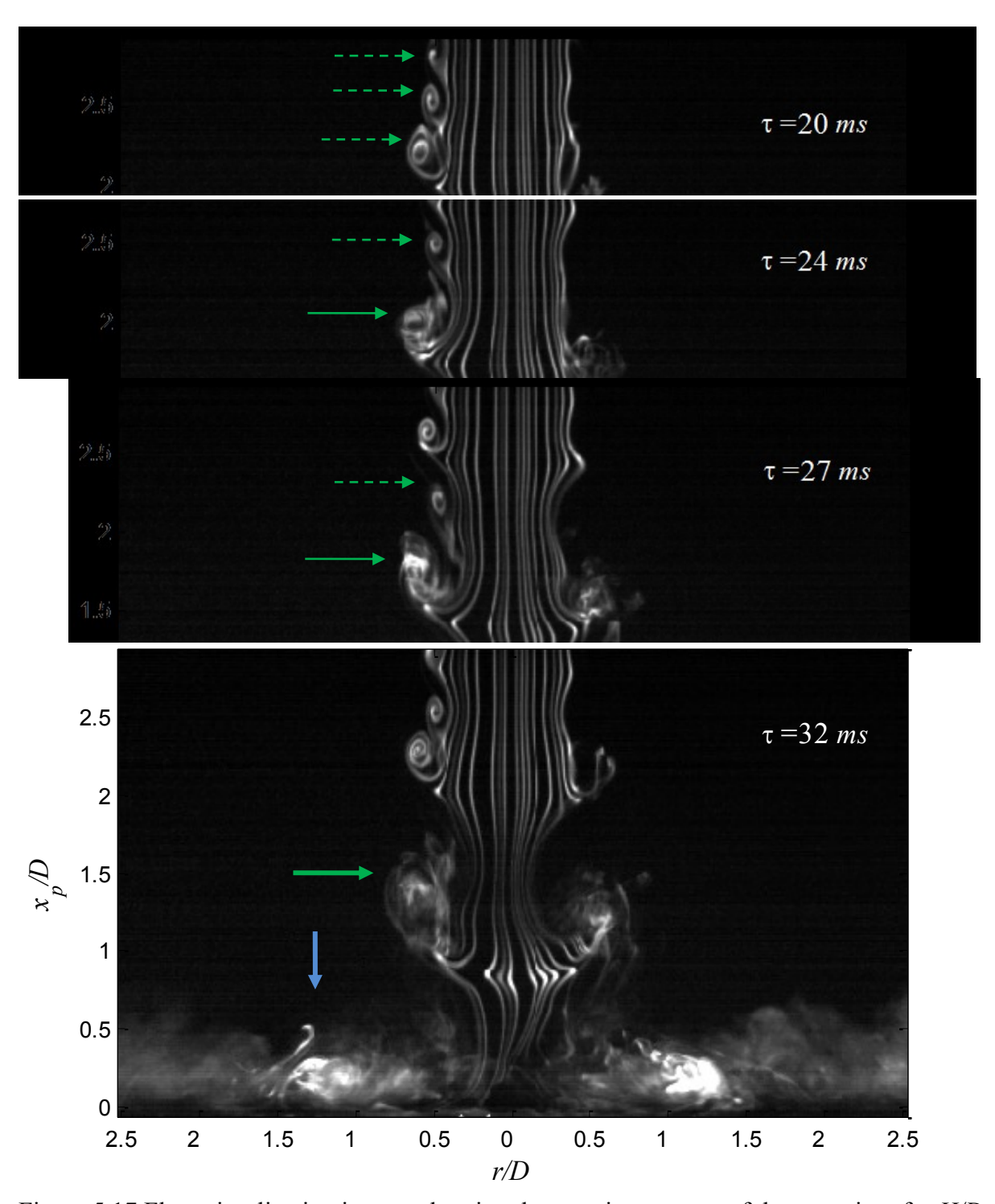


Figure 5.17 Flow visualization images showing the merging process of three vortices for H/D=4

The image at τ =32 ms in Figure 5.17 shows two vortical structures; one is a product of merging of four vortices (pointed to by blue arrow) and the second is a product three merged

vortices (pointed to by green arrow). The corresponding surface pressure measurements when these two structures convect above the wall (shown in Figure 5.18) are examined by computing the power spectral density from short pressure time series recorded concurrently. Figure 5.19 depicts these results in the radial range of $0 \le r/D \le 1.33$. The spectra depict two prominent peaks at Strouhal numbers of 0.32 and 0.52; the lower Strouhal number is related to the passage of the structure resulting from the merging of four vortices. This is verified by examining other signals occurring at the time of passage of only structures that were produced by four vortices. This also implies that the higher Strouhal number of 0.52 is related to the passage of the merged three vortices.

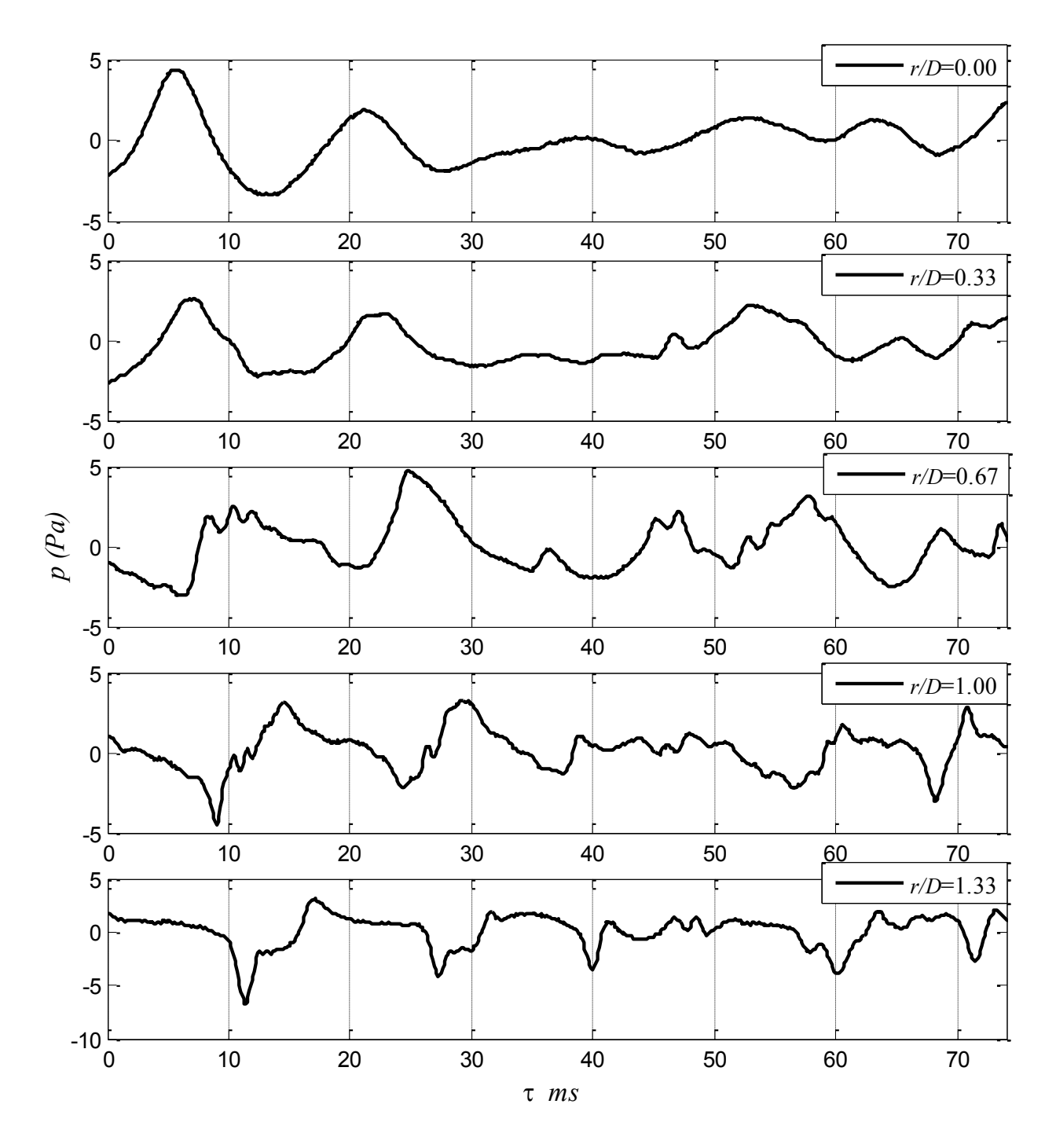


Figure 5.18 Temporal pressure signature in the range r/D =0-1.33 for normal impingement and H/D=4

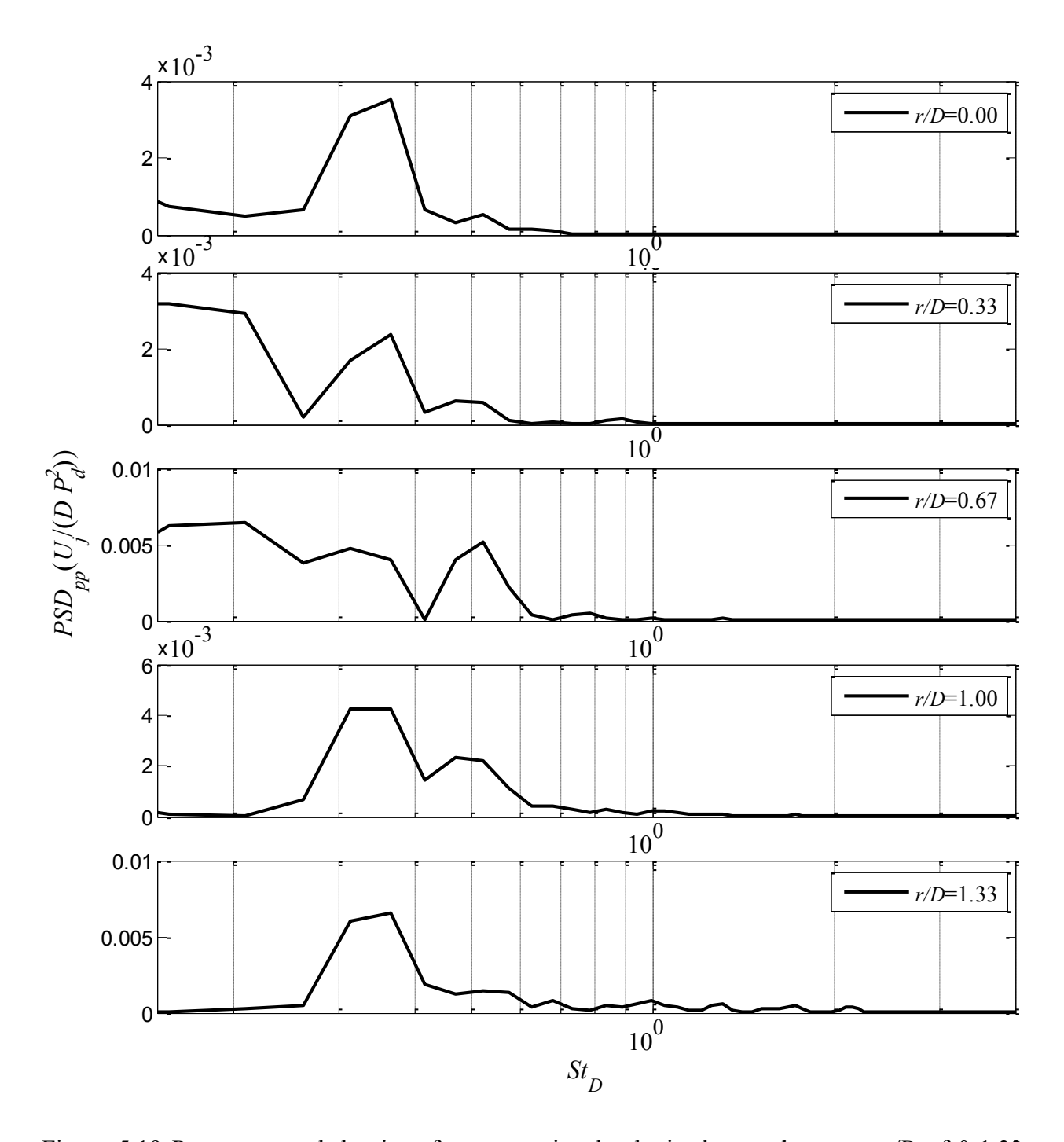


Figure 5.19 Power spectral density of pressure signals obtained over the range r/D of 0-1.33 during the passage of vortices resulting from merging of three and four structures in normal impingement and H/D=4

5.1.1 Stagnation point pressure signature

The above discussion has focused predominantly on the wall-pressure behavior in the radial domain $0.67 \le r/D \le 2.33$, which stretches from the "outer" part of the stagnation zone into the wall-jet zone. In the immediate vicinity of the stagnation point, where the flow is predominantly non-vortical and inviscid (i.e. potential) over the H/D range examined here, the physics of pressure generation is different. The microphone located at r/D=0 is utilized to study the temporal pressure signature at the stagnation point while examining the simultaneous flow visualization at H/D of 3 and 4 in normal impingement: see Figure 5.20 and Figure 5.21, respectively. The latter figures are constructed in a similar manner to Figure 5.5. The pressure signals for both H/D=3 and 4 portray a sinusoidal-like behavior with the amplitude of the signal occurring in the latter case being much stronger. The signals show local maxima at τ = 21 ms and 37 ms for H/D=4 and 3 respectively. By inspecting the corresponding images, it is seen that these maxima occur when the potential core is narrowest in radial extent immediately above the stagnation point. It is also clear from the images that the narrowest cross section of the potential core occurs at the same wall-normal location as that of the center of the core of the vortex ring. It is well known that the wall-normal component of the velocity induced by the vortex ring will be largest at the same height where the core center is present. In contrast, in between vortices, the potential core is wider, and the induced wall-normal velocity is expected to reach the smallest value at the "fattest" cross section of the potential core (half-way between successive vortices). The images in Figure 5.20 and Figure 5.21 show that the minima in the sinusoidal-like pressure signature at r/D = 0 coincide with the occurrence of the fatter portion of the potential core at stagnation and vice versa. Therefore, it appears that the stagnation point pressure fluctuation simply reflect modulation of the potential core velocity by the jet's vortices leading to larger

stagnation pressure at high induced velocity and vice versa. Because the vortex circulation and size increases with every vortex pairing, the corresponding induced velocity modulation is also expected to increase in strength. Therefore, it is not surprising to see that the stagnation pressure fluctuation are stronger for H/D=4, where the vortices have undergone two pairings before reaching the wall, than for H/D=3, where they have experienced only one pairing event. Because of the same reason, one would expect the stagnation pressure fluctuation to be even smaller for H/D=2, which can be verified by comparing the wall-pressure rms values at r/D=0 for the three different H/D values (see Figure 4.2). However, the relationship between the stagnation pressure fluctuation and the vortices is not as easily detectable for H/D=2 as for the larger H/D cases since the vortices are much small, having not undergone any pairing yet, and visual modulation of the potential-core cross section is not as obvious as for the larger H/D values.

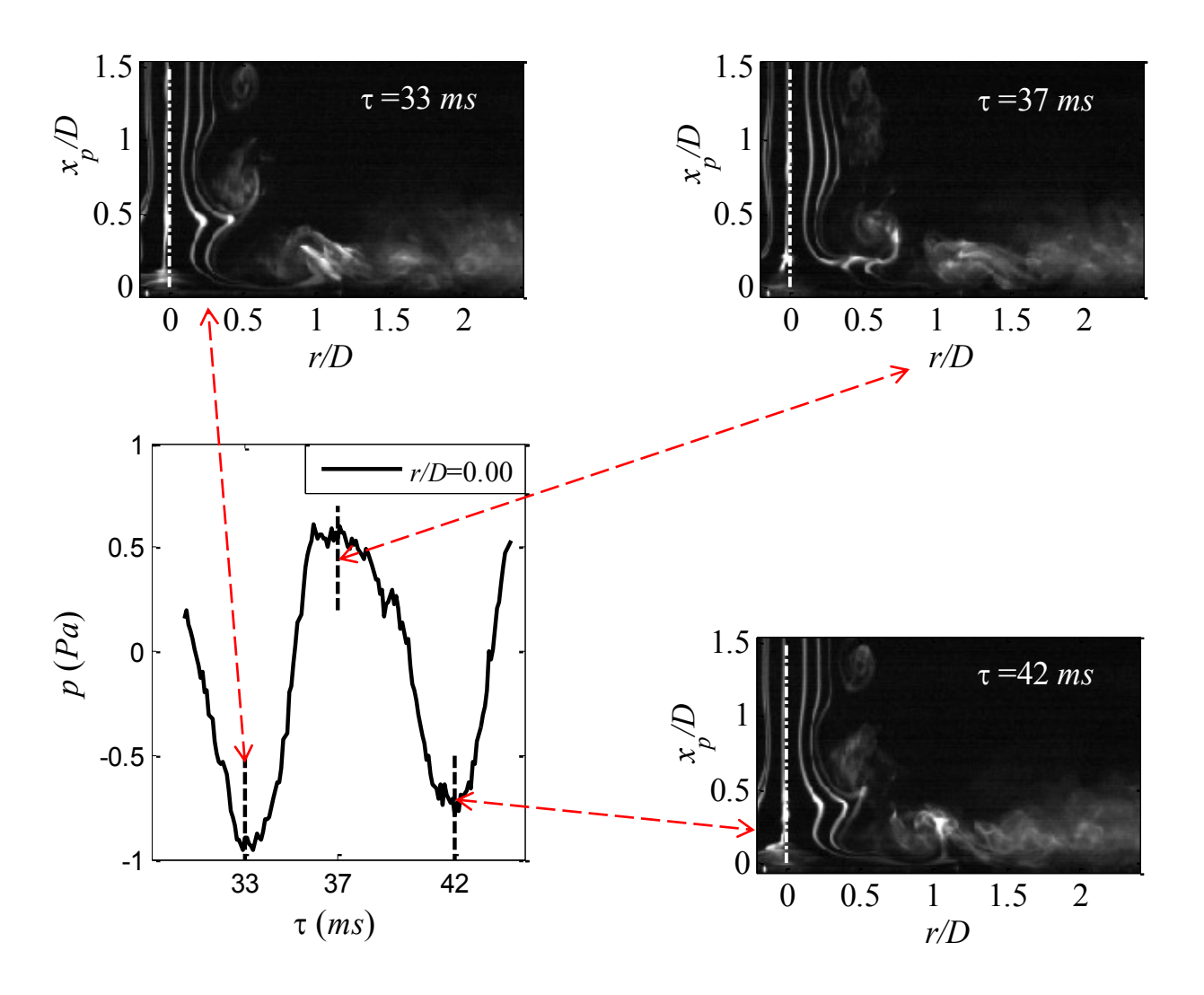


Figure 5.20 Temporal pressure signature at r/D=0, for H/D=3 and normal impingement

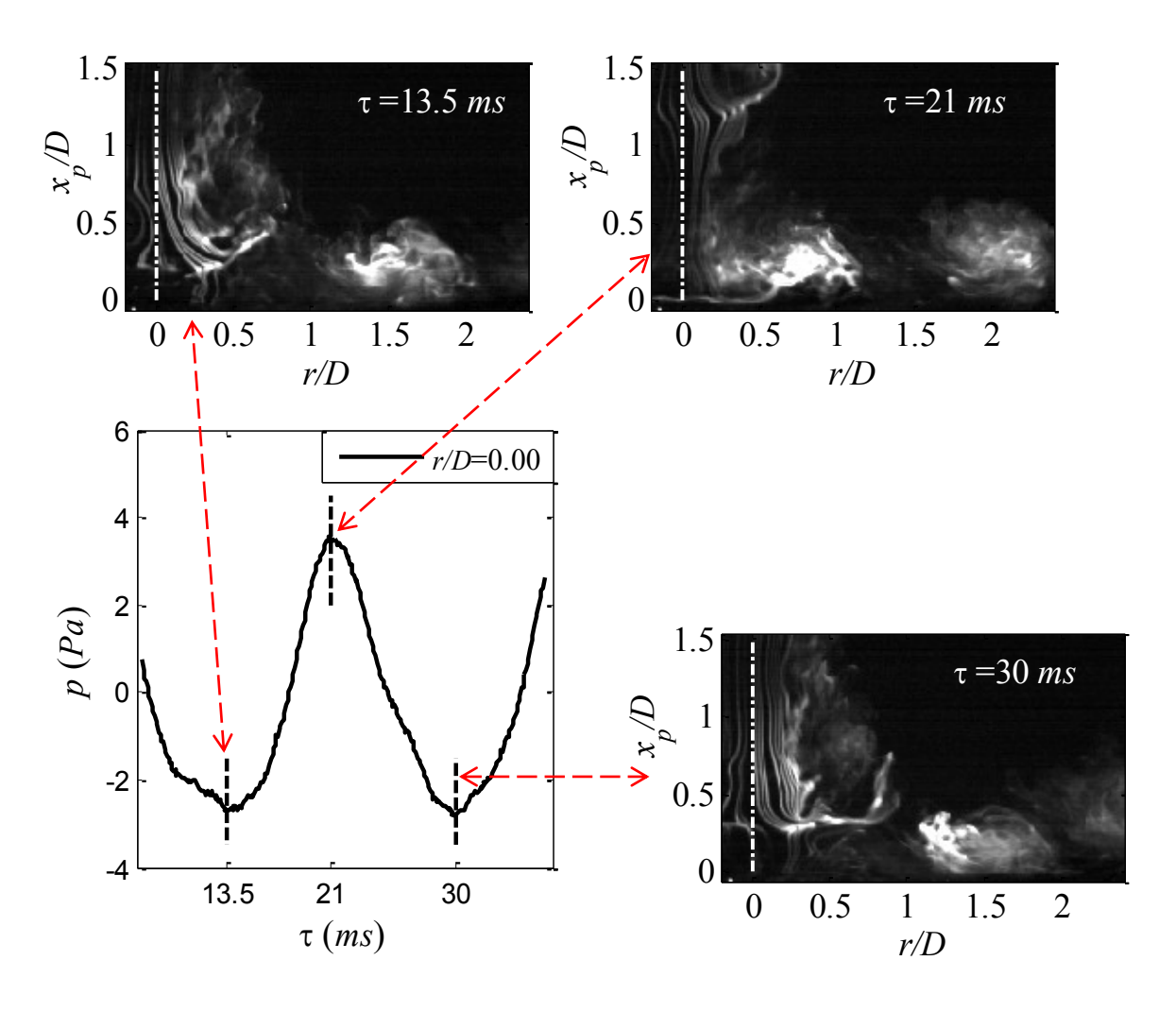


Figure 5.21 Temporal pressure signature at r/D=0, for H/D=4 and normal impingement

5.2 Oblique Impingement Forward Flow

Simultaneous time-resolved flow visualization and unsteady surface pressure measurements are also conducted for oblique impingement with 30 incidence angle. This section focuses on the forward-turning flow side where the plate makes an obtuse angle with the initial jet flow direction (see Figure 2.1 for definition). For H/D = 2, vortices forming as a result of the initial shear layer instability almost always perform their first pairing before or just when they encounter the wall and turn to move parallel to it. Subsequently, these vortical structures either perform a second pairing while traveling past the wall, or convect in the radial direction without interaction, analogous to the mechanisms of vortex merging and vortex passage discussed in the

normal impingement section. The key difference, however, between the normal and oblique cases is that in the former case the first pairing happens within the wall-jet zone (r/D > 1), whereas in the latter case, it takes place upstream of the same zone. Consequently, one can expect that the pressure signature produced by the flow structures on the forward side of oblique impingement will contain a Strouhal number half of what is observed in normal impingement.

Figure 5.22 depicts spatial pressure signature at consecutive time instants for vortex merging in oblique impingement, forward flow side. Each spatial pressure signature is accompanied with the corresponding flow visualization image. The flow visualization image at $\tau = 13$ ms show two vortices approaching the wall (pointed by to two broken white arrows) and two larger vortices above the wall (pointed to by solid white arrows). Each of the larger vortices is formed at an earlier time from the first pairing event of two smaller vortices approaching the wall, similar to those pointed to by the broken arrows. The smaller vortices are seen to wrap around each other until they merge into one larger vortex imposing a local minimum in the surface pressure directly underneath, as shown in the image at $\tau = 21.5$ ms. The two larger vortices imprint negative pressure peaks on the wall, seen at $\tau = 13$ ms, and as they convect in the radial direction, the pressure underneath the trailing vortex, depicted in $\tau = 18.5$ ms, intensifies which could be due to the secondary vortex separation. This high negative peak occurs in the vicinity of r/D=1.3, which is consistent with the rms pressure distribution in Figure 4.3. The generation of the strong negative peak is accompanied by movement of the leading vortex away from the wall and "squeezing" of the trailing one against the wall, as the two vortices interact and merge near r/D=1.5-2 forming an even larger vortical structure. The numerical calculations presented in Chapter 6 depicts more details about the secondary vortex separation and its surface pressure signature which complements the observations at $\tau = 18.5$ ms.

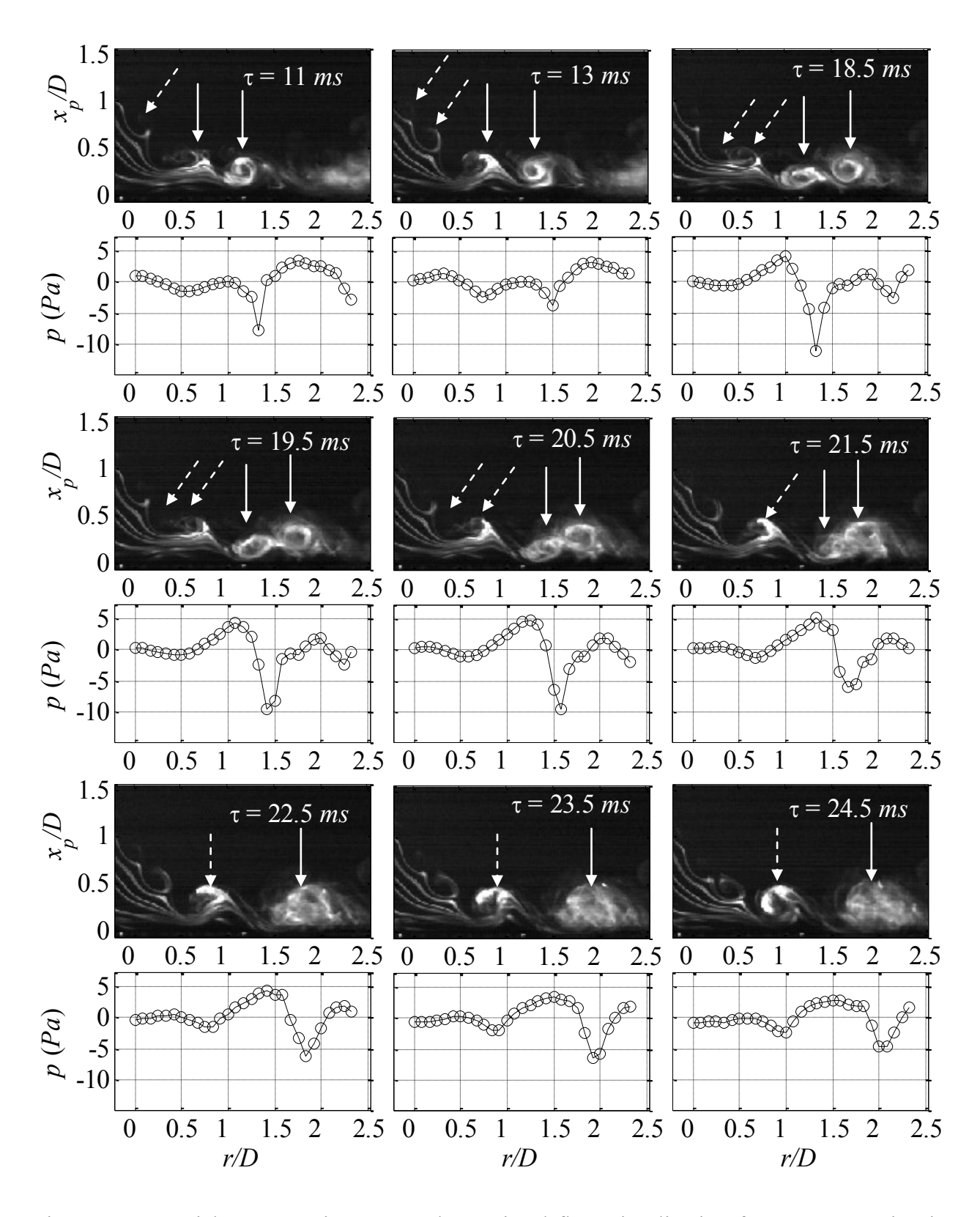


Figure 5.22 Spatial pressure signature and associated flow visualization for vortex merging in oblique impingement (forward flow) at H/D = 2

Figure 5.23 depicts temporal pressure signals associated with vortex merging from the microphones located in the range of r/D=0.33-1.67 for a period of time of 70 ms. The charactristics of the temporal pressure signature shown at r/D=0.67 are very analogous to those observed in normal impingement and related to vortex merging in Figure 5.4. The signature contains two negative peaks per one period cycle (two red arrows point to a cylce as an example); these peaks exist also farther out in the radial direction at later times. For each such pair of peaks, the peak occurring later in time (corresponding to the trailing vortex) becomes stronger while the leading one diminishes with increasing r/D.

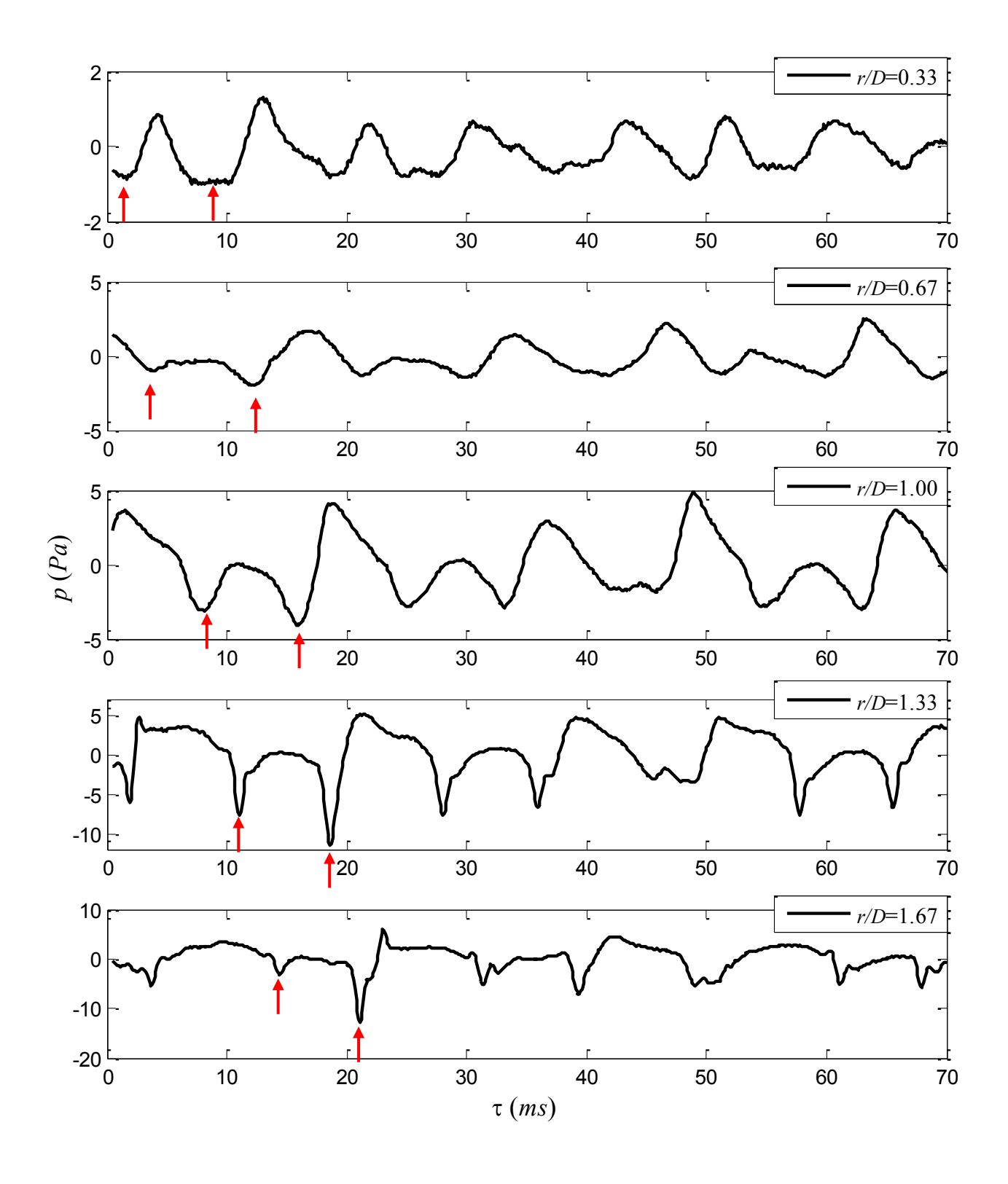


Figure 5.23 Temporal pressure signals at r/D of 0.33 to 1.67 beneath the forward flow in oblique impingement at H/D = 2; (red arrows point to two negative peaks per cycle)

A sample temporal pressure signature at r/D=0.33 during $\tau=13-22$ ms is tracked as it propagates in the radial direction during a vortex merging scenario, as shown in Figure 5.24 through Figure 5.28. The figures are structured similar to Figure 5.5 for the case of normal impingement. Unlike in the normal impingement case, the pressure signal acquired from the microphone at r/D=0.33 is also influenced directly by the vortical structure passage since the stagnation point shifts toward the back flow side in the oblique impingement. The pressure signature at r/D=0.67 is modified from that observed at r/D=0.33, assuming a w-like shape with two local minima corresponding to the passage of two vortical structures (each resulting from the first pairing event upstream of the plate) and local maxima during the time in between. Notably, the local maximum between $\tau = 21$ ms and $\tau = 30$ ms is much lower than the other two local maxima, in fact it maintains a negative pressure value. This is because of the shortening distance between the two vortices which will lead them to merge farther downstream. Such a behavior intorduces another frequency to the pressure signal as will be seen later in the spectral analysis. The signature at r/D=1 preserves the same shape as that seen at r/D=0.67 but it reflects the presence of stronger pressure fluctuations, which could be due to the closer proximity of the vortical structure to the wall at r/D = 1.

Figure 5.27 and Figure 5.28 portray the temporal pressure signature of the same vortical structures tracked in Figure 5.24, Figure 5.25 and Figure 5.26, as they travel past the locations r/D=1.33 and 1.67. The signature at r/D=1.33 demonstrates two strong negative spikes; each corresponds to one of the pair of vortical structures producing the w-like pressure signature at r/D=0.67 and 1.0 in Figure 5.24, Figure 5.25 and Figure 5.26. The earlier spike decpicted in the signature at r/D=1.33 is associated with double peaks when at r/D=1.67 location; this can be related to secondary vortex formation which will be discussed in more details in chapter 6. By τ

= 39.5 ms, the two vortices are interacting with the leading vortex moving away from the wall while orbiting around the trailing one on their way to merge.

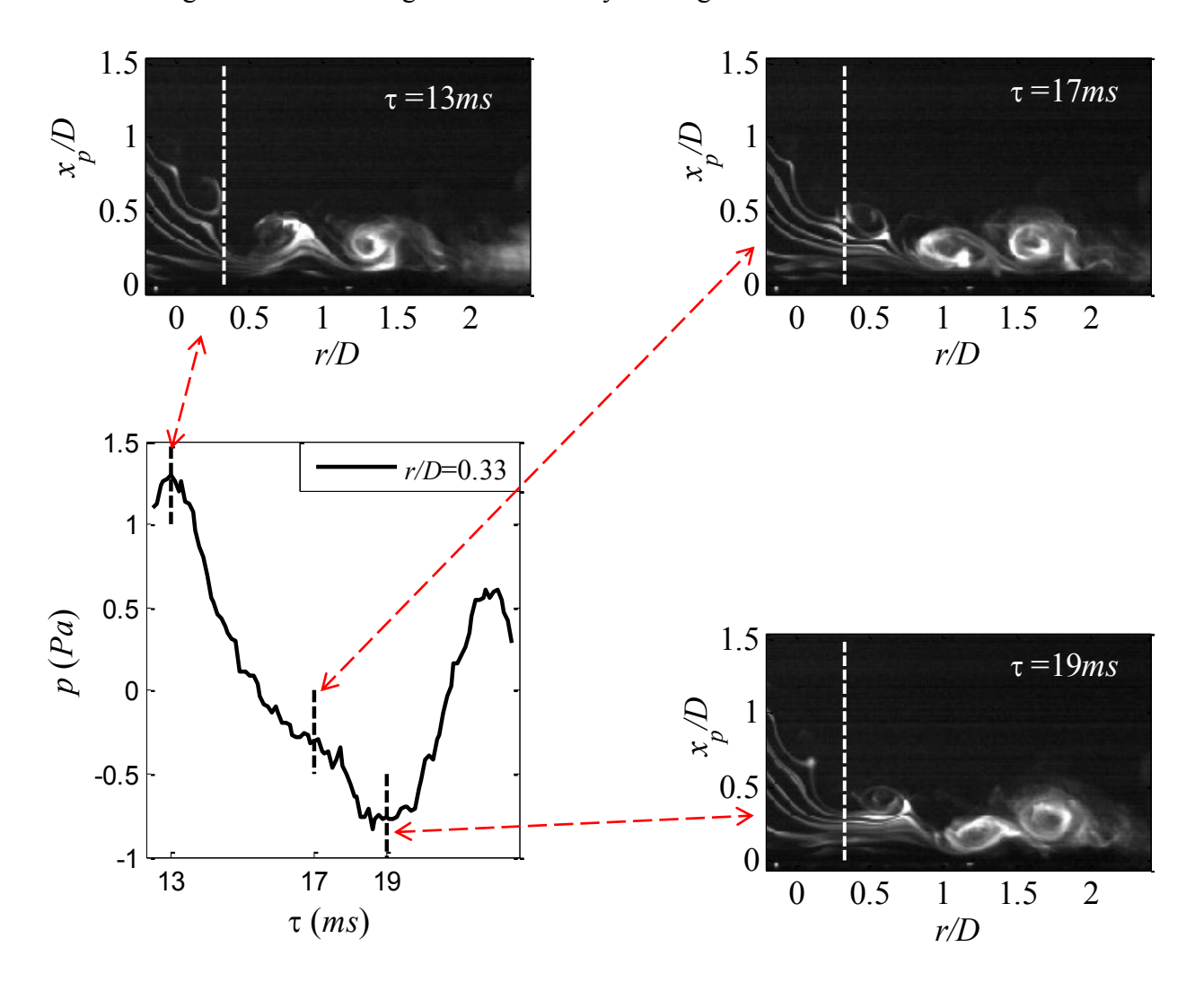


Figure 5.24 Vortex merging temporal pressure signature at r/D of 0.33 beneath the forward flow in oblique impingement at H/D=2

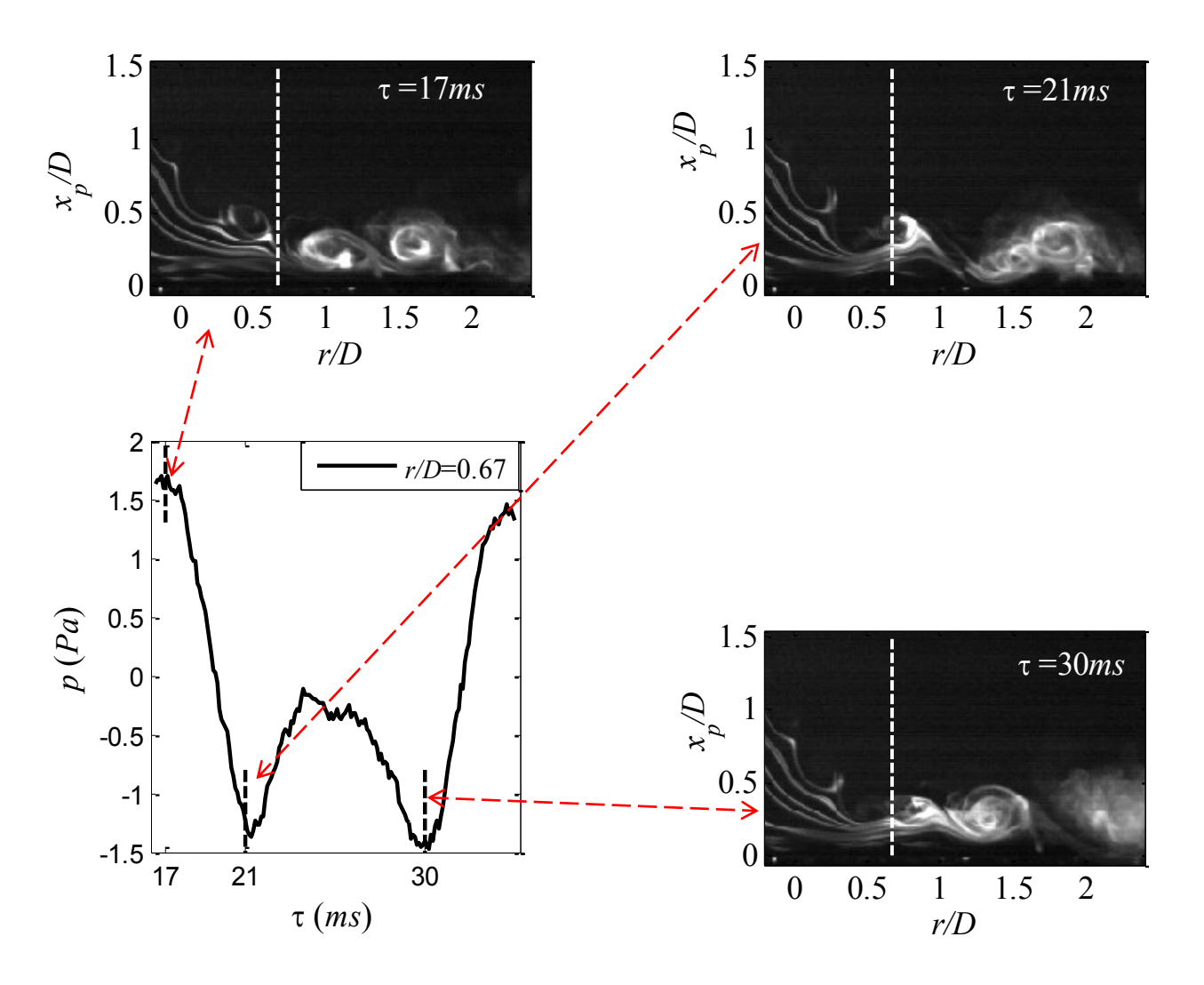


Figure 5.25 Vortex merging temporal pressure signature at r/D of 0.67 beneath the forward flow in oblique impingement at H/D = 2

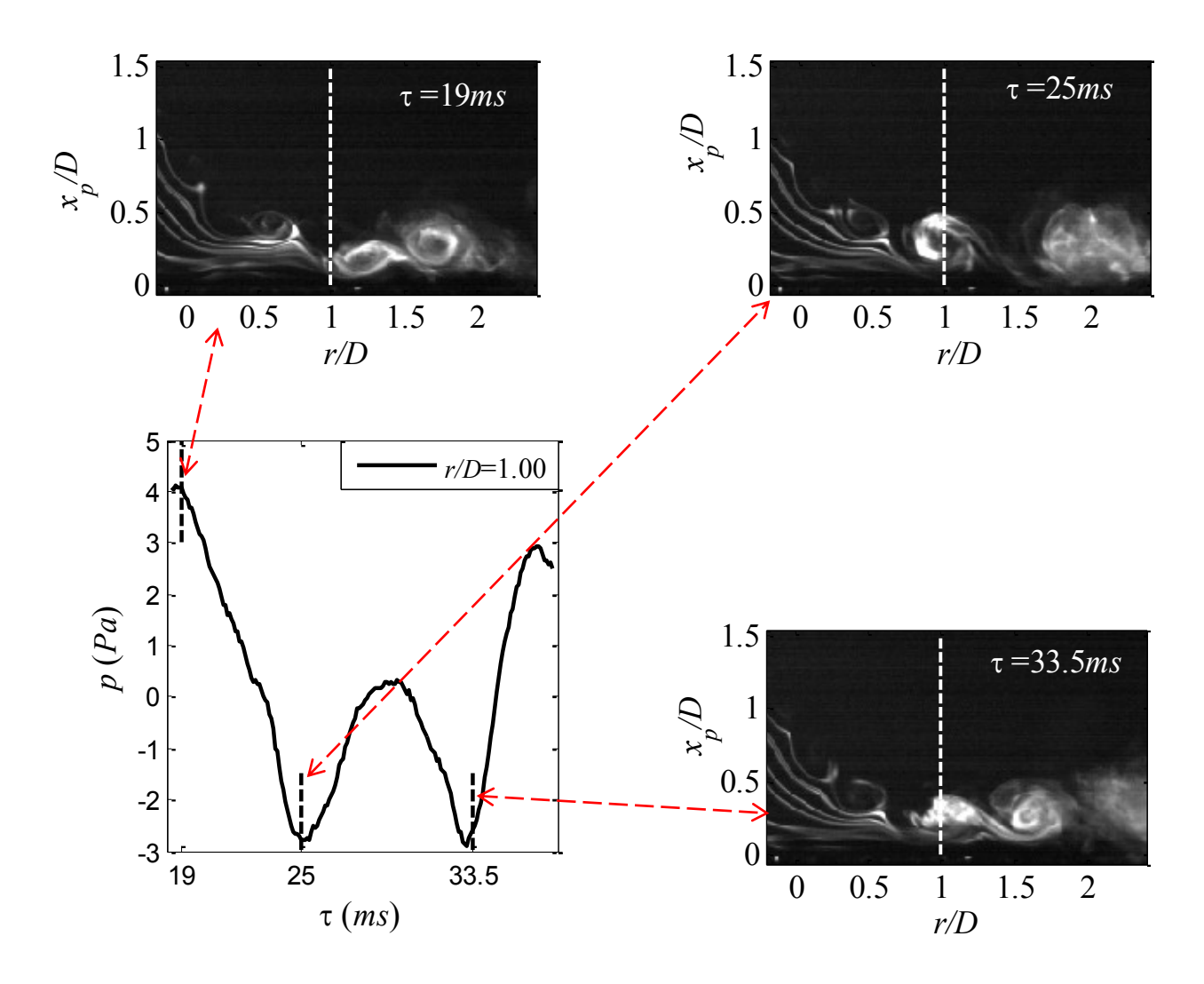


Figure 5.26 Vortex merging temporal pressure signature at r/D of 1 beneath the forward flow in oblique impingement at H/D=2

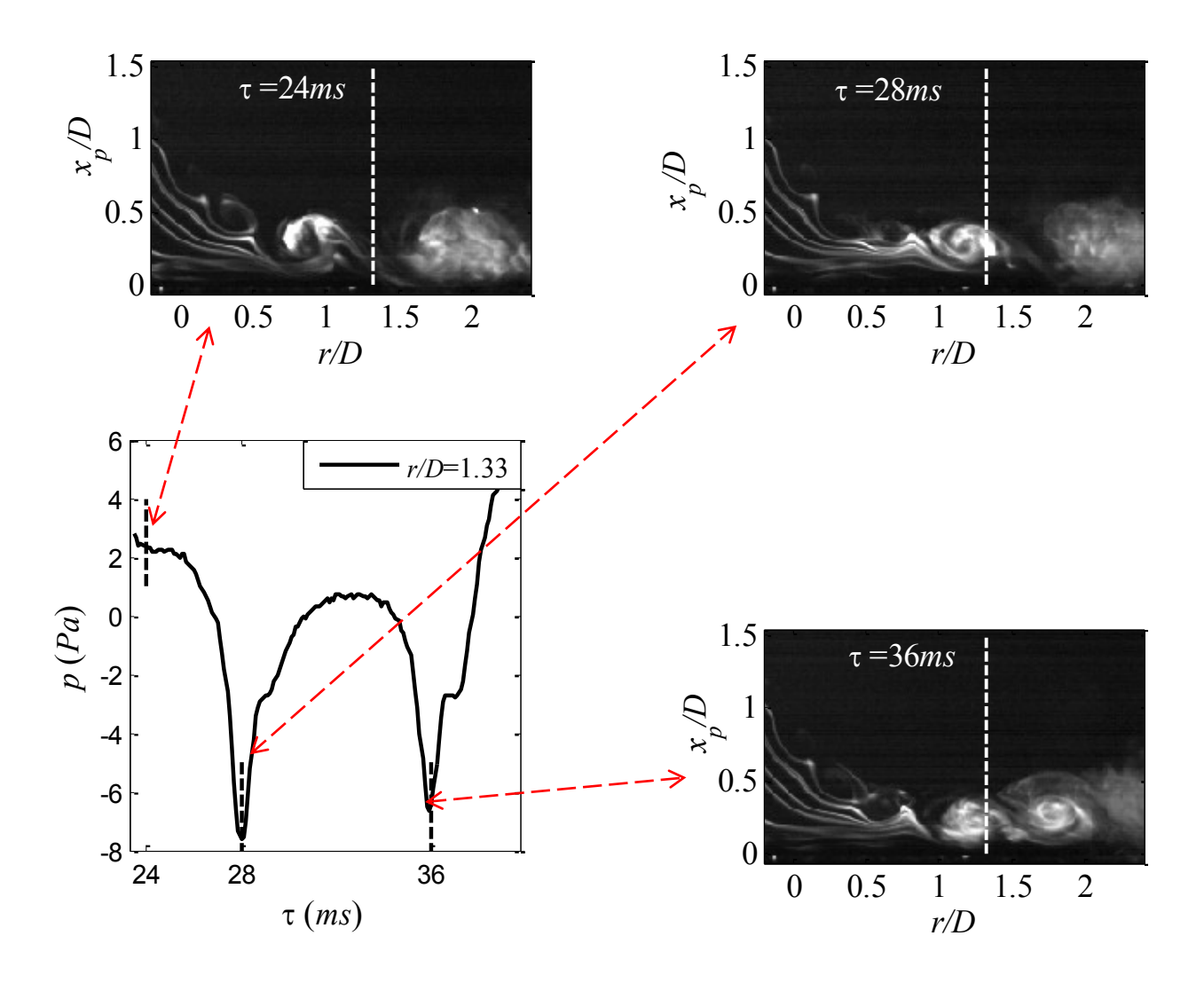


Figure 5.27 Vortex merging temporal pressure signature at r/D of 1.33 beneath the forward flow in oblique impingement at H/D = 2

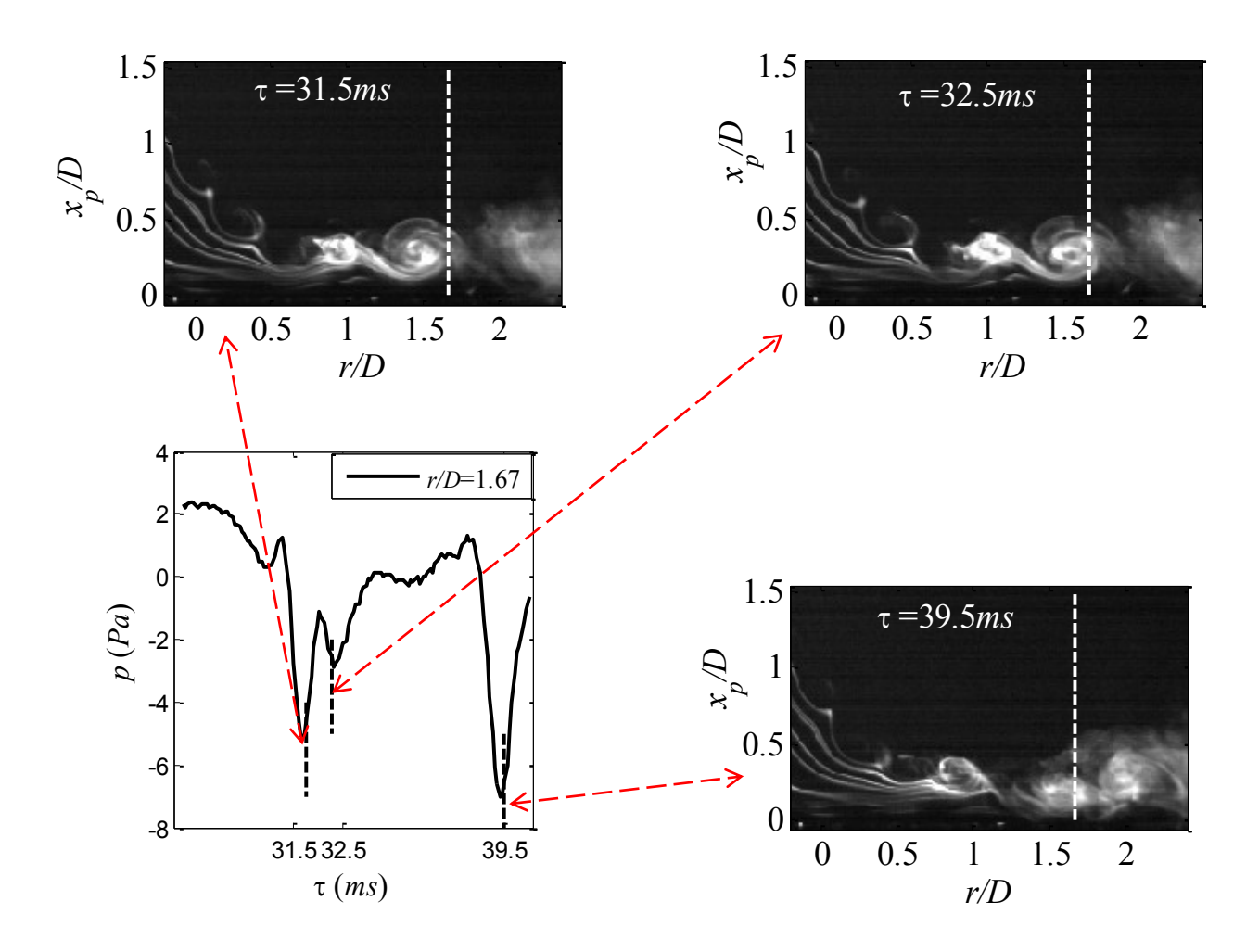


Figure 5.28 Vortex merging temporal pressure signature at r/D of 1 beneath the forward flow in oblique impingement at H/D = 2

The frequency content is examined for the temporal pressure signals depicted in Figure 5.23 which correspond to instances where vortex merging is occurring. Power spectral density results computed from these signals are shown in Figure 5.29 for the signals measured at r/D=0.33-1.67. The figure shows the strongest spectral peak to be at at $St_D\approx0.64$ in the range of r/D=0.33-1.33; this Strouhal number is half the value of the passage frequency of the vortices forming from the initial shear layer instability. This is sensible since vortices already pair once by the time they reach r/D = 0.33. Another peak at $St_D\approx0.32$ grows in the radial direction reaching its maximum amplitude at r/D=1.33. This Strouhal number is related to the second merging which occurs

above the wall. The $St_D\approx0.64$ and 0.32 are analogous to the Strouhal numbers of 1.3 and 0.64 associated with vortex merging in normal impingement and are also half of their values. This is understandable behavior since it is found that an extra pairing process takes place in the oblique impingement case. At r/D=1.67 the Strouhal number of 0.32 maintains its value while the other spectral peaks, which are harmonics of 0.32, become weaker but remain visible.

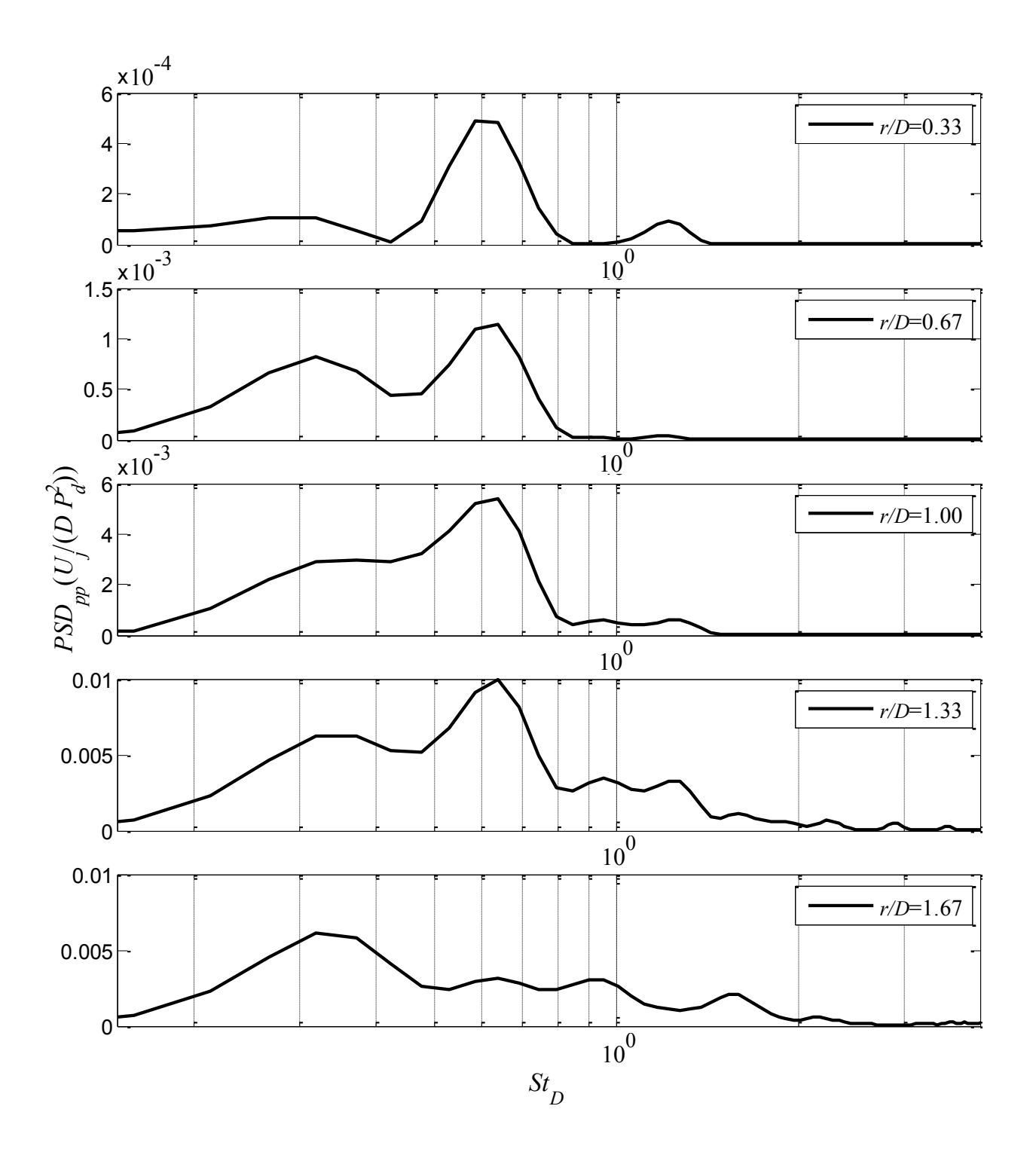


Figure 5.29 Power spectral density for vortex merging at r/D of 0.33-1.67, measured beneath the forward flow in oblique impingement and H/D = 2

There are times in oblique impingement, forward-flow side, when vortices perform the first pairing as they encounter the wall but then convect parallel to in the radial direction without executing a second pairing as they travel past the wall. This is the same as the vortex-passage scenario found in normal impingement. One would expect that the dominant Strouhal number in such a case to be half of the initial shear layer instability frequency since only one pairing occurred before encountering the wall.

Figure 5.30 portrays spatial pressure signatures and associated flow visualization images at consecutive time instants for vortex passage in oblique impingement, forward flow side. The time reference above each image has no relation to the time given in the vortex merging case discussed earlier in connection with Figure 5.22. The image at $\tau = 13$ ms shows two vortices moving toward the wall (pointed to by broken arrows), and three larger vortical structures (pointed to by solid arrows) convecting in the radial direction. The smaller vortices shown in the image at $\tau = 13$ ms start to interact with each other while imprinting a broad negative pressure peak on the wall, as shown in the image at $\tau = 17$ ms. These vortices complete their merging by the time they reach the vicinity of r/D=0.5-1 at $\tau=21$ ms. On the other hand, the larger vortical structures, formed by pairing of the smaller vortices at earlier time, impose negative pressure peaks on the wall. These peaks travel in the outward radial direction and change their magnitude as the corresponding vortical structures move parallel to the wall with no mutual interaction. The peak related to the trailing larger vortical structure, in the image at $\tau = 17$ ms, gets its most strength around r/D=1.33 location which is consistent with the peak location in the rms pressure distribution in Figure 4.3. The same vortical structure is near r/D=1.5 at $\tau=21$ ms, and it induces separation and secondary vortex formation in the same vicinity.

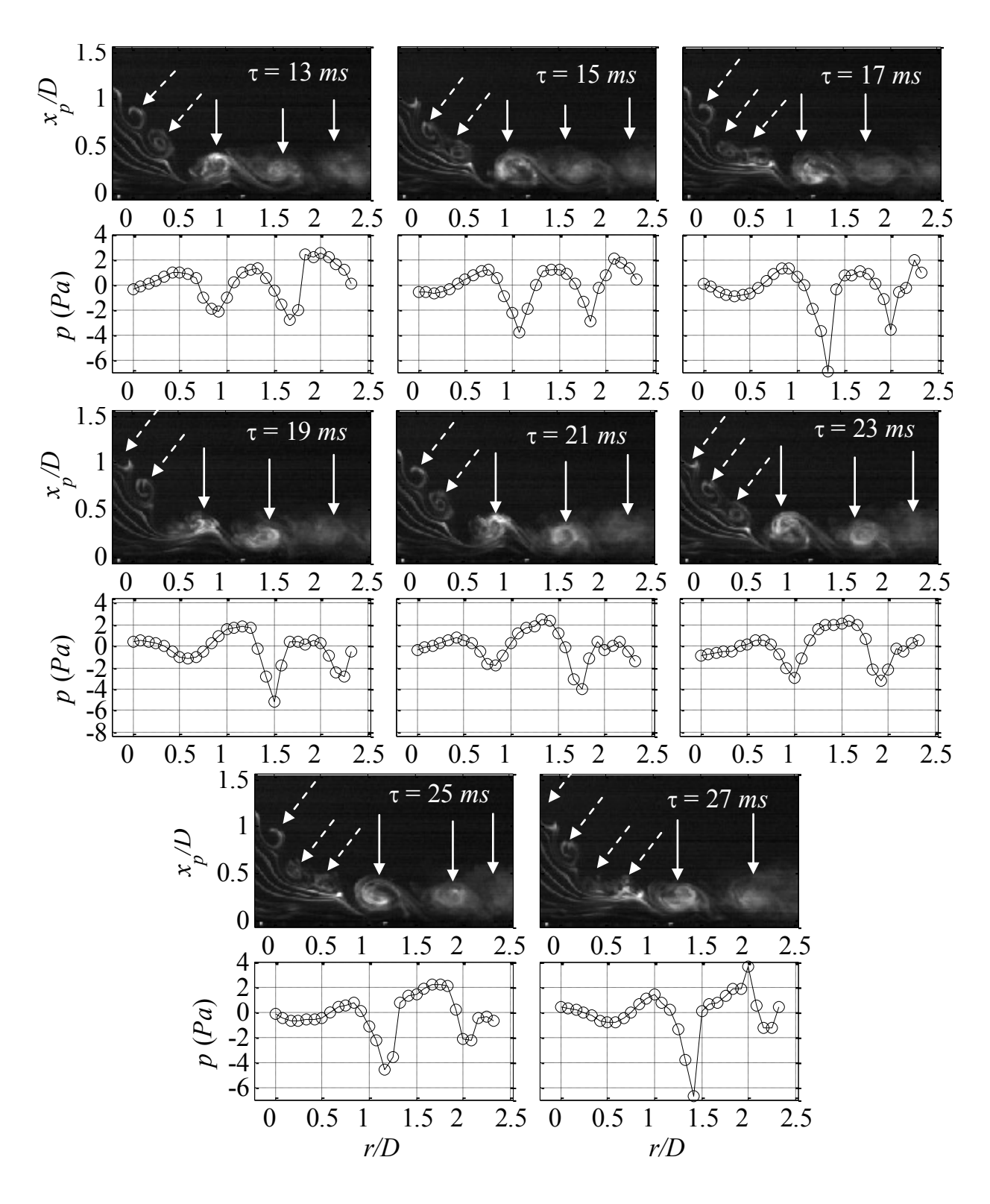


Figure 5.30 Spatial pressure signature and associated flow visualization for vortex passage in oblique impingement, forward flow, at H/D = 2

Figure 5.31 depicts the temporal pressure signals associated with the vortex passage mechanism, discussed in Figure 5.30, obtained from the microphones located in the range of r/D=0.33-1.67 over a period of 30 ms. The signals in the range of r/D=0.33-1 are nearly sinusoidal with the local minima corresponding to the vortical structures (an example is pointed with red arrow) as they pass over these locations (this will be confirmed from Figure 5.32 through Figure 5.36). When the vortical structures are in the vicinity of the radial locations r/D=1.33-1.67 the pressure signal becomes pulsatile with stronger negative peaks. The time delay between the negative peaks does not change significantly, supporting the observation from flow visualization that the spacing between the vortical structures fairly invariant throughout the radial domain considered, and consequently no second pairing takes place.

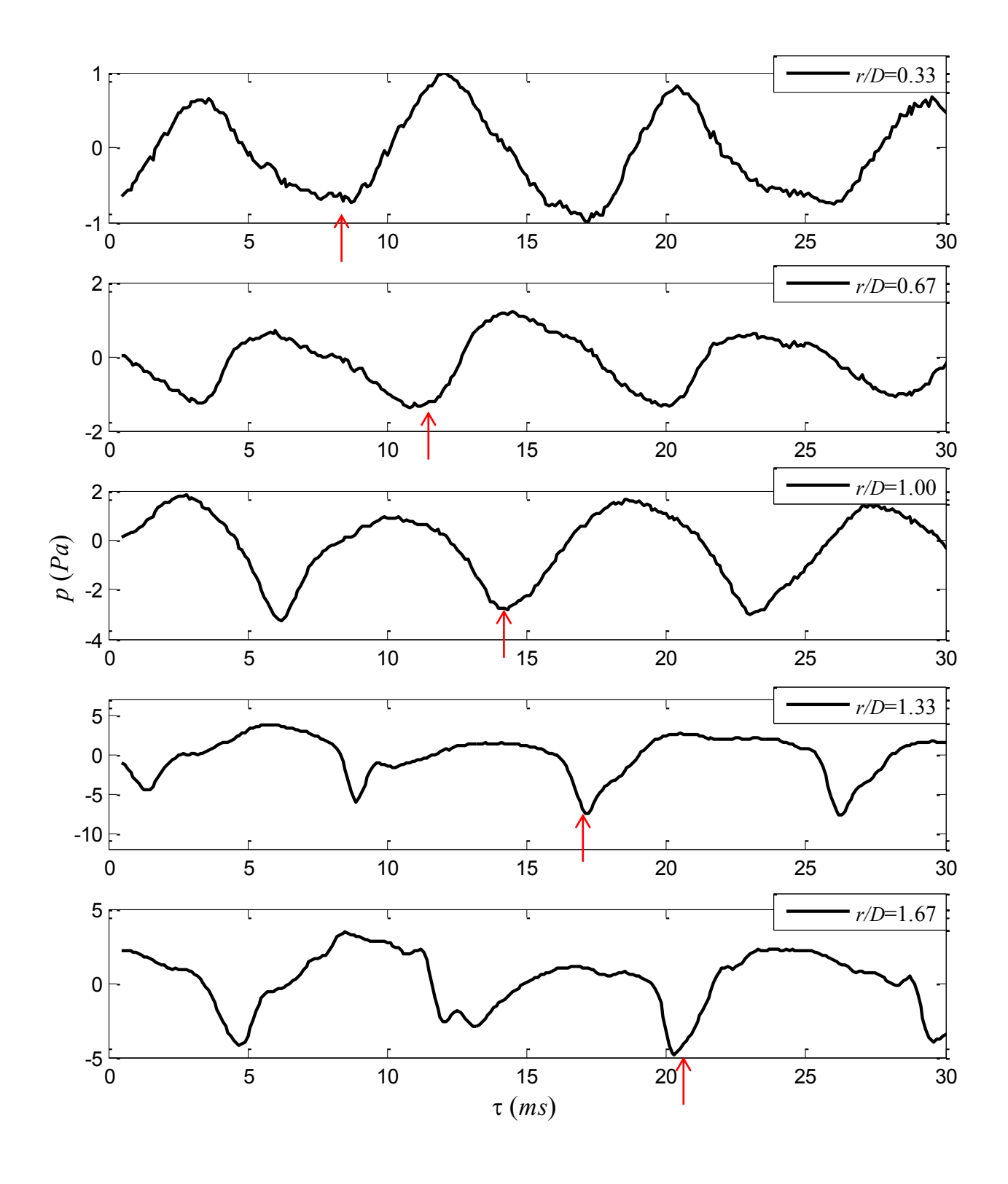


Figure 5.31 Temporal pressure signals at r/D of 0.33 to 1.67 beneath the forward flow in oblique impingement at H/D = 2

Figure 5.32 through Figure 5.36 demonstrate samples of temporal pressure signatures at selected radial locations associated with vortex passage. The signatures in these figures are accompanied with their corresponding flow visualization images to characterize the important flow features. The sinusoidal signature at r/D=0.33 (Figure 5.32) is produced by the vortices approaching the wall. Even though the first pairing is not complete at this stage, the spacing between the vortices involved in pairing is close enough so that they act like one larger vortex imposing a single negative pressure peak. The vortices complete the first pairing in the vicinity of r/D=0.6-1 where the pressure signature preserves its sinusoidal shape while gaining more strength. The larger vortical structure, after the first pairing, starts to impose negative pressure "pulses" which are strongest at r/D=1.33. From the flow visualization images, it is clear that the larger vortical structures maintain their radial separation in comparison to the ones observed in the vortex merging mechanism. This distance obviously prevents the larger vortical structures from performing a second merging; this is can also be inferred from the longer time delay between the negative peaks at r/D=1.33 and 1.67 in comparison to vortical merging case. The vortical structure, shown in the image at $\tau = 29.5$ ms in Figure 5.36 at r/D = 1.67 location, induces a secondary vortex formation which imposes a strong negative pressure peak whereas the primary one seems to have insignificant effect at this stage. This pressure signature, which corresponds to secondary vortex formation, is consistent with the results in chapter 6 obtained from the numerical calculations.

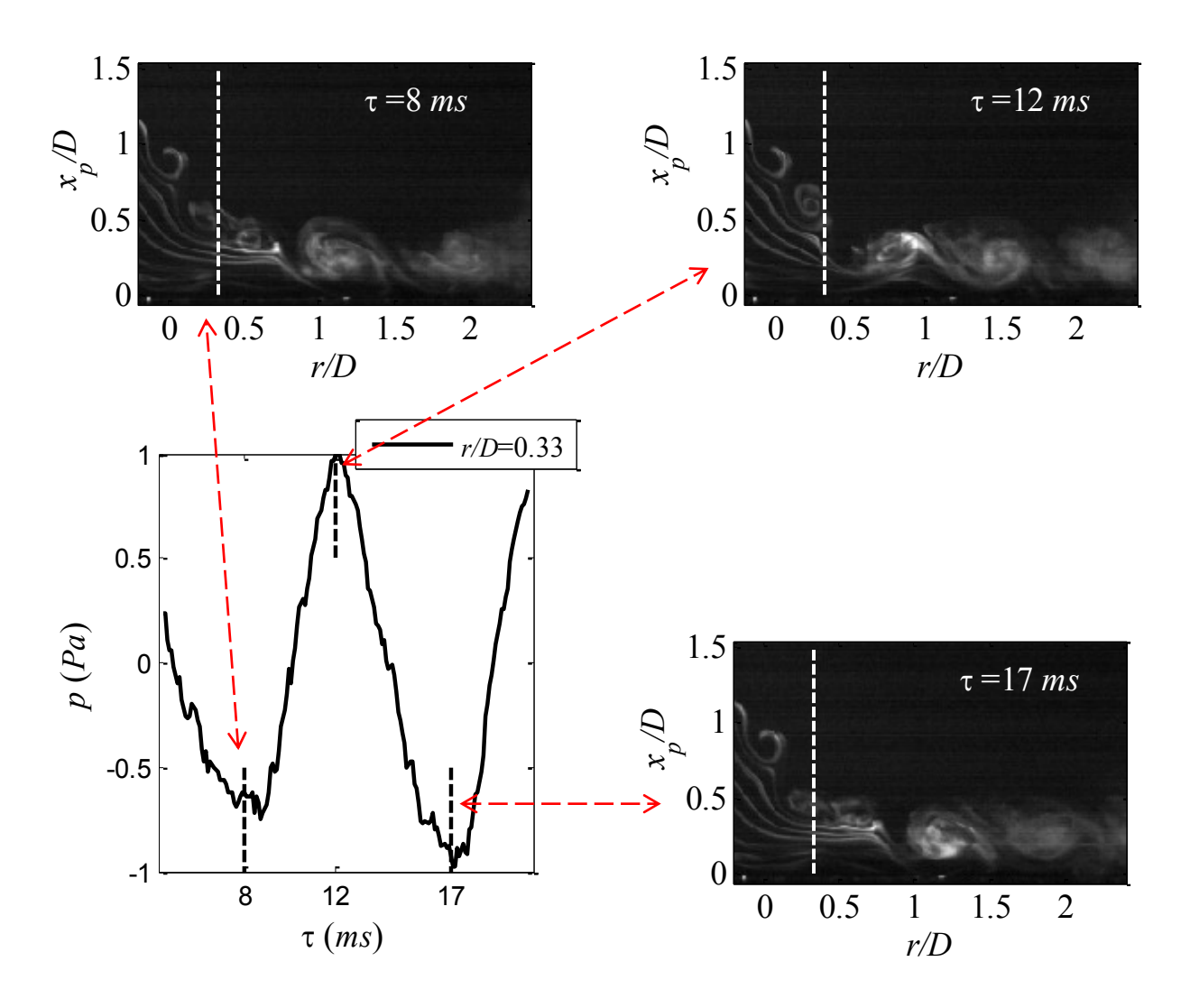


Figure 5.32 Vortex passage temporal pressure signature at r/D of 0.33 beneath the forward flow in oblique impingement at H/D = 2

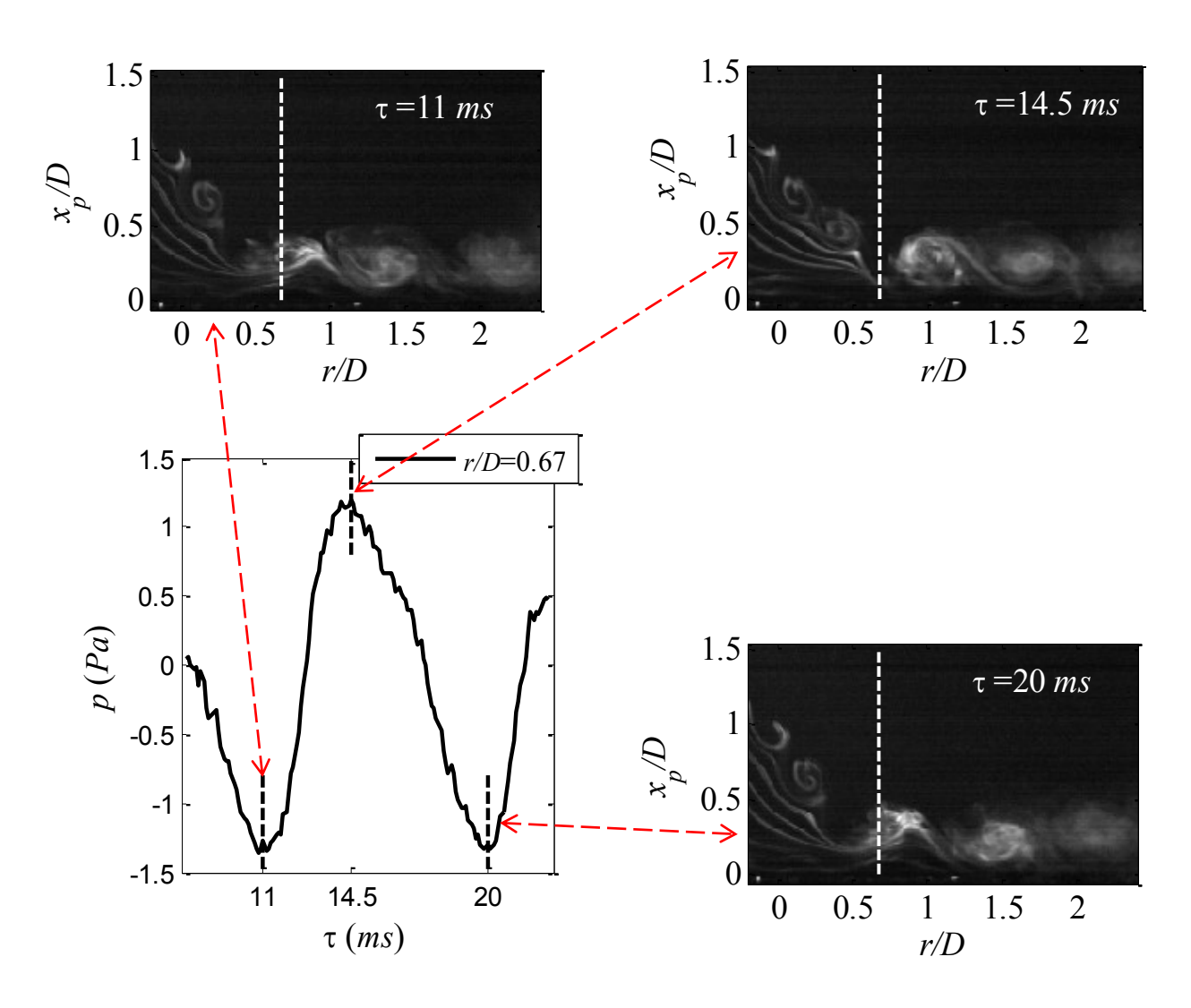


Figure 5.33 Vortex passage temporal pressure signature at r/D of 0.67 beneath the forward flow in oblique impingement at H/D = 2

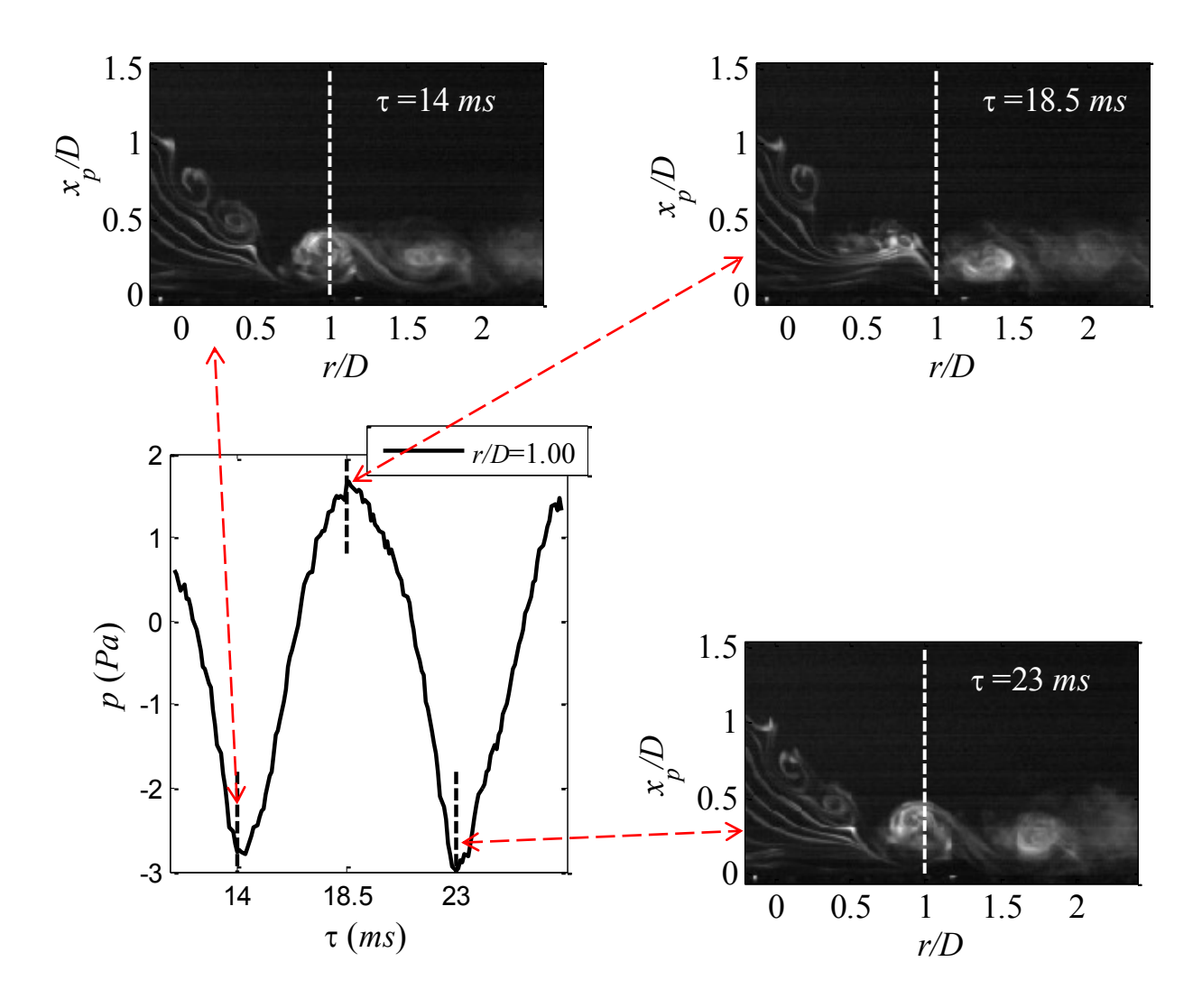


Figure 5.34 Vortex passage temporal pressure signature at r/D of 1 beneath the forward flow in oblique impingement at H/D=2

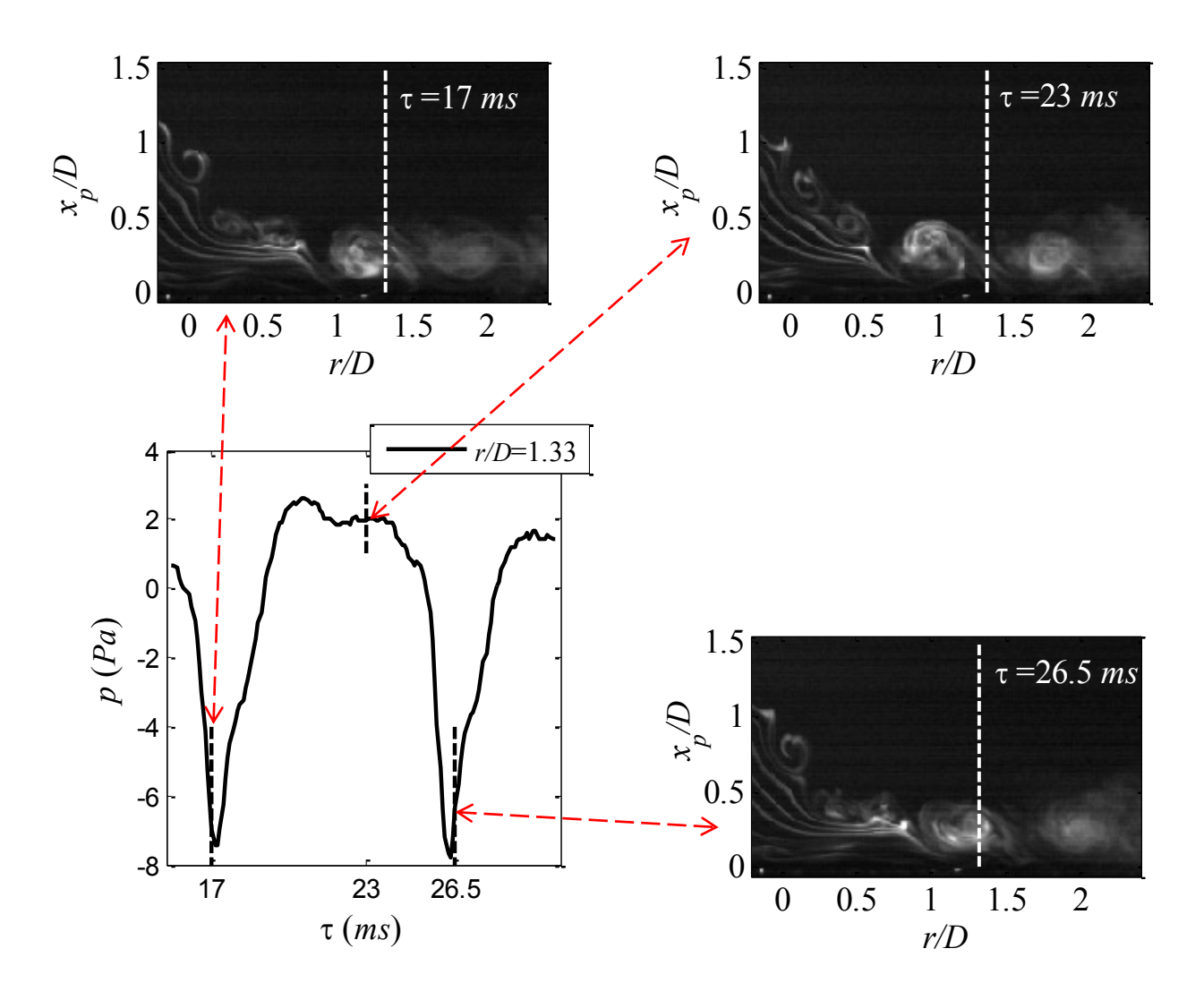


Figure 5.35 Vortex passage temporal pressure signature at r/D of 1.33 beneath the forward flow in oblique impingement at H/D = 2

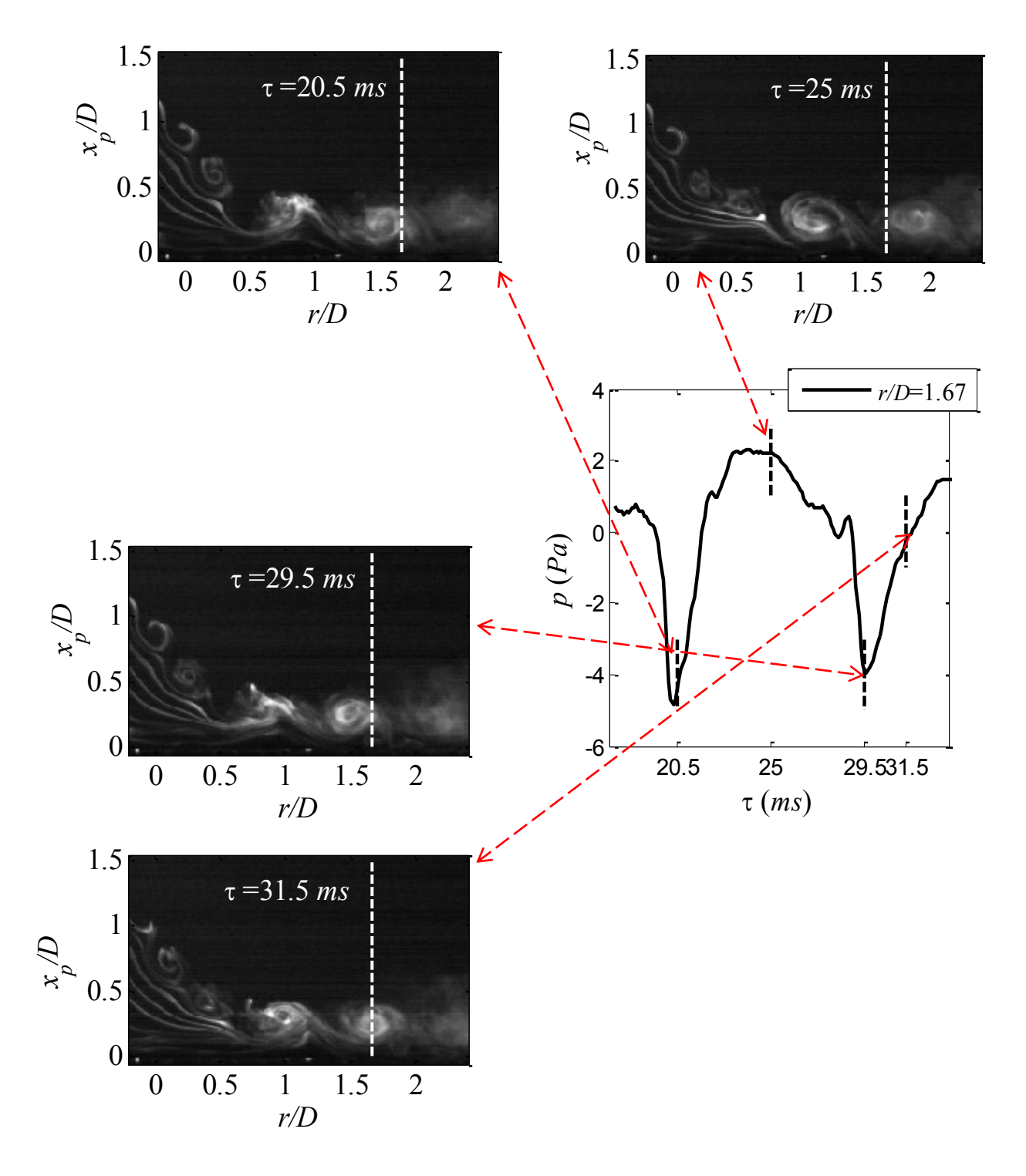


Figure 5.36 Vortex passage temporal pressure signature at r/D of 1.67 beneath the forward flow in oblique impingement at H/D = 2

Figure 5.37 demonstrates power spectral density for the pressure signals shown in Figure 5.31 in the case of vortex passage. A distinct peak at Strouhal number of 0.64 is apparent at all radial

locations with the exception of r/D=1.67 where there is some shift to a higher Strouhal number of 0.69. The dominant peak at 0.64 represents the Strouhal number at which the larger vortices pass above the wall. The Strouhal number of 0.64 is half of the value at which vortices initially form from the shear layer roll-up.

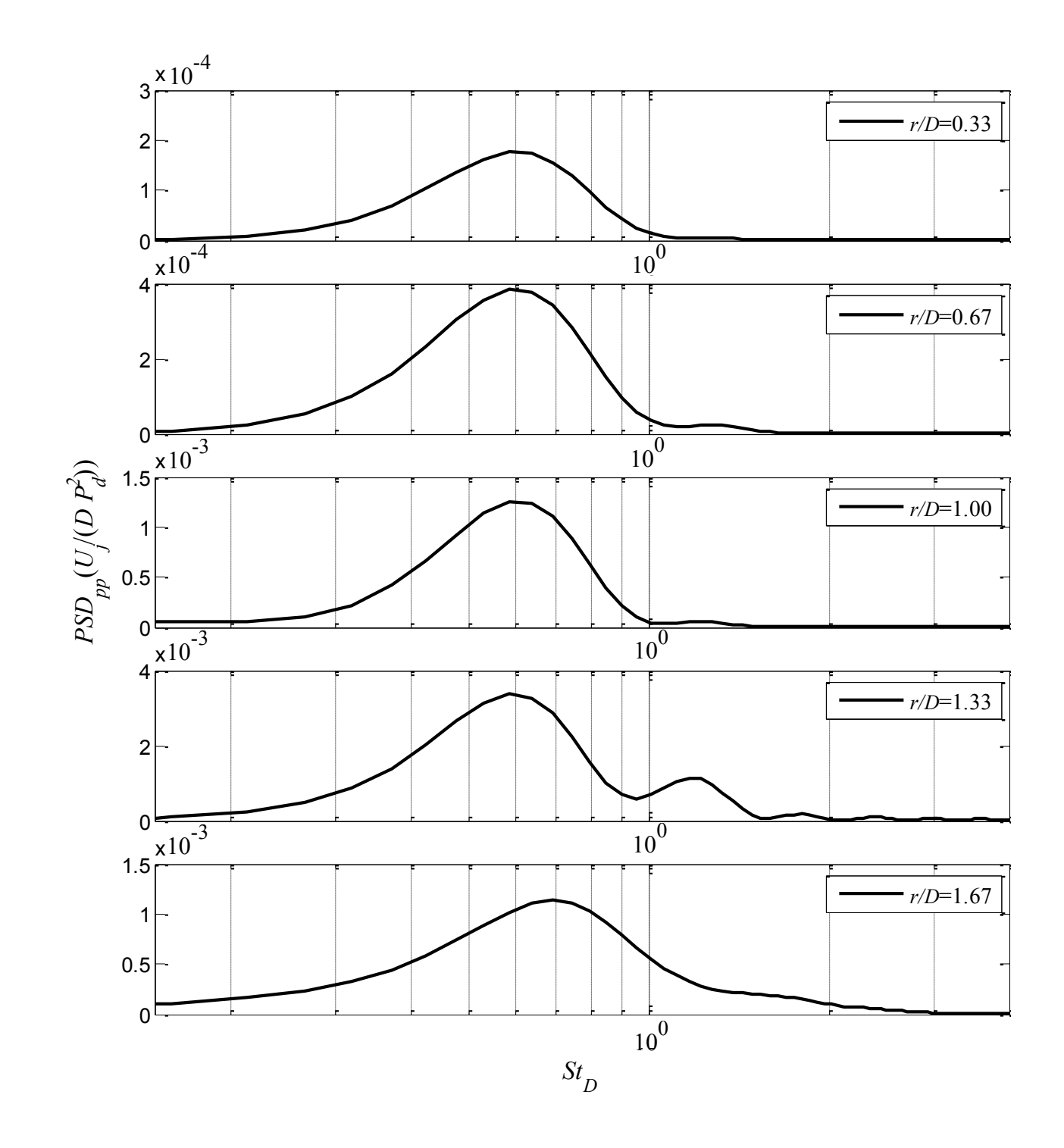


Figure 5.37 Power spectrum density for vortex passage at *r/D* of 0.33-1.67

To summarize the observations concerning the oblique impingement case (forward flow side) at H/D=2, the vortices, which form downstream of the jet at Strouhal number of approximately

1.3, perform the first pairing before or just when they encounter the wall which drops the Strouhal number to 0.64. After the first merging, the flow structures change travel direction to be parallel to wall and they will either maintain their radial spacing, and $St_D\approx0.64$, or perform another merging above the wall which drops the Strouhal number further to be 0.32.

When the impingement plate is placed at H/D=3 for the jet in oblique impingement, the flow structures on the forward flow side depict similar behavior of vortex passage and vortex merging as well as similar spatial and temporal characteristics of the pressure signatures as in the case of H/D=2. At H/D=4 the flow structures also show merging of three vortices and four vortices before reaching the wall, as observed in the normal impingement at H/D=4.

5.3 Oblique impingement back flow

This section focuses on the back-side flow in the oblique impingement case where the wall makes an acute angle with initial jet direction. The radial array of eight microphones is placed at $\theta = 180^{\circ}$ to coincide with the back-flow side where the microphones are located in the range of r/D from 0 to 2.33.

Figure 5.38 depicts spatial pressure signatures at consecutive times for oblique impingement, back-flow side, accompanied with their corresponding flow visualization images at H/D=2. In this case, pressure data are interpolated, as described previously, only in the radial range of $1 \le r/D \le 2.33$, where the flow structures turn to convect parallel to the plate. The images in this figure portray the stagnation point shift towards the back-flow side to be in the vicinity of r/D=0.5, which means that pressure data at r/D of 0 and 0.33 in fact represent the forward flow side.

Inspection of Figure 5.38 shows that vortices, which form downstream of the jet from the shear layer roll up, become closest to the wall near r/D=1. This is commensurate with the

presence of the rms pressure peak at r/D=1 in Figure 4.3. The vortices imprint prominent negative pressure peaks at the same radial location where they are present and as they convect, they are identifiable in the images up to r/D of 1.67. In general, vortices on this flow side persist for longer times without any sign of merging, before they loose their coherence/dissipate, in comparison to their counterparts on the forward-flow side. Moreover, the size of the vortices in this side of the vortex rings is smaller which is consistent with Lim [14] who studied the interaction of an isolated vortex ring with an inclined solid boundary.

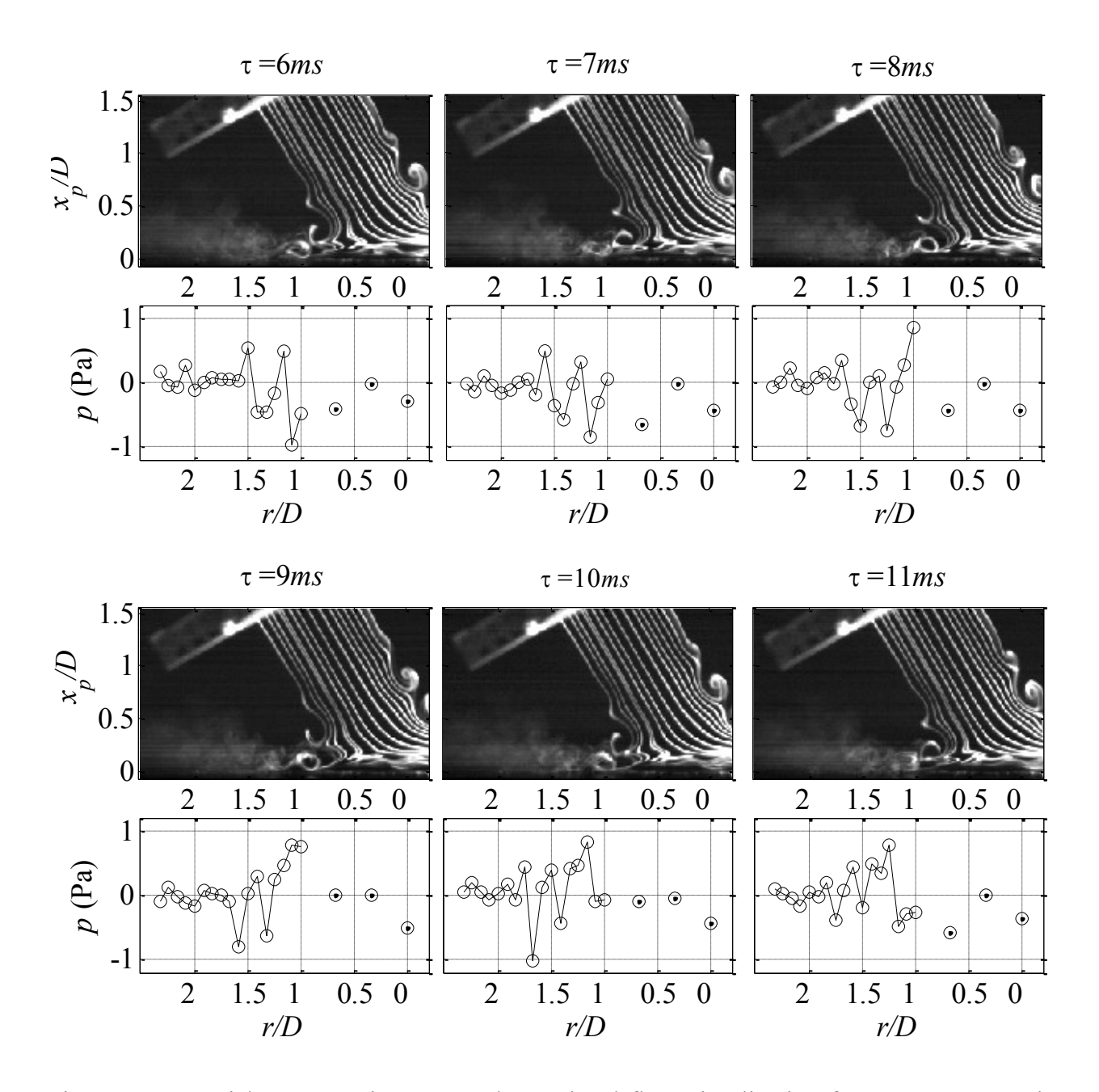


Figure 5.38 Spatial pressure signature and associated flow visualization for vortex passage in oblique impingement, back flow, at H/D = 2

The temporal pressure signals in oblique impingement, back-flow side, are examined in Figure 5.39 in the radial range of 1 to 2 for a period of 30 ms. The signals at r/D of 1 and 1.33 show repetitive organized patterns where the negative peaks corresponding to the passage of the vortices as will be seen clearly in Figure 5.40. On average, the negative peaks are found to be the

strongest and most persistent at r/D=1 while they exhibit more variability at r/D=1.33. The signal at r/D=1.67 is less organized and is weaker while at r/D=2 it is almost flat. This suggests that the vortices' life time as they travel past the plate spans the radial range r/D=1 to 1.33: a substantially shorter life time than in normal impingement and the forward flow side.

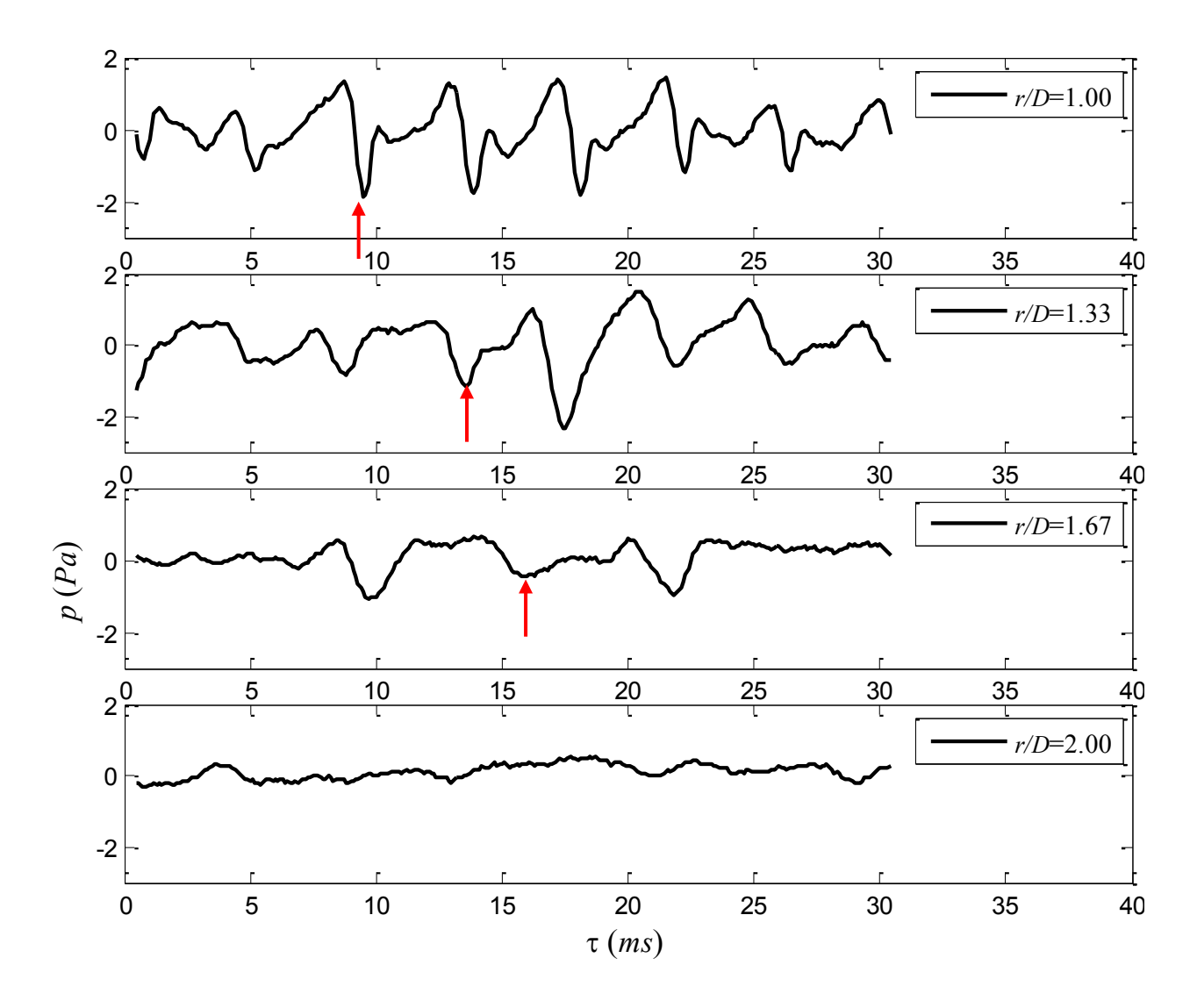


Figure 5.39 Temporal pressure signals at r/D of 1 to 2 beneath the back flow in oblique impingement at H/D=2

A sample temporal pressure signature, corresponding to passage of a vortex at r/D=1, for the time window between 8-13 ms is shown in Figure 5.40. The figure is accompanied with four

flow visualization images recorded at different time instants during the occurrence of the signature. The first image at $\tau = 8.5$ ms is when there is no vortical structure above the location r/D = 1; the signal shows a positive peak at this time. When a vortex structure reaches this location, at $\tau = 9.5$ ms, the signature exhibits a strong negative peak. This confirms that each negative peak in the temporal signal shown in Figure 5.39 at this radial location corresponds to the passage of a vortical structure.

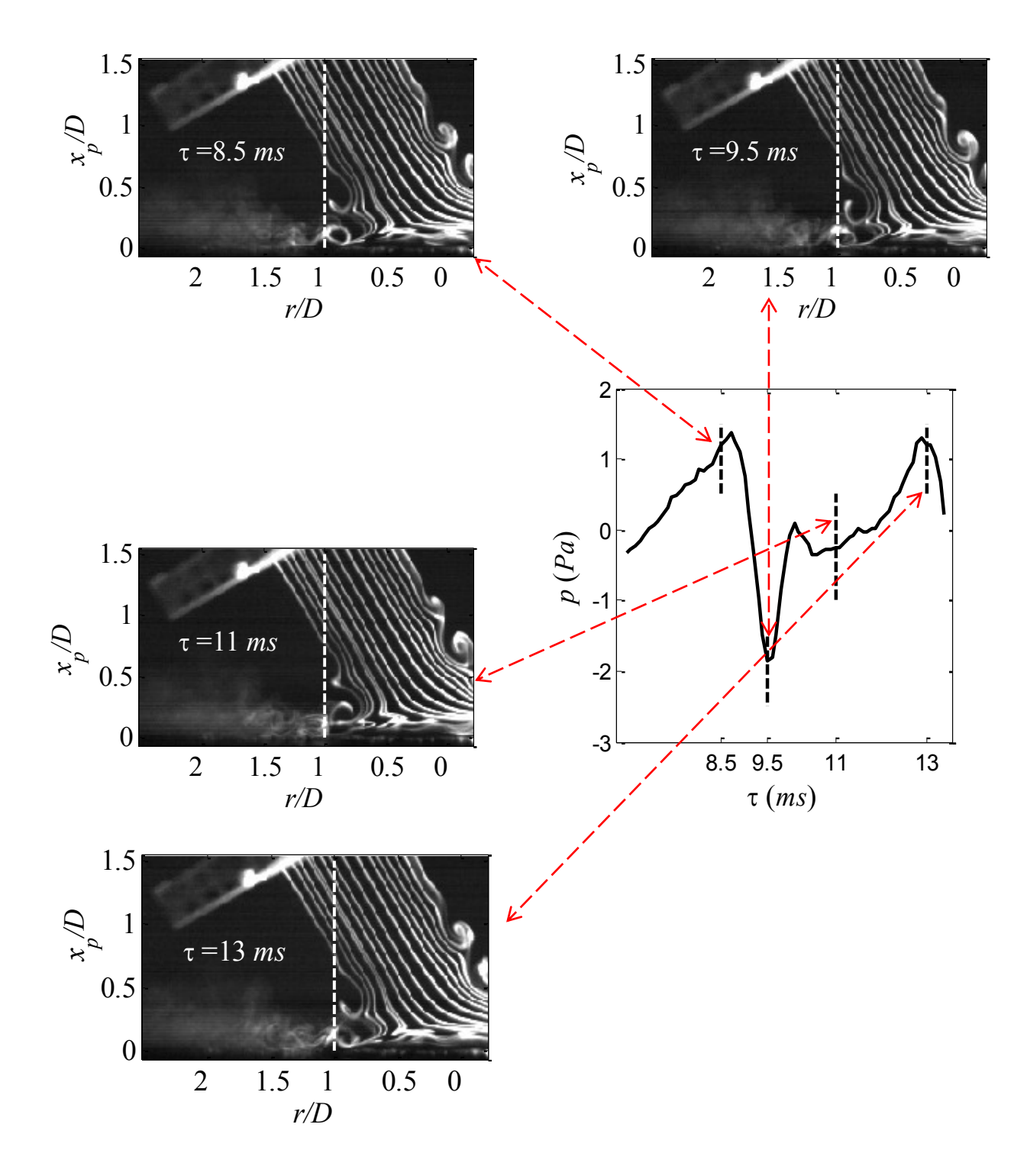


Figure 5.40 Vortex passage temporal pressure signature at r/D=1 in oblique impingement, backflow side and H/D=2

Figure 5.41 depicts power spectral density computed for the pressure signal at r/D=1, shown in Figure 5.39. The spectrum demonstrates a strong peak at Strouhal number of 1.3. This peak is 149

the same as the one associated with the initial shear layer instability since the vortices from and subsequently interact with wall at the same rate. This Strouhal number is also seen in the average power spectral density depicted in Figure 4.7. The peaks at the higher Strouhal numbers in Figure 5.41 are harmonics of 1.3.

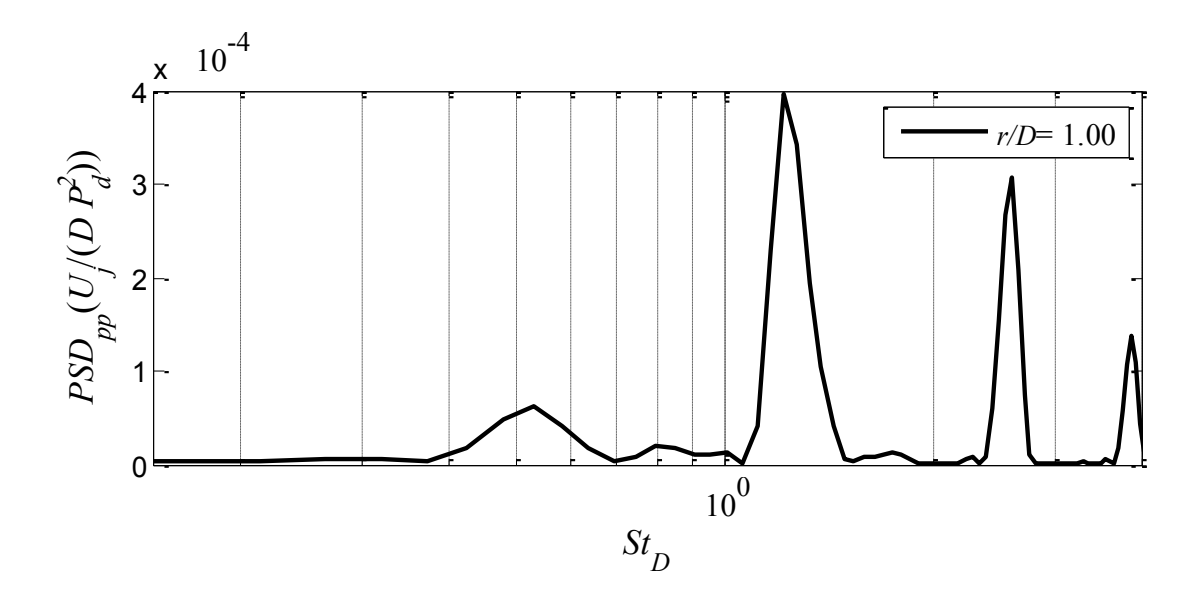


Figure 5.41 Power spectrum density for vortex passage at r/D of 1 in oblique impingement, back-flow side and H/D = 2

Secondary vortex formation is also observed in oblique impingement, back-flow side, at H/D=2. Figure 5.42 depicts flow visualization images tracking a vortex, pointed to by an arrow, as it "impinges" on the wall and forms a secondary vortex ($\tau=30$ ms). The primary and secondary vortices then eject away from the wall and diffuse near r/D=1.5 (shown in the image at $\tau=33$ ms). The size of the secondary vortex is relatively small and the whole process of the vortex impinging on the wall, forming secondary vortex and then ejecting away from the wall takes place in the radial range of 1 < r/D < 1.3, within which there is no microphone located to help characterize the pressure associated with this phenomenon. However, one can hypothesize that

the secondary vortex formation and its ejection away from the wall along with the primary one leads to the break up and hence decay in the strength of the pressure signature.

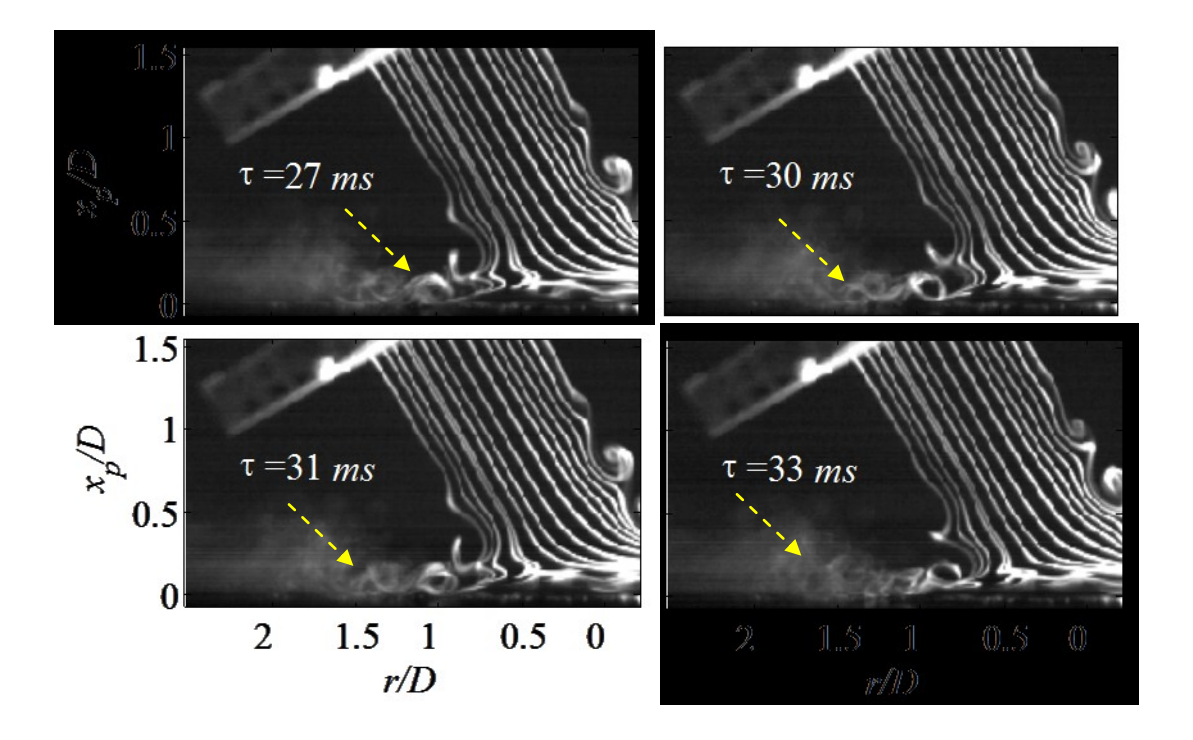


Figure 5.42 Flow visualization images showing secondary vortex formation on the back-flow side of oblique impingement at H/D=2

When the separation between the jet and impingement plate is increased to H/D=3, vortices have enough distance to sometimes merge before they impinge on the wall. Figure 5.43 depicts flow visualization images of this scenario as well as of the scenario when the vortices do not merge before reaching the wall. Figure 5.43a shows three vortices, pointed to by arrows, that reach the wall and then change direction to convect parallel to the wall with no sign of merging. On the other hand, while Figure 5.43b portrays two vortices, pointed to by arrows, that interact and merge as they reach the wall. The presence of the merging and passage mechanisms clarify the presence of two peaks at $St_D \approx 0.64$ and 1.3 in the power spectral density in Figure 4.7. For

oblique impingement, back-flow side, at H/D=4, flow structures still perform merging similar to those seen in the normal impingement of three or four vortices merging before they reach the impingement plate. Hence, Strouhal numbers similar to those found in normal impingement are expected in this case. This is consistent with $St_D \approx 0.32$ and 0.53 found in the corresponding power spectral density in Figure 4.7.

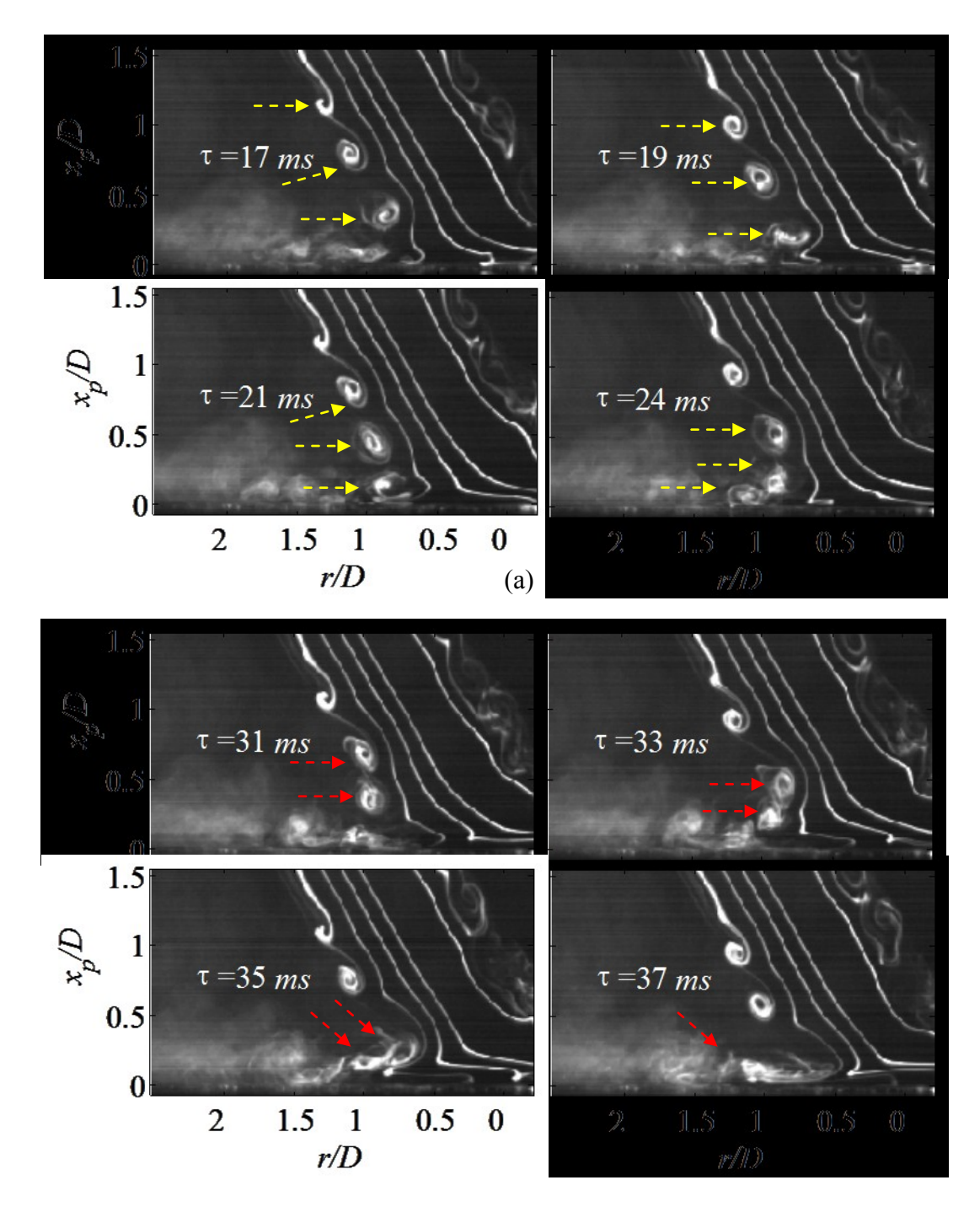


Figure 5.43 Flow visualization images showing (a) vortex passage and (b) vortex merging in oblique impingement back flow side at H/D=3

Chapter 6: Wall-Pressure Generation From

Axisymmetric Vortex Rings Interacting With a Wall

This chapter is focused on developing deeper understanding of the mechanisms of wallpressure gneration in the wall-jet region of the axisymmetric jet in normal impingement. As found in Chapter 5, within this region the jet vortices may simply convect without interacting with one another or they may mutually interact via pairing. In the former case, the wall-pressure signature has a simple convecting sinusoidal wave form along the radial direction with the sinusoid's valleys lying immediately underneath the vortices and the peaks being in between successive vortices. The wall-pressure generation mechanisms in this case are easy to understand via inspection of the right hand side of Poisson's equation (see equation 1.2) where the high vorticity regions at the vortex cores are responsible for generation of the valleys in the sinusoid and the high strain-rate regions inbetween the vortices result in the sinusoid peaks. On the other hand, when vortex pairing occurs near the wall, the pressure signature is more complex and evolves more dynamically in the radial direction. Therefore, there is a need to better understand the wall-pressure generating sources in this case. In addition, a persistent flow feature that is seen in both the vortex passage and vortex merging cases is the formation of secondary vortices as a result of boundary layer separation produced by the interaction of the jet (primary) vortices with the wall. Understanding the details of the wall-pressure generation and the relative role of the primary and secondary vortices in this case is also important.

To explore the nature of the wall-pressure generating sources associated with secondary vortex formation and vortex pairing near a wall, two *model* problems are studied

computationally. The first problem involves the impingement of an axisymmetric vortex ring on a flat wall, and the second one considers two such rings interacting with the wall. The attractiveness of these problems stems from the fact that they exhibit the same behvior of secondary vortex formation and primary vortices pairing as seen in the impinging jet problem, while being much simpler and therfore suited for studying the fundamental physics of pressure generation associated with these flow features. In addition, given the axisymmetric geometry of these problems, they are relatively simple to compute. The use of computations in this case, rather than experiments, also has the advantage of providing results with high spatial and temporal resolution to capture physical details that can not be observed using the flow viualization and the relatively coarse microphones inter-spacing grid.

The induced boundary layer separation near the wall and the secondary vortex formation phenomena, which are also observed in this study, were investigated by Didden and Ho [5] in normal impinging jets, and were studied in details for the case of an isolated vortex interacting with the wall by Gendrich *et al.* [23] and Naguib and Koochesfahani [22], among others. Didden and Ho [5] employed hot-wire anemometry and wall-pressure measurements in a harmonically excited jet. There analysis was based on conditional averages and they did not study the physics of the pressure generating sources (i.e. the right hand side of equation 1.2), which is facilitated in the present work from the space-time information available from the computation. Gendrich *et al.* [23] did not consider the wall pressure, while Naguib and Koochesfahani [22] did identify a characteristic pressure signature associated with the boundary layer separation and secondary vortex formation. In addition, Naguib and Koochesfahani examined the nature of the generating wall-pressure sources. However, Naguib and Koochesfahani employed experimental data which may not have had sufficient spatial resolution in the separating boundary layer to capture the

source terms with sufficient accuracy. In addition, Naguib and Koochesfahani's analysis of the wall-pressure generating sources was not as detailed as done in the present study, *and* they did not consider the case involving the interaction of *two* vortex rings with the wall.

6.1 Experimental Observations

Prior to considering the details of the computational effort, sample experimental observations of the fundamental flow features to be examined are first discussed.

6.1.1 Secondary Vortex Formation

Secondary vortex formation is apparent in Figure 6.1, which depicts an example of this phenomenon that for H/D=3 and normal impingement. The white arrow in the visualization images points to a jet vortex ring at different locations as it convects above the wall in the domain of, approximately, 0.7 < r/D < 1.3 for a period of time of 6 ms. The vortex shown in the image at τ =82.5 ms is a product of two vortices that previously merged downstream of the jet exit before encountering the wall. The concurrent pressure signature, displayed beneath the same image, shows a distinct negative pressure peak underneath this vortex that moves together with the corresponding vortex farther out along the radial direction at later times. The negative pressure peak that is correlated with the vortex demonstrates some important change when at τ = 85.5 and 86.5 ms. Specifically, the peak does not lie directly beneath the vortex anymore. Instead, the peak shifts in the downstream direction (this phenomenon will be termed Negative Peak Downstream Shift, or NPDS), while a much weaker local minimum is now seen directly beneath the vortex. This indicates some dynamic changes in the flow. Examining the flow visualization images at the same time instants, one notices the generation of a small circular streakline pattern located very close to the wall, downstream of the primary vortex. Even though

it is not possible from the static images depicted in Figure 6.1 to conjecture the rotation direction of the small circular streak pattern and the primary vortex, in the time-resolved videos it is clear that the primary vortex and the small circular pattern rotate in directions opposite to each other, suggesting that the latter represents secondary vortex formation from separation of the boundary layer. The strong negative pressure peak lies directly under the secondary vortex, which suggests that NPDS is the result of secondary vortex formation. Because NPDS is also found to be associated with weakening of the negative pressure signature of the primary vortex, it appears that the secondary vortex formation is also responsible for this weakening. The mechanisms leading to these phenomena will be clarified from the computational analysis. Finally, at τ =87.5 and 88.5 ms, the secondary vortex is more pronounced in the flow visualization images and the corresponding pressure signature has a single local minimum peak under the secondary vortex, with no local peak found beneath the primary vortex.

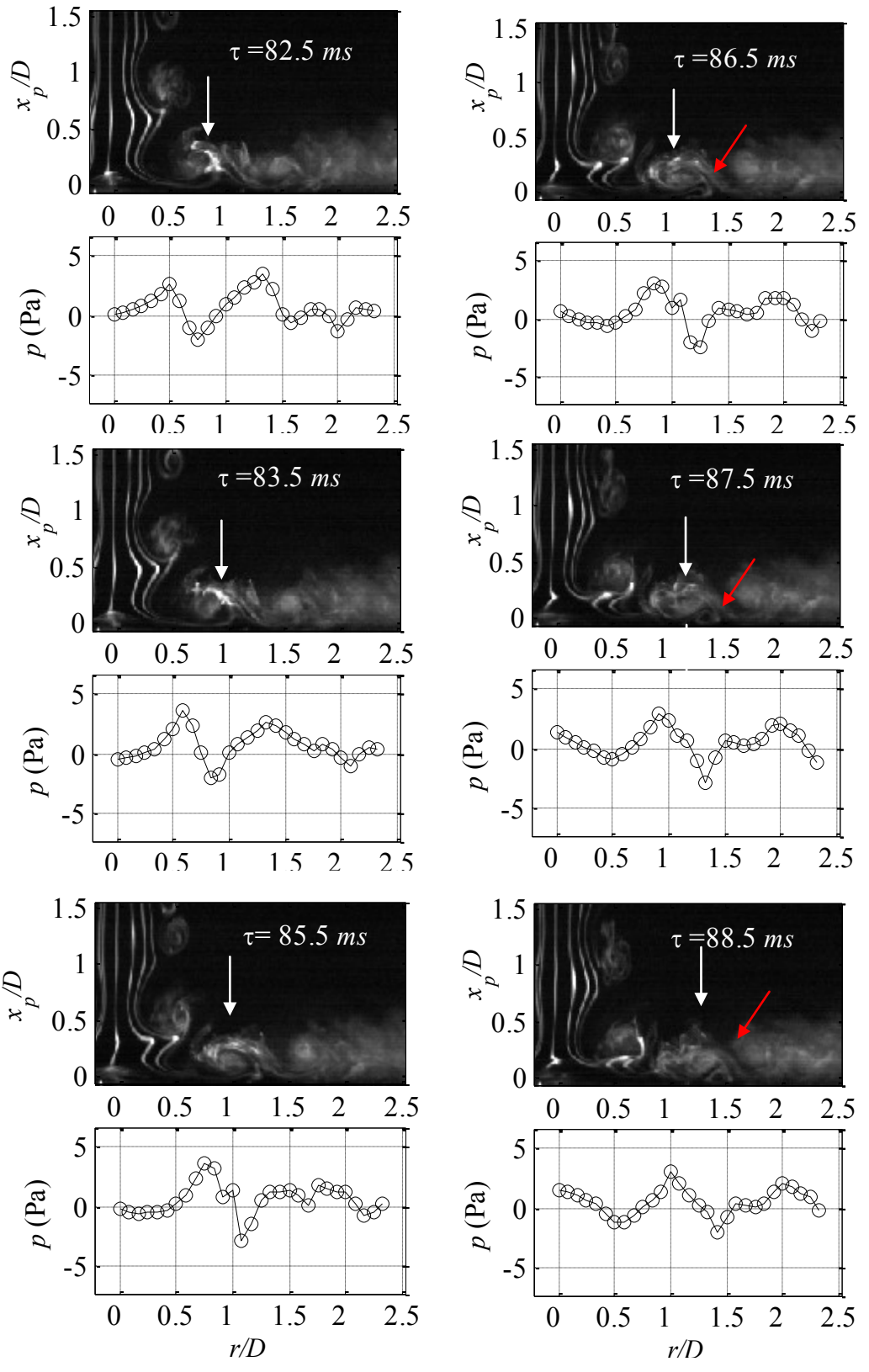


Figure 6.1 Example of the surface pressure signature during the flow evolution leading to the formation of a secondary vortex in normal impingement at H/D=3

6.1.2 Near-Wall Vortex Merging

Figure 6.2 depicts the spatial pressure signature for the impinging jet in the case when two vortices interact above the wall for H/D=2 in normal impingment. The figure is used to track the two vortex rings pointed to by white arrows in the flow visualization images for a total period of 10 ms; the images are accompanied with the corresponding wall-pressure signatures. At $\tau = 2$ ms the figure shows two vortices downstream of the jet; the leading vortex is closer to the wall and farther out in the radial direction than the trailing vortex. At τ =4 ms the trailing vortex moves closer to the leading one, possibly due to a combination of the induced velocity by the leading on the trailing vortex as well as the lower wall-normal velocity of the leading vortex because of its closer proximity to the wall. Later, at $\tau=6$ ms, the vortex pair seems to be streched and reoreinted to be parallel to the wall. The related pressure signature portrays a broad negative peak that correlates with the size and the location of the two vortices together. During τ = 8 and 9 ms the trailing vortex becomes more flat and seems to be pulled under the leading vortex, merging with it at $\tau=12$ ms. The corresponding negative pressure signature that initially forms beneath the vortices at τ =4 ms gains more strength in time, developing to a strong negative spike at τ =12 ms that is located at downstream of the merged vortices. As will be seen in the computational results shown in section 6.2.3.2, the development of such strong negative pressure spikes downsteram of, rather than beneath, the merged vortices is the result of boundary layer separation and secondary vortex formation. When the separation is induced by merging vortices, the negative spike is particularly strong, as seen at $\tau = 12$ ms in Figure 6.2 where the spike is almost equal to the dynamic head based on the jet exit velocity. It is emphasized here that the conclusions relating the observed behavior of the wall-pressue signature and the secondary vortex formation

can not be made using the flow visuzliaztion since the smoke in too diffuse to discern the near wall details in Figure 6.2.

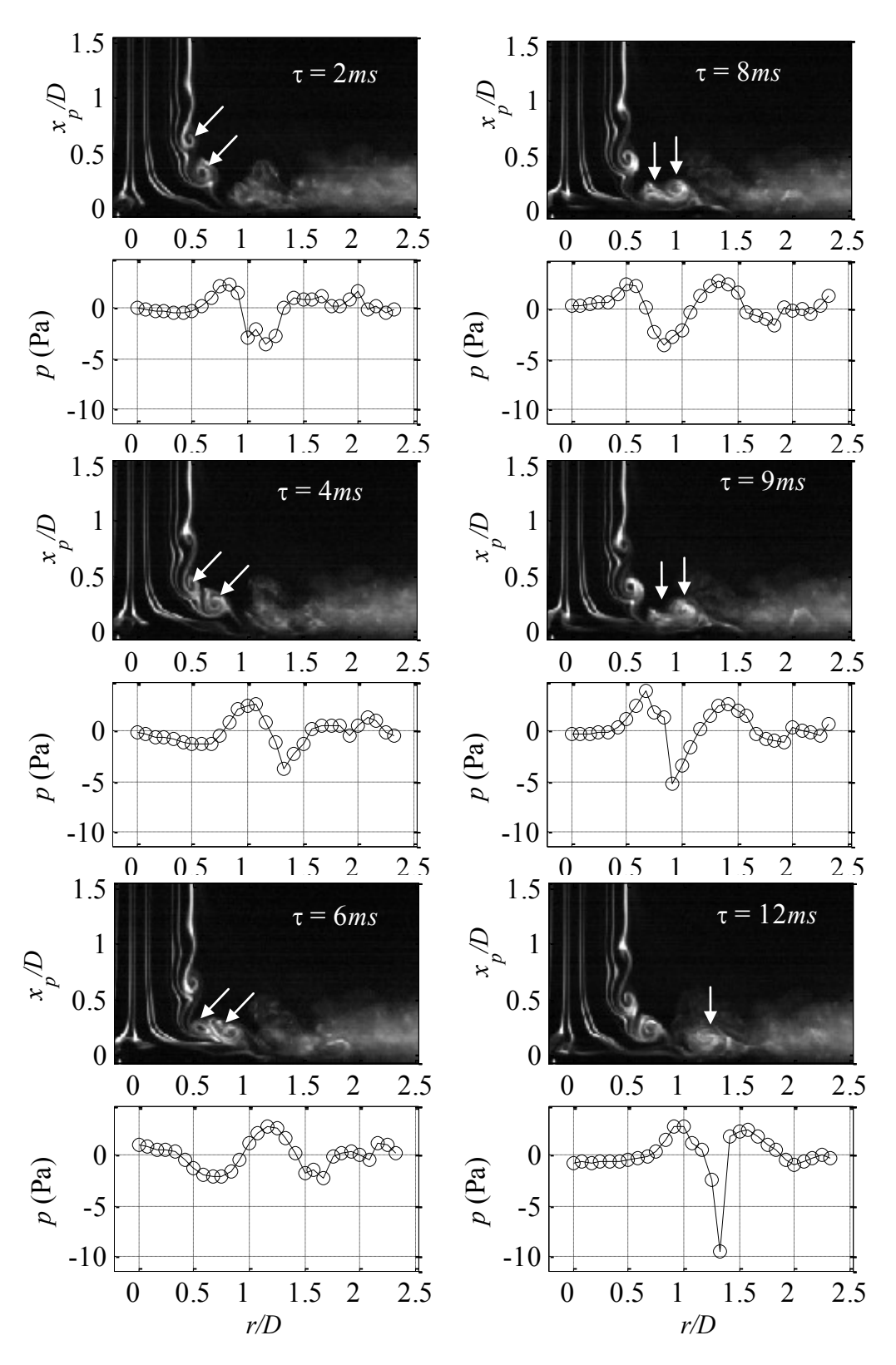


Figure 6.2 Spatial pressure signature associated with merging of two vortices above the wall in normal impingement for H/D=2

6.2 Simulation of the Model Problems

The current numerical simulations are based on the previous work by Shrikhande [32] at Michigan State University. Shrikhande simulated the flow field arising from an initial condition consisting of an axisymmetric vortex ring, having Gaussian-shaped core-vorticity distribution, that is located in a quiescent surrounding near a solid wall. The sense of vorticity is such that at subsequent times, the ring travels towards the wall due to the "self-induced" velocity, ultimately leading to impingement and interaction of the ring with the wall. The computational results were validated against Molecular Tagging Velocimetry data obtained by Gendrich *et al.* [36], demonstrating good agreement regarding the evolution of the vortical structures. For convenience, the comparison between the experimental and computational data reported by Shrikhande [32] are included in Appendix (E).

The first model problem investigated in the current study is the same as that computed by Shrikhande [32]. For this problem, the data from Shrikhande [32] are simply employed to examine the wall-pressure generation physics (which was not studied by Shrikhande). For the second model problem, new simulations were done using the same simulation parameters as Shrikahnde [32] except for the initial condition. The latter was changed such that at time zero, two concentric vortex rings are present above the wall in order to study the interaction between the two rings with each other as well as with the wall, and the consequent effects on the wall-pressure generation.

6.2.1 Geometry of Computational Model

Figure 6.3 shows a sketch of the computational geometry domain and associated initial and boundary conditions. The figure depicts a square domain of 0.06×0.06 m with x_p along the

ordinate being the axis of axial symmetry and r along the abscissa coinciding with the impingement wall. One or two vortex rings (with identical Gaussian core-vorticity distribution and core radius in the latter case) with the core center located at a prescribed distance from the bottom wall and asxis of symmetry define the initial condition of the flow field. The Gaussian vorticity distribution is given by:

$$-\frac{(r-r_o)^2 + \left(x_p - x_{p_o}\right)^2}{R_c^2}$$

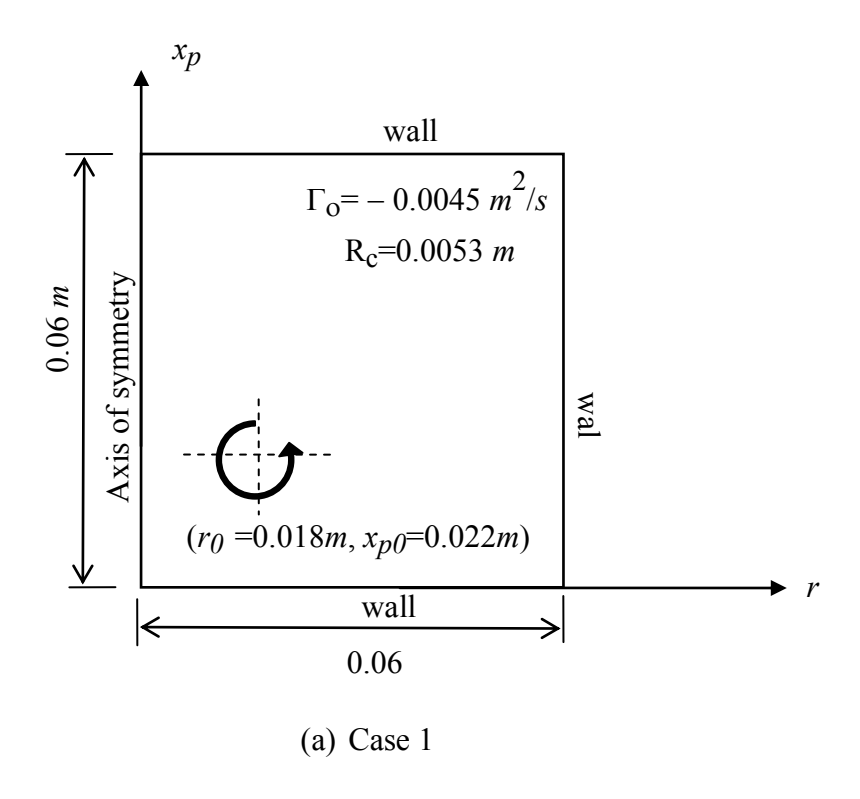
$$\omega_\theta = \omega_0 e \qquad (6.1)$$

$$\Gamma_0 = \pi R_c^2 \,\omega_0 \tag{6.2}$$

Where, ω_{θ} is the out of plain vorticity, ω_{0} is the maximum initial vorticity at the vortex core center, r_{o} and x_{po} are the radial and normal coordinates, respectively, of the vortex core center, R_{c} is the initial radius of the vortex core and Γ_{0} is the initial circulation. The initial convection velocity of the vortex ring is predicted to be 5.4 *cm/s* applying the formula developed by Saffman [37]

$$U_0 = \frac{\Gamma_0}{4\pi R_0} \left[\ln \left(\frac{8R_0}{R_c} \right) - 0.558 \right]$$
 (6.3)

Where U_0 is the initial vortex ring convection velocity and R_0 is initial the vortex ring radius.



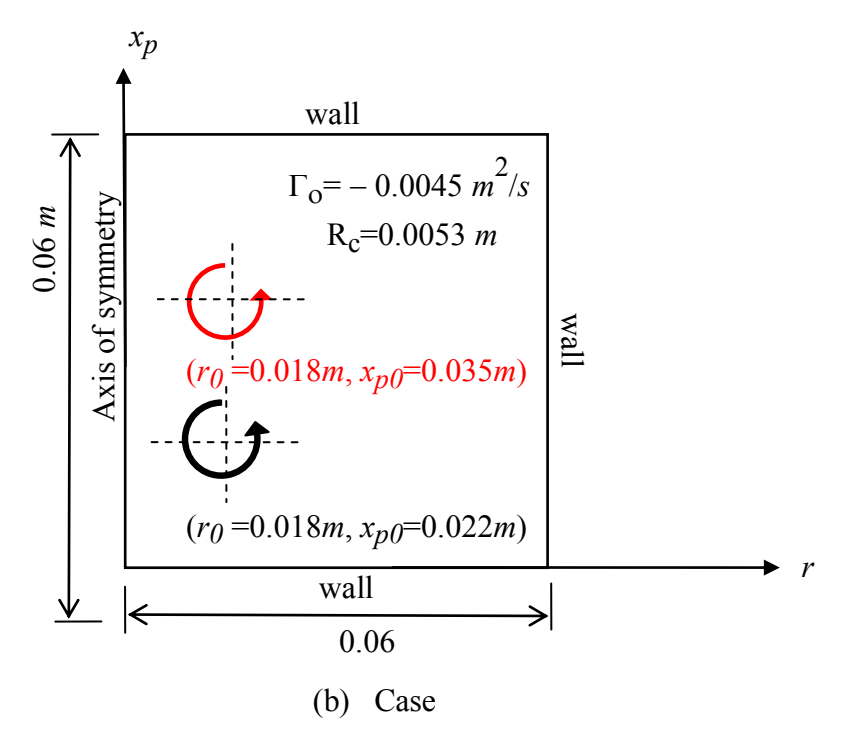


Figure 6.3 Sketch illustrating the numerical domain and boundary and initial conditions for two different cases: (a) one vortex ring and (b) two vortex rings

6.2.2 Simulations Using ANSYS-Fluent

ANSYS-Fluent solver is employed to conduct the computations using Direct Numerical Simulation (DNS) scheme to time-resolve the flow field with a time step of 0.005 seconds (0.0075 when normalized by the vortex ring initial diameter D_0 and convection velocity U_0). The two-dimensional computational domain, boundary and initial conditions, mesh and flow field properties are the same as used by Shrikhande [32]. The Reynolds number for the computation based on the vortex ring initial diameter D_0 and convection velocity U_0 is 1,936.

As seen from Figure 6.3, the flow domain is bounded by rigid walls on three sides (top, bottom and right) while the x_p axis on the left side of the domain is identified as the axis of symmetry. The domain, which is defined using Gambit, is divided by 715×715 of equally spaced grid points. The corresponding grid size is $0.0839 \ mm$ ($0.0023 \ D_0$). For the computation of the two-vortex-ring problem, the initial condition is altered by introducing another axisymmetric vortex ring in the flow domain with known Δx_p from the first one but located at the same radial location of r to simulate when merging downstream of the jet (case 2). To modify the initial condition for the second model problem, a program is written in C language to give the initial values of the two velocity components (as given by equations 6.4 below, where u and v are the radial and wall-normal components respectively) at the computational grid locations. The program is imported into Fluent using the User Defined Function (UDF) feature. The flow substance is water, with density of $998 \ kg/m^3$ and dynamic viscosity of $1.002 \times 10^{-3} \ (N \ s/m^2)$.

$$u_{r} = -\frac{\Gamma_{0}}{2\pi} \left[1 - e^{-\frac{\left(r - r_{0}\right)^{2} + \left(x_{p} - x_{p0}\right)^{2}}{R_{c}^{2}}} \right] \frac{\left(x - x_{p0}\right)}{\left[\left(r - r_{0}\right)^{2} + \left(x_{p} - x_{p0}\right)^{2}\right]}$$
(6.4)

$$u_{xp} = \frac{\Gamma_0}{2\pi} \left[1 - e^{-\frac{(r - r_0)^2 + (x_p - x_{p0})^2}{R_c^2}} \right] \frac{(r - r_0)}{[(r - r_0)^2 + (x_p - x_{p0})^2]}$$

The computations are carried out with 300 iterations for each step time of 0.005 seconds; this insured insignificant residuals after solving for the flow field. The data for the flow field velocity are saved at each time step in (.dat) format, which is subsequently converted to text format for post-processing by MATLAB, using Tecplot-10 software.

6.2.3 Simulation Results.

6.2.3.1 Model Problem I: Secondary Vortex Formation

Before considering the wall-pressure physics, it is important to describe the flow evolution leading to secondary vortex formation. To aid this description, results from Shrikhande [32] are presented in Figure 6.44. The figure portrays the development of the azimuthal vorticity field every $0.05 \ s$ for a period of $0.35 \ s$. As seen from the figure, with time progression, the initial (primary) vortex ring moves simultaneously towards the wall and in the increasing r direction. The ring induces flow in the positive r direction along the wall, leading to the formation of a boundary layer, which ultimately separates (under the action of the pressure gradient imposed by the primary vortex). The separated shear layer rolls up to form a secondary vortex with a sense of

rotation opposite to that of the primary vortex. Due to their mutual interaction, both the primary and the secondary vortices eject away from the wall.

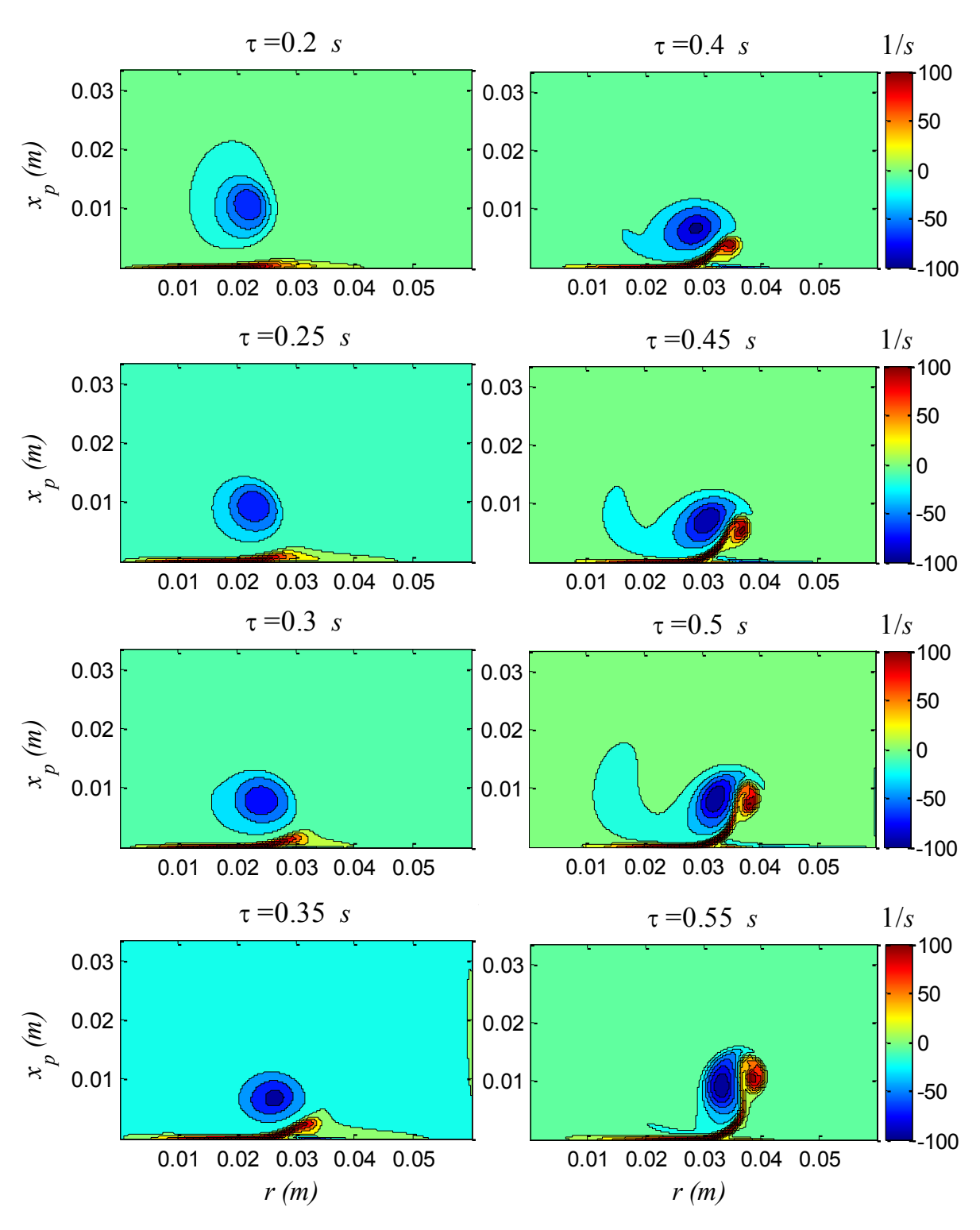


Figure 6.4 Vorticity field evolution obtained from the simulation of an axisymmetric vortex ring interacting with a flat wall by Shrikhande[32]

Although the surface-pressure information associated with the vortex ring-wall interaction is available directly from the computation, in the present study the computed velocity-field is employed in conjunction with the solution to Poisson's equation (see equation 1.1) written in a cylindrical coordinate system to calculate the pressure, as follows:

$$p_{w}(r_{0},\theta_{0},\tau) = \frac{1}{2\pi} \left[\int \int \frac{q(r_{s},x_{p,s},\tau)}{\sqrt{r_{s}^{2} - 2r_{0}r_{s}\cos(\theta_{s} - \theta_{0}) + r_{0}^{2} + x_{p,s}^{2}}} \times r_{s}dr_{s}d(\theta_{s} - \theta_{0})dx_{p,s} \right]$$

$$+ \int \int \frac{\mu \partial^{2} u_{xp}(r_{s}, x_{p,s}, \tau) / \partial x_{p,s}^{2}}{\sqrt{r_{s}^{2} - 2r_{0}r_{s}\cos(\theta_{s} - \theta_{0}) + r_{0}^{2}}} \times r_{s} dr_{s} d(\theta_{s} - \theta_{0})$$
(6.5)

Where the coordinates with subscripts s and θ denote the locations of the source and wall-pressure observation respectively (note that θ_0 may be set to any value, with zero being the simplest, given the axisymmetry of the wall-pressure field), u_{xp} is the velocity component in the x_p direction and q is given by:

$$q = \rho \left\{ \left(\frac{\partial u_r}{\partial r} \right)^2 + 2 \frac{\partial u_r}{\partial x_p} \frac{\partial u_{xp}}{\partial r} + \left(\frac{\partial u_{xp}}{\partial x_p} \right)^2 + \left(\frac{u_r}{r} \right)^2 \right\}$$
 (6.6)

The use of Equations (6.5) and (6.6) to compute the wall pressure instead of simply using the wall pressure values available from the simulation is motivated by the ability to examine the spatial distribution of the pressure-generating sources (given by equation 6.6), and hence gain insight into the mechanisms leading to the observed patterns of wall pressure. In addition, by breaking the integral (6.5) into sub-integrals, each associated with a flow feature of interest, it

becomes possible to understand the relative importance/role of the different flow features and structures in generating the surface pressure.

In order to compute the surface pressure at a given time instant, the integral (6.5) is computed at the same time instant for a given r_0 over a cylindrical volume with axis coinciding with x_p and having a radius of $0.06 \ m$ and a height of $0.06 \ m$. The derivatives in Equation (6.6) are numerically computed using first- and second-order-accurate finite difference for the first and second derivatives respectively; specifically having the following forms for a generic function $\zeta(x)$:

$$\frac{\partial \zeta(x)}{\partial x} = \frac{\zeta(x_{i+1}) - \zeta(x_i)}{\Delta x} \tag{6.7}$$

$$\frac{\partial^2 \zeta(x)}{\partial x^2} = \frac{\zeta(x_{i+1}) - 2\zeta(x_i) + \zeta(x_{i-1})}{\Delta x^2} \tag{6.8}$$

The integration (6.5) is computed numerically by dividing the integration volume into "infinitesimal" volumes having the same geometry as the computational grid of 715×715 in a given r- x_p plane and azimuthal extent $\Delta\theta_S=2^0$. The integration has a singularity when $\cos(\theta_S-\theta_0)$ is one and r_S equals r_0 (that is when the source and observation locations coincide). In order to avoid this singularity, the integration limits of θ_S are set to $0-2\pi$ (which, for the numerical solution, yields discrete values of $\theta_S=0$, 2, 4, 6, etc; given in degrees for simplicity), and the azimuthal location for the solution θ_0 is offset to a value of one degree which assures that none of the spatially-discrete source locations will coincide with the pressure observation location.

The velocity fields corresponding to the vorticity fields at τ =0.3, 0.35 and 0.4 seconds (shown in Figure 6.4) are chosen to compute the surface-pressure signature. This period is selected to be from the early stages when the vortex starts to interact with the wall forming a boundary layer, which ultimately separates and leads to secondary vortex formation until both vortices (primary and secondary) are about to eject away from the wall. Subsequent times involving substantial movement of the vortices away from the wall due to ejection are not considered since such strong ejections were not observed in the impinging jet flow (at least within the domain where the smoke patterns did not diffuse substantially due to turbulence/three-dimensionality and the flow structure could be discerned without ambiguity). Figure 6.5 depicts the vorticity fields for the aforementioned time instants. These plots are accompanied with the concurrent surfacepressure signatures computed using Equations (6.5) and (6.6), blue lines, and those determined using Fluent (red lines) to verify the accuracy of the computations based on the solution of Poisson's equation. At τ =0.3 seconds, the top left plot in Figure 6.5 shows the boundary layer with vorticity having opposite sign to that of the primary vortex as the latter "impinges" on the wall. The corresponding surface pressure signature depicts a broad negative peak directly beneath the vortex radial location. At τ =0.4 seconds the separated shear layer has already rolledup into a secondary vortex having vorticity of opposite sign to the primary one. The corresponding wall-pressure signature exhibits two local negative peaks (identified with arrows), where notably the stronger peak lies under the secondary vortex and the one lying under the primary one has weakened relative to the earlier time instant. It is quite interesting that this behavior of the dominant negative pressure peak shifting from being under the primary vortex to being under the secondary one is very similar to the NPDS (negative peak downstream shift) phenomenon noted in the discussion of Figure 6.1 results for the impinging jet flow. This

supports the idea that the formation of the secondary vortex in the impinging jet causes the NPDS. Of course, this does not clarify why the negative pressure signature beneath the primary vortex weakens. However, with access to the pressure source distribution in the computation, an explanation will be given in the analysis that follows.

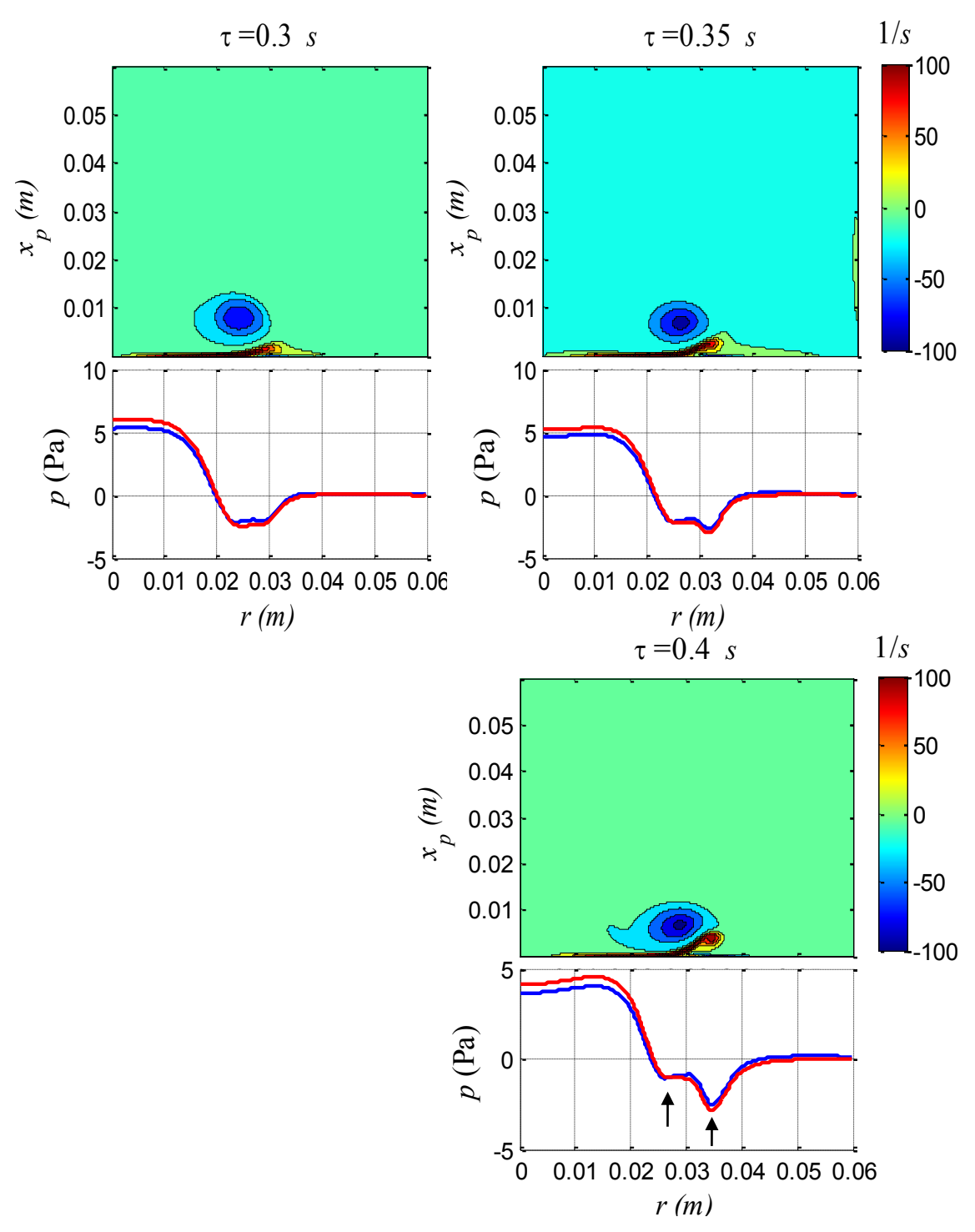


Figure 6.5 Azimuthal vorticity field and associated wall-pressure signature of the axisymmetric vortex ring-wall interaction problem at three consecutive times over a time period where the evolution of the vortices is representative of the observed behavior of vortices in the impinging jet flow; the blue line is the pressure signature computed from the solution of Poisson's equation and the red line is the pressure signature obtained from the Fluent solution

Understanding the significance of each flow feature noted in the discussion of Figure 6.5 in terms of contribution to the wall pressure remains unclear by just studying the surface pressure signature. Specifically, the latter is determined by taking into account all the pressure sources in the flow domain (given the integral nature of the solution (6.5)). In order to comprehend the contribution of each flow structure (primary and secondary vortices, and boundary layer) to the surface pressure signature, the wall pressure is computed by considering only a particular feature at a time. For instance to determine the surface pressure generated by the primary vortex, the wall pressure is calculated by integrating equation (6.5) over a sub-volume that only contains the primary vortex ring. This is achieved by setting vorticity and pressure-source filtering criteria for each flow feature when computing the wall pressure signature. The criteria are set for the flow features as follows: (I) for the primary vortex, negative vorticity and negative pressure source; (II) for the secondary vortex, positive vorticity and negative pressure source; and (III) for the boundary layer, positive vorticity and positive pressure source (note that the correspondence between a given vorticity sign and the associated pressure source will become clear in the discussion in the next paragraph). The flow field at τ =0.4 seconds is selected for this exercise. Procedurally, one of these three criteria is selected then the partial integration is obtained by setting to zero the value of the source (q) at spatial locations that do not meet the selected criterion.

Before presenting the analysis conducted for each flow feature, it is important to map them against the distribution of pressure sources in the flow domain, recalling that the flow mechanisms leading to negative and positive wall pressure in the characteristic signature are regions with dominant vorticity and high strain rate respectively (see equation 1.5). Figure 6.6 depicts the vorticity field (top plot) and the source field (bottom plot) of the simulated flow at the

same time instant (τ =0.4 s) for the results in Figure 6.5. In the source field plot in Figure 6.6, the regions occupied by the primary and secondary vortices are seen to coincide with negative source magnitudes, confirming that these structures do generate negative pressure. On the other hand, the region occupied by the separated boundary layer contains positive source magnitude, thus the pressure signature of the boundary layer is positive. The negative source associated with the primary vortex and the positive source relating to the strain rate of the boundary layer line-up vertically within the same radial domain. Hence, the wall-pressure at the same radial location, which is predominantly influenced by these features of opposite sign, is weak.

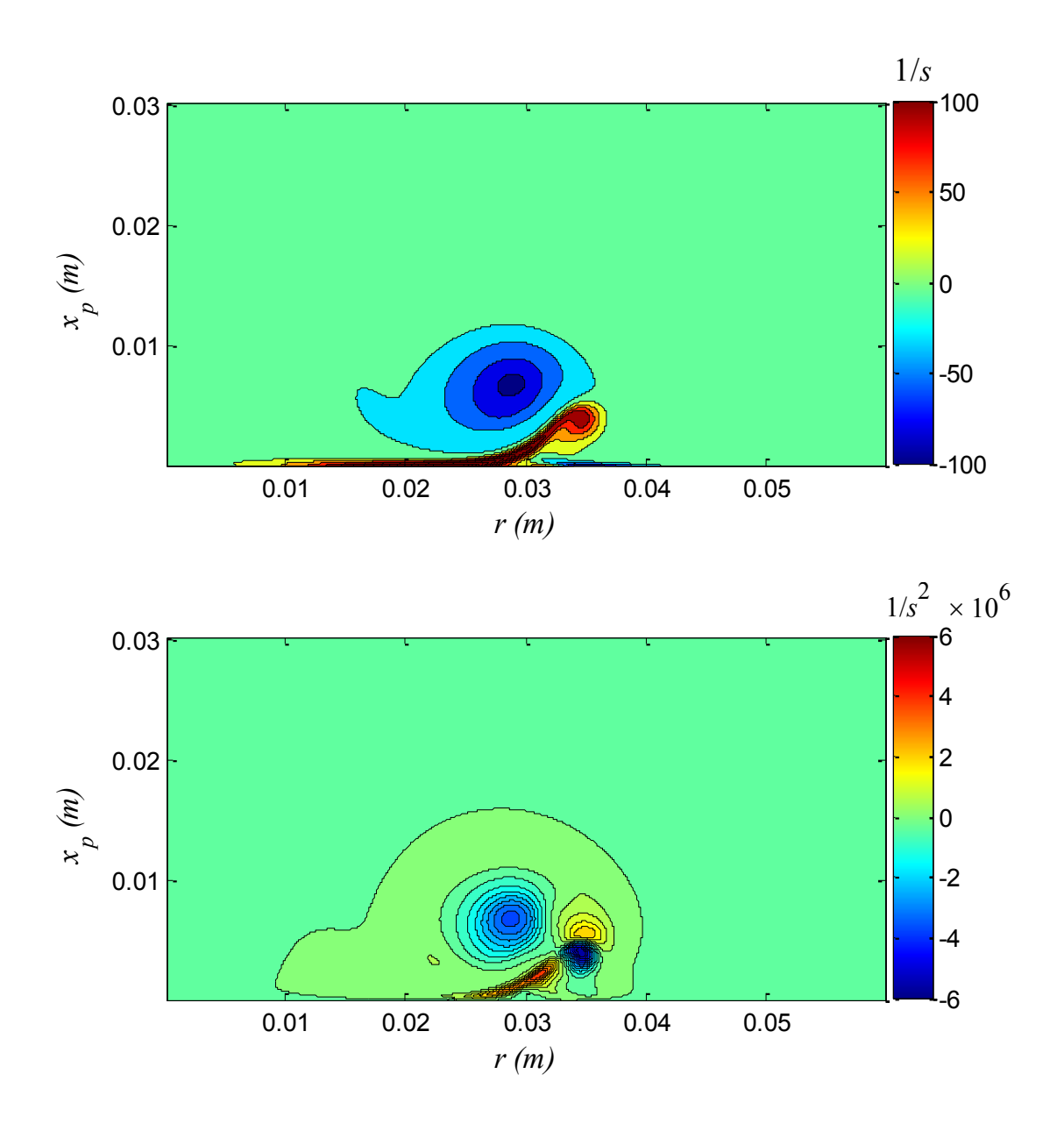


Figure 6.6 Vorticity (top plot) and source (bottom plot) fields of the simulated vortex ring impinging on a wall at time instant τ =0.4 s

Figure 6.7 shows the decomposition of the wall-pressure signature at τ =0.4 seconds into contributions from the individual flow features of interest. Figure 6.7b depicts the surface pressure signature that is calculated only for the primary vortex. The pressure signature shows a broad negative peak with high negative magnitude of -80 Pascal that lies under the radial

location of the primary vortex; however, the negative peak seems not to align perfectly with the vortex core center. Figure 6.7c shows the wall pressure signature computed for the secondary vortex; the signature also shows a negative peak that lies underneath the radial location of the vortex. The peak location for this case correlates well with the core center location of the vortex; it is a sharper peak than that of the primary vortex pressure peak but with less negative magnitude (-25 Pascal). At this point it is interesting to note how the negative peak associated with the secondary vortex is stronger than the one related to the primary vortex in the total pressure signature shown in Figure 6.7a; whereas the pressure signatures computed for the isolated vortices (Figure 6.7b and Figure 6.7c) depict the opposite. This suggests that there must be other important flow structures that have significant positive wall-pressure contribution that weakens the primary-vortex negative-pressure signature in the overall pressure signature. Such a structure, which is found to predominantly lie under the primary vortex as shown in Figure 6.7d, is associated with the separating boundary layer. As seen from the figure, the surface-pressure magnitude generated by the boundary layer is positive and strong at the radial locations where the primary-vortex pressure signature is strongest. Thus, it is the pressure generated by the boundary layer that is responsible for weakening the negative wall pressure associated with the primary vortex, as found in the overall surface pressure signature (Figure 6.7a), which gives the false impression that the secondary vortex has a stronger negative pressure effect. More generally, these findings suggest that the idea that the presence of a vortex above a wall creates a local strong negative pressure, which is widely accepted in the literature, is true as long as the vortex does not interact with the wall. If the vortex interacts with the wall leading to the formation of high-strain zone beneath the vortex, the positive pressure generated in this zone

coupled with its proximity to the wall works to practically nullify the wall-pressure imprint of the vortex.

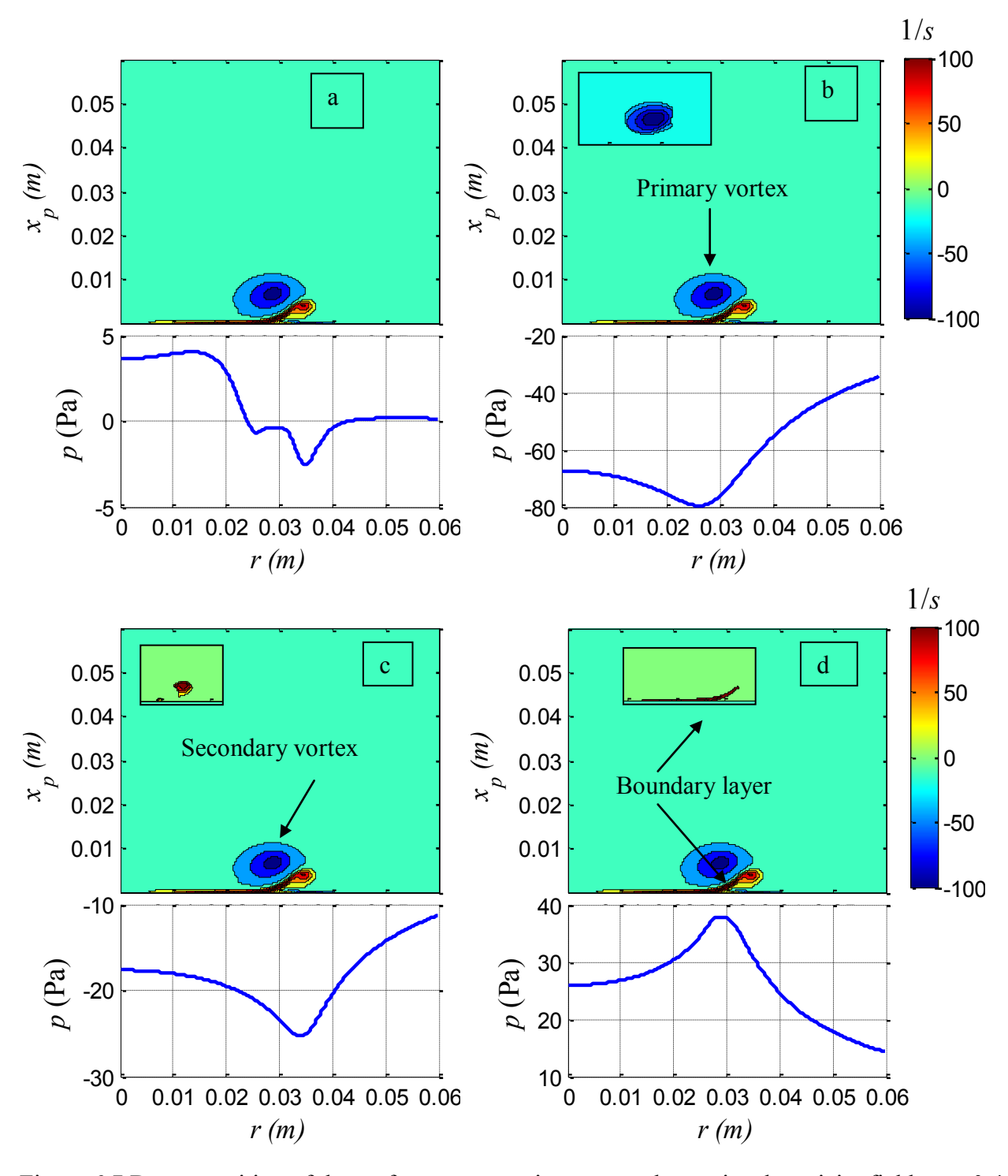


Figure 6.7 Decomposition of the surface pressure signature and associated vorticity field at τ =0.4 second; the total signature(a), primary vortex signature (b), secondary vortex signature (c) and boundary layer signature (d)

In Order to reconstruct the original wall-pressure signature of the vortex ring impinging on the wall, shown in Figure 6.7a, by adding the individual pressure signatures obtained for the primary vortex, secondary vortex and boundary layer, shown in Figure 6.7b through d, a wall pressure signature with a forth criterion of negative vorticity and positive pressure source needs to be computed. Figure 6.8 shows the wall pressure signature computed with the latter criterion. The signature depicts a general positive pressure with higher magnitude in the radial range where r < 0.03 m. Even though the vorticity field does not show a clear flow feature that can be responsible for the high pressure, one possible explanation is that the primary vortex induces flow towards the wall in the region where r is smaller than the radial location of the primary vortex's center due to the vortex's counter-clockwise rotation, and the secondary vortex induces flow at r values larger than the radial location of the secondary vortex's core because of the vortex's rotation in the clockwise direction.

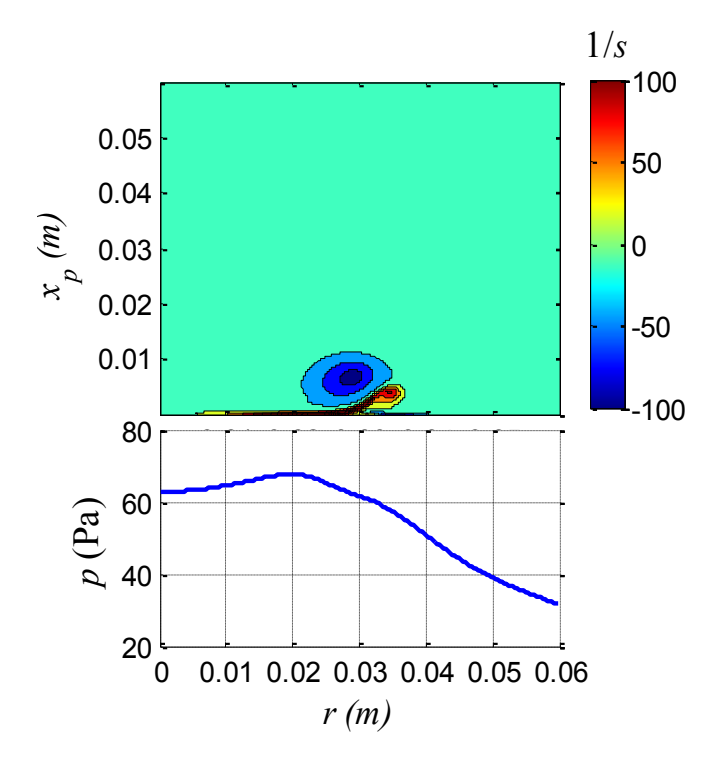


Figure 6.8 Wall-pressure signature computed for the flow field with negative vorticity and positive pressure source criteria

Figure 6.9 depicts the surface pressure signature of the simulated vortex ring flow at consecutive times as the vortex ring interacts with the wall. The evolution of these signatures clearly depicts the NPDS phenomenon associated with the weakening of the negative pressure peak beneath the primary vortex and the formation of a negative peak "ahead" of the vortex. The overall signature seems to be the strongest as the primary vortex encounters the wall, at τ =0.35 seconds, with double local negative peaks corresponding to the primary and the secondary vortices (where the latter is in the early stages of formation). Moreover, the pressure near the stagnation point (at r=0) has the highest magnitude τ =0.3 seconds. In general, the wall-pressure signature beneath the vortices weakens at later times and shifts in the positive radial direction. The negative peak associated with the primary vortex continuously loses strength, while that associated with the secondary one initially increases in magnitude then decreases at a lower rate

than the rate at which the negative primary vortex's negative peak decays. Concurrently, the local maximum, associated with the boundary layer in between, becomes more visible. The high pressure seen at τ =0.3 seconds near the stagnation point also weakens with increasing time; this is because the vortex ring weakens due to viscosity and it moves farther out in the radial direction, leading to smaller induced velocity towards the wall.

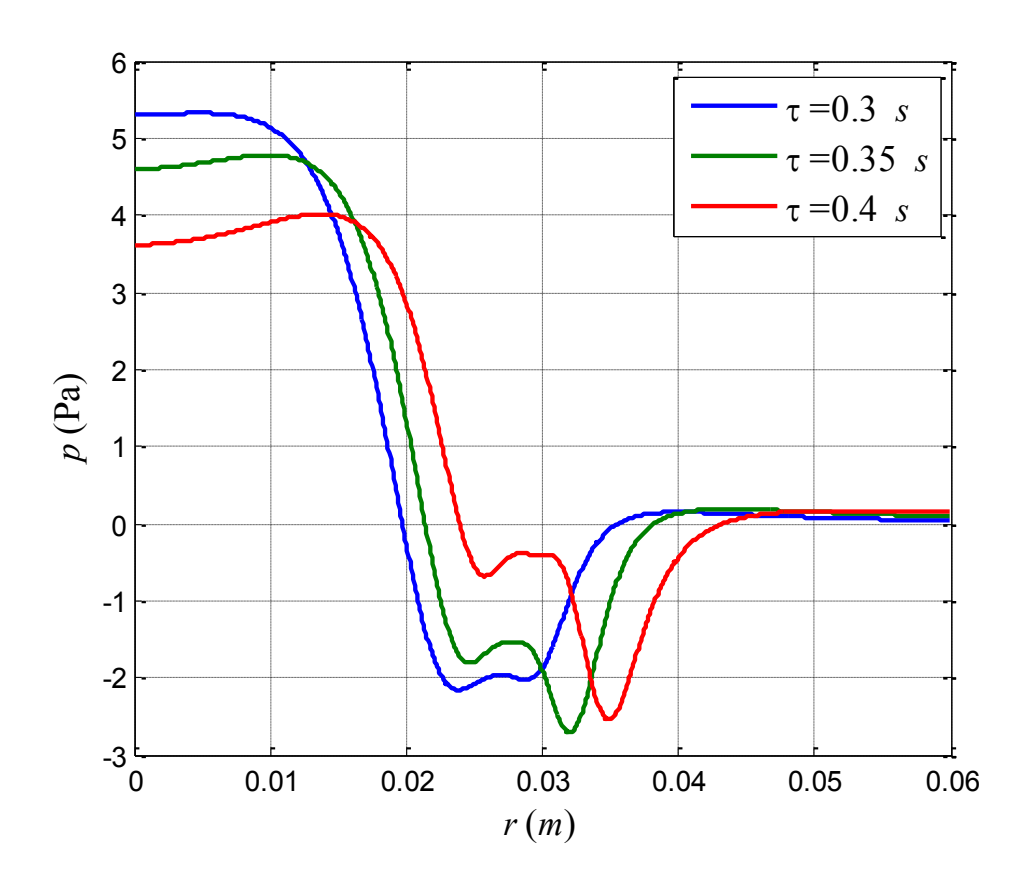


Figure 6.9 Surface pressure signature of the simulated vortex ring flow at consecutive times covering the same duration as the results shown in Figure 6.5

The pressure signatures computed for the primary vortex are shown in Figure 6.10 at the same time range as in Figure 6.9. Generally, the negative pressure generated by the primary vortex appears to predominantly be in the left half of the computational domain (r < 0.03 m). The pressure signature at τ =0.3 seconds shows a broad negative peak, with magnitude of

approximately -68 Pascal, that corresponds well with the size and the radial location of the primary vortex. Unlike the total pressure signatures seen in Figure 6.9, the pressure signature related to the primary vortex increases in magnitude at later times until τ =0.4 second. The negative peak appears at locations farther out in the radial direction with increasing time which is a reflection of the vortex convecting in the same direction. The pressure in the radial range near the stagnation point depicts a broad local maximum at r=0; this local maximum seems to shift towards negative value in proportional to the change in the negative peak (minimum).

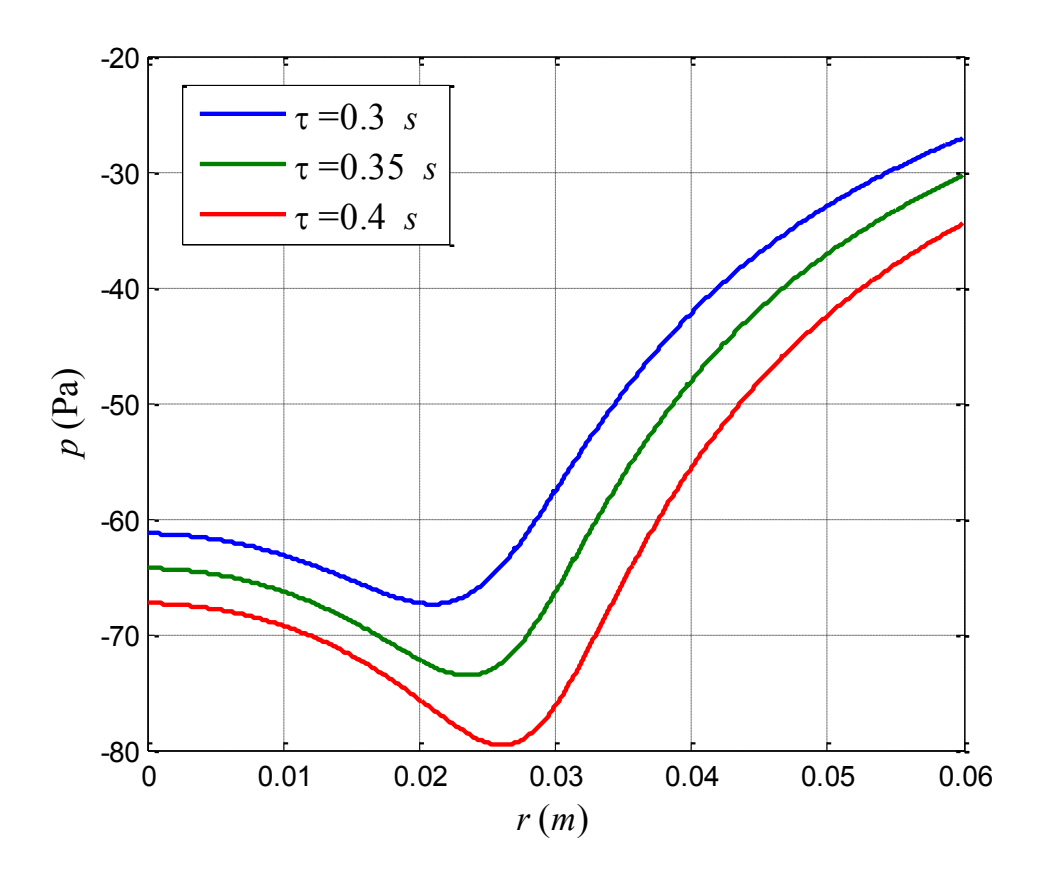


Figure 6.10 Surface pressure signature computed for the primary vortex in the simulated vortex ring flow at consecutive times covering the same duration as the results shown in Figure 6.5

Figure 6.11 portrays the pressure signatures calculated for the secondary vortex at consecutive times. The behavior of the signature is analogous to the one seen in Figure 6.10 for the primary

vortex. The pressure signature has a broad negative peak which is correlated to the smaller size of the secondary vortex in comparison with the primary one. The negative peak gains strength with increasing time (until τ =0.4 second) and its imprint enlarges. The difference in the pressure level between the right and left sides of the negative peak is much less than its counterpart for the primary vortex.

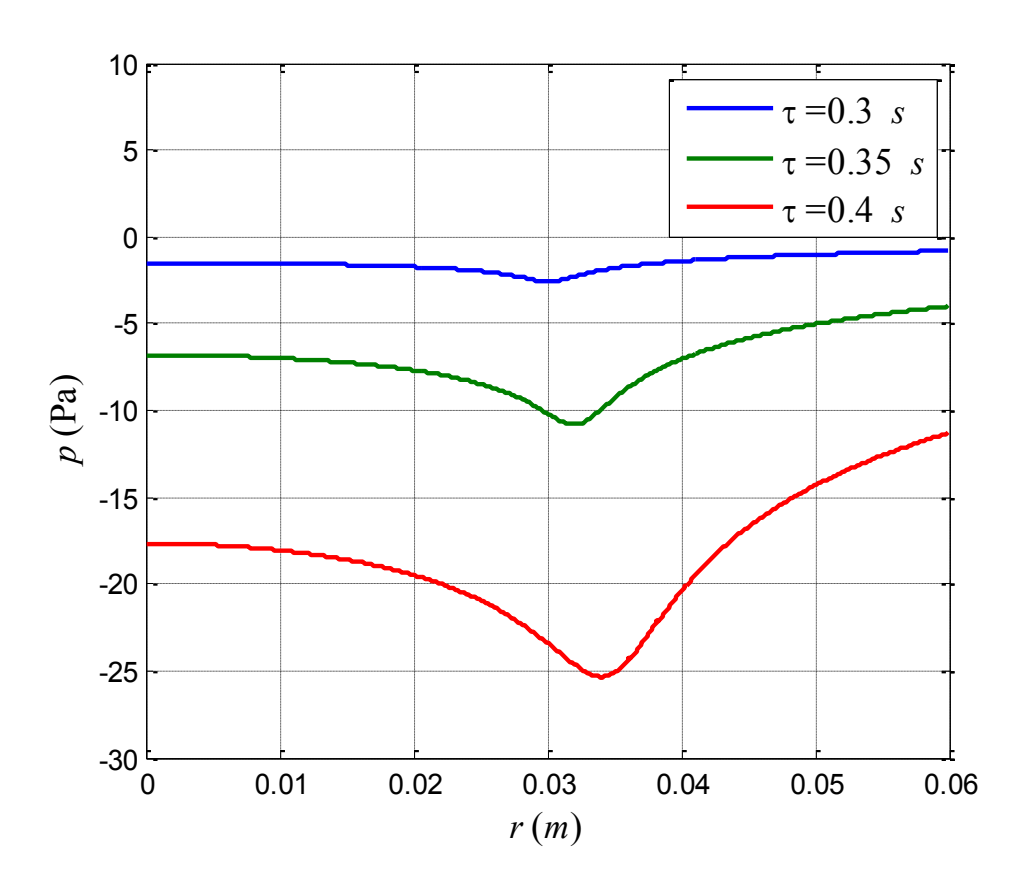


Figure 6.11 Surface pressure signature computed for the secondary vortex in the simulated vortex ring at consecutive times covering the same duration as the results shown in Figure 6.5

The boundary layer which lies underneath the primary vortex has a significant contribution to the surface pressure generation. Figure 6.12 depicts the surface pressure signature associated with this flow feature at consecutive times. The figure shows a positive pressure peak with considerable magnitude that grows in time. The peak also moves farther out in the radial

direction with increasing time, similar to the observations made in regard to wall pressure signatures of the primary and secondary vortices. The pressure level on the left side of the peak is higher than the one on the right side. The significance of this boundary layer surface pressure signature is that it is what makes the negative peak associated with the secondary vortex to appear to be stronger than that of the primary vortex in the total surface pressure signature in Figure 6.9, even though the negative pressure generated by the primary vortex is in fact stronger when the wall pressure for both structures (primary and secondary vortices) are examined individually. The boundary layer produced pressure is also what makes the magnitude of the total surface pressure signature decay over the time window 0.35 < t < 0.4, although the pressure generated by the primary and the secondary vortices increases in strength during the same time window.

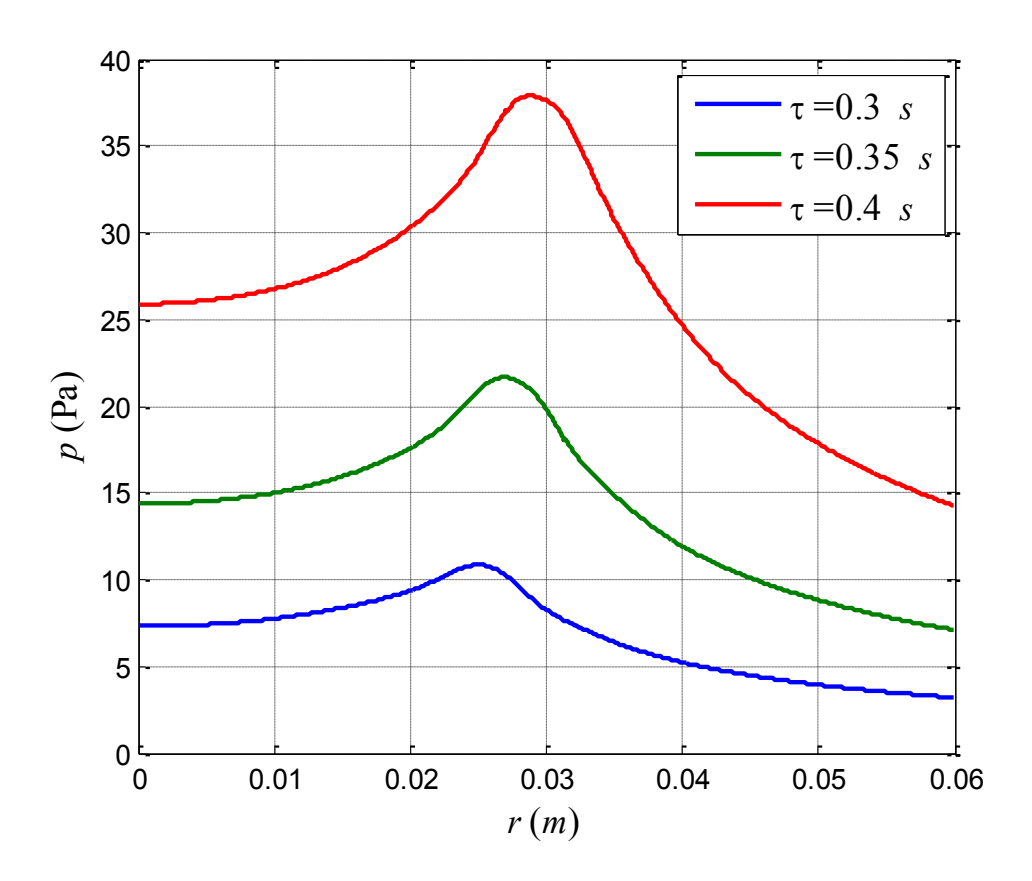


Figure 6.12 Surface pressure signature computed for the boundary layer in the simulated vortex ring at consecutive times covering the same duration as the results shown in Figure 6.5

6.2.3.2 Model Problem II: Near-Wall Vortex Merging

As discussed in Chapter 5 and further exemplified in section 6.1.2. and Figure 6.2, an important mechanism influencing the evolution of the wall pressure is when two successive vortex rings interact with each other in the wall-jet region and merge near the wall.

In order to study the two different cases of vortex merging in more details, simulations are conducted for two vortex rings with core centers placed at the same radial (r) location but with Δx_p spacing, in one case, and at the same x_p location but with Δr spacing in another case to draw analogies to two vortex-merging cases seen in the experimental results: vortex merging prior to the merged vortices turning to travel parallel to the wall (in the wall-jet region), and vortex

merging while the two vortices are advecting in the wall-jet region. Figure 6.13 depicts a simulation of two Gaussain Vortex rings that have core centers initially located at $(r = 0.018 m_{\odot})$ $x_p = 0.022$ m) and (r = 0.018 m, $x_p = 0.035$ m). This simulation represents the case where the vortices merge before they hit the wall. The figure shows the vorticity field at selected time instants when the changes in the flow field are noteworthy. Each vorticity field is accompanied with the corresponding wall pressure signature. The vorticity field at $\tau = 0.12$ seconds portrays the vortex ring that is initially located closer to the wall to move farther out in the radial direction and torwards the wall while dragging the other vortex ring, which seems to be stretched in the vertical direction as a result. At this time the wall-pressure signature depicts a high pressure near r = 0 because of the induced flow towards the wall by the vortex rings. At $\tau = 0.22$ seconds, the two vortex rings almost compete merging, before they interact with the wall, forming a larger vortex eventhough it does not depict a Gaussian-like vorticity (i.e. a single-peaked vorticity distribution) distribution at this point. The produced larger structure imposes a broad negative peak on the surface and it induces the formation of a boundary layer on the wall. The latter separates, leading to the roll-up of a secondary vortex with vorticity sign opposite to that of the primary, as shown in the rest of the plots. The corresposnding wall-pressure signature demonstrates a double negative peaks that correlate with the primary and secondary vortices and the peak associated with the latter vortex gains more strength with increasing time.

The phenomenon decribed above for the simulation is also obseved in the experimental flow visualization shown in Figure 6.1 which depicts the spatial pressure signature at consuctive times in normal impingment at H/D=3. The figure depicts two vortices in the vicinity of $x_D/D=1.3$ at

 τ =85.5 ms that have merged by the time τ = 88.5 ms. This is shown in more details in Figure 6.14 using flow visulization images with smaller time step.

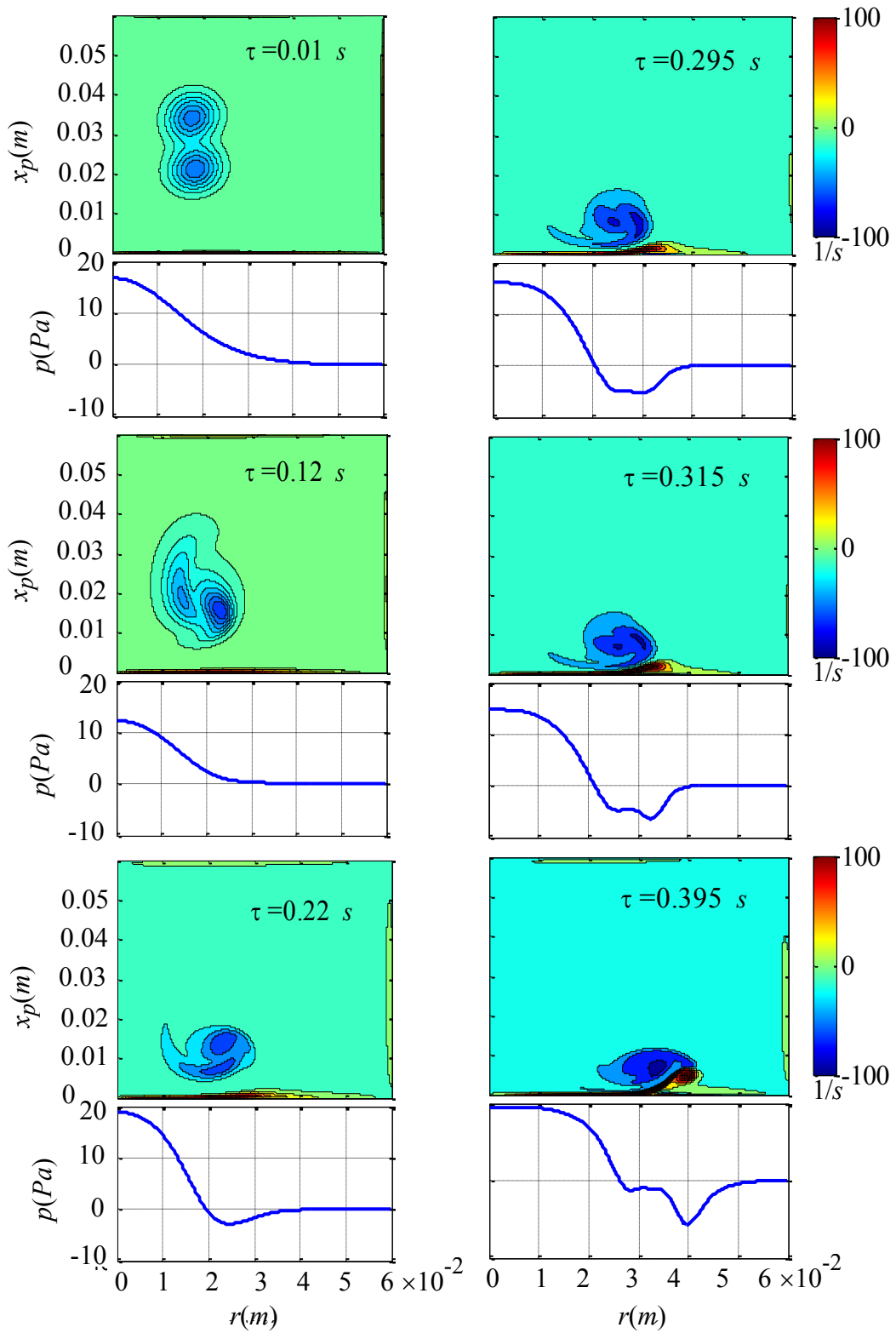


Figure 6.13 Simulation of two Guassian vortex rings with initial locations of $(r = 0.018 m, x_p = 0.022 m)$ and $(r = 0.018 m, x_p = 0.035 m)$

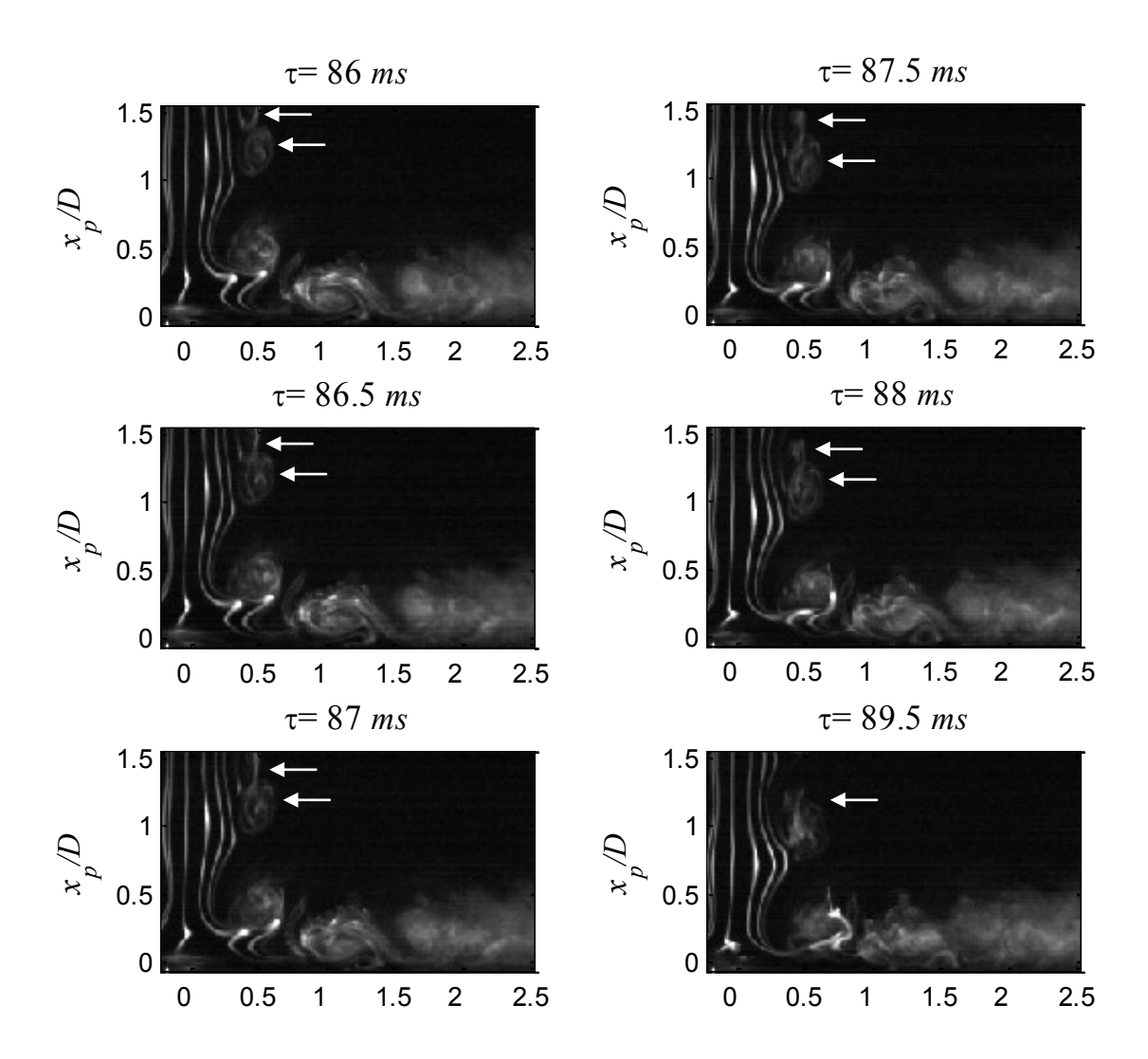


Figure 6.14 Flow visualization images at H/D=3 and normal impingement showing two vortices merging downstream of the jet (pointed by arrows)

Figure 6.15 depicts the vorticity field and associated wall-pressure signature from a simulation where the two core centers of two Guassain vortex rings are initially introduced at $(r=0.018 \ m, x_p=0.01 \ m)$ and $(r=0.029 \ m, x_p=0.01 \ m)$ locations; i.e. two different radial locations but the same height above the wall. The vorticity field at $\tau=0.06$ seconds shows that the trailing vortex, which is initially located at smaller radial location, is being "squished" against the wall and stretched in the radial direction due to the action of the leading vortex. The associated pressure signature exhibits a broad negative peak, that correlates with the size of the two vortices

together, as well as positive pressure near the r=0. During $\tau=0.1$ and 0.11 seconds, the trailing vortex is stretched further and moved in the positive r direction, becoming sandwitched between the other vortex and the induced boundary layer flow, before the two vortices ultimately merge. The negative peak in the corresponding wall pressure signature at τ =0.11 seconds starts to shift forward towards a radial location "ahead" of the two merged vortices. The vorticity field at τ =0.225 seconds shows secondary vortex formation with vorticity sign opposite to the primary merged vortices. The characteristic wall-pressure signature, at these time instants, depicts a significant negative peak that is associated with the secondary vortex and the one which is related to the merged structure becomes very weak. This behavior is again very consistent with the NPDS pressure signature found in the impinging jet and in the single vortex ring computation. The main difference between the single- and two-vortex-ring results is that in the latter case, the negative peak under the secondary vortex becomes substantially stronger approaching -15 Pa (at $\tau = 0.13$ seconds in Figure 6.15), in comparison to -3 Pa in the case of the single vortex ring (Figure 6.5). This suggests that vortex merging near the wall should produce stronger spiky negative pressure excursions in comparison to the pressure signature produced by passing, non-merging vortices.

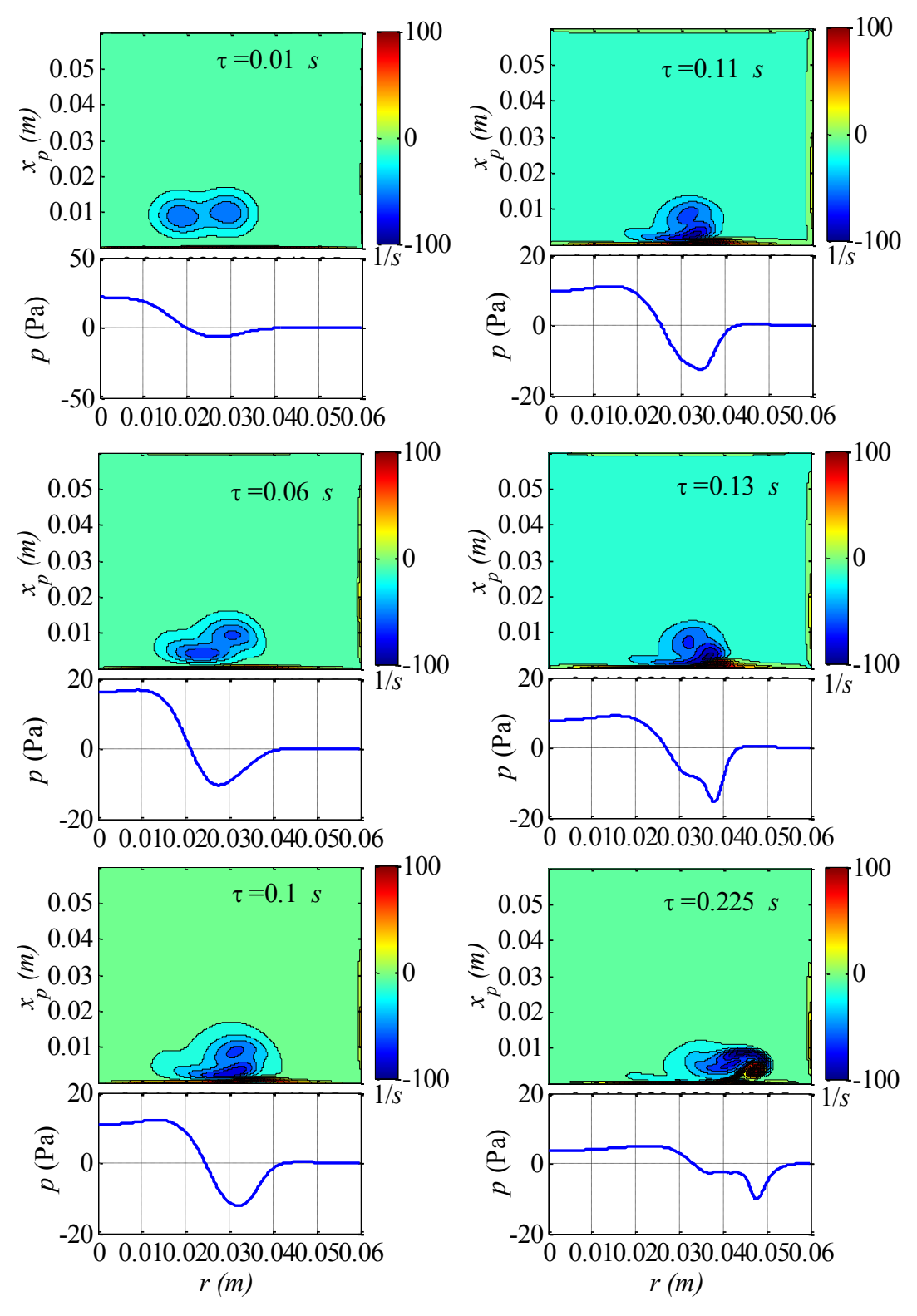


Figure 6.15 Vorticity field and associated wall-pressure signal obtained from the simulation of the flow produced by two vortex rings above a wall with initial core center locations of (r=0.018 m, x_p =0.01 m) and (r=0.029 m, x_p =0.01 m)

Chapter 7: Conclusions and Recommendation

Investigated in the current study is the relationship between the flow structures of an axisymmetric impinging jet at Reynolds number of 7334, based on jet exit velocity (U_j) and diameter (D), and the wall-pressure fluctuations, for normal and oblique jet incidence. The investigation utilizes simultaneous time-resolved flow visualization and unsteady surface pressure measurements using a radial array of eight microphones and smoke wire/high speed camera. The current analysis focuses on the results from microphones located in the radial range of r/D of 0 to 2.33 (measured from the jet's centerline) for normal and oblique (30° inclination) impingements and jet-to-impingement plate separations H/D of 2, 3 and 4.

The results reveal that for normal impingement, the radial measurement domain may be subdivided into four sub-domains based on the unsteady wall pressure characteristics: (I) the immediate neighborhood of the stagnation point (r/D < 0.5); (II) the region within which the vortices turn and start advecting parallel to the wall (in the vicinity of r/D = 1); (III) the "early" wall-jet flow where the pressure fluctuations reach their peak *rms* value (centered around r/D = 1.33); (IV) the "late" wall-jet flow where the pressure fluctuations strength decays monotonically with increasing r/D > 1.33.

In sub-domain I, the pressure fluctuations are found to be produced by modulation of the potential-core flow by the passage of the jet vortex rings. In sub-domain II, the pressure time series is dominated by the quasi-periodic passage of the jet vortical structures where the negative pressure peaks occur beneath the vortices and the positive ones in between. The temporal

pressure signatures are observed to have one of two forms: w-like (meaning the negative pressure temporal signature has a shape like the letter W) and sinusoidal-like signatures that characterize different vortical structures interaction mechanisms. The flow visualization shows these two scenarios correspond to "vortex merging" and "vortex passage mechanisms, respectively, that occur in the early wall-jet zone.

In sub-domain III, where the pressure fluctuation intensify to reach their peak value, the pressure signature is found to develop strong negative spikes that can reach values of the order of the dynamic head of the jet (~ 10 Pa) in the case of vortex merging. Those spikes are observed to be related to secondary-vortex formation when a jet vortex structure interacts with the wall. This is especially apparent in the flow visualizations when H/D=3 since the vortical structures are larger in this case because their first merging is always complete before reaching the wall. The secondary vortex formation produces a characteristic spatial pressure signature that is associated with the establishment of the aforementioned strong negative pressure spike beneath the secondary vortex. Thus, as the jet vortices advect through sub-domains II and III, the negative pressure peak shifts from lying beneath the jet vortices (in sub-domain II) to being underneath the secondary vortex (in sub-domain III) while amplifying substantially (particularly when vortex merging occurs). This phenomenon is referred to in this study as Negative Peak Downstream Shift, or NPDS. The resultant signature depicts a much stronger negative peak associated with the secondary vortex when compared with the one corresponding to the primary (jet) vortex.

Downstream of region III (i.e. sub-domain IV), the pressure fluctuations are seen to decay in all cases. The concurrent flow visualization exhibit strong dispersion of the smoke, suggesting

that the vortical structures become highly turbulent in this sub-domain, which likely weakens the vortical structures and leads to the decay of their associated wall pressure footprint.

Applying Fast Fourier Transform (FFT) to short pressure signals that correspond to when a certain flow structure is observed in the simultaneous flow visualization helps to draw links between the observed behavior of the structure and the identified characteristics of the unsteadypressure spectrum. This analysis reveals that the jet flow initially forms vortical structures at St_D (Strouhal number based on jet exit velocity and diameter) of 1.3, and when the jet is at H/D=2and normal impingement, these vortical structures will either pass above the wall (vortex passage) preserving the initial Strouhal number or each two vortices will merge (vortex merging) generating a sub-harmonic mode of St_D =0.64. This mode also exists when the jet is placed at H/D=3 and normal impingement where vortices almost always merge before they encounter the wall with no sign of additional merging above the wall. At H/D=4 and normal impingement a Strouhal number 0.32 is related to the merging of four vortices; where each two vortices first merge forming larger vortices in the range of $x_i/D = 2-3$; then another merging of these two larger vortices takes place just before or when interacting with the plate at H/D=4. There are other times when only three vortices merge before interacting with the wall which results in pressure fluctuations at St_D of 0.53.

When the jet is set at the oblique impingement angle of 30°, analysis is conducted for the forward- and back-flow sides. In general, when a vortex rings interacts with the wall at this incidence angle, the vortex core diameter becomes larger on the forward-flow side than its counterpart on the back-flow side. Also from the streaklines in the flow visualization, it is

observed that the stagnation point shifts towards the back-flow side to be in the vicinity of r/D=0.5

On the forward-flow side, at H/D=2 and 3, the vortical structures almost always perform the first vortex merging before reaching the impingement plate and sometimes a second merging takes place above the wall resulting in Strouhal numbers of 0.64 and 0.32 respectively. The completion of vortex merging before reaching the plate can be related to the extra distance of the shear layer development before reaching the impingement plate when compared to the normal incidence. At H/D=4, the vortex merging mechanism is performed twice (merging of total of four vortices) generating St_D of 0.32. On the back-flow side at H/D=2, the vortical flow structures maintain the passage mechanism (preserving the initial St_D of 1.3) over a shorter radial distance. On the other hand, at H/D=3, both mechanisms of vortex passage and merging are observed resulting in fluctuations at St_D of 1.3 and 0.64; whereas at H/D=4 the flow structures depict the same Strouhal numbers as in the normal impingement at this particular H/D location. Overall, a particularly significant characteristic of the back-flow-side pressure fluctuations is that they decay very rapidly with increasing r/D, in comparison to both the forward-flow side and normal impingement.

To further study the mechanisms leading to the generation of the strong negative pressure spikes in sub-domain III and the peak *rms* pressure fluctuations, numerical simulations are conducted using Ansys Fluent of two model problems having vortical structures that interact with each other and the wall in a similar manner as observed in the wall jet. The problems involve the evolution of single and dual axisymmetric vortex rings with Gaussian core vorticity distribution above a flat wall. Similar to the impinging jet flow, the simulation results also depict

vortex merging (in the two-vortex-ring problem) and secondary vortex formation with spatial pressure signature that is qualitatively similar to the one observed in the experimental data. Applying Green's function solution of Poisson's equation of pressure on the computational databases the spatial pressure signature for individual flow features (primary vortex, secondary vortex and separating boundary layer) could be determined via partial integration of the solution. The calculation reveals that the primary vortex produces the strongest negative wall pressure, which conflicts with the behavior of the overall pressure signature associated with the negative peak shifting under the secondary vortex (NDPS). However, the separating boundary layer, which lies almost at the same radial location as the primary vortex, imposes a strong positive pressure which significantly weakens the negative pressure peak felt at the wall beneath the primary vortex. This explains the mechanism leading to NDPS. The analysis of the computational data also shows that the overall magnitude of the wall pressure and the intensification of the negative pressure spike in the two-vortex-ring problem, where vortex merging occur, are significantly higher than in the one-vortex-ring problem. This is consistent with observations in the impinging jet flow where the vortex-merging scenario leads to the establishment of stronger pressure fluctuations and amplification of the negative pressure spike.

The current study relies on flow visualization to obtain flow-field information, which only provides qualitative information regarding the vortical structures. Conducting simultaneous wall-pressure measurements and time-resolved flow field measurements utilizing Particle Image Velocimetry (PIV), for instance, can provide greater details about the vortical structures and the associated wall-pressure generation mechanisms. Alternatively, direct or large-eddy numerical simulations may be used for such investigation.

In oblique impingement, there is a significant difference between the evolution of a vortex ring on the back-flow in comparison to the forward-flow side of the same ring. Understanding the mechanisms leading to the difference in evolution between these two sides as the vortex ring interacts with the wall is needed to "complete the picture" in oblique impingement. This can be accomplished by conducting three-dimensional simulations of a vortex ring impinging on an inclined wall, as well as, by applying three-dimensional flow-field measurements in the same type of problem.

APPENDICES

Appendix A: Jet Nozzle

The fifth order polynomial contoured nozzle is designed following:

$$y(x)=a_0+a_1x+a_2x^2+a_3x^3+a_4x^4+a_5x^5$$
 7.1

Boundary conditions

$$y_{(x=0)} = 111.5 \, mm \quad , \quad y_{(x=210 \, mm)} = 12.5 \, mm$$

$$\frac{\partial y}{\partial x}\Big|_{(x=0)} = 0 \quad , \quad \frac{\partial y}{\partial x}\Big|_{(x=210 \, mm)} = 0$$

$$\frac{\partial^2 y}{\partial x^2}\Big|_{(x=0)} = 0 \quad , \quad \frac{\partial^2 y}{\partial x^2}\Big|_{(x=210 \, mm)} = 0$$

, with,

$$a_0 = 111.5$$
, $a_1 = 0$, $a_2 = 0$, $a_3 = \frac{-11}{102900}$, $a_4 = \frac{11}{1440600}$, $a_5 = \frac{-11}{7563150000}$

The coefficients in polynomial [A.1] can be determined by making y(x) and its first and second derivatives adhere to the above six boundary conditions. The resulting polynomial is fed into CAD software (SolidWorks) to draw the contoured nozzle profile, as shown in Figure A.1. The figure depicts the jet design with 223 mm inlet and 25mm outlet diameters. The nozzle is fabricated using rapid prototyping with 3 mm shell thickness and 231 mm overall length. An integrated flange is used to attach the nozzle to the flow conditioning box, and an extruded lip at the same side fits into the flow conditioning box with rubber material in between to reduce air leakage.

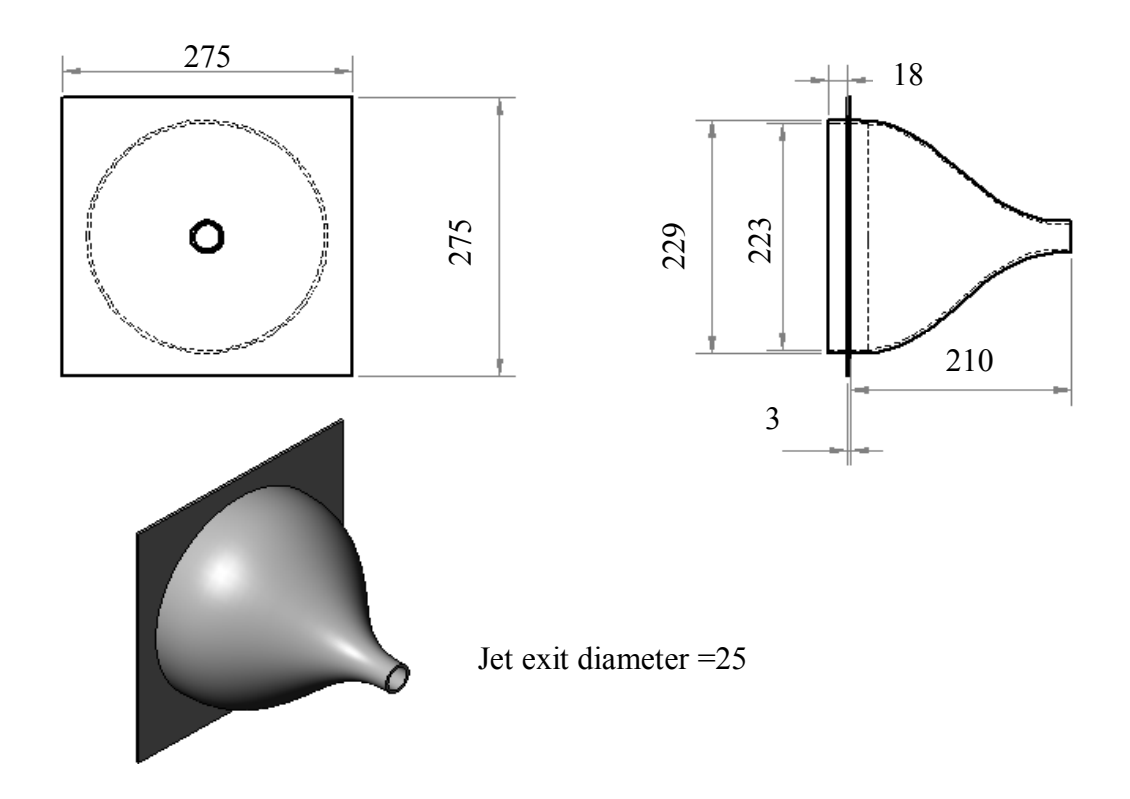


Figure A. 1 Detailed CAD drawing of the jet (dimensions in mm): end (top left) and side (top right), and isometric (bottom) views

Appendix B: Synchronization Set-up

Figure B.1 depicts three dimensional drawing of the flow visualization setup; the figure depicts the physical arrangement of the hardware while Figure B.2 displays a block diagram of the synchronization of the flow-visualization and pressure-measurement in the same setup. A stainless steel 'smoke wire', with 0.1mm diameter, is placed horizontally in the symmetry plane of the axisymmetric jet at a location immediately downstream of the exit. The wire is coated with small drops of model-train oil, which form streaklines when heating the wire using a DC voltage that is applied across the wire for 2 seconds. Simultaneously, a Sony CCD camera (model: XC-75/75CE) coupled with a standard video (EIA) National Instruments frame grabber (model: IMAQ PCI-1408) is used to capture the top view of the streaklines, which are illuminated using a light sheet emerging from a fiber-optic-coupled strobe light (Perkin-Elmer MVS-2060). Capturing of flow visualization images, at standard video rate of 30 frames/second, is synchronized with the acquisition of time series from the microphone array. The latter is accomplished employing a PC-based National Instruments 12-bit data acquisition board (PCI-6024E) at sampling frequency of 5 KHz.

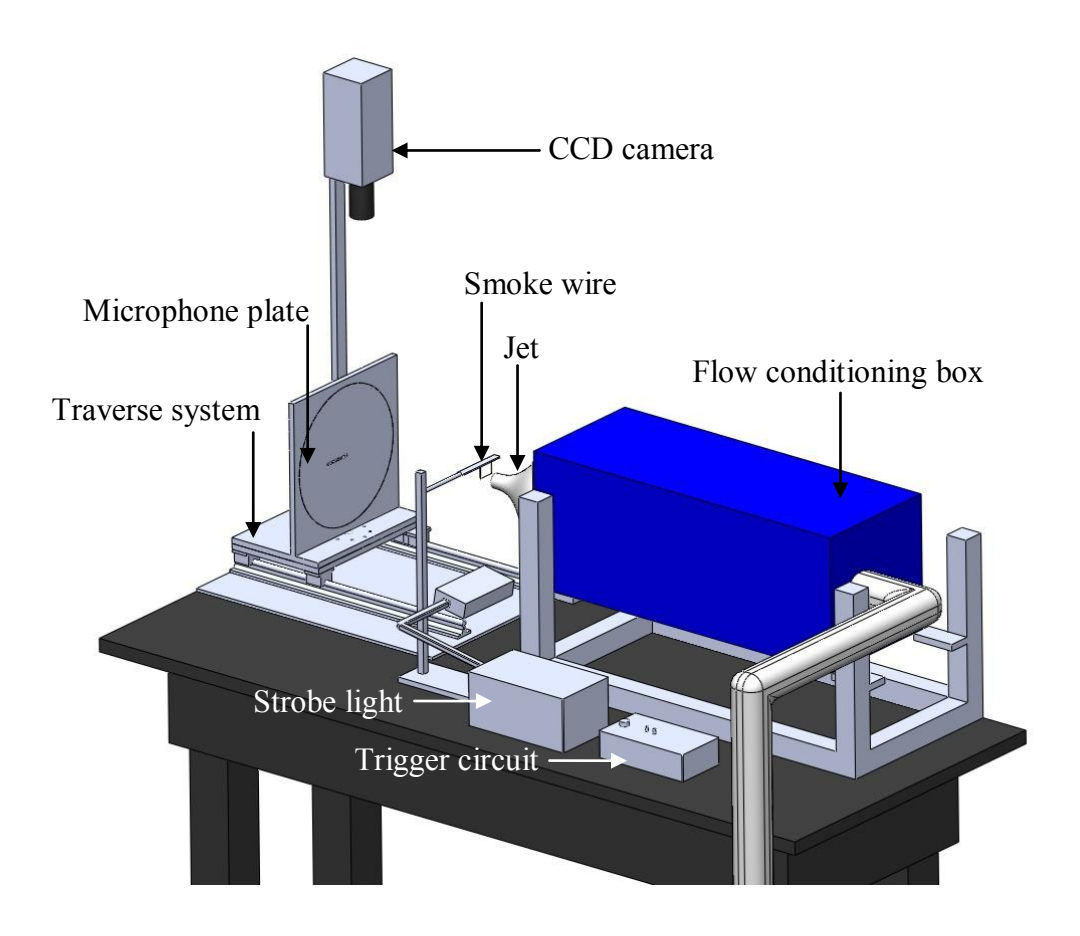


Figure B. 1 Three dimensional drawing of the flow visualization setup

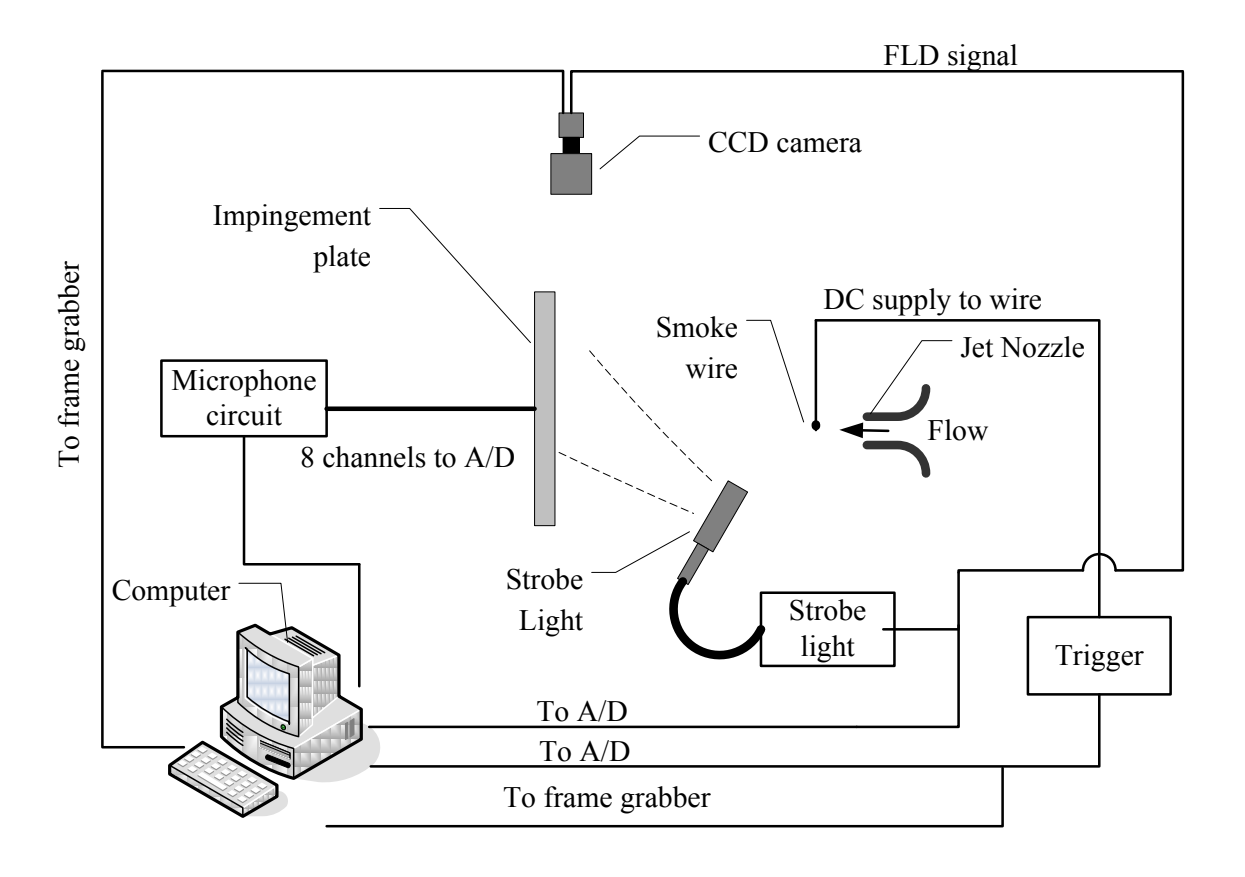


Figure B. 2 Block diagram of flow-visualization and pressure-measurement setup

Synchronization of image and data acquisition is based on employing the field (FLD) signal of the CCD camera as a 'master clock'. The FLD signal is used to trigger the strobe light at video rate, ensuring a light pulse for each camera frame. By acquiring this signal simultaneously with the microphone data, it is possible to identify the times at which images are captured by the camera. The precise time of the image capture is the instant at which the 12 µsec wide strobe light pulse occurs. This is determined by connecting the FLD signal and the output of a photodetector, while illuminated by the strobe light, to an oscilloscope. An image of the oscilloscope screen is shown in Figure B.3 where top line represents the FLD signal and bottom line corresponds to the photodetector output. As seen from the figure, the light pulse occurs less than 50 µs (the width of a grid cell in the scope display) after the falling edge of the FLD signal.

Since this time difference is negligible relative to the flow time scales (less than 0.4 *ms* in the flow investigated), the image capture instant is taken as that of the falling edge of the FLD signal.

Two LabVIEW programs are employed at the same time in order to capture the synchronized flow-visualization images and pressure data; one program is designed to grab images while the other is used to acquire the pressure and synchronization signals. The image acquisition program is started first in idles state awaiting an external signal to trigger the frame grabber. The trigger is provided from a manual switch that causes a negative-going pulse to be sent to the grabber board, while simultaneously initiating the heating of the smoke wire. The trigger pulse is also captured simultaneously with the FLD signal and microphone data, the recording of which is initiated after the image-grabbing program is started but before the trigger switch is depressed. An example is shown in Figure B.4 of the acquired trigger (blue line) and FLD (green line) signals. After the trigger is set (corresponding to the voltage drop from approximately 5 to zero volts in Figure B.4), each falling edge occurrence of the green trace represents a flow visualization image that is captured up to a pre-set total number of images. If the trigger signal falling edge occurs ahead of the rising edge of the FLD signal, the image count starts from the first FLD falling-edge encountered after that of the trigger signal; however if the trigger signal occurs ahead of the falling edge of the FLD signal, the image count starts from the second FLD falling-edge encountered after the trigger signal. This adjustment was necessary to accommodate a delay in the capturing that was determined through validation tests of the synchronization process.

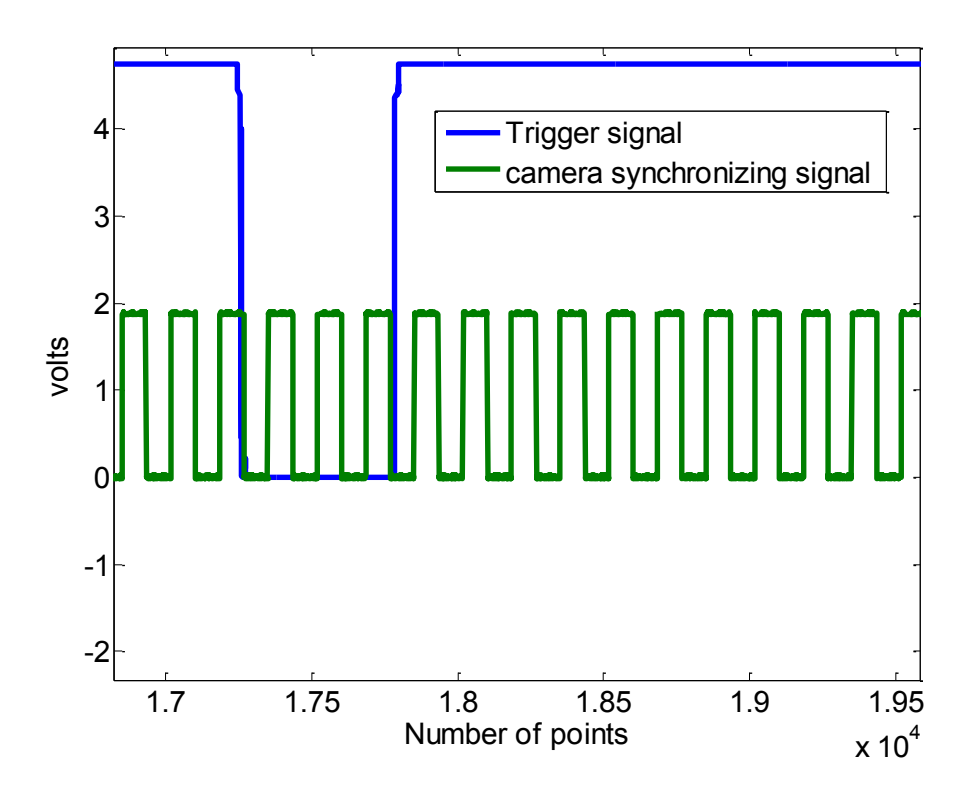


Figure B. 3 A sample of trigger and FLD signals used to synchronize image and data acquisition

Appendix C: Wave-path interpolation method

In order to demonstrate that the wall-pressure spatial interpolation method described in section 5.1 works perfectly for interpolating a constant-amplitude propagating wave, synthetic sine wave signals with frequency of 250Hz are generated at 10 kHz sampling frequency to represent the pressure time series at 29 spatial locations in the path of a constant-amplitude pressure wave propagating in the radial direction with constant convection velocity. The convection velocity is arbitrarily chosen such that the phase difference between the signals measured at two successive spatial locations is $\pi/6$. Figure C.1 shows the generated sine wave signals for the first five radial locations for demonstration purposes; signals plotted using filled circles indicate the locations where measurements of the pressure are available.

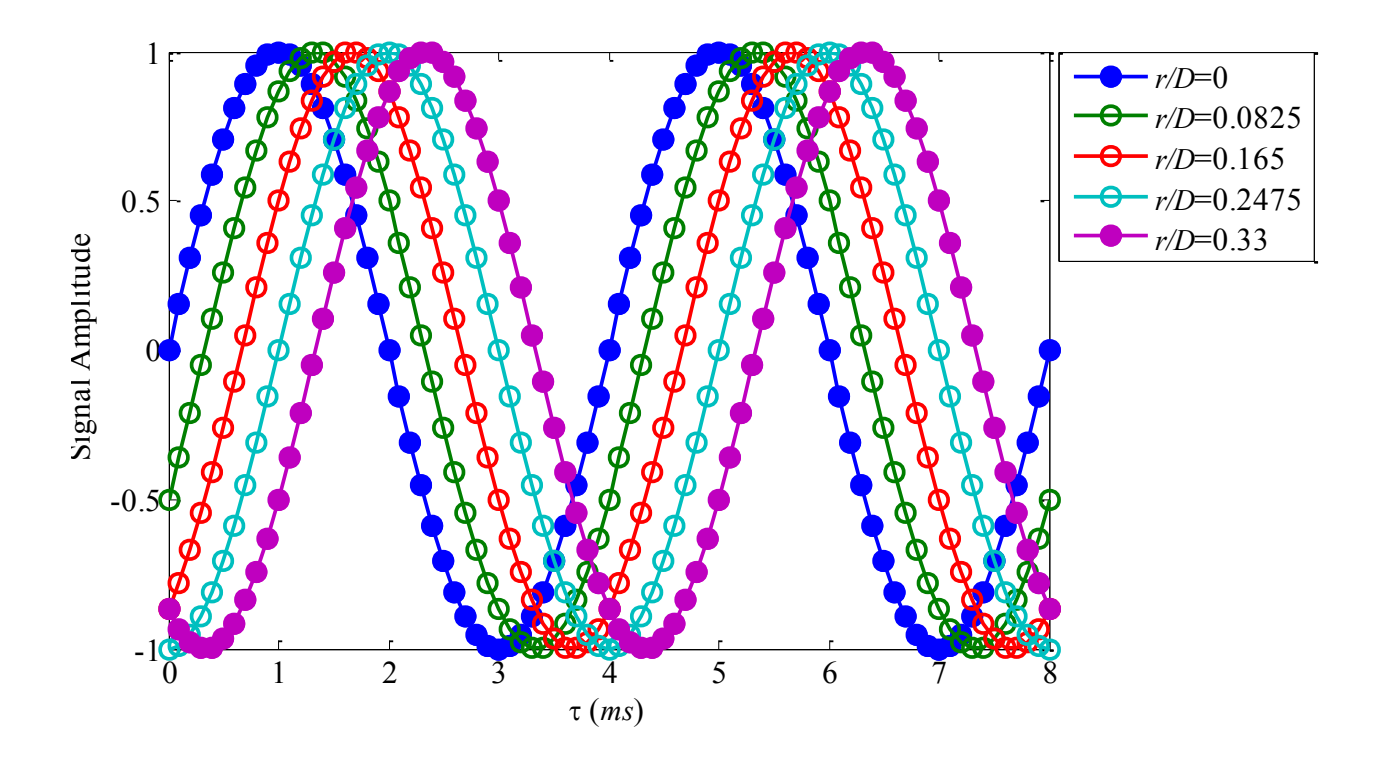


Figure C. 1 Synthetically generated sine wave signals with $\pi/6$ phase delay in between to simulate the spatio-temporal pressure variation created by a traveling pressure wave

To replicate the interpolation process implemented on the experimental data, the generated signals at r/D=0, 0.33, 0.67, 1, 1.33, 1.67, 2 and 2.33 (the first two of which are depicted using filled symbols in Figure C.1) are employed to interpolate and obtain three additional signals (exemplified by the signals shown with open symbols in Figure C.1) between successive radial locations where measurements are available, taking into account the phase delay between the two measured signals (as described earlier in this section). Figure C.2 depicts a comparison between the *true* spatial signal, known from the generated sine waves, and the one recovered from the interpolation technique. There is excellent agreement between the two which demonstrates the

ability of the technique to recover the spatial structure of the wave with very coarse spatial measurements for constant-amplitude convecting waves.

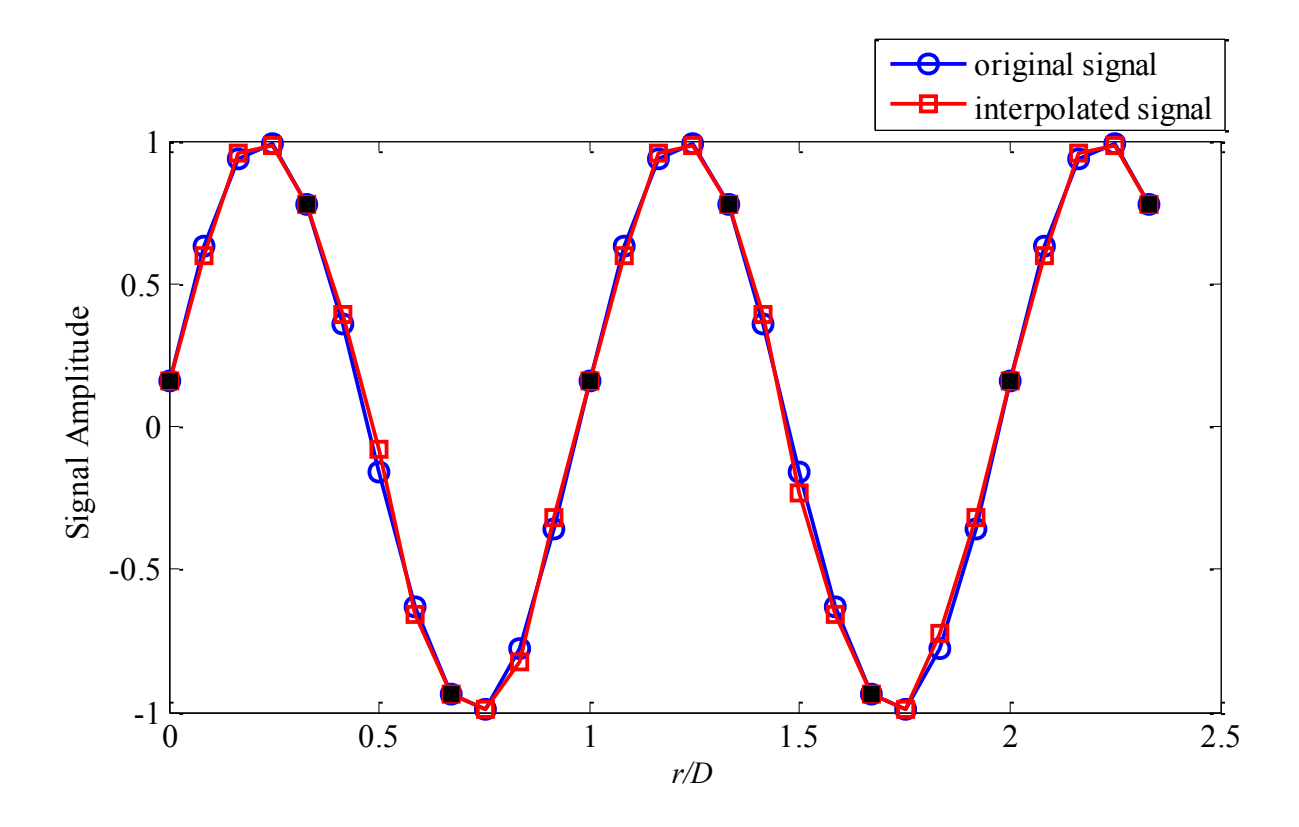


Figure C. 2 Comparison between the spatial profile of the generated and the interpolated sine waves

Appendix D: Temporal and Spatial Signature at

H/D=3 and Normal Impingement

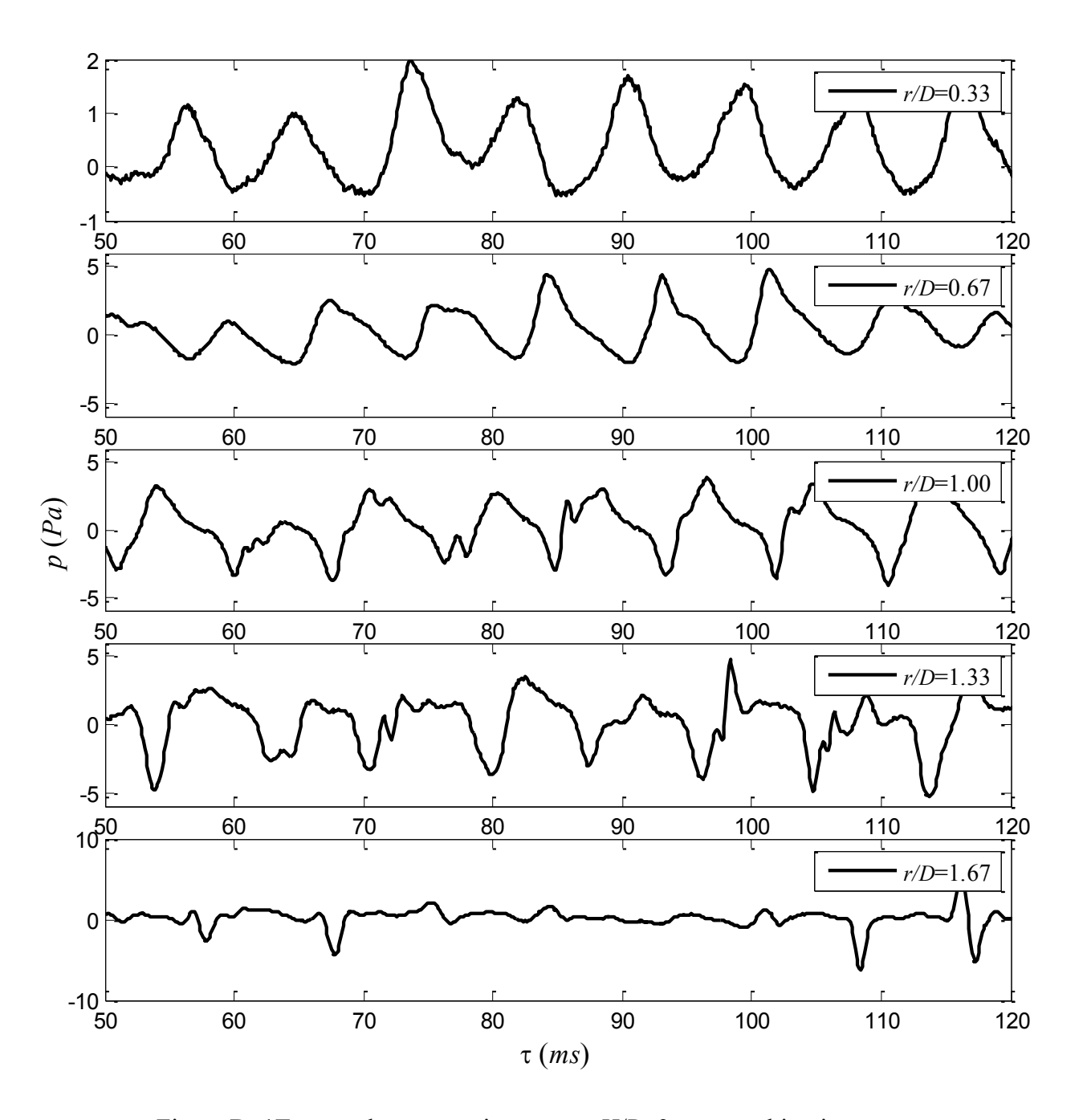


Figure D. 1Temporal pressure signature at *H/D*=3 at normal impingement

Appendix E: Comparison Between the Experimental and Computational Data Reported by Shrikhande [30]

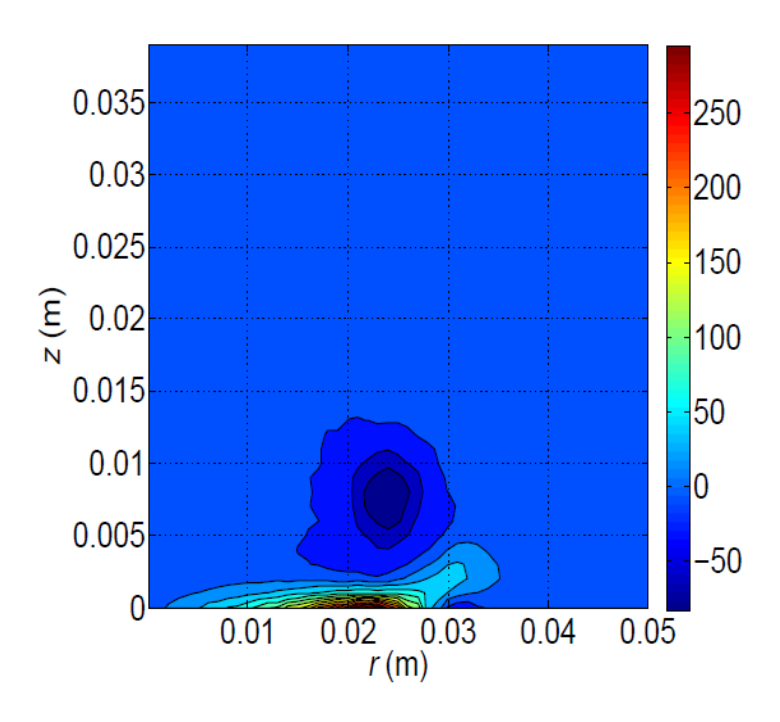


Figure E. 1 Vorticity (ω_{θ}) contour of the experimental flow-field at t=0.3 s (measured relative to the time of occurrence of the velocity field used to set the initial Gausian vortex parameters for the computation: t=1.4s relative to the solenoid opening) [30]

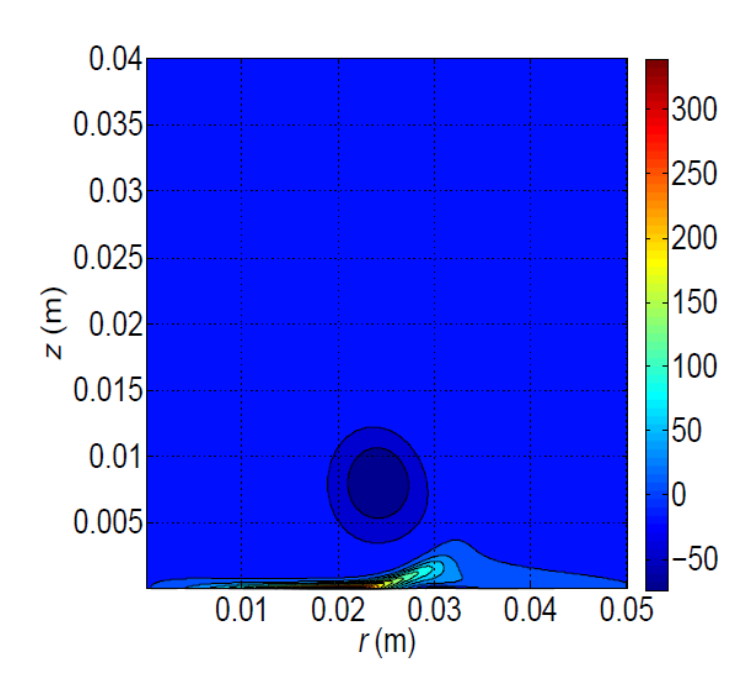


Figure E. 2 Vorticity (ω_{θ}) contour of the simulated flow-field at t=0.3s [30]

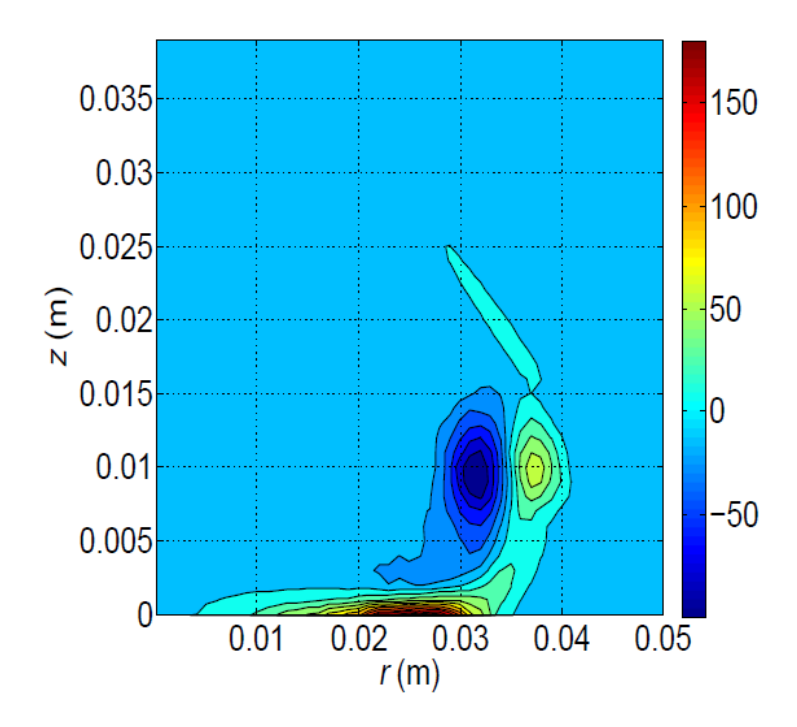


Figure E. 3 Vorticity (ω_{θ}) contour of the experimental flow-field at t=0.5 s (measured relative to the time of occurrence of the velocity field used to set the initial Gausian vortex parameters for the computation: t=1.4s relative to the solenoid opening) [30]

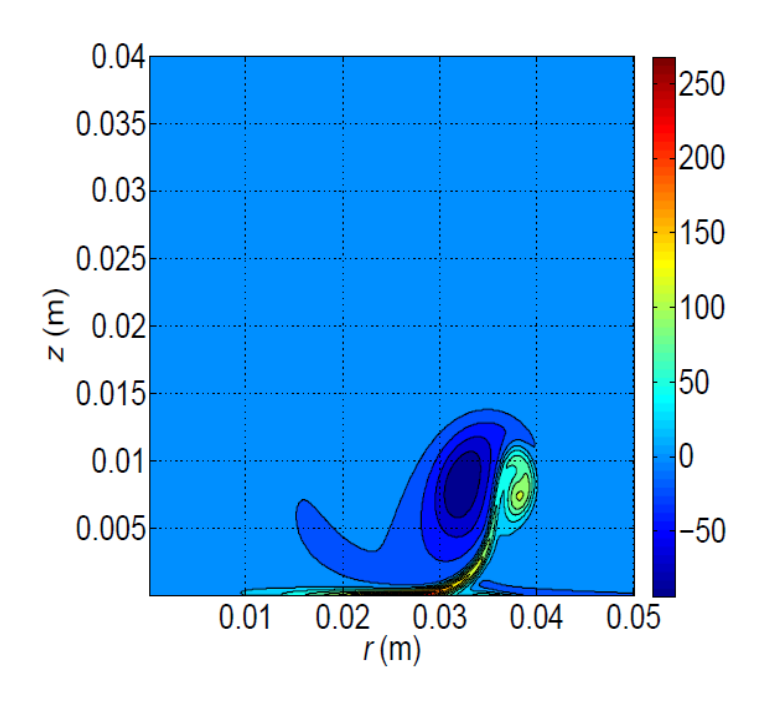


Figure E. 4Vorticity (ω_{θ}) contour of the simulated flow-field at t=0.5s [30]

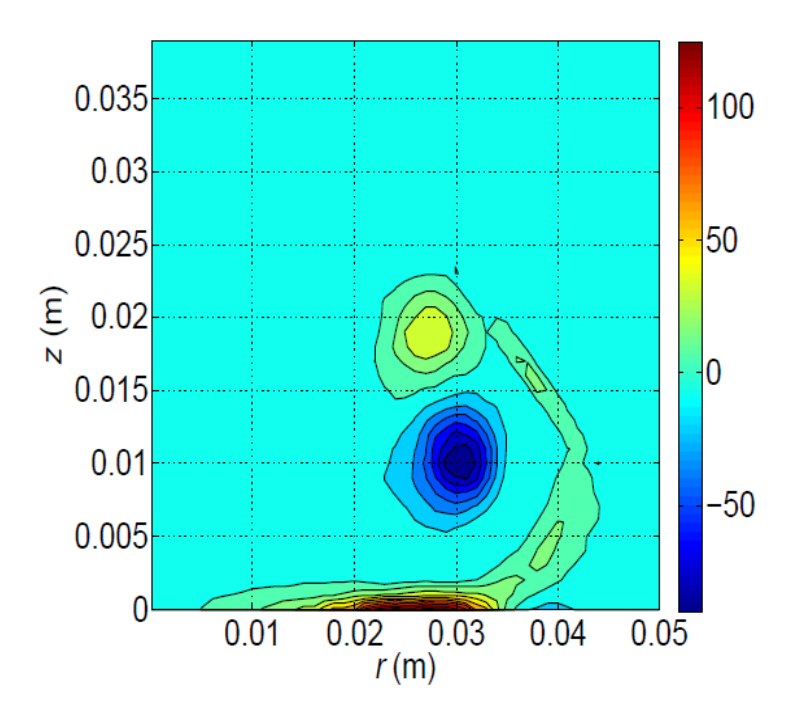


Figure E. 5 Vorticity (ω_{θ}) contour of the experimental flow-field at t=0.8 s (measured relative to the time of occurrence of the velocity field used to set the initial Gausian vortex parameters for the computation: t=1.4s relative to the solenoid opening) [30]

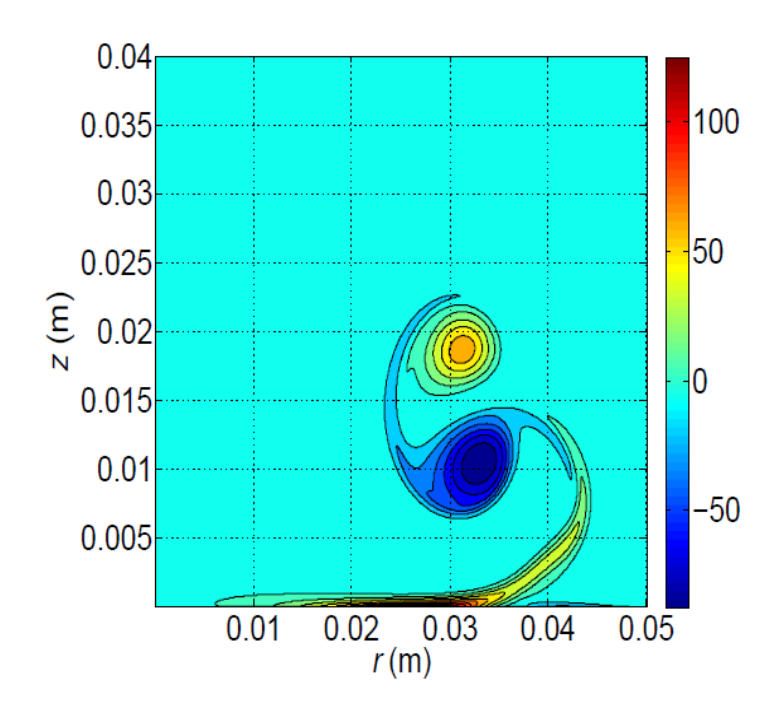


Figure E. 6 Vorticity (ω_{θ}) contour of the simulated flow-field at t=0.8s [30]

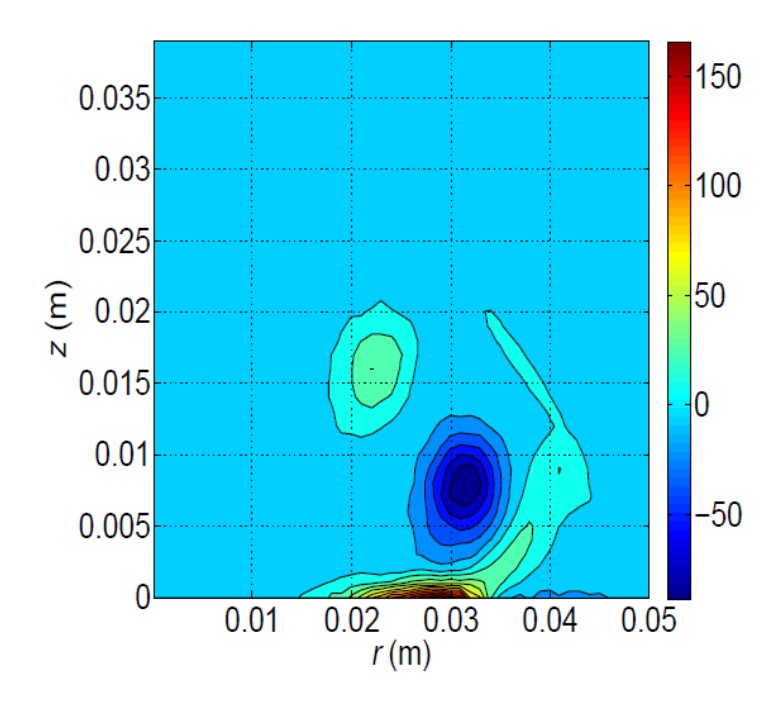


Figure E. 7 Vorticity (ω_{θ}) contour of the experimental flow-field at t=1 s (measured relative to the time of occurrence of the velocity field used to set the initial Gausian vortex parameters for the computation: t=1.4s relative to the solenoid opening) [30]

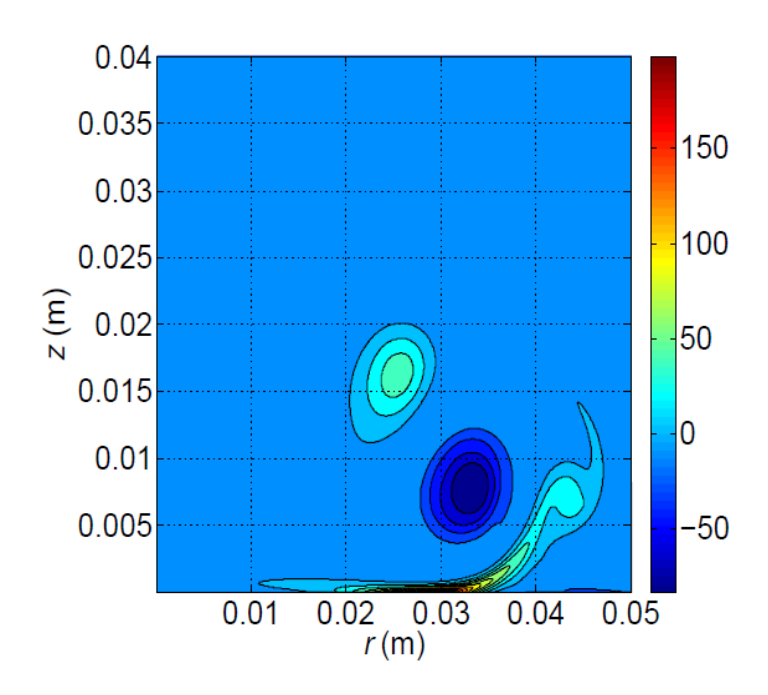


Figure E. 8 Vorticity (ω_{θ}) contour of the simulated flow-field at t=1s [30]

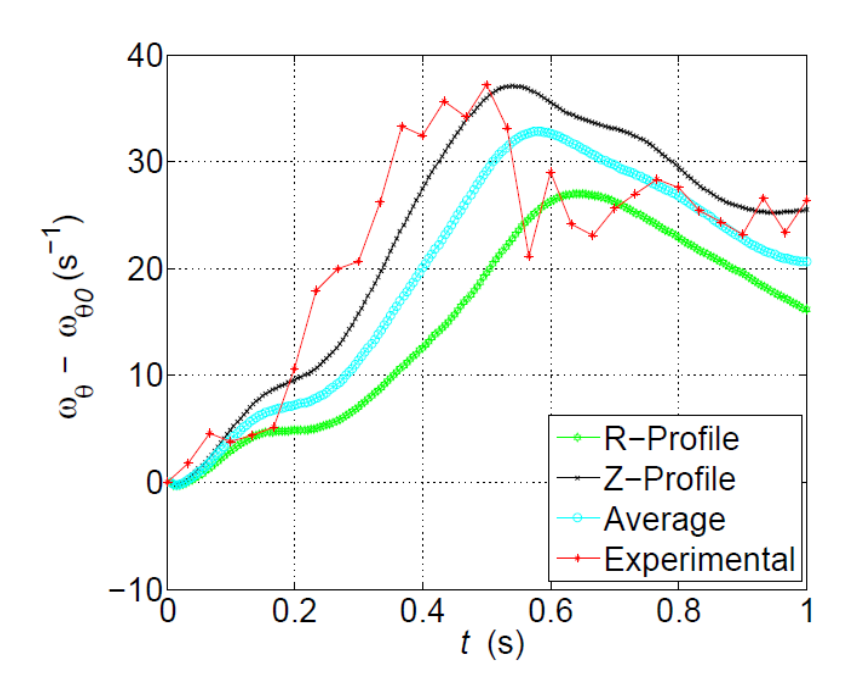


Figure E. 9 Comparison of the temporal evaluation of the vorticity at the center of the primary vortex. Results from simulations based on three-parameter r, z and avg (r,z) Gaussian profiles are compared with those from MTV experiments [30]

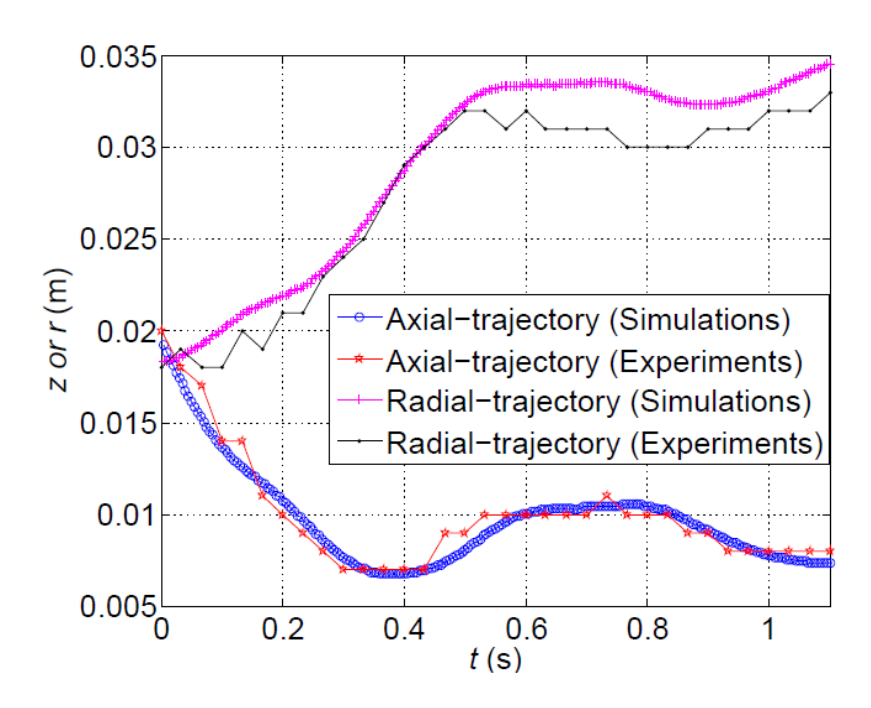
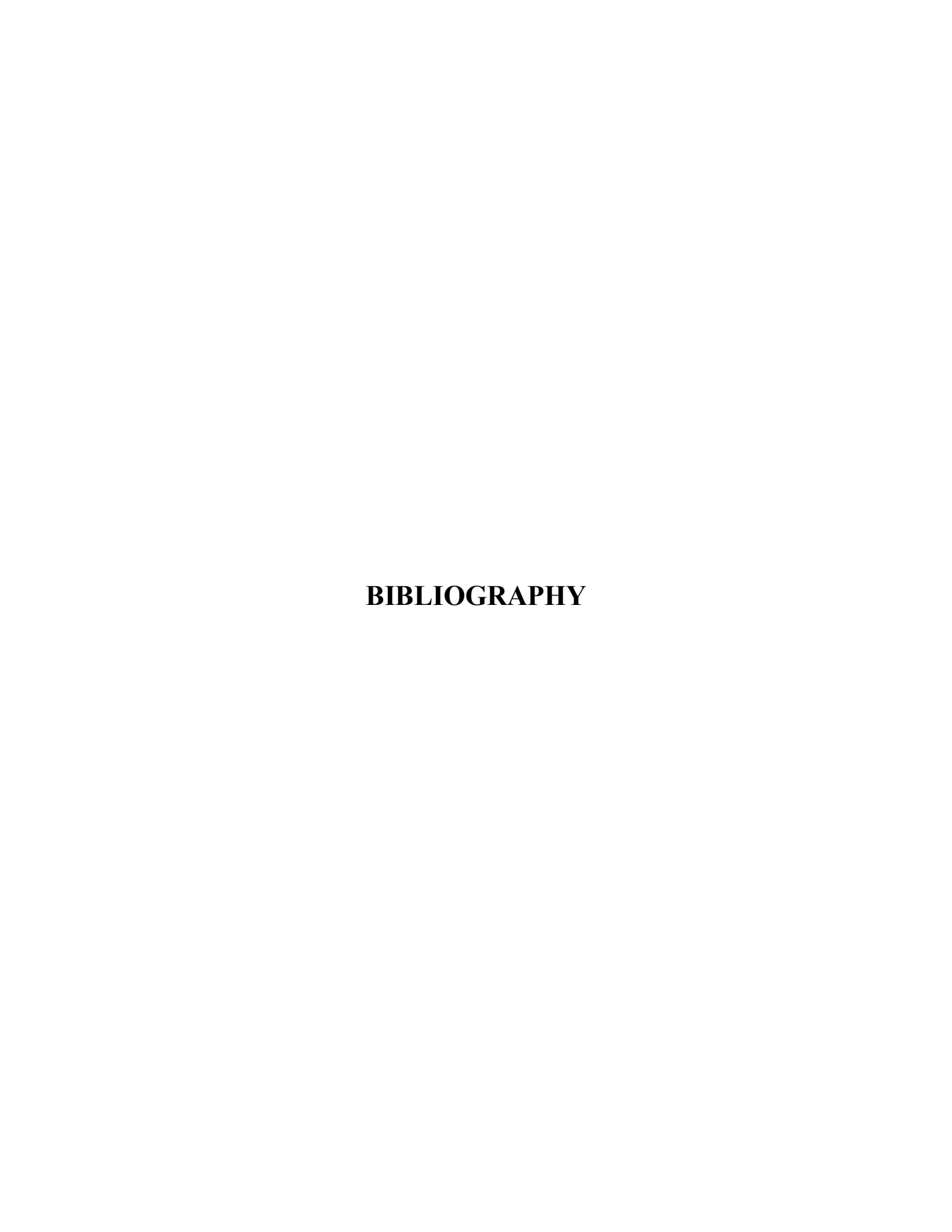


Figure E. 10 Axial- (z), and radial- trajectories of the center of the primary vortex



BIBLIOGRAPHY

- ¹Drubka, R.E, Reisenthel, P, and Nagib, H.M., "The Dynamics of Low Initial Disturbance Turbulent Jets," *Physics of Fluids*, Vol. 1, No 10, 1989, pp. 1723,1735
 - ²Drazin, P. G., & Reid, W. H., "Hydrodynamic stability". *Cambridge university press*.2004
- ³Michalke, A.," The Instability of Free Shear Layers." *Progress in Aerospace Sciences*, Volume 12, 1972, Pages 213-216
- ⁴Popiel, C.O., and Trass, O., "Visualization of a Free and Impinging Round Jet," *Experimental Thermal and Fluid Science*, Vol. 4, 1991, pp. 253, 264
- ⁵Ho, C. M., & Huang, L. S., "Subharmonics and vortex merging in mixing layers". *J. Fluid Mech*, 119, 1982., Pages: 443-473.
- ⁶Kusek, S. M., Corke, T. C., & Reisenthel, P., "Seeding of helical modes in the initial region of an axisymmetric jet. *Experiments in Fluids*, Vol10(2-3),1990, Pages:116-124.
- ⁷Bradshaw, P., and Koh, Y.M., "A Note on Poisson's Equation for Pressure in a Turbulent Flow," *Physics of Fluids*, Vol. 24, No. 4, 1981, p. 777
- ⁸Blake, W. K., "Mechanics of flow-induced sound and vibration—Volume II—Comple flow structure interactions," *Applied Mathematics and Mechanics*, Vol. 17 ~Academic, Ne York, 1986.
- ⁹Naguib, A.M., and Koochesfahani, M.M., "On Wall-Pressure Sources Associated with the Unsteady Separation in a Vortex-Ring/Wall Interaction," *Physics of Fluids*, Vol. 16, 2004, pp. 2613, 2622
- ¹⁰Hall, J.W., and Ewing, D., "The Development of the Large-scale Structures in Round Impinging Jets Exiting Long Pipes at Two Reynolds Numbers", *Experiments in Fluids*, Vol. 38, 2005, pp. 50, 58
- ¹¹Hall, J.W., and Ewing, D., "On the Dynamics of the Large-Scale Structures in Round Impinging Jets," *Journal of Fluid Mechanics*, Vol. 555, 2006, pp. 439, 458

- ¹²El-Anwar, M., Zhang, K., Naguib, A., and Abouel-Fotouh, A.M., "Pressure Fluctuations Produced by a Jet Impinging on a Wall at Normal and Oblique Incidence," *7th World Conference on Experimental Heat Transfer, Fluid Mechanics and Thermodynamics*, 28 June 3 July, 2009, Krakow, Poland
- ¹³Jiang, W., Zhang, K., Naguib, A., El-Anwar, M., and Abouel-Fotouh, A.M., "Array Measurements of the Unsteady Surface Pressure in a Sharp-edged Impinging Jet," *40th Fluid Dynamics Conference and Exhibit*, AIAA paper 2010-4851, 28 June 1 July, 2010, Chicago, Illinois
- ¹⁴Harvey, J. K., & Perry, F. J.. "Flowfield produced by trailing vortices in the vicinity of the ground". *AIAA Journal*, Vol 9(8),1971,Pages: 1659-1660.
- ¹⁵Didden, N., and Ho, C., "Unsteady Separation in a Boundary Layer Produced by an Impinging Jet," *Journal of Fluid Mechancis*, Vol. 160, 1985, pp. 235, 256
- ¹⁶Landreth, C.C., and Adrian, R.J., "Impingement of a Low-Reynolds Number Turbulence Circular Jet onto a Flat Plate at Normal Incidence," *Experiments in Fluids*, Vol. 9, 1991, pp. 74, 84
- ¹⁷Fabris, D., Liepmann, D., and Marcus, D., "Quantitative experimental and numerical investigation of a vortex ring impinging on a wall". *Physics of Fluids*, Vol. 8 No 10, 1996, pp. 2640, 2649
- ¹⁸Lim, T.T., "An experimental study of a vortex ring interacting with an inclined wall" *Experiments in Fluids*, Vol 7, 453-463, 1989
- ¹⁹Couch L. D., and Krueger P. S., "Experimental investigation of vortex rings impinging on inclined surfaces". *Experiments in Fluids*, Vol. 51, 2011, pp. 1123, 1138
- ²⁰Yan, X., Baughn, J.W., and Mesbah, M., "The Effect of Reynolds Number on the Heat Transfer Distribution from a Flat Plate to an Impinging Jet. Fundamental and applied heat transfer research for gas turbine engines," *ASME Heat Transf. Div.*, Vol. 226, 1992, pp. 1, 7
- ²¹Viskanta, R., "Heat Transfer to Impinging Isothermal Gas and Flame Jets," *Experimental Thermal and Fluid Science*, Vol. 6, 1997, pp. 111, 134
 - ²³Lytle, D., and Webb, B.W., "Air Jet Impingement Heat Transfer at Low Nozzle-Plate

- Spacings," International Journal of Heat and Mass Transfer, Vol. 37, 1994, pp. 1687, 1697
- Webb, B.W., and Ma, C.F., "Single-phase Liquid Jet Impingement Heat Transfer," *Advances in Heat Transfer*, Vol. 26, 1995, pp. 105, 217
- ²⁵Al-Aweni, M.O., and Naguib, A.M,."Simultaneous Flow Visualization and Unsteady-Surface-Pressure Measurements in Normal and Oblique Impinging Jets", AIAA 2012-1227, 50th *AIAA Aerospace Sciences Meeting including the New Horizons Forum and Aerospace Exposition*, 09 12 January 2012, Nashville, Tennessee.
- ²⁶Daoud, M., and Naguib, A.M., "A Doppler Sensor for High Spatial Resolution Measurements of Unsteady Surface Pressure", *Measurement Science and Technology*, Vol. 14, 2003, pp. 13, 23
- ²⁷Kinsler, L. E, Frey, A, R., Coppens, A. B. and Sanders, J. V., "Fundamentals of Acoustics", 3rd edition, John Wiley and Sons, New York, 1982.
- ²⁸Warhaft, Z.," Passive Scalars In Turbulent Flows", *Annu. Rev. Fluid Mech.* 2000. 32:203–240
- Green, S.I., (1996)." Fluid Vortices," ISBN 0-7923-3376-4, *Kluwer Academic Publisher*. The Netherlands
- ³⁰Lock, R.C.," The Velocity Distribution in The Laminar Boundary Layer Between Parallel Streams", Qurt. Joun. Mech and Applied Math, Vol IV Pt.1, 1951
- ³¹Cimbala, J.M., Nagib, H.M., Roshko, A.," Large Structure in the Far Wakes of Two-Dimensional Bluff
- ³²Shrikhande, G.," Assessment of Taylor-Series Model for Estimation of Vortex Flows Using Surface Stress Measurements," Michigan State University, East Lansing, 2012
- ³³Narayanan, S., Hussain, F.," Chaos Control in Open Flows: Experiments in a Circular jet", *28th AIAA Fluid Dynamics Conference*", AIAA paper 97-1822, Houston, Texas
- ³⁴Benedict L. H., Gould R. D., "Towards better uncertainty estimates for turbulence statistics", *Experiments in Fluids*," Vol. 22 (1996) 129-136

³⁵O'Donovan, T.S., and Murray, D.B., "Fluctuating Fluid Flow and Heat Transfer of an Obliquely Impinging Air Jet," *International Journal of Heat and Mass Transfer*," Vol. 51, 2008, pp. 6169, 6179

³⁶Gendrich, C. P., Bohl, D., and Koochesfahani, M. M. [1997] Whole _eld measurements of unsteady separation in a vortex ring/wall interaction, *AIAA* Paper No. AIAA-97-1780.

³⁷Saffman, P. G. The Velocity of Viscous Vortex Rings. In Aircraft Wake Turbulence and its Detection, eds. J. H. Olsen, A. Goldberg, and M. Rogers, New York, Plenum, pp. 9-10, 1971.